Molybdenum Nitrides: Structural and Reactivity Studies

Stuart Michael Hunter

BSc (Hons.), MSc

Submitted in fulfilment of the requirements for the

Degree of Doctor of Philosophy

School of Chemistry

College of Science and Engineering

University of Glasgow

February 2012

Abstract

This thesis describes the preparation, structure and activity of a range of binary, ternary and quaternary molybdenum nitrides. It has been shown that all of the samples analysed can be formed through the reaction of the respective molybdate precursor with either ammonia or 3:1 H_2/N_2 gas mixture.

The structures of the nitrides have been studied in detail. These structural findings were then linked to the activity potential of the materials to act as stores of activated nitrogen. The main body of work focused on the ternary molybdenum nitrides of cobalt, iron and nickel with a view to understanding their differences and similarities. Full structural analysis was performed using powder X-ray diffraction (PXRD) and neutron diffraction (PND).

The activity of the nitrides was examined by reaction with 3:1 H_2/N_2 and with 3:1 H_2/Ar at various temperatures. Particular attention was paid to the reactivity of lattice nitrogen. The cobalt molybdenum nitride was shown to be special case in this regard where the nitrogen is mobile and relocates within the lattice to a different crystallographic site. This mobility and relocation is concomitant with the loss of 50% of the lattice nitrogen from the system resulting in a phase change from Co_3Mo_3N to the unprecedented Co_6Mo_6N phase. The physical and chemical properties of this novel phase have been fully characterised and studied. Interestingly, the isostructual Fe_3Mo_3N behaves differently and the nitrogen remains fixed and the structure and stoichiometry constant throughout the testing procedure. Further studies of the ternary molybdenum nitrides extended to nickel molybdenum nitride, which was shown to be the least active when tested under both gas mixtures, and analogously to the iron molybdenum nitride the nitrogen is fixed within the β-Mn structured nitride.

Further investigations were undertaken, resulting in the successful formation of a series of quaternary nitrides ($Fe_{3-x}Co_xMo_3N$). These materials show properties similar to the Co-Mo-N system when the material is cobalt rich and behave similarly to the Fe-Mo-N system when iron rich.

Declaration

The work contained in this thesis, submitted for the degree of Doctor of Philosophy, its own original work, except where due reference is made to other authors.

Magnetic Measurements were conducted with the help of Dr Mark Murrie and analysis completed with the assistance of Professor Duncan Gregory (both located at: School of Chemistry, University of Glasgow, UK).

Isotopic Exchange Reactions were conducted with the kind assistance of Professor Daniel Duprez and Dr Nicolas Bion, analysis was conducted by Dr Nicolas Bion (both located at: LACCO, University of Poitiers, France).

No material within has been previously submitted for a degree at this or any other institution.

Stuart Michael Hunter

List of Figures

List of Tables

Publications

Towards nitrogen transfer catalysis: reactive lattice nitrogen in cobalt molybdenum nitride.

D. Mckay, D. H. Gregory, J. S. J. Hargreaves, S. M. Hunter, X. L. Sun; Chem. Commun.; 29 (2007) 3051.

Topotactic nitrogen transfer; structural transformation in cobalt molybdenum nitrides.

S. M. Hunter, D. Mckay, R. I. Smith, J. S. J. Hargreaves and D. H. Gregory; Chem. Mater.; 22 (2010) 2898.

On the regeneration of Co_3Mo_3N from Co_6Mo_6N with N_2.

D. H. Gregory, J. S. J. Hargreaves and S. M. Hunter; Catal. Lett.; 141 (2011) 22.

Further future publications anticipated.

Acknowledgements

1   Introduction

1.1   Background

1.1.1   Nitrides

Significant and rapid progress in nitride chemistry has been made over the last decade or so with improved classification and development of new synthetic routes leading to new nitride materials. The synthesis of nitrides is still very complex with large thermodynamic barriers which occur from the making and breaking of N≡N bonds (945 KJmol^{-1} for N≡N compared to 498 kJmol^{-1} for O=O).[1] Many nitrides, especially those containing s-block elements, are air and moisture sensitive, and rapidly form oxides, hydroxides and ammonia upon contact with oxygen or moisture. These factors can therefore contribute to the low abundance of nitride compounds, compared to those of the oxides or carbides.[2] Recent developments in the handling methods for air sensitive samples and improved diffraction techniques have led to a revival in the area of nitride chemistry and thus a large increase in research.

Nitrides can be sub-divided into ionic, covalent and interstitial types.[2,3] An alternate general classification of nitrides, based on bonding classification, as ionic, covalent and metallic has also been applied. Ionic or "salt-like" nitrides formed by electropositive elements such as Li, Mg, Ca, Sr, and Ba all possess formulae which correspond to those expected on the basis of the combination of the metal ion with N^{3-} ions. However, metals such as Cu, Zn and Hg also form ionic or salt-like nitrides. Nitrides of the Group III metals are also salt-like but are either metallic conductors, or at least semi-conductors, and therefore represent the transition to the metallic or interstitial nitrides.

Interstitial nitrides are formed by some transition metals and generally refer to those which have structures in which the nitrogen atoms reside in the interstitial space in close packed metal structures. In moving from left to right along the 1st row transition series, the size of the metal atom decreases and it becomes increasingly difficult for the nitrogen atom to be accommodated into the metal lattice; hence the thermal stability of the nitride also decreases. As a consequence of the smaller atomic radii, nitrides of Group VII-X transition metals do not form interstitial compounds but are generally classed with the ionic or salt-like nitrides (e.g. Cu_3N as mentioned above).

Non-metallic Group XIII and XIV elements, such as B, Si, P and C, form nitrides which are characterised predominately by their covalent bonding. Due to the chemical

inertness and the high heat capacity of these materials, many covalent type nitrides, in particular BN and Si_3N_4, have been investigated as catalyst supports and are used within the ceramic industry.[12] However it is quite often that more than one type of bond exists within the compound which can make classification by this method somewhat arbitrary. These sub-divisions are to a lesser or greater extent random and the nitrides/oxynitrides/carbonitrides are further classified as binary (containing one metal within the main structure), ternary[4] (containing two metals) and quaternary (containing three metals). Nitrides which are described as interstitial have attracted the greatest interest within catalytic studies.

The progression to studying higher nitrides was initially hampered by issues with synthetic procedures and the analytical methods used. This however has meant that numerous binary nitrides of metals and non-metals are well characterised. Many have very useful applications such as semiconductors (Cu_3N, GaN),[5,6] optoelectronic devices (TiN, BN, AlN, GaN and InN)[7,8,9,10] and high temperature refractory ceramics (AlN, BN and TiN, Si_3N_4).[2,11,12]

Alkali metal nitrides are dominated by lithium nitride, Li_3N. There two methods of producing Li_3N, the reaction of nitrogen with lithium dissolved in liquid sodium[13] and the high temperature reaction of solid lithium under nitrogen. The existence of heavier alkali metal nitrides is debatable due to their low thermodynamic stability. Recent work has been conducted into sodium nitride[14,15,16] and potassium nitride.[17] Sodium nitride has been synthesised via the deposition of the desired elements as an atomic level dispersion and the resulting solids formed at liquid nitrogen temperatures with ordered structures being formed on heating.[18] However, more recently, a plasma assisted synthesis has been described by Vajenine,[15] in which elemental sodium with gaseous nitrogen is activated by capacitive high frequency discharge at pressures of up to 4 mbar without heating.

Alkaline earth nitrides have also been synthesised by reactions involving non-gaseous sources of nitrogen, e.g. decomposition of sodium azide.[19,20] Sodium flux reactions also take advantage of this decomposition, from which the sodium is derived. This method has been shown to be a superior way of producing single crystals of a good enough quality for single crystal X-ray diffraction analysis. NaN_3 decomposition reactions generate high pressures when the metal and gaseous N_2 form, thus autoclaves or sealed vessels are used.

More reactive gaseous nitrogen sources, such as ammonia or mixtures of hydrogen and nitrogen, have been used in reactions with oxide, halide or sulfide precursors to form both binary and ternary transition metal nitrides. These have been reported to be successful at much lower temperatures than the more traditional solid state synthesis methods.[21,22,23] This approach is limited to a very specific temperature range outside of which an incomplete reaction, a partially crystalline product, or thermal decomposition is observed. Oxynitrides especially can be very difficult to distinguish from nitride products, leading to the theory that many nitrides assigned in the literature are possibly imides, amides and oxynitrides.[24]

1.1.2   Nitride catalysts

The current interest in nitrides for catalysis has centered around two themes:

    (i)   the ability of some transition metal nitrides to exhibit properties similar to those of platinum group metals

    (ii)   the acid-base properties of nitrides and oxynitrides.

The literature has been mostly concerned with the applications of a very small number of nitride/oxynitride compounds to a restricted number of reactions. However recent work has seen an expansion in the range of reactions catalysed by nitrides and also the application of nitrides to established catalytic reactions and as such this is a vibrant field with many significant advances reported. However the catalytic behaviour of most of the reported nitride based materials is largely unknown; the literature focuses mainly on the preparative procedures rather than their catalytic properties.

Metal nitrides have been shown to catalyse a wide range of reactions, mainly due to researchers investigating the well documented ability of some transition metal nitrides to exhibit catalytic properties similar to those of the platinum group metals. The range of reactions studied is shown in Table 1-1.

Different nitrides have attracted significant attention as active catalysts for hydrotreating reactions within the petroleum refining industry. This process requires removal of heteroatoms from feedstream molecules and involves hydrodenitrogenation (HDN), hydrodesulfurisation (HDS) and hydrodeoxygenation (HDO). Studies have been conducted using model heterocyclic compounds such as thiophene, pyridine, quinolone and benzofuran, and it was shown that nitrides are particularly effective in HDN type reactions, which requires high temperature and pressure with commercial Co-Mo/Al_2O_3 and Ni-Mo/Al_2O_3 hydrotreating catalysts. When transition metal nitrides

of Groups IV-VI were compared for HDS and HDN activity, it was shown that the activity follows the order of Group VI > Group V > Group IV with Mo_2N showing the highest activity for both types of reaction.[25] Bulk Co_4N and Fe_3N showed higher pyridine HDN removal than Mo_2N, but these nitrides are difficult to prepare and often have low surface areas.[26] These studies illustrate the potential that bulk nitrides may have to replace commercial hydrotreating catalysts. Another exciting area in which nitrides may be utilised is in both PEM (proton exchange membrane) and DM (direct methanol) fuel cells.[27,28,29,30] There have recently been investigations into the prospect of replacing noble metals such as Pt and Ru with less expensive but durable compounds such as CrN and TiN as coatings for the stainless steel cathodes and anodes. Mo_2N/C has been investigated as an alternative cathode material by Zhong and co-workers, and it was shown to have activity for the oxygen reduction reaction in the presence of methanol.[30]

Various studies of the binary nitride compounds as catalysts have been undertaken with the gamma Mo_2N (γ-Mo_2N) phase being investigated most widely. Many of the studies of γ-Mo_2N were concerned with the structural properties.[31] The preferred synthetic method which gives a high surface area nitride is the temperature programmed ammonolysis[32] which is the method used in this work. The effects of synthetic parameters on the structural properties of the nitride have been described by Thompson *et al.*[33] γ-Mo_2N was shown to be active for ammonia synthesis at ambient pressure; other nitride materials such as vanadium and uranium nitride have been investigated for ammonia synthesis at higher pressures[34,35] although the possibility of them being active at lower pressures has not been ruled out.

The formation of beta molybdenum nitride (β-$Mo_2N_{0.78}$) has been shown to be possible via the temperature programmed reaction of MoO_3 under a flow of 3:1 H_2/N_2 gas. However, Wise and Markel reported that this procedure formed γ-Mo_2N.[36] In addition to the formation of β-$Mo_2N_{0.78}$ via the reaction with 3:1 H_2/N_2 gas, the formation of the beta phase via the decomposition of γ-Mo_2N has been reported for ammonolysis at temperatures above 1073 K[37] or via heating γ-Mo_2N to high temperatures (up to 1273 K) under an inert atmosphere.[38]

The search for catalysts to be used in the synthesis of ammonia has been pursued for the last 90 years. In 2005 the worldwide production of ammonia totalled 121 million tonnes[39] with 80% of this being used for fertilisers. New catalysts are being sought in order to allow for the current Haber-Bosch process (iron catalyst) which uses high

pressures (~250 atm) and moderate temperatures (673 - 823 K) to be superseded by a reaction which requires less harsh conditions. Schlögl in his review[40] looks at the progress of new ammonia synthesis catalysts which are being seen as a possible replacement of the current iron catalyst.

Table 1-1: Various catalytic uses for nitride based materials.

Reaction	Catalyst
Ammonia synthesis	V_2O_2,[41,42] VN,[43] γ-Mo_2N,[44,45,31] Cs/γ-Mo_2N,[46] Cs/Co_3Mo_3N,[47,48,49,50,51,52,53,54] Fe_3Mo_3N,[48,52] Ni_2Mo_3N,[48,52] Ti-TMS-1 (N_2 treated),[55] Re_3N[56]
Ammonia decomposition	VN,[43,57,58] γ-Mo_2N,[57,59,60,61] β-$Mo_{16}N_7$,[60,61] δ-MoN [60,61]
Hydrazine decomposition	Mo_2N/γ-Al_2O_3,[62,63] NbN,[64] W_2N,[62] γ-Mo_2N[63]
Amination	γ-Mo_2N, VN, W_2N, NbN, TiN[59] W_2N/γ-Al_2O_3, W_2N/TiO_2 [65]
Amoxidation	VAlON[66,67,68,69]
NO Removal	γ-Mo_2N,[70,71,72] VN,[71] Co_3Mo_3N,[70] W_2N,[71,73] Ni_3N [74]
Hydrotreating and hydrogenation	γ-Mo_2N,[75,76] Mo_2N/γ-Al_2O_3,[77] $MoO_{1.83}N_{0.36}$,[78] VN,[79] Co_3Mo_3N,[80] YbN,[81] EuN,[81] $Mo_2N_{0.6}O_{1.46}P$,[82] $WN_{1.09}O_{0.8}P_{0.28}$,[83] $CoMoN_x$ [84]
Photocatalysis	TiO_2 (nitrogen doped Anatase),[85,86,87,88,89,90] TiO_2 (nitrogen doped Rutile),[91] TaON [92,93]

One alternative for this would be molybdenum nitride.[94,95,96,97] Binary molybdenum nitrides have been long known for their ammonia synthesis efficacy.[31,46,95,98] The rate determining step was originally thought (according to Hillis *et al.*[94]) to be the conversion of adsorbed nitrogen to gas phase NH_3 rather than the actual nitrogen adsorption. Subsequently this was investigated by Aika and Ozaki[95] who argued that the adsorption of nitrogen was the rate determining step. With various molybdenum nitride structures possible the surface area and activity of the catalyst is variable. It is therefore

possible to produce high and low surface area catalysts of γ-Mo_2N. This means that the synthetic route to the nitride will have a large effect on the catalytic activity of the catalyst.[98]

The best of the nitrides reported to date is cobalt molybdenum nitride, Co_3Mo_3N.[52,98] Applying the volcano principle (in which components possessing both weak and strong nitrogen binding strengths are combined to form a catalyst with optimal binding strength) Jacobsen et al.[53] rationalised the high activity of Co_3Mo_3N. Structural nitrogen is proposed to be a requirement due to its ability to stabilise the active (111) surface plane.

Cs^+ doped Co_3Mo_3N has a remarkably high activity for ammonia synthesis[52,99] as shown in Table 1-2. It has been shown that Cs-promoted catalyst at 673 K under 3.1 MPa reaches 40% of the equilibrium yield, and is four times more active than the doubly promoted iron catalyst. The location of the dopant within the structure is not known and as such this is not discussed here.

Table 1-2: Ammonia synthesis activities of various catalysts[98].

Catalyst	Rate / $\mu mol.hr^{-1}g^{-1}$	Surface Area / m^2g^{-1}	Specific Activity / $\mu mol.hr^{-1}m^{-2}$
$Fe-K_2O-Al_2O_3$	330	14	24
Co_3Mo_3N	652	21	31
Co_3Mo_3N-K (5 mol %)	869	17	51
Co_3Mo_3N -K (30 mol %)	364	8	46
Co_3Mo_3N -Cs (2 mol %)	986	16	62
Co_3Mo_3N -Cs (10 mol %)	586	10	59

Although the number of applications in which nitrides are utilised has grown significantly, these are still somewhat limited and it is apparent that much work is needed to develop other potential uses. Interest in nitride materials in terms of catalysis has generally been directed on either the acid base properties or the noble metal like properties; there is very little evidence within the literature which has alluded to the use of nitrides as potential carriers in nitrogen transfer reactions and their possible application seems to have been largely overlooked in this respect. The potential reactivity of lattice nitrogen was first referred to in early ammonia synthesis studies by Segal and Sebba.[100] It was reported that 'extra' nitrogen was incorporated into the

surface layers of a uranium nitride catalyst, under a H_2/N_2 gas mixture, and which was subsequently found to participate in the ammonia synthesis reaction. One of the main issues associated with potential nitrogen transfer materials is the ability for the material to reversibly adsorb and desorb the reacting species. Studies by Itoh and Machida have reported on the ability of rare earth intermetallic compounds to reversibly store large amounts of nitrogen.[101,102,103] These compounds form the corresponding nitrides by heating in either N_2 or NH_3 at elevated temperatures, with the nitrogen being incorporated into the interstitial sites within the crystal lattice. The stored nitrogen can subsequently be lost in the form of ammonia when the systems are heated under hydrogen. This is one of the first examples in which nitride based materials have been shown to regenerate to their original phase, once depleted, by reaction with a gas phase nitrogen source.

1.2   Aim

This project was designed to investigate further the structure and reactivity of a number of binary, ternary and quaternary nitride based compounds containing molybdenum.

Initial investigations into the structure of the binary molybdenum nitrides, (beta, delta and gamma) were undertaken in order to confirm the structure and also give a basis for further work conducted on the ternary and quaternary systems.

The primary focus for the project was in the ternary nitride system and in particular the cobalt molybdenum nitride phase (Co_3Mo_3N) which has been shown to exhibit nitrogen storage properties. In addition to the Co-Mo-N system two other ternary systems Fe-Mo-N and Ni-Mo-N were also investigated in order to observe the differences in the structure and related properties to nitrogen storage.

The systems having been investigated previously as possible catalysts for ammonia synthesis are interesting as possible stores of activated nitrogen. The aim was to produce and characterise the samples and then, through knowing their structure and properties, to manipulate the systems to enhance their possible nitrogen storage properties.

In order for full characterisation and understanding of the systems all of the products and reactants of the synthesis were fully characterised using powder X-ray diffraction (PXRD) and powder neutron diffraction (PND) where available. The data obtained were then used to follow any changes in the structure of the samples and to give further insight into the mechanisms and processes involved. In addition to the crystallographic

data, use of complementary analyses such as thermogravimentric analysis (TGA), elemental analysis (CHN) and surface area measurements (BET) were used to obtain a detailed understanding of the system and thus explain the possible uses either as a catalyst or reagent for different processes.

The systems were tested as catalysts for the production of ammonia in mock reactions which were analysed to show the amount of activated nitrogen that could be stored within the system and under what conditions this activated nitrogen could be used and replaced.

Further to the ternary system, a series of quaternary nitrides were also investigated. In order to view the effects of varying the metals on the catalytic behaviour and activity of the system a mixed metal, Fe-Co-Mo-N, system was investigated.

1.3 References

[1] www.webelements.com [August 2010]

[2] D. H. Gregory; J. Chem. Soc. Dalton Trans.; (1999) 259.

[3] F. A. Cotton and G. Wilkinson; *Advanced Inorganic Chemistry*, 5th Ed., Wiley, New York, 1988.

[4] R. Juza, K. Langer and K. von Benda; Angew Chem. In. Ed. Eng.; 7 (1968) 360.

[5] D. J. As; Microelectronics Journal; 40 (2009) 204.

[6] M. G. Moreno-Armenta, G. Soto and N. Takeuchi; J. Alloys. Compd.; 509 (2011) 1471.

[7] A. Baiker and M. Maciejewski; J. Chem. Soc, Faraday Trans. 1; 80 (1984) 2331.

[8] R. Niewa and F. J. DiSalvo; Chem. Mater.;10 (1998) 2733.

[9] W. Lengauer; J. Alloys. Compd.; 186 (1992) 293.

[10] Z. G. Chen, L. Cheng, G. Lu and J. Zou; Chem. Eng. Journal; 165 (2010) 714.

[11] G. Husnain, F. Tao and Y. Shu-De; Physica B; 405 (2010) 2340.

[12] B. Yuan, J. X.Liu, G. J. Zhang, Y. M. Kan and P. L. Wang; Ceramics International; 35 (2009) 2155.

[13] C. C. Addison and B. M. Davis; J. Chem. Soc. (A); (1969) 1827.

[14] D. Fischer and M. Jansen; Angew. Chem. Int. Ed.;41 (2002) 1755.

[15] G. V. Vajenine; Inorg. Chem.; 46 (2007) 5146.

[16] R. Niewa; Angew Chem. Int. Ed.; 41 (2002) 1701.

[17] D. Fischer, Z. Cancarevic, J. C. Schön and M. Jansen; Z. Anorg. Allg. Chem.; 630 (2004) 156.

[18] D. Fischer and M. Jansen; Angew. Chem. Int. Ed.; 41 (2002) 1755.

[19] S. J. Clarke, G. R. Kowach and F. J. DiSalvo; Inorg. Chem.; 35 (1996) 7009.

[20] S. J. Clarke and F. J. DiSalvo; Inorg. Chem.; 37 (1997) 1143.

[21] S. H. Elder, L. H. Doerrer, F. J. DiSalvo, J. B. Parise, D. Guyomard and J. M. Tarascon; Chem. Mater.; 4 (1992) 928.

[22] R. Marchand, F. Tessier and F. J. DiSalvo; J. Mater. Chem.; 9 (1999) 297.

[23] R. Marchand, Y. Laurent, J. Guyader, P. L'Haridon and P. Verdier; J. Euro. Ceramic Soc.; 8 (1991) 197.

[24] N. E. Brese and M. O'Keeffe; *Structure and Bonding* (Berlin); 79 (1992) 307.

[25] S. Ramanathan and S. T. Oyama; J. Phys. Chem.; 99 (1995) 16365.

[26] K. Milad, K. J. Smith, P. C. Wong and K. A. R. Mitchell; Catal. Lett.; 52 (1998) 113.

[27] B. Avasarala and P. Haldar, Electrochimica Acta; 55 (2010) 9024.

[28] B. Wu, Y. Fu, J. Xu, G. Lin and M. Hou; J. Power Sources; 194 (2009) 976.

[29] V. D. Noto, E. Negro, S. Lavina, S. Gross and G. Pace; Electrochimica Acta; 53 (2007) 1604.

[30] H. Zhong, H. Zhang, G. Liu, Y. Liang, J. Hu and B. Yi; Electrochemistry Commun.; 8 (2006) 707.

[31] L. Volpe and M. Boudart; J. Phys. Chem.; 90 (1986) 4874.

[32] L. Volpe and M. Boudart; J. Solid State Chem.; 59 (1985) 332.

[33] J. G. Choi, R. L. Curl and L. T. Thompson; J. Catal.; 146 (1994) 218.

[34] D. A. King and F. J. Sebba; J. Catal.; 4 (1965) 253.

[35] N. Sengal and F. J. Sebba; J. Catal.; 8 (1967) 105.

[36] R. S. Wise, E. J. Markel; J. Catal.; 145 (1994) 335.

[37] M. Nagai, Y. Goto, A. Miyata, M. Kiyoshi, K. Hada, K. Oshikawa and S. Omi; J. Catal.; 182 (1999) 292.

[38] W. Zhaobin, X. Qin, P. Grange and B. Delmon; J. Catal.; 168 (1997) 176.

[39] U. S. Geological Survey;

http://minerals.usgs.gov/minerals/pubs/commodity/nitrogen/nitromcs07.pdf

[40] R. Schlögl; Angew. Chem. Int. Ed.; 42 (2003) 2004.

[41] D. A. King and F. Sebba; J. Catal.; 4 (1965) 253.

[42] D. A. King and F. Sebba; J. Catal.; 4 (1965) 430.

[43] J-G. Choi, J. Ha and J-W. Hong; Appl. Catal. A: Gen.; 47 (1998) 168.

[44] M. R. Hillis, C. Kemball and M. W. Roberts; Trans. Faraday Soc.; 62 (1966) 3570.

[45] K-I. Aika and A. Ozaki; J. Catal; 14 (1969) 311.

[46] R. Kojima and K-I. Aika; Appl. Catal. A: Gen.; 219 (2001) 141.

[47] R. Kojima and K-I. Aika; Chem. Lett. (2000) 514.

[48] R. Kojima and K-I. Aika; Appl. Catal. A: Gen.; 215 (2001) 149.

[49] R. Kojima and K-I. Aika; Appl. Catal. A: Gen.; 218 (2001) 121.

[50] R. Kojima and K-I. Aika; Appl. Catal. A: Gen.; 219 (2001) 157.

[51] C. J. H. Jacbonsen, M. Brorson, T. Sehested, H. Teunissen and E. Törnqvist; US Patent; (1999) 6,235,676 to Haldor, Topsøe A/S.

[52] C.J. H. Jacobsen; Chem. Commun. (2000) 1057.

[53] C. J. H. Jacobsen, S. Dahl, B. S. Clausen, S. Bahn, A. Logadottir and J. K. Nørskov; J. Am. Chem. Soc.; 123 (2001) 8404.

[54] A. Boisen, S. Dahl and C. J. H. Jacobsen; J. Catal.; 208 (2002) 180.

[55] M. Vettraino, M. Trudeau, A. Y. H. Lo, R. W. Schurko and D. Antonelli; J. Am. Chem. Soc.; 123 (2001) 8405.

[56] R. Kojima and K. I. Aika; Appl. Catal. A: Gen.; 209 (2001) 317.

[57] W. J. McGill and F. Sebba; J. Catal.; 2 (1963) 104.

[58] S. T. Oyama; J. Catal.; 133 (1992) 358.

[59] M. K. Neylon, S. K. Bej, C. A. Bennett and L. T. Thompson; Appl. Catal. A: Gen.; 232 (1998) 13.

[60] R. Bafrali and A. T. Bell; Surf. Sci.; 278 (1992) 353.

[61] H. J. Lee, J-G. Choi, C. W. Colling, M. Mudholkar and L. T. Thompson; Appl. Surf. Sci.; 89 (1995) 121.

[62] J. A. J. Rodriguez, G. M. da Cruz, G. Bugli, M. Boudart and G. Djega-Mariadassou ; Catal. Lett.; 45 (1997) 1.

[63] X. Chen, T. Zhang, L. Xia, T. Li, M. Zheng, Z. Wu, X. Wang, Z. Wei, Q. Xiu and C. Li; Catal. Lett.; 79 (2001) 21.

[64] R. Brayner, G. Djega-Mariadassou, G. M. da Cruz and J. A. J. Rodriguez ; Catal. Today; 57 (2000) 225.

[65] R. C. Bowman, M. H. Tegen and G. E. Hartwell; US Patent; (1990) 4,922,024 to The Dow Chemical Company.

[66] M. Florea, R. Prada-Silvy and P. Grange; Catal. Lett.; 87 (2003) 63.

[67] M. Florea, R. Prada-Silvy and P. Grange; Appl. Catal. A: Gen.; 255 (2003) 289.

[68] R. Prada-Silvy, M. Florea. N. Blangenois and P. Grange; AIChE Journal; 49 (2003) 2228.

[69] M. Olea, M. Florea, I. Sack, R. Prada-Silvy E. M. Gaignaux, G.B Marin and P. Grange; J. Catal.; 232 (2005) 152.

[70] C. Shi, A. M. Zhu, X. F. Yang and C. T. Au; Catal. Lett.; 97 (2004) 9.

[71] C. Shi, A. M. Zhu, X. F. Yang and C. T. Au; Appl. Catal. A: Gen.; 255 (2003) 289.

[72] H. He, H. X. Dai, K. Y. Ngan and C. T. Au; Catal. Lett.; 71 (2001) 147.

[73] C. Shi, X. F. Yang A. M. Zhu and C. T. Au; Catal. Today; 93-5 (2004) 819.

[74] Y. Egashira and H. Komiyama; Ind. & Engin. Chem. Res.; 29 (1990) 1583.

[75] G. S. Rhantora, A. T. Bell and J. A. Reimer; J. Catal., 40 (1987)108.

[76] A. Guerrero-Ruiz, Y. Zhang, B. Bachiller-Baeza and I Rodriguez-Ramos; Catal. Lett. 165 (1998) 55.

[77] Z. Wu, Z. Hao, P. Ying, C. Li and Q. Xin; J. Phys. Chem. B.; 104 (2000) 12275.

[78] Y. Li, Y. Fan and Y. Chen; Catal. Lett.; 82 (2002) 111.

[79] P. Rodriguez, J. l. Brito, A. Albornorz, M. Labadi, C. Pfaff, S. Marrero, D. Moronta and P. Betancourt; Catal. Commun; 5 (2004) 79.

[80] H. A. Al-Megren, T. Xiao, S. L. Gonzalez-Cortes, S. H. Al-Khowaiter and M. L. H. Green; J. Mol. Catal. A: Chem.; 225 (2005) 143.

[81] H. Imamura, T. Nuruyu, T. Kawasaki, T. Teranishi and Y. Sakata, Catal. Lett.; 96 (2004) 185.

[82] P. Perez-Romo, C. Potvin, J-M. Manoli, M. M. Chehimi and G. Djega-Maraidassou; J. Catal, 208 (2002) 187

[83] P. Perez-Romo, C. Potvin, J. M. Manoli, R. Contant and G. Djega-Mariadassou; J. Catal.; 205 (2002) 191.

[84] H. A. Al-Megren, T. Xiao, S. L. Gonzalez-Cortes, S. H. Al-Khowaiter and M. L. H. Green, J. Mol. Catal. A: Chem.; 225 (2005) 143.

[85] H. Irie, Y. Watanabe and K. Hashimoto; J. Phys. Chem. B; 107 (2003) 5483.

[86] M. Miyauchi, A. Ikezawa, H. Tobimatsu, H. Irie, K. Hashimoto; Phys. Chem. Chem. Phys.; 6 (2004) 865.

[87] S. Yiu, H. Yamaki, M. Komatsu, Q. Zhang, J. Wang, Q. Tang, F. Saito and T. Sato; J. Mater. Chem.; 13 (2003) 2996.

[88] T. Sano, N. Negishi, K. Koike, K. Takeuchi and S. Matsuzawa; J. Mater. Chem.; 14 (2004) 380.

[89] S. Sakthivel and H. Kisch; ChemPhysChem.; 4 (2003) 487.

[90] T. Ihara, M. Miyoshi, Y. Iriyama, O. Matsumoto and S. Sugihara; Appl. Catal. B: Env.; 42 (2003) 403.

[91] O. Diwald, L. Thompson, E. G. Goralski, S. D. Walck and J. T. Yates Jr.; J. Phys. Chem. B; 108 (2004) 52.

[92] Hitoki, T. Taneka, J. N. Kondo, M. Hara, H. Kobayashi and K. Domen; Chem. Commun.; (2002) 1698.

[93] M. Hara, T. Takata, J. N. Kondo and K. Domen; Catal. Today; 90 (2004) 313.

[94] M. R. Hillis, C. Kemball, and M. W. Roberts; Trans. Faraday Soc.; 62 (1966) 3570.

[95] K-I. Aika and A. Ozaki; J. Catal.; 14 (1969) 311.

[96] L. Volpe and M. Boudart, J. Phys. Chem.; 90 (1986) 4874.

[97] R. Kojima and K-I. Aika; Appl. Catal. A; 219 (2001) 141.

[98] J. S. J. Hargreaves and D. Mckay; *Specialist Periodical Reports in Catalysis*, RSC Cambridge; 19 (2006) 84.

[99] Z-H. Zhong and K-I. Aika; J Catal; 173 (1998) 535.

[100] N. Segal and F. Sebba; J. Catal.; 8 (1967) 113.

[101] M. Itoh, K. Machida, M. Yamamoto, K. Hirose and G. Adachi; J. Alloys Compd.; 364 (2004) 208.

[102] M. Itoh, K. Machida, K. Hirose, T. Sakata, H. Mori and G. Adachi; J. Phys. Chem. B; 103 (1999) 9498.

[103] M. Itoh, K. Machida, H. Nakajima, K. Hirose and G. Adachi; J. Alloys Compd.; 288 (1999) 141.

2   Experimental and methodology

2.1   Reactor design

The reactors for the nitridation and testing were set-up following a method as previously used and described by Mckay *et al.*[1] During the course of this project two reactors were used. Both of these reactors had controlled gas flows with quartz glass reactor tubes used for housing the sample.

2.1.1   Ammonolysis reactor

The ammonolysis reactor was used for the nitridation of precursors with ammonia to form the required nitride. The set-up is shown in Figure 2-1. The gases employed were ammonia (BOC grade N3.8) [NH_3], nitrogen (BOC oxygen free, 99.998%) [N_2] and 2% O_2/Ar (BOC). These were introduced into a vertical quartz glass reactor, 10.5 mm i.d. (with a sintered disc mounted halfway along the tube) via ¼ inch stainless steel tubing (Swagelok). The flow of gas was controlled using a series of Brooks 5850 TR mass flow controllers. The effluent gas was flowed through a sulfuric acid bath to neutralise any remaining ammonia present, and all experiments were carried out within a well ventilated fume cupboard. Utilising a Carbolite furnace fitted with a Eurotherm temperature controller, the nitriding process could be programmed to proceed through various heating regimes (as specified in the relevant sections).

Typical experimental conditions used for nitriding of the oxide precursors are outlined below and have been described by Mckay *et al.*[1] Approximately 1 g of material to be nitrided was placed in a vertical quartz glass reactor and reacted under a 95 mLmin^{-1} flow of NH_3. The reaction underwent a strict heating regime during the nitriding process as shown in Table 2-1.
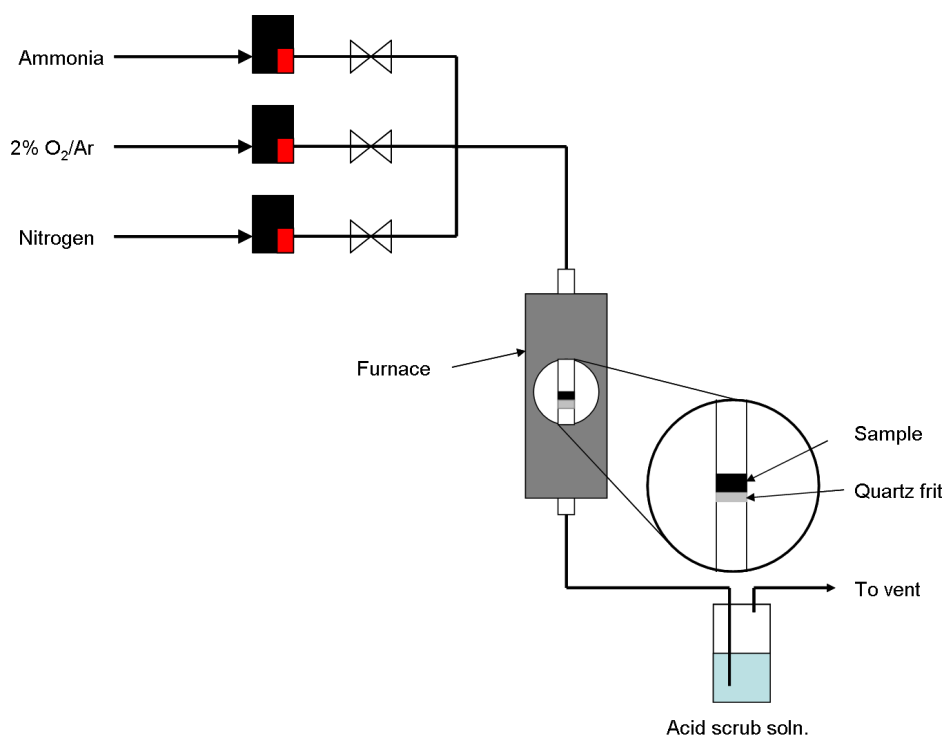
Figure 2-1: Ammonolysis Reactor for nitriding precursors.

Table 2-1: Heating regime for nitridation process.

Start Temperature / K	Final Temperature / K	Time / mins	
Ambient	630	60	Ramp
630	720	180	Ramp
720	1058	180	Ramp
	1058	300	Dwell
1058	Ambient	120	Furnace Cool
Ambient	Ambient	180	Passivation

Once the temperature had reached 1058 K and had stabilised, a dwell period of five hours was started; following this dwell period, the furnace was allowed to cool with the sample under the flow of ammonia. On reaching ambient temperature the system was flushed through with nitrogen gas at 100 mLmin^{-1} for 15 minutes to remove any residual ammonia from the system. Subsequently, in order to prevent any pyrolysis on exposure of the nitrided material to the air, the material was passivated using a 100 mLmin^{-1} flow of a 0.1% oxygen-containing gas mixture (95%/4.9%/0.1% N$_2$/Ar/O$_2$) for three hours at ambient temperature, to give the nitride a protective oxide layer. A schematic showing the different stages is shown in Figure 2-2.
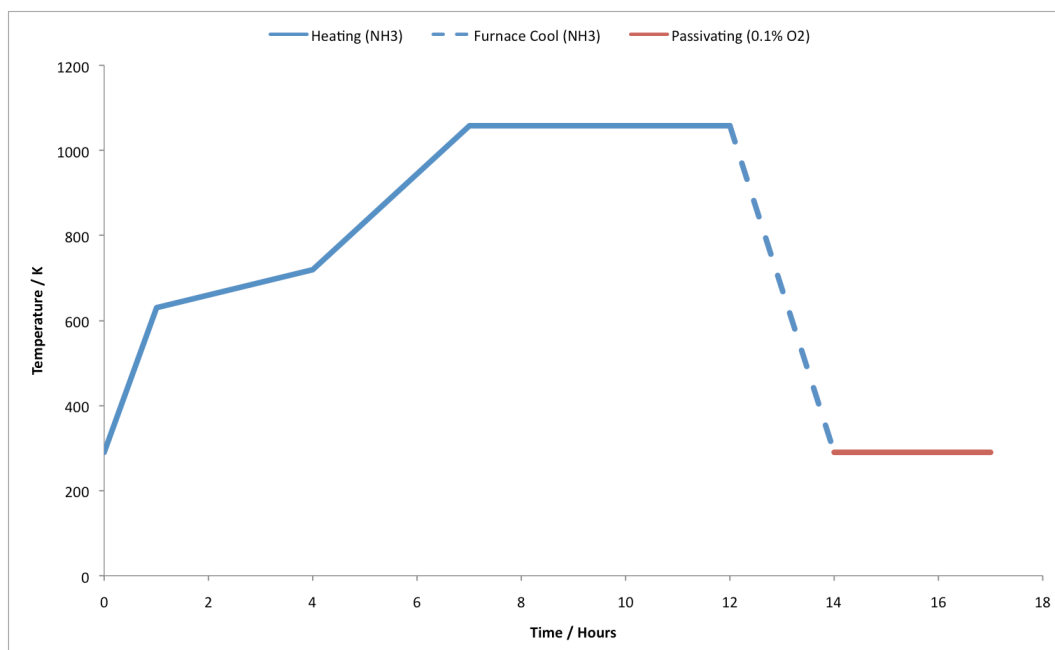
Figure 2-2: Schematic showing the heating regime for the nitridation process.

2.1.2 Testing reactor

The testing reactor is shown in Figure 2-3. This was a fixed bed, continuous flow reactor. A 10.5 mm i.d. quartz glass reactor was used to house the sample. The sample, in powder form, was held centrally (using silica wool plugs) within the reactor tube which was housed within a Carbolite furnace. The feed gas mixtures were introduced through ¼ inch stainless steel tubing (Swagelok). A total flow rate of 60 mLmin^{-1} was used for all reactions and this was controlled through Brooks 5850 TR mass flow controllers. Gases that were used in this reactor were:

(i) BOC 25% nitrogen in hydrogen (stoichiometric NH_3 synthesis mixture, H_2 – 99.998%, N_2 – 99.999%) [3:1 H_2/N_2],

(ii) BOC 25% argon in hydrogen (H_2 – 99.998%, Ar – 99.998%) [3:1 H_2/Ar], BOC methane [CH_4], BOC argon [Ar], BOC oxygen-free nitrogen (99.998%) [N_2], or a combination of up to any three of these gases. The effluent gases were bubbled through a dilute solution of sulfuric acid and then vented through a fume cupboard.
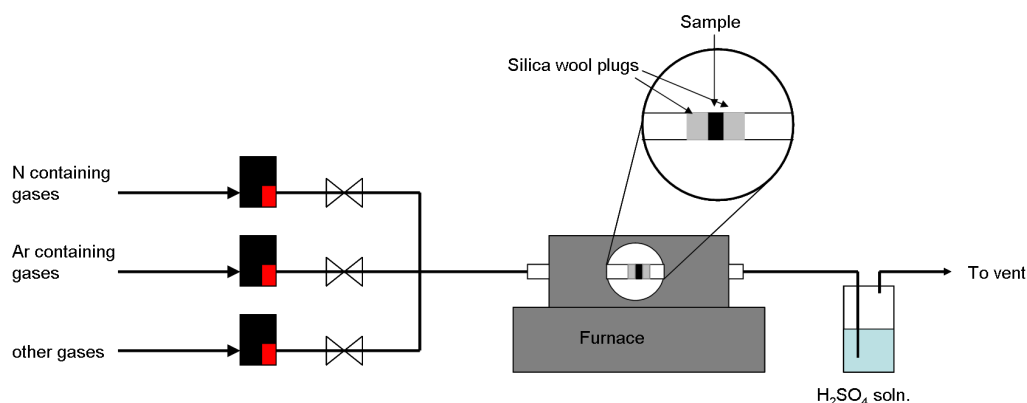
Figure 2-3: Testing reactor set-up.

2.2   Sample preparation

Detailed procedures and conditions for synthesis of compounds are described more fully in the relevant chapters.

2.2.1   Binary systems

Three binary molybdenum nitrides were synthesised during this project; beta (β-$Mo_2N_{0.78}$), delta (δ-MoN) and gamma (γ-Mo_2N). These compounds are prepared using routes described in the literature. Beta molybdenum nitride was formed from the direct reaction of molybdenum trioxide (MoO_3) with a 3:1 H_2/N_2 gas mixture at 973 K for three hours. Delta molybdenum nitride was synthesised through the ammonolysis of molybdenum sulphide (MoS_2) at 1048 K for 60 hours followed by a passivation at room temperature for two hours under a flowing 0.1% oxygen-containing gas mixture. Gamma molybdenum nitride was formed from the ammonolysis of molybdenum trioxide using a strictly controlled heating regime (Table 2-1) to 1058 K, then held at that temperature for five hours before cooling under ammonia and then passivating for two hours under a 100 mLmin^{-1} flow of a 0.1% oxygen-containing gas mixture.

2.2.2   Ternary systems

2.2.2.1   Cobalt compounds

Hydrated cobalt molybdenum oxide ($CoMoO_4$) was the starting point for the synthesis of ternary cobalt nitrides and carbides. The oxide was formed by one of two methods:

(i)   From a solution of ammonium heptamolybdate ($(NH_4)_6Mo_7O_{24} \cdot 4H_2O$) and cobalt nitrate ($Co(NO_3)_2 \cdot 6H_2O$) which was heated and mixed, the precipitate filtered, washed with distilled water and ethanol and dried for 12 hours.

(ii)   Dropwise addition of cobalt nitrate solution to a solution of sodium molybdate ($NaMoO_4 \cdot 2H_2O$) which is mixed, the precipitate filtered, washed with distilled water and ethanol and dried for 12 hours.

In each case the mixture of the oxides was calcined at 773 K for five hours. The calcined material was reacted with ammonia at 1058 K for five hours (with the heating rates controlled strictly in order to maximise the surface area of the resultant nitride, see Table 2-1) followed by a room temperature passivation stage under a flow of 0.1% oxygen-containing gas. A two hour activation stage was required for the formation of the crystalline nitride. This was conducted at 973 K under flowing 3:1 H_2/N_2 gas.

2.2.2.2   Iron compounds

Iron molybdenum oxide ($FeMoO_4$) was the starting compound for the synthesis of the resultant ternary nitrides. The oxides were synthesised through one of two ways:

(i)   Dropwise addition of an aqueous solution of iron (III) nitrate ($Fe(NO_3)_3 \cdot 9H_2O$) to a solution of sodium molybdate.

(ii)   Dropwise addition of an aqueous solution of iron (II) chloride ($FeCl_2 \cdot 2H_2O$) to a solution of sodium molybdate.

In both cases the resultant precipitate was filtered, washed and dried and calcined under a flow of nitrogen at 773 K. The oxide was then reacted under ammonia following the same procedure as for the cobalt system.

2.2.2.3   Nickel compounds

Ternary nickel compounds were synthesised from nickel molybdate (synthesised using an analogous process to that for iron molybdate but replacing iron nitrate with nickel

nitrate ($Ni(NO_3)_2 \cdot 6H_2O$)). In addition the solution was heated to around 323 K to aid the crystallisation of the molybdate. The oxide was reacted with a flowing 3:1 H_2/N_2 gas mixture at 973 K for three hours to form the nitride.

2.2.3   Quaternary systems

The quaternary compounds studied in this project were limited to the quaternary phases of iron-cobalt-molybdenum nitride.

For mixed 3d metal compounds the method employed was to form a mixed metal oxide from the dropwise addition of solutions of iron nitrate and cobalt nitrate to a sodium molybdate solution. The precipitate was filtered and washed with water and ethanol, then dried for 12 hours and calcined at 773 K. The oxide was then nitrided as per the conditions used for the ternary cobalt and iron systems described previously.

2.3   Reactivity testing

The samples were tested at ambient pressure for ammonia production. The method employed used a fixed bed reactor through which reactant gas (60 mLmin^{-1}) of either 3:1 H_2/N_2 gas or 3:1 H_2/Ar gas was flowed. The production of ammonia was measured by the change in conductivity of a 200 mL, 0.00108 molL^{-1} sulfuric acid solution as effluent gas was flowed through it, a procedure adopted by Aika and co-workers.[2] The samples were tested under either 3:1 H_2/N_2 gas mixture or 3:1 H_2/Ar gas mixture. The 3:1 H_2/N_2 gas mix allows for the samples to be tested for their ability to form ammonia with an external source of nitrogen. The 3:1 H_2/Ar gas mix demonstrates the ability of the sample to produce ammonia with the only source of available nitrogen being that present associated with the nitride itself. Thus the reactivity of the 'lattice' nitrogen can be assessed.

The reaction conditions were kept constant with a fixed amount of sample (0.4 g) and an initial pre-treatment stage in which the sample was exposed to 3:1 H_2/N_2 gas for two hours at 973 K. This pre-treatment stage is used in an attempt to remove any surface oxide layers present. The reactor was then cooled to 673 K, the appropriate reaction gas was selected and the conductivity measurements started. Each sample was tested under both feed gases. The reaction with the 3:1 H_2/N_2 gas mixture was conducted for 5 hours at 673 K. For the 3:1 H_2/Ar gas, the feed gas was changed after the renitriding stage and then measurements were taken once the feed gas had been changed to the 3:1 H_2/Ar gas.

During the reaction, the temperature was raised by 100 K intervals to 773 K, 873 K and finally to 973 K.

The samples examined were all subject to elemental analysis both before and after reaction to determine the effects of the different reactant gases. The combination of data from elemental analysis and reaction profiles was used to observe and calculate the extent to which the 'lattice' nitrogen was active in the samples, as any change in the weight percentage of nitrogen can be linked to the activity of the nitride.

2.4   Characterisation

2.4.1   Diffraction

During this project, powder X-ray diffraction (PXRD) and powder neutron diffraction (PND) were used as the main methods of characterisation. The further technique can be used to identify known phases rapidly and estimate sample purity. Further, by the process of indexing diffraction data, unit cell parameters, crystal systems and cell symmetry for samples can be determined and refined.

Bragg devised a method of explaining diffraction, where a crystal is regarded as a layered construct, which gives a regularly repeating structure. Diffraction occurs when the perpendicular distance between the layers (planes) are of a similar scale to that of the wavelength (λ) of the incident radiation and thus the crystal acts as a diffraction grating Figure 2-4.
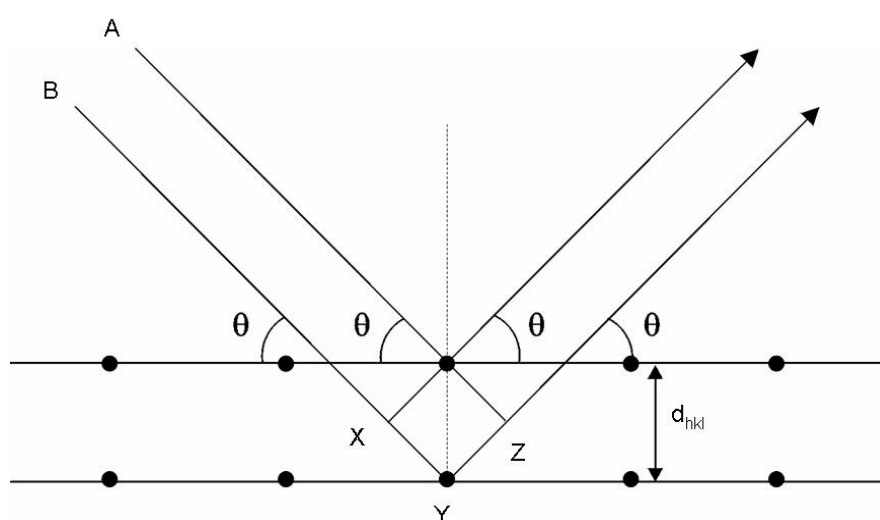
Figure 2-4: Diagram of diffraction and illustrating Bragg's Law.

Two parallel incident X-ray beams, A and B, must be in phase to produce constructive interference. Beam B must travel an extra distance, XYZ, compared to beam A. This distance is related to the interplanar spacing d_{hkl} and the angle of incidence by:

Equation 1

$$XYZ = 2d \sin \theta$$

Where d = plane separation, θ = Bragg angle and XYZ is the path difference.

For constructive interference to occur and produce a reflection XYZ must be equal to a whole number of wavelengths:

Equation 2

$$XYZ = n\lambda$$

Where n = an integer and λ = radiation wavelength.

Bragg's law[3] can be achieved through a combination of Equation 1 and Equation 2.

Equation 3

$$n\lambda = 2d \sin \theta$$

In the case of powder (polycrystalline) materials, the sample can be considered to be a large number of small randomly orientated single crystals. Due to the random orientation of the crystallites the scattered radiation emerges not as a single narrow beam, but as continuous cones of intensity (Figure 2-5). Discrete cones of scattered radiation are produced simultaneously for all reflections of *hkl*. Taking a slice through the cones a 2-dimensional pattern is obtained. Therefore a powder diffraction pattern can be recorded by measuring the scattering over a range in 2θ.
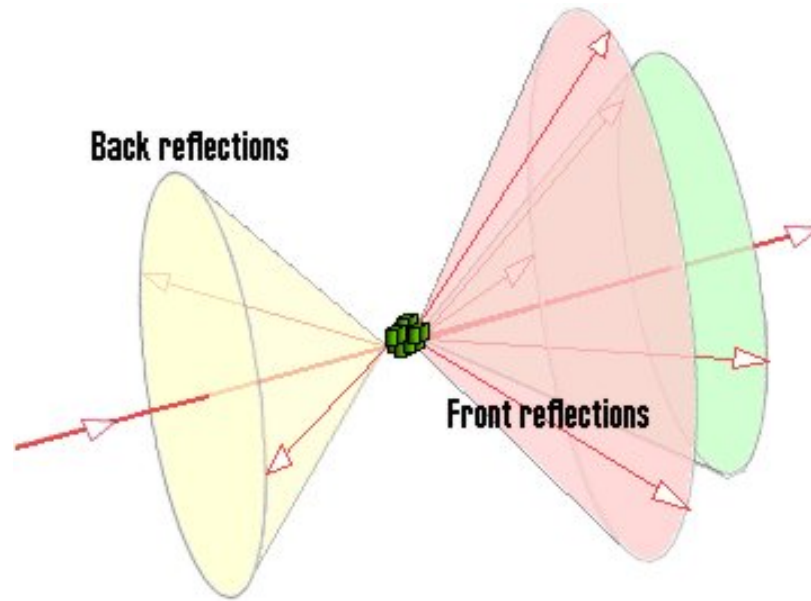
Figure 2-5: Diffraction from a powder (polycrystalline) sample.[4]

Crystal systems are derived from the d-values associated with observed reflections. Planes are defined by the Miller indices, *hkl*, the reciprocal positions where the planes cut the *a*, *b* and *c* axes respectively. If, for example, the plane intersects axes at $x = 1$, $y = 1$ and $z = \infty$, the Miller index of the plane is $h = 1$, $k = 1$, $l = 0$ or (110). The values are either positive/negative integers or zero and useful in explaining the plane separation of a crystal. Each crystal system (cubic, tetragonal, etc) has an expression that denotes the plane separation (d_{hkl}); these are shown in Table 1-2.

Table 2-2: Table of d-spacings in different crystal systems.

Crystal System	Expression for d_{hkl}
Cubic	$$\frac{1}{d_{hkl}^2} = \frac{h^2 + k^2 + l^2}{a^2}$$
Tetragonal	$$\frac{1}{d_{hkl}^2} = \frac{h^2 + k^2}{a^2} + \frac{l^2}{c^2}$$
Orthorhombic	$$\frac{1}{d_{hkl}^2} = \frac{h^2}{a^2} + \frac{k^2}{b^2} + \frac{l^2}{c^2}$$
Hexagonal	$$\frac{1}{d_{hkl}^2} = \frac{4}{3}\left(\frac{h^2 + hk + k^2}{a^2}\right) + \frac{l^2}{c^2}$$
Monoclinic	$$\frac{1}{d_{hkl}^2} = \frac{1}{\sin^2\beta}\left(\frac{h^2}{a^2} + \frac{k^2\sin^2\beta}{b^2} + \frac{l^2}{c^2} - \frac{2hl\cos\beta}{ac}\right)$$
Triclinic	$$\frac{1}{d_{hkl}^2} = \frac{1}{V^2}\left(\begin{array}{l} h^2b^2c^2\sin^2\alpha + k^2a^2c^2\sin^2\beta + l^2a^2b^2\sin^2\gamma \\ + 2hkabc^2(\cos\alpha\cos\beta - \cos\gamma) + skla^2bc(\cos\beta\cos\gamma - \cos\alpha) \\ + 2hlab^2c(\cos\alpha\cos\gamma - \cos\beta) \end{array}\right)$$ where $$V = abc\sqrt{\left(1 - \cos^2\alpha - \cos^2\beta - \cos^2\gamma + 2\cos\alpha\cos\beta\cos\gamma\right)}$$

2.4.1.1 Powder X-ray diffraction (PXRD)

X-ray diffraction was conducted primarily using lab based diffractometers. X-rays are generated by accelerating electrons from a tungsten filament towards a target by applying a high voltage. Electrons with enough energy eject core electrons from their atomic orbitals causing electrons in higher energy orbitals to decay, emitting X-ray radiation (Figure 2-6 and Figure 2-7). The most commonly used examples are Cu or Mo giving K_α wavelengths of 1.5148 Å and 0.7107 Å for Cu and Mo respectively. The K_α X-ray wavelength is selected by using a monochromator.
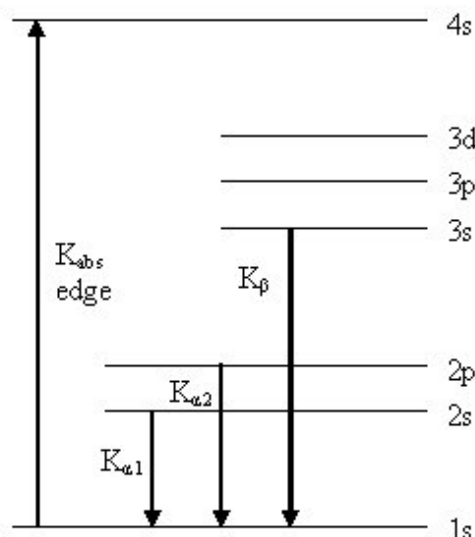
Figure 2-6: Atomic levels involved in copper emission.
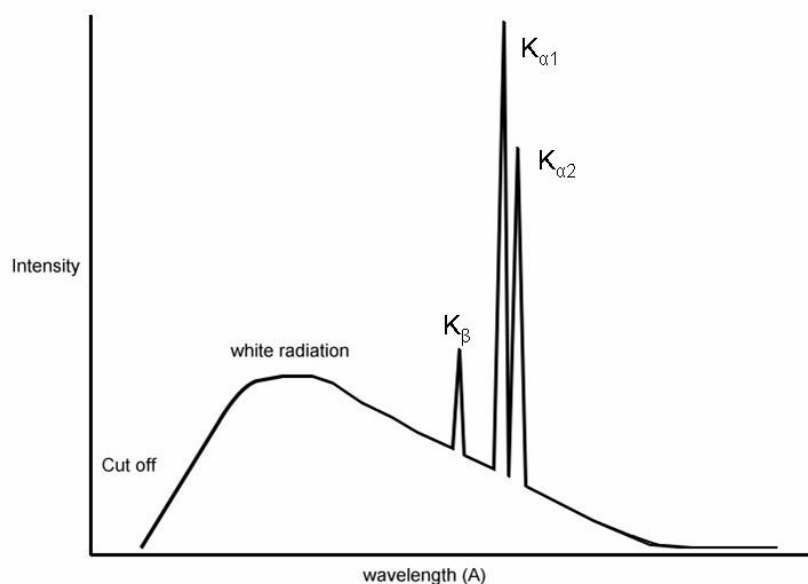
Figure 2-7: Characteristic and continuous radiation emitted by a copper X-ray tube.

In a typical powder X-ray diffraction experiment performed during this project, the sample is irradiated from a moving source and a moving detector measures the intensity of the diffracted X-rays. The measurements are carried out in the so-called Bragg-Brentano geometry as a flat plate sample. An X-ray diffraction pattern is obtained from the elastic scattering of the X-rays by the electrons within the sample. Heavier elements have a greater number of electrons and will therefore scatter X-rays more and this increases the intensity of the observed peaks. Lighter elements (especially hydrogen) have very few electrons and as such do not scatter the X-rays as well (Figure 2-8). Liquids, glasses and amorphous solid compounds lack long range order and do not

produce characteristically defined diffraction patterns and thus cannot be characterised using this technique.

X-ray Scattering Factors f
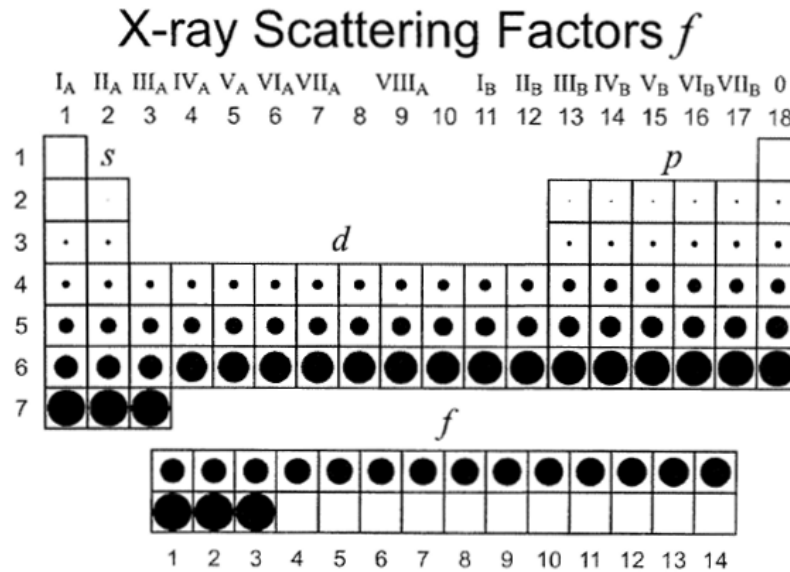
Figure 2-8: Scattering factors for X-rays.

Showing the effect of increased atomic number Z on the scattering of X-rays.

PXRD data were collected using a Siemens D5000 instrument (Figure 2-9), utilising Cu-K$_\alpha$ radiation at room temperature. The samples were ground using a pestle and mortar in order to make sure that the maximum number of crystals were randomly orientated. The powder was then mounted in a depression on the sample holder, and the surface flattened so that the surface of the sample was level with the surface of the sample holder in order to reduce the errors associated with changes in sample height within the X-ray beam.

Two types of detector were used on the D5000 during the period of work, a standard scintillation detector and a SOL-X detector. The SOL-X detector allows an energy window to be defined and only X-rays that lie within this window are then detected. The advantage of this set-up is that it is possible to tune out fluorescence. The presence of iron and cobalt in the sample, which interact with the copper radiation, can cause fluorescence. This results in a very high and noisy background, which may obscure low intensity peaks.[5]
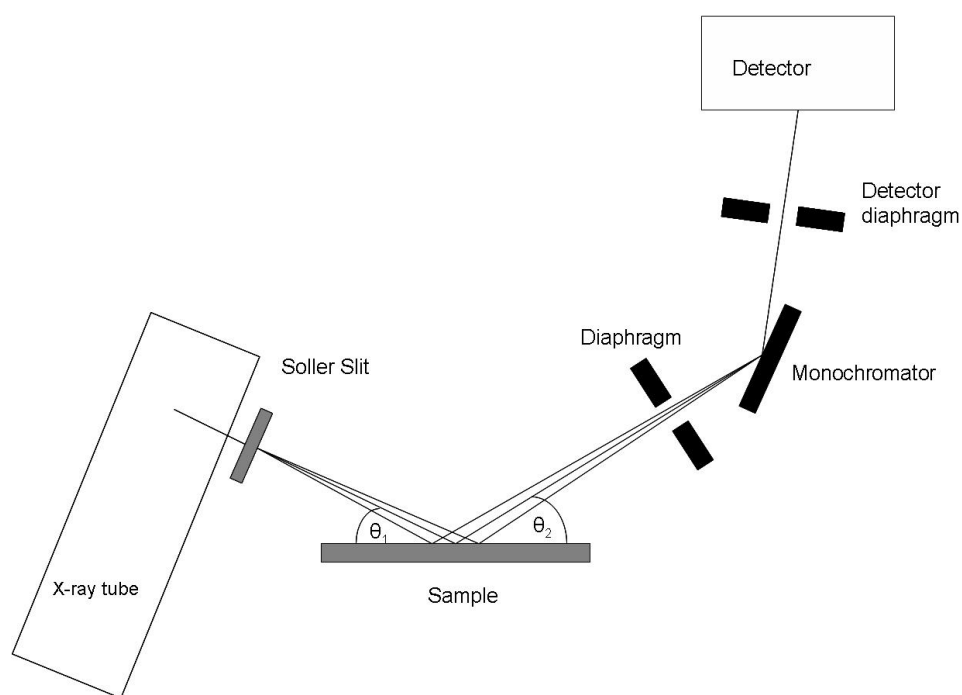
Figure 2-9: D5000 schematic showing so called Bragg Brentano geometry.

The generator and detector move (θ_1 and θ_2) around a fixed sample giving 2θ readings.

The patterns were collected using a step scan of size 0.02 °2θ over a $5 - 85$ °2θ range and a step time of 0.8 seconds. When diffraction data were required for structural refinement, higher intensities and a wider 2θ range were needed. This was achieved by increasing the step time to 11 seconds and increasing the range from $5 - 120$ °2θ. The patterns were compared with known patterns on the Inorganic Crystal Structure Database, (ICSD) or the Joint Committee on Powder Diffraction Standards, (JCPDS) database.

2.4.1.2 Powder neutron diffraction (PND)

The wave-like properties of neutrons were first demonstrated in 1936 by Mitchell and Powers.[6] They produced neutrons from a radium-beryllium source with paraffin wax acting as a moderator. 16 MgO crystals were mounted around the circumference of the cylinder with an inclination of 22° to satisfy the Bragg condition for 1.6 Å neutrons, which were detected by a change in intensity at the detector.

Unlike in an X-ray diffraction experiment, where the radiation is scattered by electrons, neutrons are diffracted by the nucleus itself and thus gives a direct measurement of the nuclear position of atoms in the sample. A typical thermal neutron with a velocity of 2200 ms^{-1} has an energy of 25 meV obtained from its kinetic energy, $\frac{1}{2}mv^2$ – and hence a wavelength $\lambda = 1.8$ Å. The scattering of neutrons is dependent on the properties of the nucleus and as such there is no equivalent form factor as in X-rays (Figure 2-10).
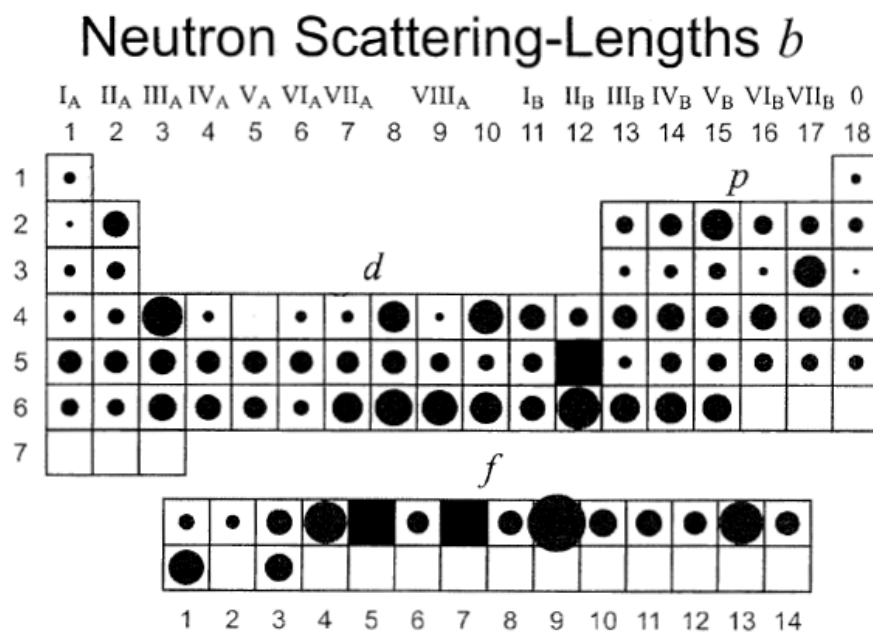
Figure 2-10: Scattering lengths of neutrons.

> The figure indicates that there is no direct link between increasing atomic number Z and the scattering length with neutrons.

PND experiments were conducted at the ISIS pulsed neutron and muon source at the Rutherford Appleton Laboratory. As this is a pulsed spallation source the diffraction is measured by time of flight (ToF) methods rather than a steady state reactor source (where, by contrast, the pattern is collected at different angles 2θ).

In ToF diffraction the sample is irradiated with a pulsed 'white' beam of neutrons of different wavelengths. The neutrons travel a known distance (L1) from the source to the sample and then from the sample onto the fixed detectors (L2) at an angle 2θ giving a total distance L (Figure 2-11). The time at which the neutrons arrive at the detector is recorded and since the wavelength of the neutron is related to its momentum through the de Broglie relationship (Equation 4) then the d-spacing can be calculated.

$$L_1 + L_2 = L$$
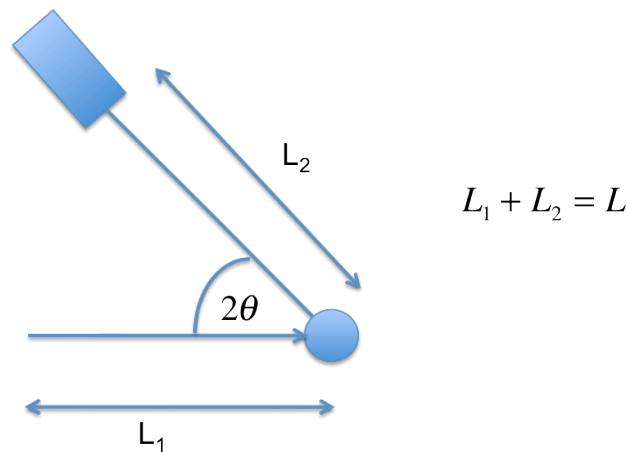
Figure 2-11: Time-of-flight diffractometer set-up.

In a pulsed source system the detection angle, θ, is fixed and the variables are d and the wavelength of a neutron, λ. The relationship between ToF and d-spacing is linear and can be derived from the de Broglie relationship and Bragg's Law (Equation 3).

Equation 4

$$\lambda = \frac{h}{p_n}$$

where

$$\lambda = \frac{h}{m_n v_n}$$

Where λ = wavelength, h = Planck's constant, p_n = *momentum of neutron*, m_n = mass of neutron, v_n = velocity of neutron.

If the primary flight path (moderator to sample) is a distance L_1 and the secondary flight path (sample to detector) is a distance L_2, with corresponding times of flight t_1 and t_2, then by substituting into Equation 4 and combining with Equation 3 gives:

Equation 5

$$\frac{h}{m_n}\left(\frac{t_1+t_2}{L_1+L_2}\right)=2d\sin\theta$$

Therefore with a total neutron flight path, L and time of flight, t, such that:

$$t_1+t_2=t$$

then,

Equation 6

$$t=2dL\left(\frac{m_n}{h}\right)\sin\theta$$

i.e. $t\propto d$

On a 12 m instrument such as POLARIS (Section 2.4.1.2.1), a 1 Å d-spacing reflection will be detected in the backscattering bank of detectors at a TOF of ~5000 μs.

2.4.1.2.1   The POLARIS diffractometer

The POLARIS instrument at ISIS is a high intensity, medium resolution powder diffractometer. The intense neutron flux on POLARIS combined with a large detector solid angle provides a high count rate, allowing experiments to be performed with short counting times or with very small samples. POLARIS receives a polychromatic 'white' beam of neutrons from the ambient water moderator. The maximum dimensions for the beam at the sample position is 40 mm (h) x 20 mm (w), however this can be adjusted to suit the requirements of the experiment.

POLARIS has a total of 434 ^{3}He gas and ZnS scintillation detectors arranged in 4 banks, two at low angles, one at 2θ ~90° and one at backscattering angles, referred to as the A, B, E, C banks respectively. Details of the detectors are shown in Table 2-3 with an overall schematic shown in Figure 2-12.

Table 2-3: POLARIS detector configuration.[4]

Bank Position (label)	Backscattering (C)	90 degrees (E)	Low angle (A)	Low Angle (B)
Detector Type	^{3}He	ZnS	^{3}He	ZnS
No. of elements	58	216	80	80
L2 / m	$0.65 - 1.35$	~0.80	$1.72 - 2.65$	~2.20
2θ range / °	$130 < 2\theta < 160$	$83 < 2\theta < 97$	$28 < 2\theta < 42$	$13 < 2\theta < 15$
Δd/d	~5 x10^{-3}	~7 x10^{-3}	~1 x10^{-3}	~3 x10^{-3}
d-range / Å	$0.2 - 3.2$	$0.2 - 4.0$	$0.5 - 8.3$	$0.5 - 21.6$
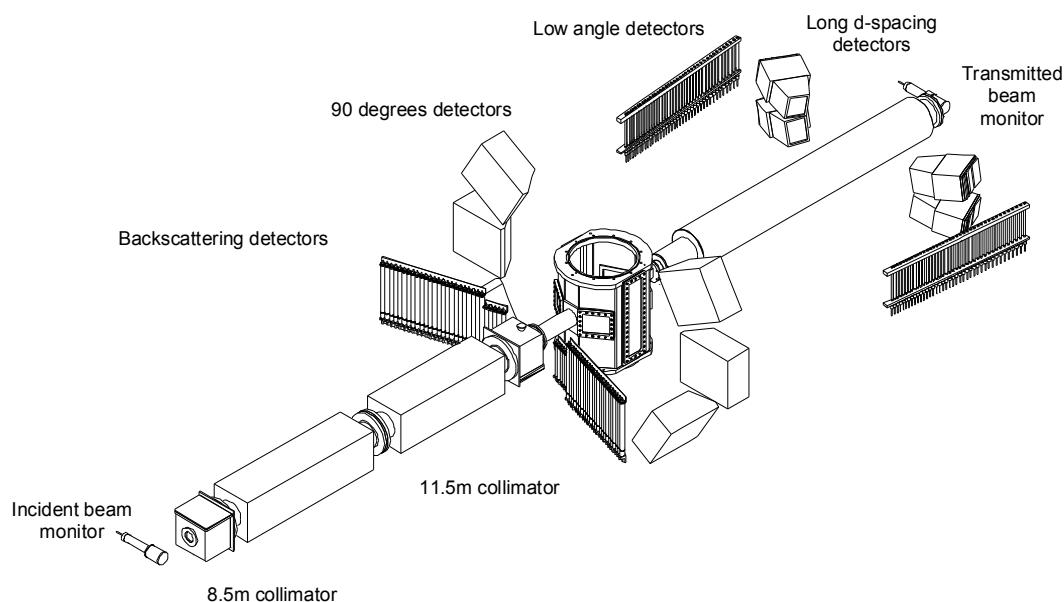
Figure 2-12: Schematic of the POLARIS instrument.[4]

The high count rate of the POLARIS diffractometer means that kinetic experiments, e.g. studies of phase changes or chemical reactions where cryostats or furnaces are used to cool or heat samples while diffractograms are collected are possible. The 90° detector banks are used exclusively when working with complex sample environments. By providing suitable collimation of the incident and scattered beams, unwanted diffraction from the sample environment apparatus can be eliminated.

During data collection, samples were held in thin walled cylindrical vanadium sample cans. These vary in length from 50 mm to 75 mm and from 5 mm to 11 mm diameter. However, for samples collected at elevated temperatures in the furnace, special cells

were used which allowed for the flow of reaction gases during data collection. These cells are sealed with gold rings to prevent leaks and the sample held centrally between silica frits within the stainless steel cell. Collimators and shielding mean that only the 90° banks of detectors could be used for data collection in these cases. The *in-situ* cell set up is shown in Figure 2-13.
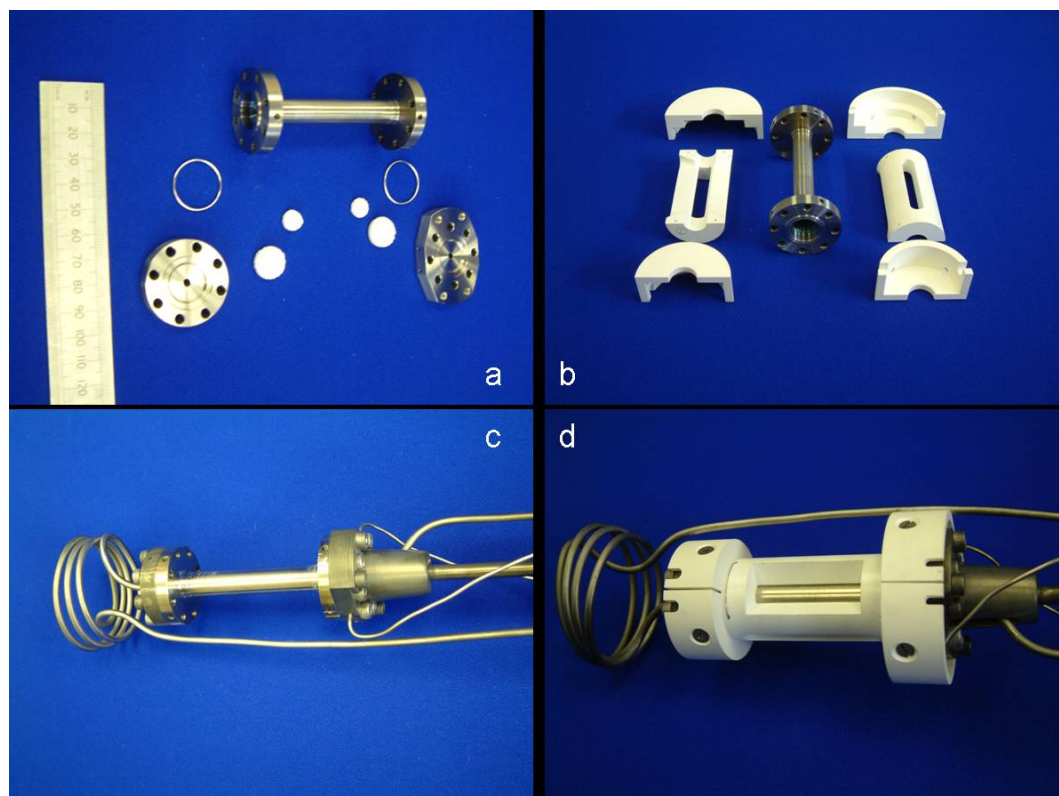
Figure 2-13: Images of the *in-situ* cell used on POLARIS.

(a) and (b) Cell prior to assembly with all the separate pieces and collimator, (c) cell attached to a centre stick, (gas flows from the LH → RH side of the image relating to a flow from the bottom→ top of the cell, (d) showing the cell and collimator attached to the stick.

For room temperature samples the can is mounted on a 'candlestick' sample holder so that the centre of the beam is centred on the sample within the can. For samples used with a cryostat or a furnace alternative centre sticks are used which have thermocouples attached to determine accurately the temperature of the sample region whilst in the neutron beam.

2.4.1.3   Structural refinement

While it was always acknowledged that powder data could provide more information than just cell type and size, extracting detailed structure information was an overriding problem due to overlap or coincidence of diffraction maxima. Diffraction from a single crystal leads to clearly defined points of intensity from each crystal plane, which can be easily measured. However a powder consists of randomly oriented crystallites leading to rings of diffraction intensity with the pattern obtained being a one-dimensional slice through the rings.

Early work was therefore restricted to trial and error structural characterisation or simple phase identification by comparison with other diffraction patterns. The situation was dramatically improved in the mid 1960s by Rietveld[7,8] who developed a refinement technique which permitted the determination of detailed structural information from powdered samples. Initial applications to powder data were limited by the fact that it was developed principally for neutron data, which had a relatively simple (Gaussian) peak shape. This, combined with the fact that the computing facilities generally available at the time were relatively poor made X-ray powder refinements less than trivial. The advent of modern computing has meant that powder X-ray diffraction has evolved into an extremely powerful tool for structure solution in materials chemistry. It permits the determination of crystal structure, particle size, detection of crystal defects and disorder, and may allow the resolution of phase transitions.

2.4.1.3.1   The Rietveld method

The Rietveld method was a revolutionary advance which has subsequently attained great importance in the extraction of detailed structural information from both powder neutron and X-ray diffraction data. Rietveld realised that although many individual reflections did overlap and thus could not be modelled as single entities, they could be fitted using simple peak shape parameters in order to determine the total intensity and peak shape of a cluster of reflections. Although initially applicable only to simple crystal systems, the advent of more powerful computers permitted the consideration of large amounts of information and hence far more complex structural problems could be solved. Initial work centred on constant wavelength PND due to its intrinsic near perfect Gaussian peak shape, however the development of more complex peak shape functions has allowed the Rietveld technique to be extended to PXRD and time of flight PND.

Today most experiments exploit the Rietveld method to yield structural information from powder samples. The process of structural refinement begins with a starting model. This is normally obtained from an isostructural analogue. As the method is one of structure refinement, rather than structure solution, having a good model is essential. Rietveld refinement without a good model is, though not impossible, a difficult procedure involving the use of other methods to get a usable starting model.

Scale factors and background parameters are the first to be introduced. As the refinement often involves the co-efficients of ordinary or orthogonal polynomials, the problem is linear and should quickly converge. Accurate determination of the Bragg reflection positions is then accomplished by variation of sample displacement, lattice parameters and a zero-point correction. Initial refinement of the peak shape parameters can also be introduced at this point. Next, atom positions are varied to fit the peak intensities followed by the temperature factors of well positioned atoms to define their thermal motion. A final refinement of the peak shape parameters is then accomplished, together with further background co-efficients, to account for asymmetry or sample broadening effects. In some cases it may be possible to vary anisotropic temperature factors. For PND data the peak shape can be modelled using a Gaussian (or related) function, however the case for PXRD data is more complicated and a pseudo-Voigt function, pV, is usually used. This is a mixture of Gaussian and Lorenzian functions:

Equation 7

$$pV = \eta L + (1-\eta)G$$

Where η = mixing parameter, L = Lorentzian function and G = Gaussian function.

The mathematical function to describe the intensity, y, at each point, i, in the diffraction pattern is:

Equation 8

$$y_i^{calc} = s\sum_i L_K |F_K|^2 \varphi(2\theta_i - 2\theta_K) P_K A + y_i^{back}$$

Where y_i^{calc} = calculated intensity at point i, s = scale factor, K = Miller indicies, L_K = contains Lorentz, polarisation and multiplicity factors, φ = reflection profile function, P_K = preferred orientation function, A = absorption factor, F_K = structure factor for the Kth Bragg peak, y_i^{back} = background intensity at point i.

The method is essentially the same for both PXRD and PND, although the preparation of data is different. The instrument parameters that can be varied are also dependent on the particular experiment carried out. The refinement process is a least squares best fit method.

The principle of the refinement process is to reduce a function, M, which represents the difference between a calculated profile y^{calc} and the observed data y^{obs}. This process is completed iteratively until a final satisfactory answer is achieved. This is when there is a 'good fit' between the experimental data and the model; this occurs when the pattern generated from the model matches the observed and the residual, M, is small.

Equation 9

$$M = \sum_i W_i \left(y_i^{obs} - \frac{1}{c} y_i^{calc} \right)$$

Where W_i is the statistical weight, c = overall scale factor such that $y_i^{calc} = c y_i^{obs}$.

The accuracy of the fit to the calculated model is measured by a series of R factors, $R_{profile}$ (R_p), $R_{expected}$ (R_{exp}), $R_{weighted\ profile}$ (R_{wp}). The most meaningful of these mathematically is R_{wp} in which the numerator is the residual that is being minimised during the refinement.

Equation 10

$$R_{profile} = R_p = \frac{\sum_i \left(y_i^{obs} - y_i^{calc} \right)}{\sum_i y_i^{obs}}$$

Where y_i = diffraction intensity.

Equation 11

$$R_{expected} = R_{exp} = \sqrt{\frac{(N - C + P)}{\sum_i w_i \left(y_i^{obs} \right)^2}}$$

Where N = number of observations, P = number of refinable parameters, C = number of constraints and $w_i = 1/y_i$.

Equation 12

$$R_{\text{weighted profile}} = R_{wp} = \sqrt{\frac{\sum_i w_i \left(y_i^{obs} - y_i^{calc} \right)^2}{\sum_i w_i \left(y_i^{obs} \right)^2}}$$

When the refinement has converged, i.e. when shift/esd <0.1 then the refinement is complete or ready for further parameters to be varied. Another measure of the quality of a refinement is χ^2 or the 'Goodness of Fit' (GofF):

Equation 13

$$\chi^2 = \left(\frac{R_{wp}}{R_{\exp}} \right)^2 = \left(\frac{\sum_i w_i \left(y_i^{obs} - y_i^{calc} \right)}{N - C - P} \right)^2$$

For a perfect fit χ^2 is equal to one, but in general a value less than five could be considered a good fit. Rietveld refinements were carried out using the Generalised Structure Analysis Suite (GSAS)[9] and EXPGUI[10] software.

2.4.2   Surface area determination

During the project, surface area measurements were performed on samples. The surface area for catalysts is very important, as high surface areas can often lead to the possibility of increased catalytic activity.

The method of calculating the surface area was described by Brunauer, Emmett and Teller (BET) in 1938[11]. This was an expansion of the Langmuir theory for monolayer molecular adsorption, to multilayered adsorption using the following hypotheses:

(i)   gas molecules adsorb infinitely on a solid in layers

(ii)   the first and second layers of a solid are seen as different to each other and subsequent layers are the same as the second layer.

The Langmuir theory can thus be applied to each layer.

Equation 14

$$\frac{p}{v_0 (p_0 - p)} = \frac{1}{v_m c} + \frac{c-1}{v_m c}\left(\frac{p}{p_0}\right)$$

Where p and p_0 are the equilibrium and the saturation pressure of adsorbates at the temperature of adsorption, v_0 is the adsorbed gas volume, v_m is the volume of gas required to complete a unimolecular adsorbed layer, and c the BET constant.

Equation 15

$$c = \exp\left(\frac{E_1 - E_L}{RT}\right)$$

Where R is the molar gas constant, T is the absolute temperature, E_1 is the heat of adsorption for the first layer and E_L is that for the second and higher layers and is equal to the heat of liquefaction.

The BET method is widely applied for the calculation of surface areas of solids by physical adsorption of gas molecules. The total surface area S_{total} and specific surface area S are found through the equations:

Equation 16

$$S_{total} = \frac{(v_m N s)}{V}$$

$$S = \frac{S_{total}}{a}$$

Where N is Avogadro's number, s is the adsorption cross section, V is the molar volume of adsorbent gas and a is the weight of the sample.
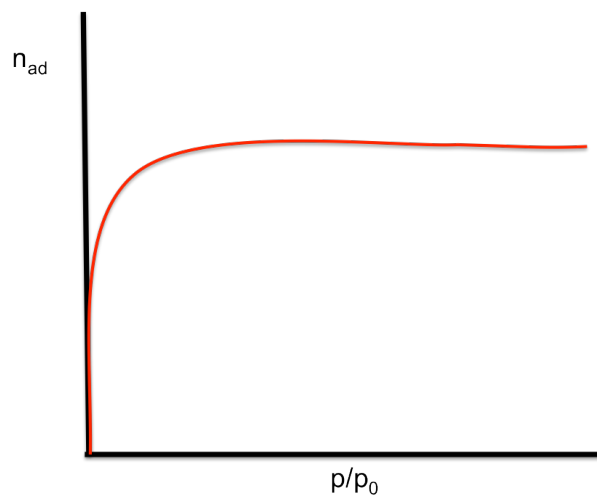
Figure 2-14: Type I Isotherm.

n_{ad} - number of adsorbed molecules

There are various types of isotherms ranging from the type I isotherm (Figure 2-14) as explained above, to the type II and IV isotherms which are based on multiple layers. Only types II and IV are used in the BET method. There are other isotherms such as types III, V and VI.
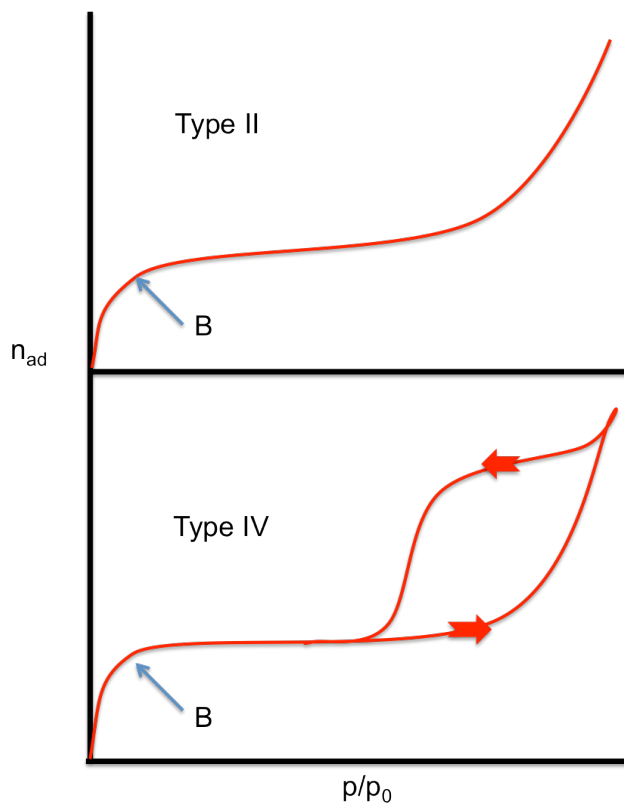
Figure 2-15: Type II and IV isotherms.

Type II isotherms are common for pore-free materials and are based on multilayer adsorption starting at point B. Type IV isotherms are similar to type II at low pressure however they show pore condensation at high pressure and they also show hysteresis. (Figure 2-15)

The surface areas of the samples during the project were determined by applying the (BET) method to nitrogen physisorption isotherms determined at liquid nitrogen temperatures. The isotherms were measured and displayed using a Micromeritics Flow Prep 060 and Gemini BET machine. The samples were degassed at 383 K overnight to remove any adsorbed moisture prior to the analysis.

Molybdenum nitrides are air sensitive and as such are passivated either by use of a 0.1% oxygen containing gas mix or through back-diffusion of air overnight as the samples are discharged from the reactor and as such the value of the surface area of the nitride may not be a true representation of the active phase's surface area.

2.4.3　Thermal analysis

Thermal analysis during this work was performed using a TA Instruments Q500 TGA to provide thermogravimetric analysis (TGA). TGA is an important technique where the mass of a sample is recorded as a function of temperature and enables quantification of events such as dehydration or decomposition. The Q500 allows for a gas to be passed over the sample during heating, simulating conditions found in a reaction. The controlled heating rate allows for events to be accurately determined in terms of time and temperature. In a controlled atmosphere, the sample can be heated at a rate between 1 and 50 Kmin^{-1}.
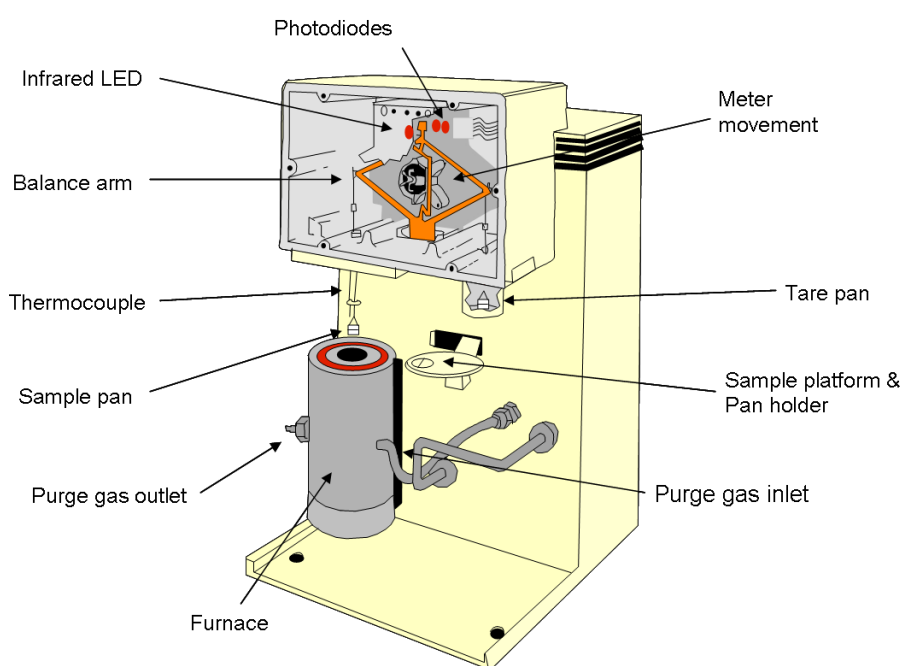
Figure 2-16: Schematic of TA Q500 TGA.[12]

The Q500 works on a null-balance principle; at the null or zero position equal amounts of light shine on the two photodiodes. If the balance moves out of the null position the amount of light shining on the two photodiodes will no longer be equal. A current is then applied to the meter movement to return the balance to the null position. The amount of current required to rebalance is proportional to the weight change.

In a typical experiment, 20 – 50 mg of sample was heated to 823 K at 1 K per minute. The temperature was held for 30 minutes to ensure any thermal events had occurred before cooling back to room temperature. Measurements were completed under air, nitrogen or argon depending on the system being investigated. Data points were

recorded every three seconds and displayed in real time. The output from the computer can then be exported for analysis using other software.

2.4.4 Magnetic measurements

The magnetic measurements were carried out using a Quantum Design Model MPMS XL 5T Superconducting Quantum Interference Device (SQUID). The SQUID consists of two superconductors separated by thin insulating layers to form two parallel Josephson junctions. This configuration can be used to detect very small magnetic fields. SQUIDs are therefore capable of amplifying small changes in the magnetic field of a material, even in the presence of a large static magnetic field. The sample is placed either in the ring itself, or more commonly in a superconducting sensing coil, inductively coupled to the SQUID. Measurements are generally recorded by variation of temperatures in a fixed magnetic field, or at a fixed temperature with a varying applied field.

The susceptibility measurements recorded give information on the magnetic behaviour of the material; paramagnetic, ferromagnetic or antiferromagnetic. The arrangement of dipole spins within these types of materials are shown in Figure 2-17.

Paramagnetism   Ferromagnetism   Anti-ferromagnetism
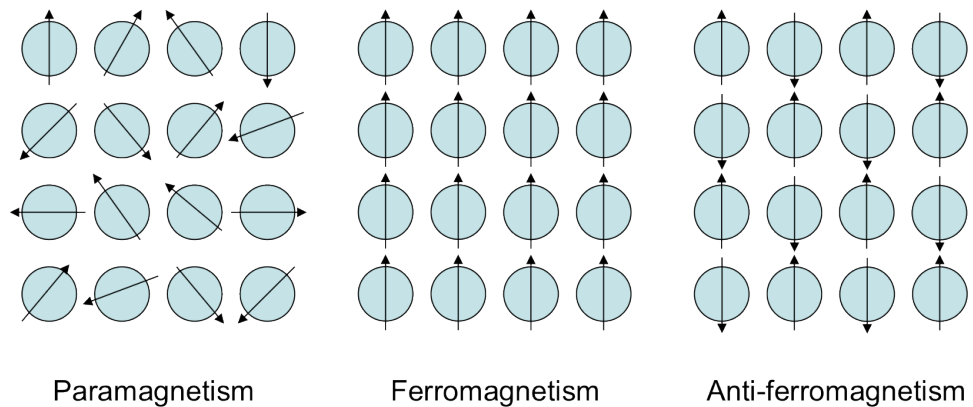
Figure 2-17: Arrangement of dipoles in different types of magnetic materials.

An ideal paramagnet follows the Curie Law.

Equation 17

$$\chi = \frac{C}{T}$$

Where χ is magnetic susceptibility, C is the Curie constant and T is temperature.

Therefore a plot of $1/\chi$ against temperature will yield a straight line through zero for an ideal paramagnet. There are limitations to the use of the Curie law as it only holds for high temperatures or weak magnetic fields. It is a special case of the more general Curie-Weiss law.

Equation 18

$$\chi = \frac{C}{T - \theta}$$

Where θ is the Weiss constant.

A plot of $1/\chi$ against temperature for this behaviour will be a straight line that does not pass through the origin.

The Curie-Weiss law can be re-written as.

Equation 19

$$\chi = \frac{N_A \mu_B^2 \mu_{eff}^2}{3k_B (T - \theta)}$$

Where N_A is Avogadro's number, μ_B is the Bohr magneton, k_B is the Boltzmann constant and μ_{eff} is the magnetic moment.

Therefore from the gradient of the line in a plot of $1/\chi$ against T we can calculate the magnetic moment.

Many materials are paramagnetic at higher temperatures, but have a transition to a different magnetic state at lower temperatures. The temperature at which the change occurs is called the Curie temperature T_c when going to a ferromagnetic state, and the Néel temperature when going to an antiferromagnetic state.

In a standard experiment, 50 mg of sample was loaded into an inverted gelatine-capsule (gel-cap) which was then firmly held centrally within a plastic straw holder. The straw was then attached to the SQUID probe ready for insertion into the SQUID. Measurements were defined by a software script, which controlled the temperature and magnetic field applied to the sample. All of the data were then analysed and evaluated using other software.

2.4.5   Elemental analysis

CHN (Carbon, Hydrogen and Nitrogen) analysis was performed by Mrs Kim Wilson using a CE-440 elemental analyser. The analysis was conducted via combustion of samples under pure oxygen. The combustion products were carried through the system by helium gas and the mixture was analysed in a series of high-precision thermal conductivity detectors.

2.5   References

[1] D. Mckay, D. H. Gregory, J. S. J. Hargreaves, S. M. Hunter and X. Sun; Chem. Commun.; (2007) 3051.

[2] K-I Aika and A. Ozaki, J. Catal. 14 (1969) 311

[3] W. L. Bragg; Proc. Camb. Phil. Soc. 17 (1913) 43.

[4] www.isis.stfc.ac.uk/instruments/POLARIS

[5] Bruker AXS; http://www.bruker-axs.de/x_ray_detectors.html.

[6] D. P. Mitchell and P. N. Powers; Phys. Rev.; 50 (1936) 486.

[7] H. M. Reitveld; Acta. Cryst.; 22 (1967) 151.

[8] H. M. Reitveld; J. Appl. Cryst.; 2 (1969) 65.

[9] A. C. Larson and R. B. von Dreele; Generalized Structure Analysis System, MS-H805, Los Alamos, NM 87545 (1990).

[10] B. H. Toby; J. Appl. Crystallogr.; 34 (2001) 210.

[11] S. Brunauer, P. H. Emmett and E. Teller; J. Am. Chem. Soc.; 60 (1938) 309.

[12] www.tainstruments.co.uk [August 2010]

3 Binary molybdenum nitrides

3.1 Introduction

Three main phases of molybdenum nitrides are currently known; beta (β-Mo$_2$N$_{0.78}$),[1] gamma (γ-Mo$_2$N) and delta (δ-MoN). Of the three, only gamma and delta have been accurately studied and their structure confirmed by PND.[2,3]

Various studies of the compounds as catalysts have been undertaken with the gamma Mo$_2$N (γ-Mo$_2$N) phase being investigated most widely. Many of the studies of γ-Mo$_2$N were concerned with the structural properties.[4] The preferred synthetic method which gives a high surface area nitride is the temperature programmed ammonolysis[5] which is the method used in this work. The effects of synthetic parameters on the structural properties of the nitride have been described by Thompson *et al.*[6] γ-Mo$_2$N was shown to be active for ammonia synthesis at ambient pressure; other nitride materials such as vanadium and uranium nitride have been investigated for ammonia synthesis at higher pressures[7,8] although the possibility of them being active at lower pressures has not been ruled out.

The formation of beta molybdenum nitride (β-Mo$_2$N$_{0.78}$) has been shown to be possible via the temperature programmed reaction of MoO$_3$ under a flow of 3:1 H$_2$/N$_2$ gas. However, this has been shown by Wise and Markel to form γ-Mo$_2$N.[9] In addition to the formation of β-Mo$_2$N$_{0.78}$ via the reaction with 3:1 H$_2$/N$_2$ gas the formation of the beta phase via the decomposition of γ-Mo$_2$N has been reported during ammonolysis at temperatures above 1073 K[10] or via heating γ-Mo$_2$N to high temperatures (up to 1273 K) under an inert atmosphere.[11] The catalytic interest in β-Mo$_2$N$_{0.78}$ has been primarily for the hydrodesulfurisation (HDS) of thiophenes by bulk and alumina supported catalysts.[12,13,14]

There has been very little reported in the literature regarding the catalytic properties of δ-MoN. Most reports describe the synthetic techniques and electronic and structural properties rather than the catalytic uses.[3,15] A number of forms of MoN have been shown to crystallise depending on the exact preparative conditions and the choice of precursor.[3,16,17]

3.2 Experimental

3.2.1 Synthesis of beta molybdenum nitride

Beta molybdenum nitride (β-$Mo_2N_{0.78}$) was synthesised by the direct reaction of molybdenum trioxide (MoO_3, Sigma Aldrich) with a 60 mLmin^{-1} flow of 3:1 H_2/N_2 gas at 973 K for three hours prior to cooling under the same gas flow. The set-up for the reaction is as described in Section 2.1.2.

3.2.2 Synthesis of gamma molybdenum nitride

The formation of gamma molybdenum nitride (γ-Mo_2N) was performed through the ammonolysis of molybdenum trioxide (MoO_3) at 1058 K under a 94 mLmin^{-1} flow of ammonia for five hours. After the heating phase the samples were cooled to room temperature and then passivated in a 100 mLmin^{-1} flow of a 0.1% oxygen containing gas mixture (95%/4.9%/0.1% $N_2/Ar/O_2$)at room temperature this was completed within the ammonolysis reactor system described in Section 2.1.1.

3.2.3 Synthesis of delta molybdenum nitride

Delta molybdenum nitride (δ-MoN) was synthesised by the ammonolysis of molybdenum sulfide (MoS_2, Sigma Aldrich) at 1098 K for 60 hours. After the heating phase the samples were allowed to cool to room temperature under the same gas flow. This heating and cooling was followed by passivation in a 100 mLmin^{-1} flow of a 0.1% oxygen containing gas mixture (95%/4.9%/0.1% $N_2/Ar/O_2$) at room temperature and was conducted within the ammonolysis reactor as shown in Section 2.1.1.

3.2.4 Characterisation

Powder X-ray diffraction (PXRD) data were collected using a Siemens D5000 diffractometer at room temperature, with Cu-K$_\alpha$ radiation. The samples were prepared as previously described in Section 2.4.1.1. The patterns were collected using a step scan of 0.02° 2θ over a 5° − 85° 2θ range and a counting time per step of 0.8 seconds. Diffraction data used for Rietveld refinements employed step times and ranges of 11 seconds and 5° − 105° 2θ respectively.

In addition to the X-ray data, powder neutron diffraction (PND) data were collected on the POLARIS instrument at ISIS. Experiments were performed on the samples at room

temperature and base temperature (4.2 K) using three banks of detectors. Samples were loaded into vanadium sample cans, to a maximum height of 40 mm and data collected as described in Section 2.4.1.2. Data were collected for approximately three hours in each case.

Magnetic measurements were performed using a Quantum Design Model MPMS XL 5T Superconducting Quantum Interference Device (SQUID). In a standard experiment, ~50 mg of sample was loaded into an inverted gelatine-capsule (gel-cap) which was then firmly held centrally within a plastic straw holder. The straw was then attached to the SQUID probe ready for insertion into the SQUID. Measurements were defined by a software script, which controlled the temperature and magnetic field applied to the sample. All of the data were then analysed and evaluated using other software.

3.2.5   Activity testing

The samples were tested at ambient pressure for their potential as ammonia synthesis catalysts. The method employed used a fixed bed reactor through which reactant gas (60 mLmin^{-1}) of 3:1 H_2/N_2 gas was flowed. The production of ammonia was measured by the change in conductivity of a 200 mL, 0.00108 molL^{-1} sulfuric acid solution as the reactor gas is bubbled through the solution.

The reactions were conducted on 0.4 g of sample which was pre-treated at 973 K under 3:1 H_2/N_2 gas for two hours prior to the reaction being started, the reactions were conducted at 673 K under 3:1 H_2/N_2 gas.

3.3   Results and discussion

The formation of the binary nitrides using the synthetic routes described was shown to be possible. The beta and gamma phases were made as single phase samples, however attempts to prepare the delta phase resulted in mixed phases of δ-MoN and Mo_5N_6. The results of the structural and catalytic study of the binary nitrides are described below, with emphasis placed on the structural studies.

3.3.1 Beta molybdenum nitride (β-Mo$_2$N$_{0.78}$)

3.3.1.1 Structural study

Previously the structure of beta molybdenum nitride had been shown by analysis of the powders by Ettmayer[1] who synthesised the nitride at high temperature and pressure. The formation of pure beta molybdenum nitride by reaction under 3:1 H$_2$/N$_2$ gas was demonstrated by Evans and Jack.[18]
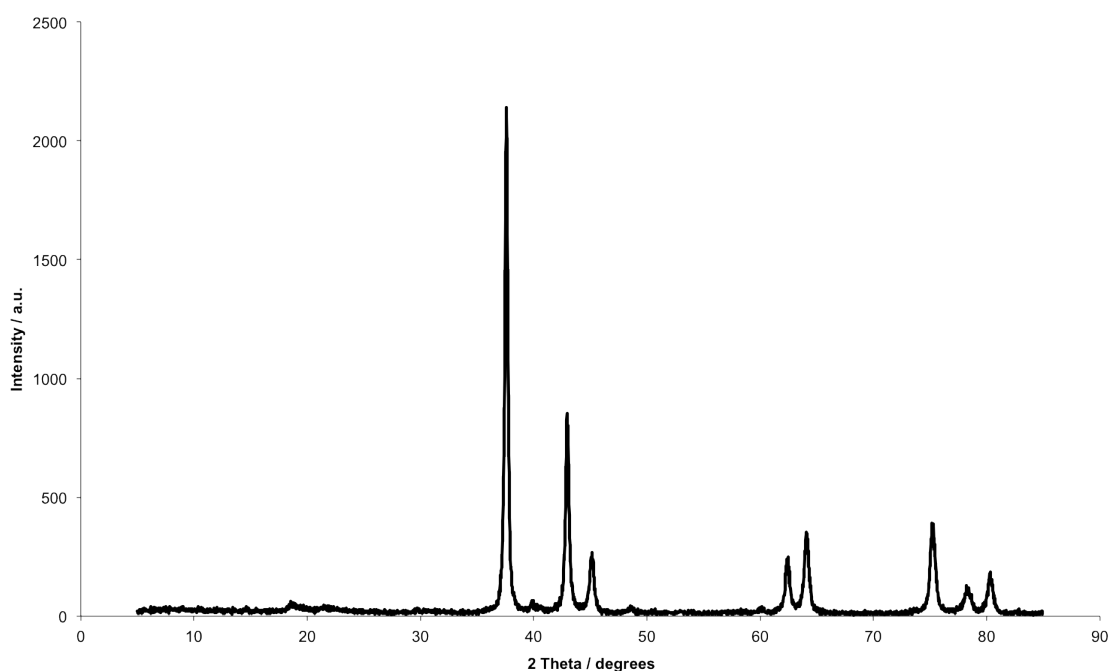
Figure 3-1: PXRD pattern of β-Mo$_2$N$_{0.8}$.

The PXRD pattern (Figure 3-1) was used to confirm the structure of the nitride by comparing the pattern to that previously shown by Mckay.[19] Literature unit cell details: Space group I4$_1$/amd, a = 4.2 Å, c = 8.0 Å, volume = 141.120 Å^3.[1] Initial cell parameters were obtained through indexing/least squares refinement procedures using Dicvol 04.[20] The data obtained from the microanalysis confirmed that that the amount of nitrogen present was 6.89 wt%. This gave a stoichiometry of Mo$_2$N$_{0.8}$, which is close to the proposed composition of Mo$_2$N$_{0.78}$.[19] The PXRD pattern shows a high degree of crystallinity from the sharp intense reflections observed. The pattern also shows crystalline impurity phases are present within the sample, although these could not be easily identified.

In order to confirm that the structure was that of beta molybdenum nitride, a refinement against PXRD data was undertaken, using GSAS.[21,22] The refinement model used

information from the crystallographic information file from Ettmayer's work,[1] however it was found that use of origin choice 2 as opposed to origin choice 1 was required to obtain a good fit to the observed pattern. The background was fitted to a shifted Chebyschev function (background function 1 in GSAS). Subsequently the lattice parameters were refined followed by the atomic parameters which, when stable, then allowed the peak profile to be refined. When the refinement had stabilised the thermal parameters were varied anisotropically. Once all of the parameters were refined a good fit to the model of beta molybdenum nitride was obtained, the results are shown in Figure 3-2, Table 3-1 and Table 3-2.
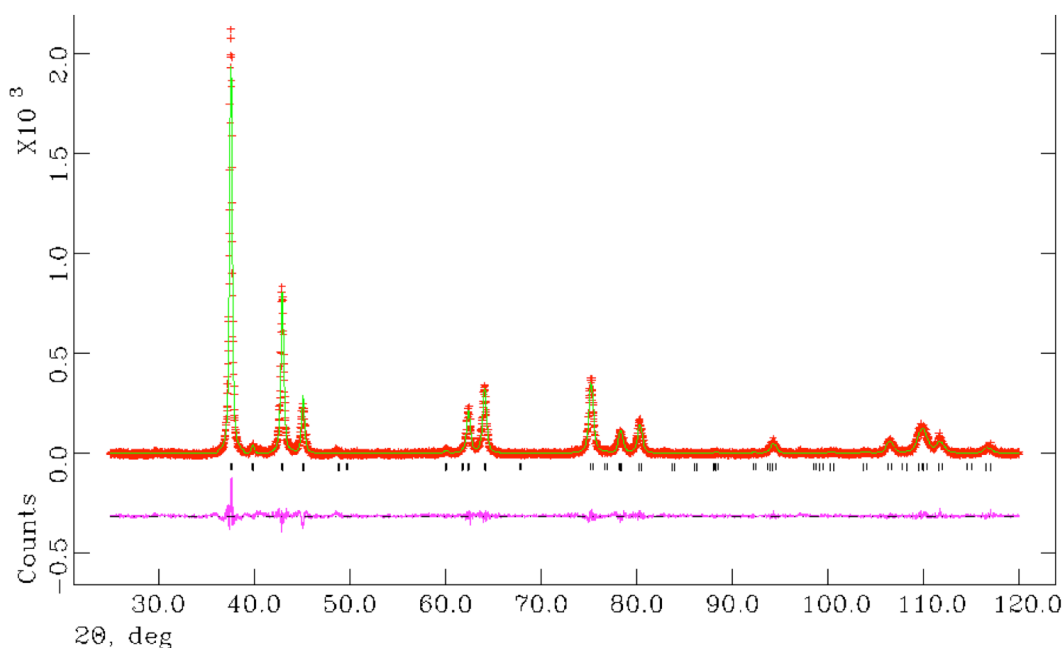
Figure 3-2: Final profile fit obtained from the refinement against the PXRD for β-Mo$_2$N$_{0.8}$.

The observed data are crosses, the calculated profile the solid line and lower continuous line the difference plot. Tick marks show allowed reflection positions.

Table 3-1: Crystallographic parameters for β-Mo$_2$N$_{0.8}$ from PXRD data.

Parameter	Value
Formula	Mo$_2$N$_{0.78}$
Crystal system	Tetragonal
Space group	I4$_1$/amd
Formula mass / gmol^{-1}	812.342
Cell parameter, a / Å (where $a = b$)	4.2043(6)
Cell parameter, c / Å	8.0264(12)
Unit-cell volume / Å^3	141.87(4)
Calculated density ρ_x / gcm^{-3}	9.508
Number of observations	4749
Number of variables	22
R$_p$ / %	12.41
R$_{wp}$ / %	18.38
χ^2	1.454

Table 3-2: β-Mo$_2$N$_{0.8}$ PXRD refined parameters.

Atoms / Site	x	y	z	Occupancy	100× U$_{iso}$ /U$_{eq}$ (Å^2)
Mo (8e)	0.500	0.250	0.3662(2)	1.00	0.76*
N (4a)	0.500	0.750	0.375	0.80‡	0.7(5)

‡ - parameters fixed.

* = Anisotropically measured – expansion is shown here:

Atoms	U$_{11}$ (Å^2)	U$_{22}$ (Å^2)	U$_{33}$ (Å^2)	U$_{12}$ (Å^2)	U$_{13}$ (Å^2)	U$_{23}$ (Å^2)
Mo	0.17(15)	0.47(15)	1.65(7)	0.00	0.00	0.00

The analysis of beta molybdenum nitride by PXRD does not allow for a definitive structural model to be obtained, as the scattering of X-rays by nitrogen is very weak in comparison with the scattering from molybdenum. PND was used to obtain a more complete model of the structure and also to confirm the nitrogen stoichiometry. The refinement against the PND data collected at 295 K (Table 3-3, Table 3-4 and Figure 3-3) confirms that the structure refined against PXRD data is fundamentally correct. Using the refined structure from the PXRD refinement as a starting model, the background was fitted to a reciprocal interpolation function (background function 8 in GSAS). In addition to the parameters refined during the PXRD refinement absorption factors were also refined. PND data collected provided a refined composition of $Mo_2N_{0.80(1)}$. The profile fit to the PND data shows one reflection that cannot be identified at a d-spacing of 1.87 Å. This is observable within the PND pattern and is not clearly identifiable in the PXRD refinement. The presence of the impurity phase could not be excluded from the refinement due to the close proximity to the beta phase reflections; possible sources of the impurity such as molybdenum metal and molybdenum oxides were investigated but yielded no matches.

Table 3-3: Crystallographic parameters for β-$Mo_2N_{0.8}$ from 295 K PND data.

Parameter	Value
Formula	$Mo_2N_{0.78}$
Crystal system	Tetragonal
Space group	$I4_1/amd$
Formula mass / $gmol^{-1}$	812.154
Cell parameter, a / Å (where $a = b$)	4.20039(6)
Cell parameter, c / Å	8.0219(2)
Unit-cell volume / $Å^3$	141.533(5)
Calculated density ρ_x / gcm^{-3}	9.529
Number of observations	7680
Number of variables	42
R_p / %	6.01
R_{wp} / %	5.96
χ^2	36.19

Table 3-4: β-$Mo_2N_{0.8}$ PND (295 K) refined parameters.

Atoms / Site	x	y	z	Occupancy	100× U_{iso}/U_{eq} ($Å^2$)
Mo (8e)	0.500	0.250	0.36723(9)	1.00	0.95*
N (4a)	0.500	0.750	0.375	0.797(5)	0.46(2)

‡ - parameters fixed

* = Anisotropically measured – expansion is shown here:

Atoms	U_{11} ($Å^2$)	U_{22} ($Å^2$)	U_{33} ($Å^2$)	U_{12} ($Å^2$)	U_{13} ($Å^2$)	U_{23} ($Å^2$)
Mo	0.500(24)	0.444(23)	1.908(35)	0.00	0.00	0.00
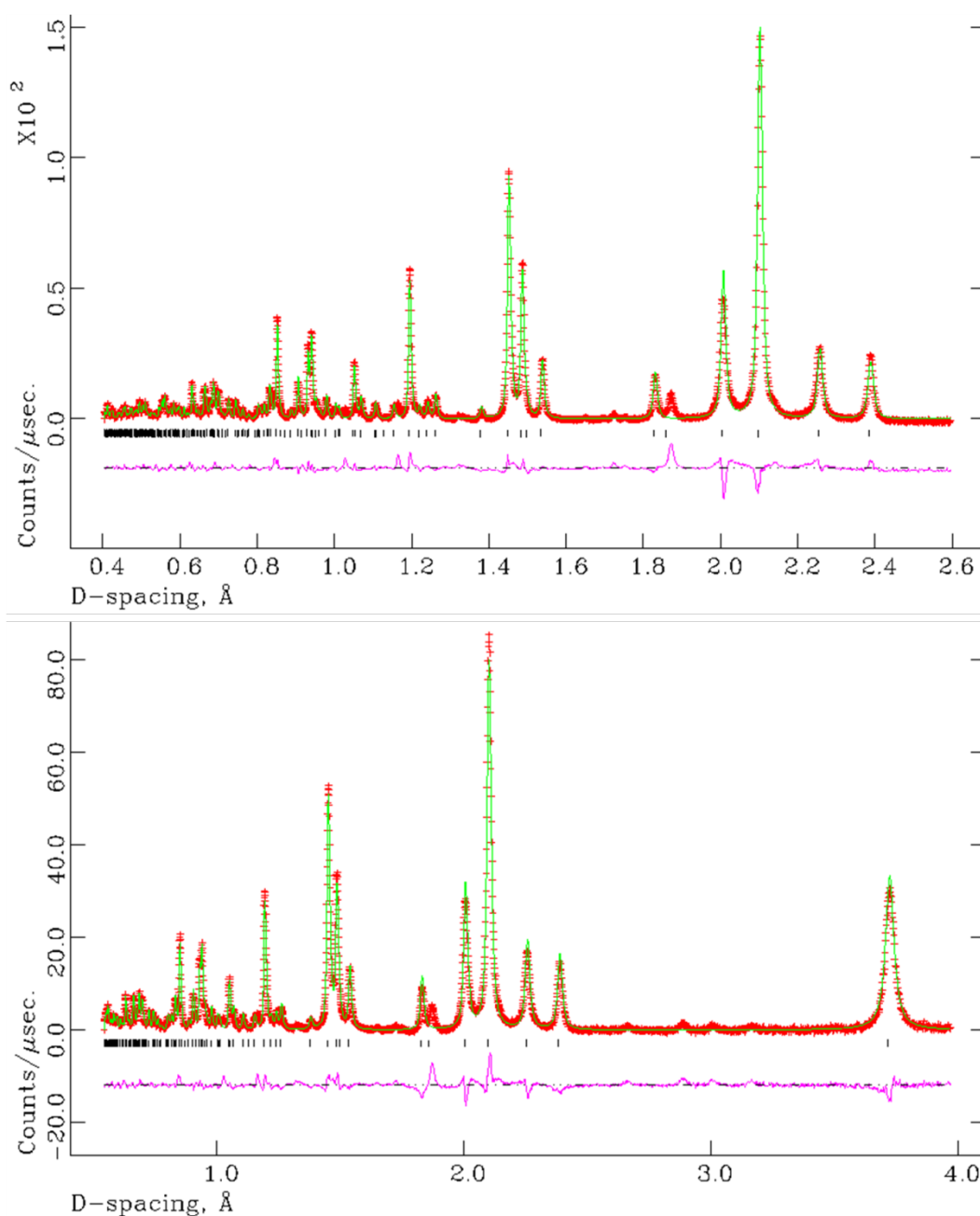
Figure 3-3: Final profile fit obtained from the refinement against PND at 295 K for β-Mo₂N₀.₈.

The observed data are crosses, the calculated profile the solid line and lower
continuous line the difference plot. Tick marks show allowed reflection positions.
Top – Backscattering detector bank <2θ> = 145°, Bottom - 90° detector bank.

The refinement of the nitrogen occupancy to a stoichiometry of $Mo_2N_{0.80(1)}$ has shown
that the structure may have some degree of variability in relation to the nitrogen content
which was discussed previously by Evans and Jack.[18] Low temperature refinements of
the beta molybdenum nitride were completed using as the starting model the room
temperature completed refinement; the results of this are seen in Figure 3-4, Table 3-5
and Table 3-6.
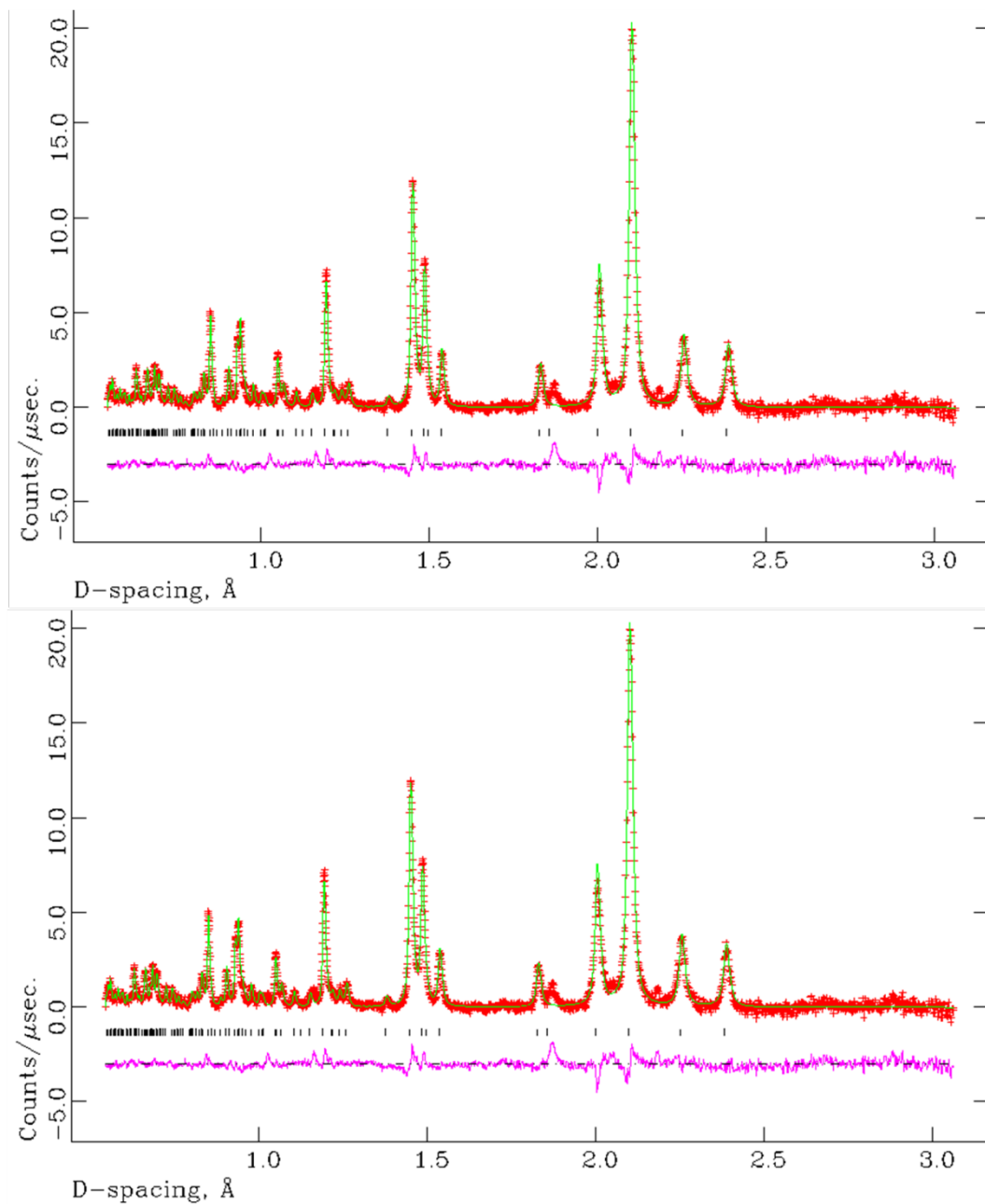
Figure 3-4: Final profile fit obtained from the refinement against PND data at 1.9 K for β-Mo₂N₀.₈.

The observed data are crosses, the calculated profile the solid line and lower continuous line the difference plot. Tick marks show allowed reflection positions. Top – Backscattering detector bank <2θ> = 145°, Bottom - 90° detector bank.

Table 3-5: Crystallographic parameters for β-Mo₂N₀.₈ from (1.9 K) PND data.

Parameter	Value
Formula	$Mo_2N_{0.78}$
Crystal system	Tetragonal
Space group	$I4_1/amd$
Formula mass / gmol^{-1}	811.478
Cell parameter, a / Å (where $a = b$)	4.19800(6)
Cell parameter, c / Å	8.01177(22)
Unit-cell volume / Å^3	141.193(5)
Calculated density ρ_x / gcm^{-3}	9.544
Number of observations	7097
Number of variables	37
R_p / %	2.51
R_{wp} / %	2.20
χ^2	3.995

Table 3-6: β-Mo₂N₀.₈ PND (1.9 K) refined parameters.

Atoms / Site	x	y	z	Occupancy	100× U_{iso} /U_{eq} (Å^2)
Mo (8e)	0.500	0.250	0.3664(1)	1.00	0.71*
N (4a)	0.500	0.750	0.375	0.785(6)	0.46*

* = Anisotropically measured – expansion is shown here:

Atoms	U_{11} (Å^2)	U_{22} (Å^2)	U_{33} (Å^2)	U_{12} (Å^2)	U_{13} (Å^2)	U_{23} (Å^2)
Mo	0.52(3)	0.36(3)	1.27(4)	0.00	0.00	0.00
N	0.16(2)	0.16(2)	1.06(7)	0.00	0.00	0.00

Selected bond lengths and angles, are shown in Table 3-7 and Table 3-8. The results show that the Mo and N are not in a regular octahedral arrangement. The refinements at both room and low temperature for the PND data show this slightly distorted octahedral Mo-N environment. The length of the Mo-N bond varies from 2.0678(7) to 2.10112(4) Å.

Table 3-7: Selected Interatomic Distances for β-Mo$_2$N$_{0.8}$ from PND data.

Temperature	290 K	1.9 K
Atomic Distance (Å)		
Mo – Mo ×4	2.90392(4)	2.90131(4)
Mo – Mo ×2	2.9914(10)	2.9976(12)
Mo – Mo ×4	2.97274(7)	2.97160(9)
Mo – Mo ×2	2.8193(9)	2.8084(11)
Mo – N ×6	2.10112(4)	2.10012(4)
Mo – N ×3	2.0678(7)	2.0715(8)

Table 3-8: Selected bond angles for β-Mo$_2$N$_{0.8}$ from PND data.

Temperature	290 K	1.9 K
Bond Angle (°)		
Mo – N – Mo ×2	176.60(4)	176.26(5)
Mo – N – Mo ×4	88.30(2)	88.13(2)
Mo – N – Mo ×4	91.70(2)	91.87(2)
Mo – N – Mo ×4	90.05(1)	90.06(1)
Mo – N – Mo	180.00(0)	180.00(0)
N – Mo – N	176.60(4)	176.26(5)
N – Mo – N ×2	88.30(2)	88.13(2)

3.3.1.2   Magnetic measurements

The low temperature PND refinement shows no sign of scattering from magnetic ordering below 4 K. SQUID measurements revealed that there is a change in the magnetic behaviour below 5 K (Figure 3-5).
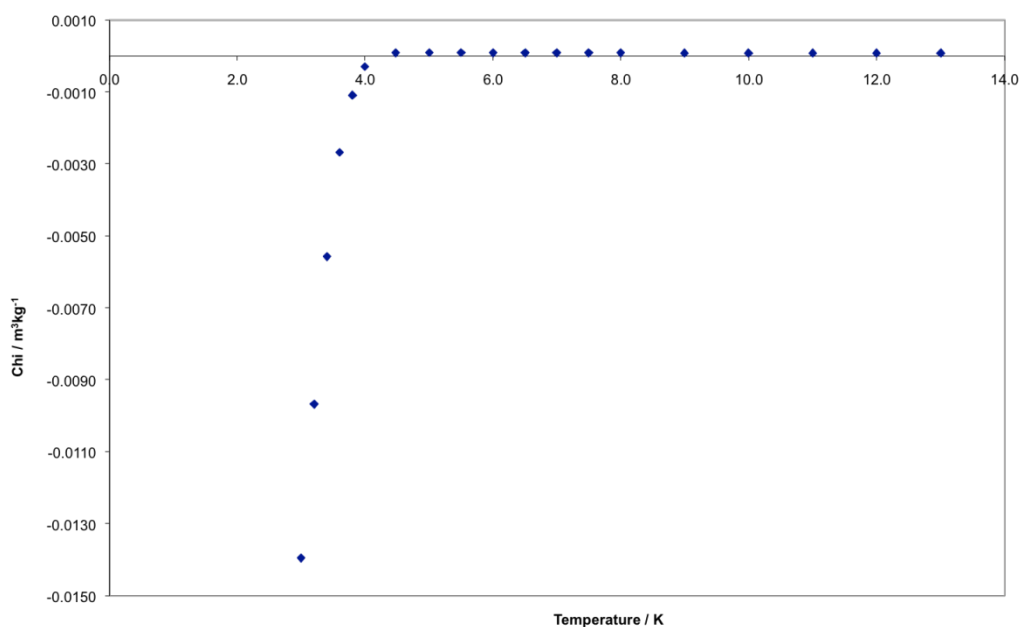
Figure 3-5: Magnetic susceptibility measurement for β-Mo$_2$N$_{0.8}$.

The literature has discussed that thin films of beta molybdenum nitride superconduct at low temperatures (5.2 K). The data presented here demonstrate that there is no change in the diffraction pattern for the nitride between 295 K and 1.9 K (with a T_c of 4.25 K) suggesting that there is no structural phase change associated with the transformation from the normal to the superconducting state <5 K.

3.3.1.3   Activity study

The catalytic activity of the beta phase molybdenum nitride in the preparation of ammonia is of interest as the formation of the nitride under 3:1 H_2/N_2 gas mixture at a reduced processing time would have a large economic and environmental benefit (using a less toxic and corrosive gas). Using the test reactor system, beta molybdenum nitride was reacted at 673 K for 5½ hours under 3:1 H_2/N_2 gas. The reaction was a steady state process with the formation of ammonia being constant throughout the reaction. This is shown in the reaction profile (Figure 3-6). From the gradient of the profile it is possible to calculate the rate of ammonia production during the reaction. This gives the beta

phase as having an ammonia synthesis rate of 59.4 $\mu molh^{-1}g^{-1}$. This is in good agreement to previous work completed on beta molybdenum nitride.[23]
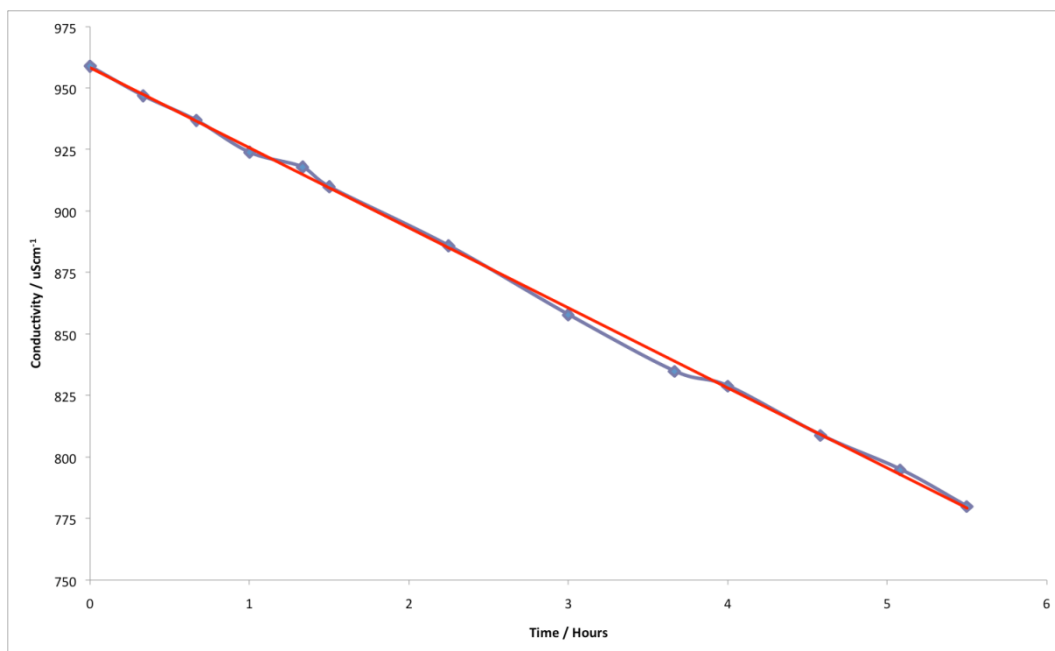
Figure 3-6: Reaction profile for β-Mo$_2$N$_{0.8}$.

The surface area of the beta phase is approximately 10 m^2g^{-1}. However as stated previously (Section 2.4.2) this may not be the value for the active phase as the nitride is pyrophoric so a passivated surface could well be characterised.
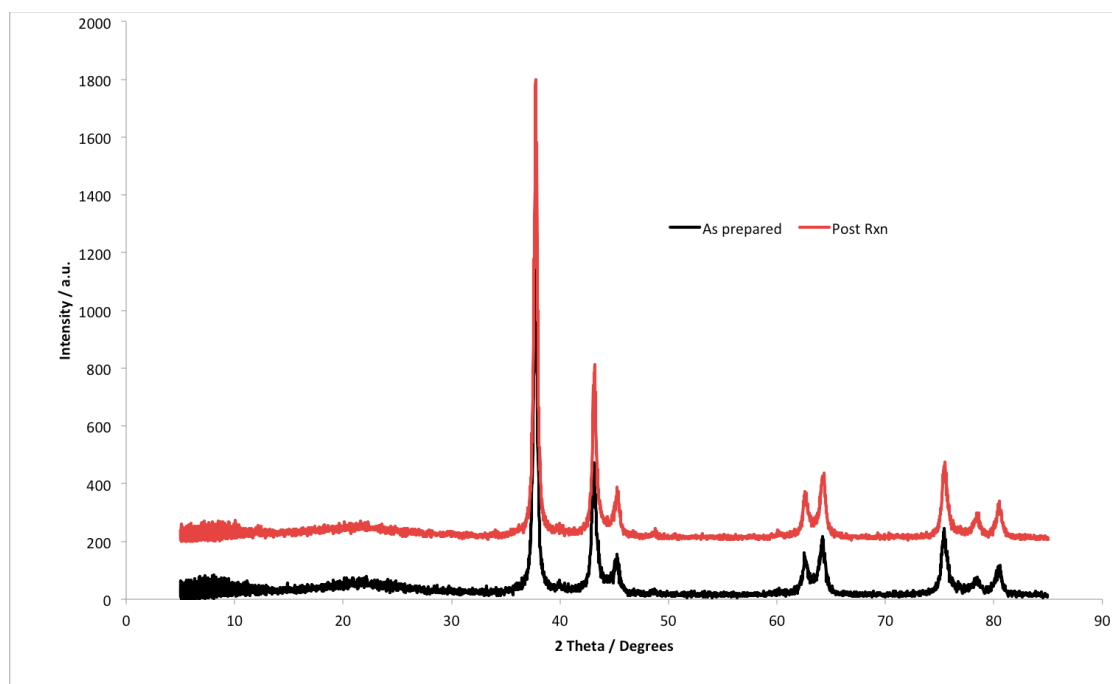
Figure 3-7: Comparison of pre- and post- reaction PXRD patterns for β-Mo$_2$N$_{0.8}$.

From studying the PXRD data for the pre- and post- reaction sample of beta molybdenum nitride it can be shown that the formation of ammonia does not apparently affect the bulk structure of the sample (Figure 3-7).

Indexing of the two patterns gives lattice parameters which are within experimental error of each other, (post-reaction parameters; a = 4.210(3) Å, c = 8.03(4) Å). The microanalysis results also showed no change in the post-reaction nitrogen content, which, in combination with the PXRD data, indicates that the structure and composition of the beta phase is unchanged following exposure to 3:1 H_2/N_2 gas.

3.3.2   Gamma molybdenum nitride (γ-Mo$_2$N)

3.3.2.1   Structural study

The formation of gamma molybdenum nitride as previously described by Bull *et al.*[2] through the direct ammonolysis of molybdenum trioxide was the method employed for the synthesis during this project. PXRD data (Figure 3-8) shows that there is a single phase present which can be matched to that of gamma Mo_2N. Literature unit cell details: Space group Fm-3m, a = 4.16158(5) Å, volume = 72.0704 Å^3.[2] Indexing of the PXRD data to a cubic space group *Fm-3m*, with parameters of 4.20(5) Å, gives good agreement to structural models reported in the literature.
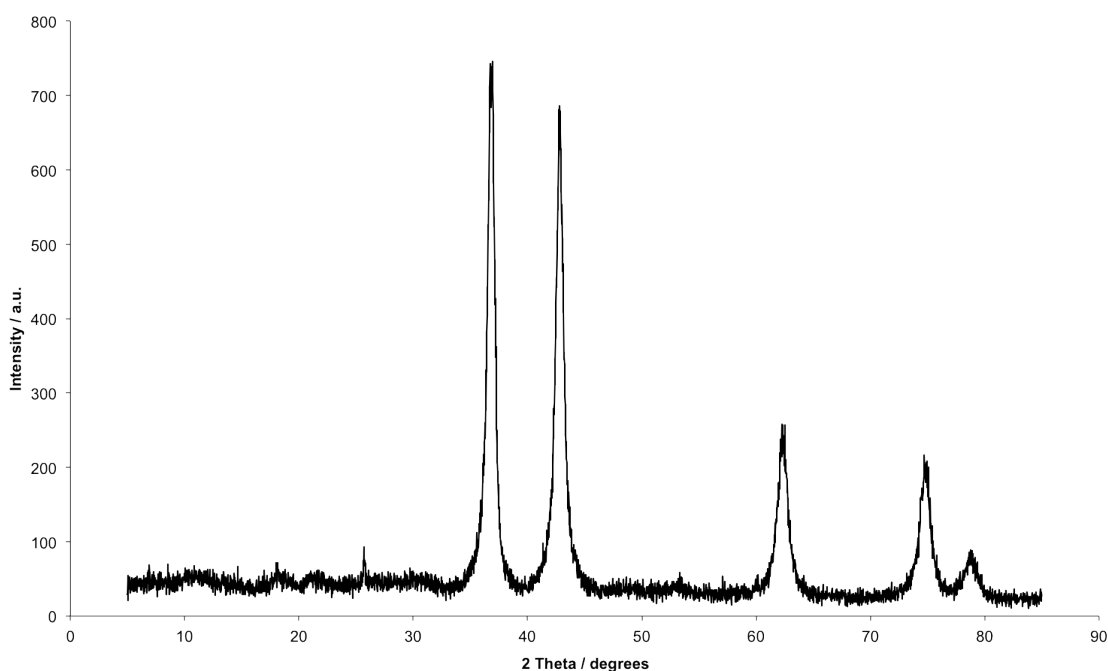
Figure 3-8: PXRD pattern of γ-Mo$_2$N.

Microanalysis results yield 8.46(3) weight% of nitrogen and a nominal stoichiometry of $Mo_2N_{1.19}$. A small amount of hydrogen however, was observed in the microanalysis results. This combined with the excess nitrogen obtained could be assigned to surface NH_x species remaining from the ammonolysis procedure.

Although the pattern matched that in the literature a refinement was performed in order to ascertain the exact stoichiometry of the material. The refinement was performed using GSAS and the background was fitted with a shifted Chebyschev function. The lattice parameters were refined followed by the atomic parameters, which when stable, then allowed the peak profile to be refined. When the refinement had stabilised the thermal parameters were varied isotropically. The fit obtained from the refinement was not completely accurate as the main reflections at 38 and 42 °2θ were not accurately modelled. The low quality data collected on the lab X-ray diffractometer does not allow for accurate determination of the fractional occupancy of the nitrogen or of the thermal parameters related to the nitrogen, these were fixed at suitable values based on a stoichiometry of $Mo_2N_{1.2}$. (Figure 3-9, Table 3-9 and Table 3-10). As such there is a disparity between the observed and calculated model for the system, further studies by PND described later are therefore used for structural analysis.
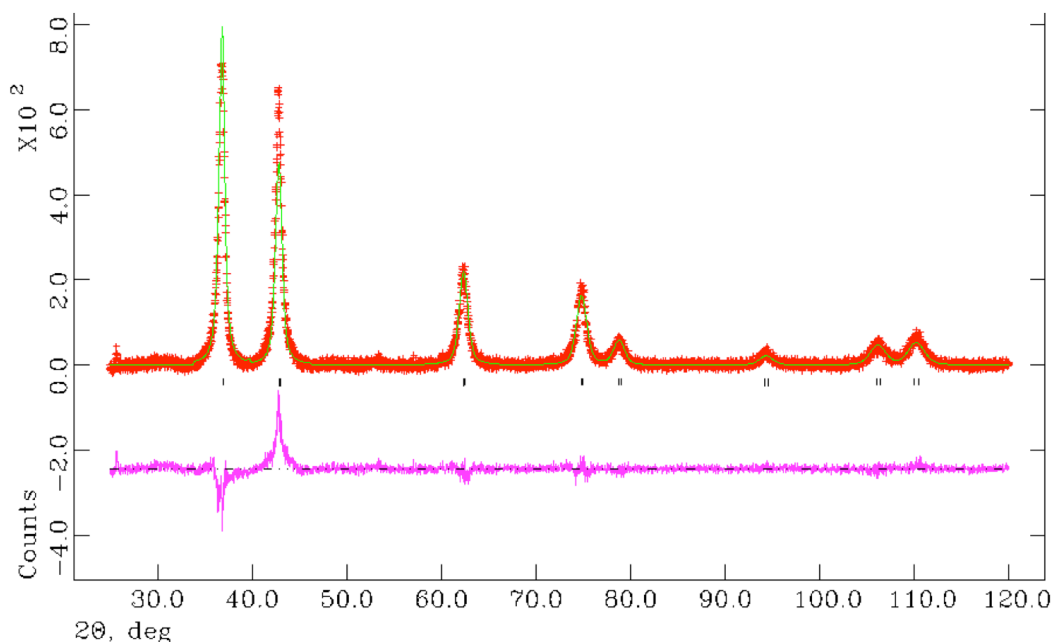
Figure 3-9: Final profile fit obtained from the refinement against PXRD data for γ-Mo₂N.

The observed data are crosses, the calculated profile the solid line and lower continuous line the difference plot. Tick marks show allowed reflection positions.

Table 3-9: Crystallographic parameters for γ-Mo$_2$N from PXRD data.

Parameter	Value
Formula	Mo$_2$N$_{1.2}$
Crystal system	Cubic
Space group	*Fm-3m*
Formula mass / gmol^{-1}	417.377
Cell parameter, *a* / Å	4.2028(6)
Unit-cell volume / Å^3	74.237(18)
Calculated density ρ$_x$ / gcm^{-3}	9.336
Number of observations	4749
Number of variables	18
R$_p$ / %	14.05
R$_{wp}$ / %	17.44
χ^2	1.626

Table 3-10: γ-Mo$_2$N PXRD refined parameters.

Atoms / Site	x	y	z	Occupancy	100× U$_{iso}$ /U$_{eq}$ (Å^2)
Mo (4a)	0.000	0.000	0.000	1.00	1.88(5)
N (4b)	0.500	0.500	0.500	0.60‡	1.50‡

‡ - parameters fixed

In order to obtain an accurate value for the nitrogen stoichiometry and a definitive structural model for gamma molybdenum nitride powder neutron diffraction was undertaken. Using the refined structure from the PXRD refinement as a starting model, the background was fitted to a reciprocal interpolation function (background function 8 in GSAS). In addition to the parameters refined during the PXRD refinement, absorption factors were also refined and the thermal parameters were varied anisotropically. The results are shown below (Figure 3-10, Table 3-11 and Table 3-12) and show that there is a good correlation to the literature model for gamma molybdenum nitride.
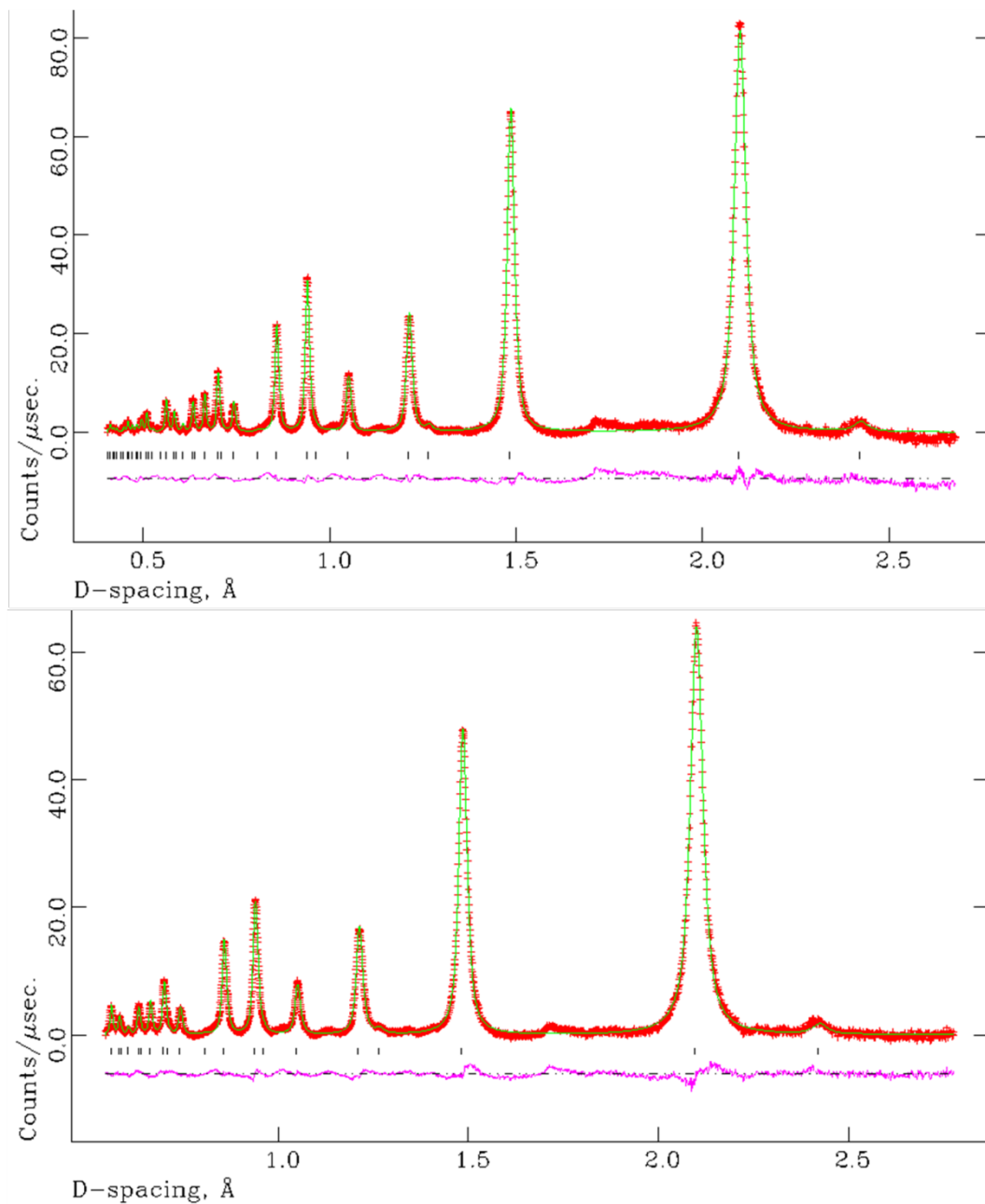
Figure 3-10: Final profile fit obtained from the refinement against PND at 295 K for γ-Mo₂N.

The observed data are crosses, the calculated profile the solid line and lower continuous line the difference plot. Tick marks show allowed reflection positions. Top – Backscattering detector bank <2θ> = 145°, Bottom - 90° detector bank.

Table 3-11: Crystallographic parameters for γ-Mo$_2$N from PND data.

Parameter	Value
Colour of powder	Black
Formula	$Mo_2N_{1.14}$
Crystal system	Cubic
Space group	*Fm-3m*
Formula mass / gmol^{-1}	415.907
Cell parameter, *a* / Å	4.19547(5)
Unit-cell volume / Å^3	73.8487(16)
Calculated density ρ_x / gcm^{-3}	9.352
Number of observations	7027
Number of variables	34
R$_p$ / %	1.79
R$_{wp}$ / %	1.83
χ^2	9.493

Table 3-12: γ-Mo$_2$N PND (295 K) refined parameters.

Atoms / Site	x	y	z	Occupancy	100× U$_{iso}$ /U$_{eq}$ (Å^2)
Mo (4a)	0.000	0.000	0.000	1.00	0.96*
N (4b)	0.500	0.500	0.500	0.574(6)	1.06*

* = Anisotropically measured – expansion is shown here:

Atoms	U$_{11}$ (Å^2)	U$_{22}$ (Å^2)	U$_{33}$ (Å^2)	U$_{12}$ (Å^2)	U$_{13}$ (Å^2)	U$_{23}$ (Å^2)
Mo	0.958(20)	0.958(20)	0.958(20)	0.00	0.00	0.00
N	1.062(25)	1.062(25)	1.062(25)	0.00	0.00	0.00

The higher than expected nitrogen content shown in the microanalysis, is observable in the refinement with the occupancy of the nitrogen refining to 0.574(6) yeilding a stoichiometry of $Mo_2N_{1.14}$. This is slightly reduced from that calculated through the microanalysis results.
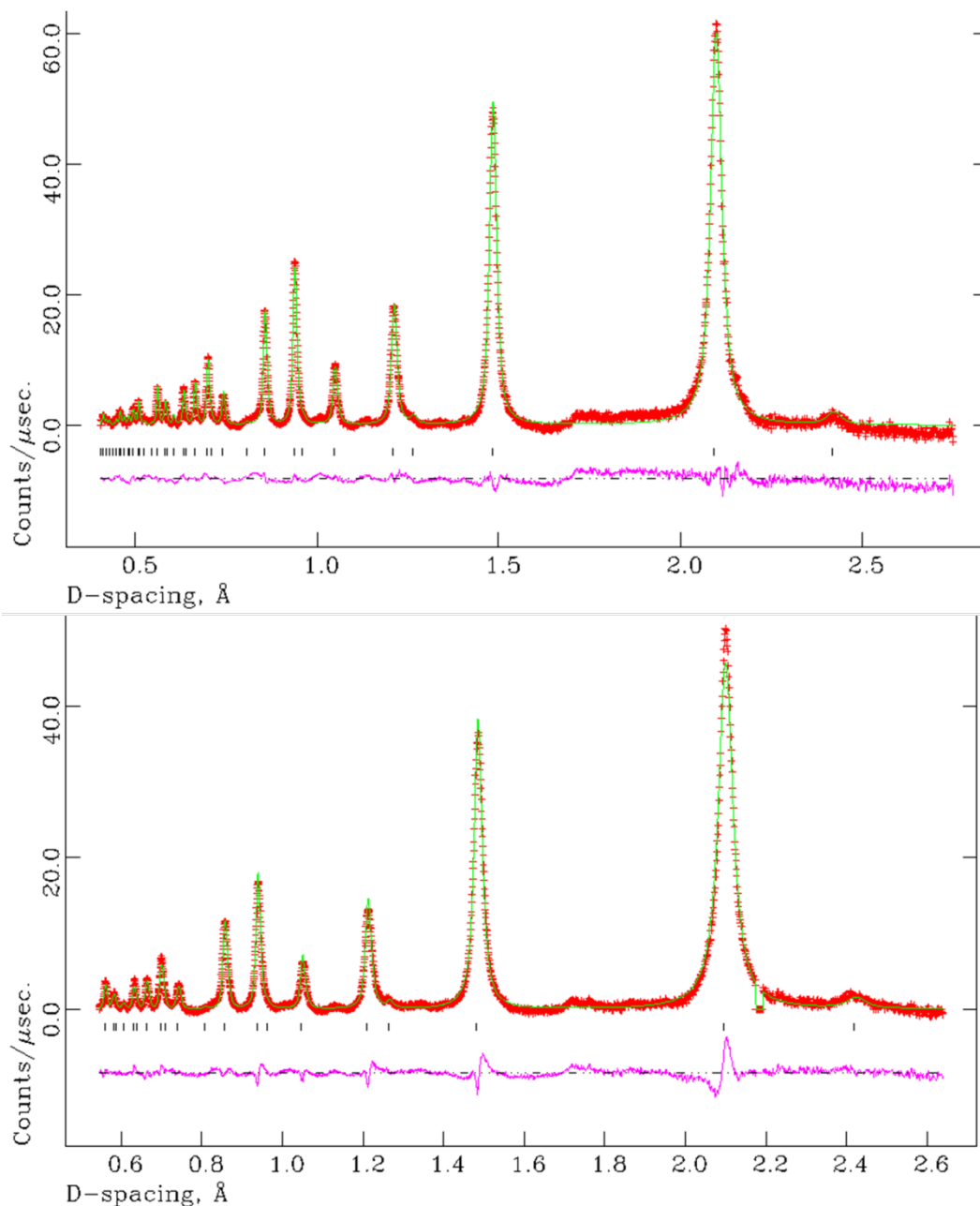
Figure 3-11: Final profile fit obtained from the refinement against PND at 4.2 K for γ-Mo₂N.

The observed data are crosses, the calculated profile the solid line and lower continuous line the difference plot. Tick marks show allowed reflection positions.
Top – Backscattering detector bank <2θ> = 145°, Bottom - 90° detector bank.

Table 3-13: Crystallographic parameters for γ-Mo₂N from 4.2 K PND data.

Parameter	Value
Colour of powder	Black
Formula	$Mo_2N_{1.11}$
Crystal system	Cubic
Space group	*Fm-3m*
Formula mass / $gmol^{-1}$	414.799
Cell parameter, *a* / Å	4.19317(6)
Unit-cell volume / $Å^3$	73.7273(18)
Calculated density ρ_x / gcm^{-3}	9.342
Number of observations	6963
Number of variables	32
R_p / %	1.61
R_{wp} / %	1.31
χ^2	7.017

Table 3-14: γ-Mo₂N PND (4.2 K) refined parameters.

Atoms / Site	x	y	z	Occupancy	$100\times$ U_{iso}/U_{eq} ($Å^2$)
Mo (4a)	0.000	0.000	0.000	1.00	0.81*
N (4b)	0.500	0.500	0.500	0.554(6)	0.94*

* = Anisotropically measured – expansion is shown here:

Atoms	U_{11} ($Å^2$)	U_{22} ($Å^2$)	U_{33} ($Å^2$)	U_{12} ($Å^2$)	U_{13} ($Å^2$)	U_{23} ($Å^2$)
Mo	0.808(22)	0.808(22)	0.808(22)	0.00	0.00	0.00
N	0.936(29)	0.936(29)	0.936(29)	0.00	0.00	0.00

Data collected at 4.2 K show that the cubic structure is retained at low temperature. The refined stoichiometry of $Mo_2N_{1.11}$, is in good agreement with microanalysis and refinement of the room temperature data. Results are shown in Figure 3-11, Table 3-13 and Table 3-14.

The crystallographic information obtained from the refinements shows that as the atoms are present on special sites the bond angles give an ordered octahedral arrangement; bond lengths are shown in Table 3-15.

Table 3-15: Selected Interatomic Distances for γ-Mo$_2$N from PND data.

Temperature	290 K	4.2 K
Mo – Mo ×12	2.96665(4)	2.96502(3)
Mo – N ×12	2.09774(3)	2.09659(3)

3.3.2.2 Activity study

In order to test the ability of the nitride to produce ammonia, the sample was reacted under 3:1 H_2/N_2 gas at 673 K for 5½ hours. The reaction profile (Figure 3-12) shows that over the initial hour there is a high rate of reaction which could be attributed to the release of NH_x species from the surface of the nitride. After the initial hour a steady state reaction was observed with a rate of 15.6 $\mu molh^{-1}g^{-1}$.

The post reaction microanalysis results show that there is 6.93(5) wt% nitrogen remaining in the sample after reaction, equating to a stoichiometry of $Mo_2N_{1.02(1)}$.
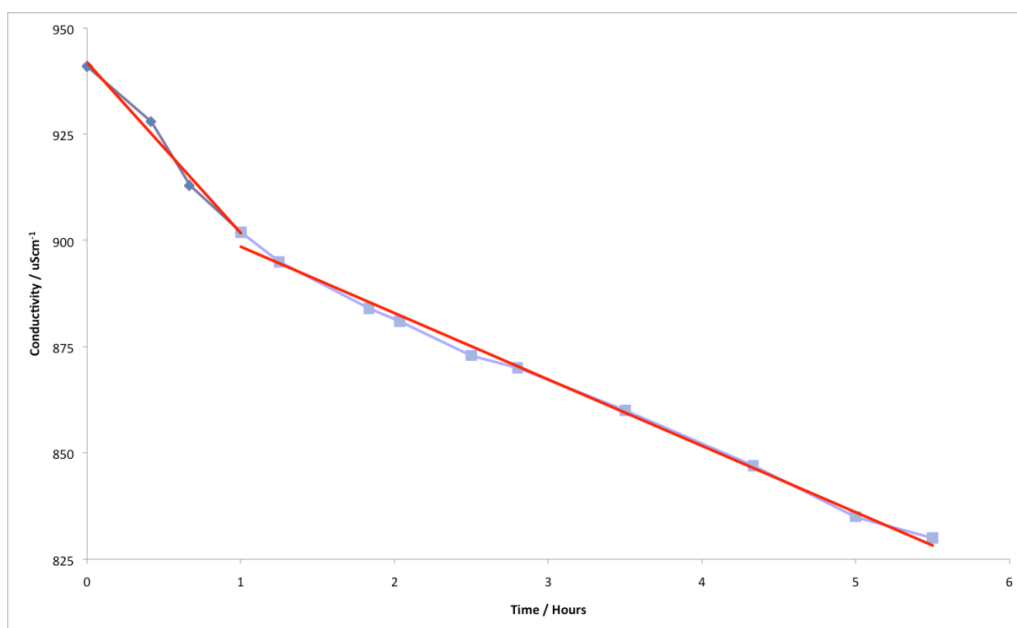
Figure 3-12: Reaction profile for γ-Mo₂N.
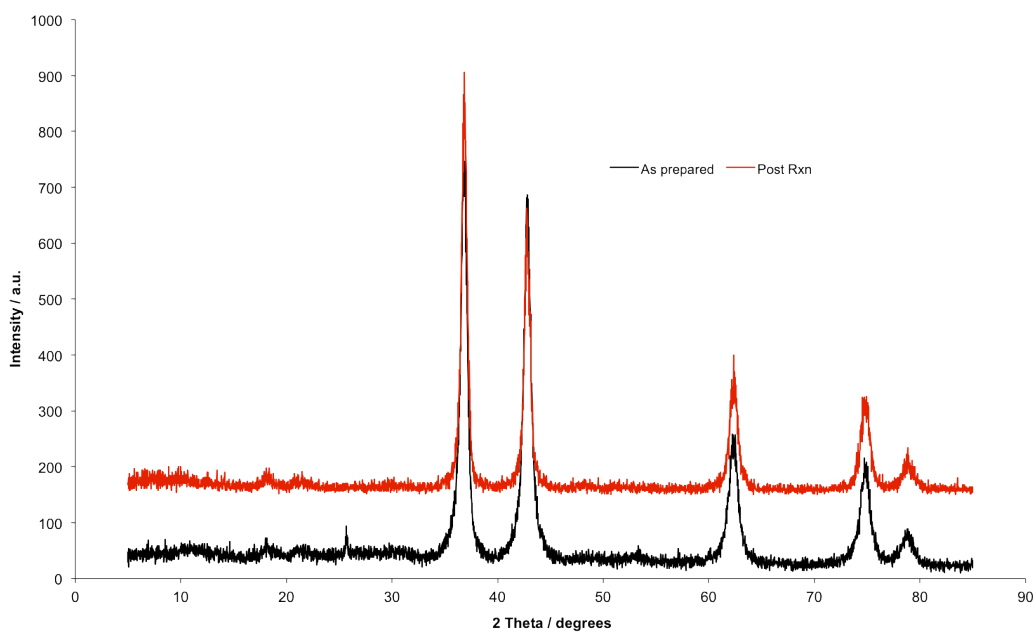
Figure 3-13: Comparison of pre- and post- reaction PXRD patterns for γ-Mo₂N.

Analysis of the PXRD patterns pre- and post- reaction (Figure 3-13) show that the gamma phase is unchanged and that the lattice parameter obtained through indexing (a = 4.2031(4) Å) are within errors of those seen prior to the reaction, indicating that there is no change to the bulk structure of the gamma phase during the reaction. However there is a suggestion that an impurity phase which can be seen in the PXRD prior to analysis as a reflection at 26 °2θ and tentatively be attributed to MoO_2, which is removed during the activity testing.

The surface area of gamma molybdenum nitride is 80 m^2g^{-1}. This is considerably higher than that of the beta phase described previously (Section 3.3.1.3) although the difference in the preparative methods has been shown to have an effect on the surface area as previously discussed in the literature.[4]

The activity of gamma molybdenum nitride as an ammonia synthesis catalyst has been investigated previously.[4,24,25] The ability of γ-Mo_2N to produce ammonia is an important factor in later work on the ternary molybdenum nitride systems.

3.3.3 Delta molybdenum nitride (δ-MoN)

3.3.3.1 Structural study

The structure of delta molybdenum nitrides has been discussed in detail by Vajenine *et al.*[3] who describe the different forms of δ-MoN from varying precursors and synthesis methods and by Marchand *et. al.*[16] who describe the formation of molybdenum nitrides and in particular δ-MoN through the direct reaction of ammonia with MoS_2. The method used to form delta molybdenum nitride was described earlier (Section 3.2.3), and is based on reactions completed by Mckay.[19]
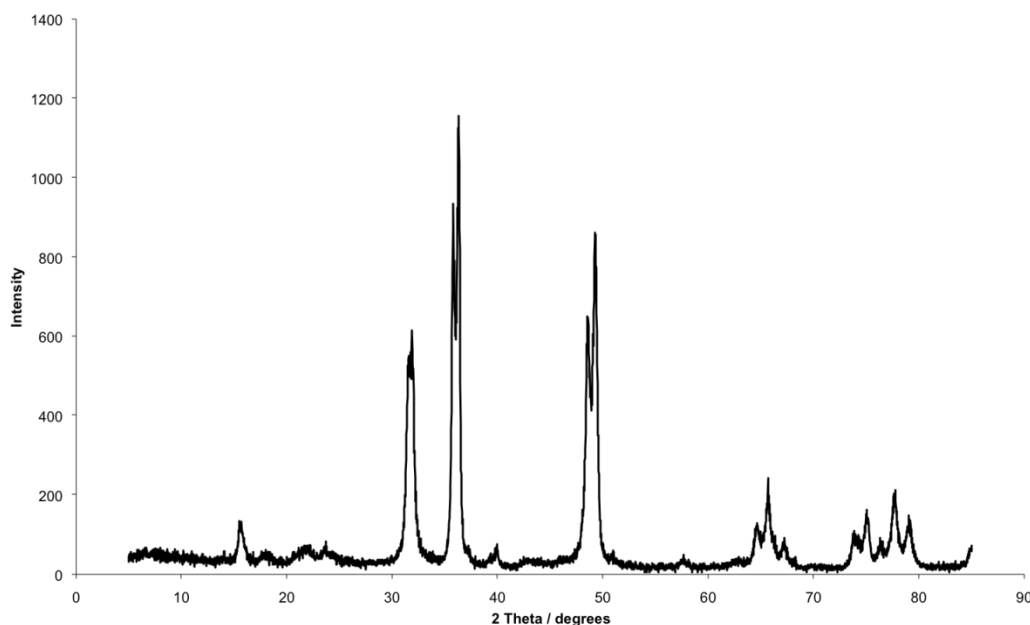
Figure 3-14: PXRD pattern of δ-Mo$_2$N.

Literature unit cell details: MoN - Space group P63mc, a = 5.73953(9) Å, c = 5.6176(1) Å volume = 160.2605 Å^3 and Mo_5N_6 . Space group P63/m, a = 4.8924(1) Å, c = 11.0643(4) Å volume = 229.341 Å^3.[3]

Analysis of the PXRD data (Figure 3-14) shows that there is the appearance of double reflections at the positions of the major reflections for δ-MoN, this could be an indication of two similar phases of δ-MoN or an impurity phase.

The literature describes the formation of Mo_5N_6 at temperatures of around 1023 K.[3] Based on this, the diffraction pattern was matched to phases of Mo_5N_6 and δ-MoN. This accounted for all of the crystalline reflections observed in the pattern.

In order to confirm the presence of both Mo_5N_6 and δ-MoN, Rietveld refinements were performed against the PXRD data. The refinement used a type 1 background function in GSAS (a shifted Chebyschev function). The lattice parameters were refined followed by the atomic parameters which when stable then allowed the peak profile to be refined. When the refinement had stabilised the thermal parameters were varied isotropically. Once the first phase had been accurately modelled the second phase was introduced and the same procedure was used for refinement of the second phase along with the phase fraction of the two phases.

The PXRD refinement data show that the phases of δ-MoN (NiAs-type structure) and Mo_5N_6 (filled 2H-MoS_2 strucutre) were present in a 51.6:49.4 ratio. The formation of mixed phases of MoN and Mo_5N_6 was possible through the use of long reaction times at a temperature of 1098 K. The formation of Mo_5N_6 occurs at ca. 1023 K and the δ-MoN phase is formed around 1098 K. Following the method previously used by Mckay, of reacting MoS_2 under flowing ammonia for 60 hours at 1073 K, one would expect from Vajenine's work that a biphasic mixture of δ-MoN and Mo_5N_6 would be formed. Refinements against the PXRD data confirm the structure of the delta phase to be that of δ$_3$-MoN previously shown by Vajenine. The results of the refinements are shown in Figure 3-15, Table 3-16 and Table 3-17.
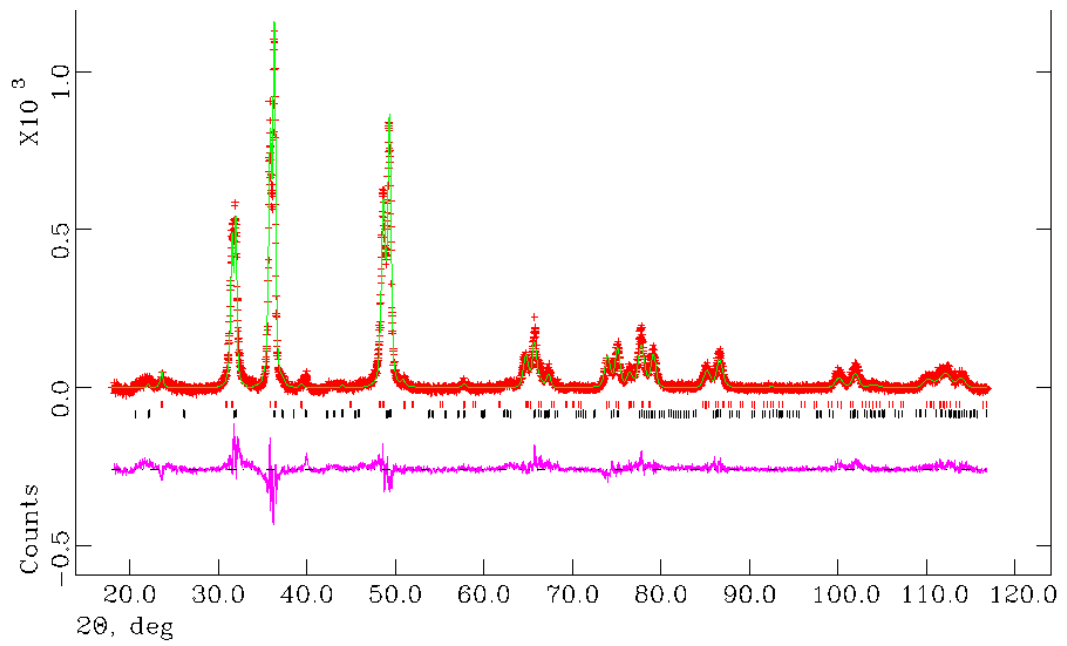
Figure 3-15: Final profile fit obtained from the refinement against PXRD for δ-MoN and Mo$_5$N$_6$.

The observed data are crosses, the calculated profile the solid line and lower
continuous line the difference plot. Tick marks show allowed reflection positions.
Red Tick-marks – Mo$_5$N$_6$, Black tick-marks - MoN.

Table 3-16: Crystallographic parameters for δ-MoN from PXRD data.

Parameter	Value
Formula	Mo_5N_6
Crystal system	
Space group	P63/m
Phase Fraction / %	50.1(5)
Formula mass / gmol^{-1}	1319.364
Cell parameter, a / Å	4.9039(4)
Cell parameter, c / Å	11.0872(12)
Unit-cell volume / Å^3	230.90(4)
Calculated density ρ_x / gcm^{-3}	9.488
Formula	δ-MoN
Crystal system	
Space group	P63mc
Phase Fraction / %	49.9(5)
Formula mass / gmol^{-1}	879.576
Cell parameter, a / Å	5.7367(6)
Cell parameter, c / Å	5.6193(7)
Unit-cell volume / Å^3	160.152(30)
Calculated density ρ_x / gcm^{-3}	9.120
Number of observations	4928
Number of variables	20
R_p / %	15.95
R_{wp} / %	21.15
χ^2	2.526

Table 3-17: δ-MoN PXND (295 K) refined parameters.

Mo_5N_6

Atoms / Site	x	y	z	Occupancy	100× U_{iso} /U_{eq} (Å²)
Mo 1 (2)	0.000	0.000	0.250	0.852(19)	2.00‡
Mo 2 (2)	0.000	0.000	0.000	1.000	2.00‡
Mo 3 (2)	0.333	0.667	0.250	0.387(16)	2.00‡
Mo 4 (2)	0.667	0.333	0.250	1.000	2.00‡
Mo 5 (4)	0.333	0.667	0.0071(10)	1.000	2.00‡
N (12)	0.0662(2)	0.3747(7)	0.10527(6)	1.000	2.00‡

MoN

Atoms / Site	x	y	z	Occupancy	100× U_{iso} /U_{eq} (Å²)
Mo 1 (2)	0.000	0.000	-0.0090	1.000	2.00‡
Mo 2 (6)	0.4881(3)	0.5119(3)	-0.0070	1.000	2.00‡
N 1 (2)	0.333	0.667	0.9452(6)	1.000	2.00‡
N 2 (6)	0.1426(1)	0.8574(8)	0.3267(6)	1.000	2.00‡

‡ - parameters fixed

3.4　Summary

In this chapter, the investigation of the structure and catalytic properties of binary molybdenum nitrides was described. The literature and previous investigations had been very thorough in the study of the gamma phase in both the formation, structure and its catalytic properties, however no conclusive studies had been performed on the structure of the beta phase.

Beta molybdenum nitride has been confirmed here as crystallising in tetragonal space group $I4_1/amd$ with a stoichiometry of $Mo_2N_{0.8}$. The data collected through PXRD and PND at show that the room temperature structure previously proposed is accurate and is invariant even at low temperatures when the material moves from the normal to the superconducting state. Despite a relatively low surface area of 10 m²g⁻¹, the beta phase

yields an ammonia formation rate of 59.4 $\mu molh^{-1}g^{-1}$ and thus is an effective material for activating nitrogen.

Gamma phase molybdenum nitride was refined with a stoichiometry of $Mo_2N_{1.2}$ which is higher than has been previously reported for the gamma phase.

The ability of the binary nitrides to produce ammonia under ambient pressures and at 673 K without being degraded or destroyed means that the possibility of the nitrides as an ammonia synthesis catalyst remains.

The structural data collected for the nitrides combined with the activity data shows that the beta phase is, under the conditions used for the testing and methods of preparation, a better choice as ammonia synthesis catalyst, than the gamma phase. It uses a non-corrosive gas in the production of the beta phase unlike the formation of gamma molybdenum nitride which uses ammonia. Also the large amount of ammonia used in the synthesis of gamma Mo_2N would be more than the sample would produce whilst acting as an ammonia synthesis catalyst.

The formation of phase impure δ-MoN, and the fact that it is not an impurity present in the ternary nitrides used in this project (see later chapters), meant that the studies of the activity towards ammonia synthesis were not completed.

The possibility of beta and/or gamma molybdenum nitride being present in the ternary systems as impurities from the preparative method means that the knowledge that both are active for ammonia synthesis was very important. This information proved important when evaluating the catalytic performance of the ternary nitrides later in this thesis.

3.5   References

[1] P. Ettmayer; Monatsh. Chem.; 101 (1970) 127.

[2] C. L. Bull, T. Kawashima, P. F. McMillan, D. Machon, O. Shebanova, D. Dalsenberger, E. Soignard, E. Takayama-Muromachi and L. C. Chapon; J. Solid State Chem.; 179 (2006) 1762.

[3] A. Y. Ganin, L. Kienle and G. V. Vajenine; J. Solid State Chem.; 179 (2006) 2339.

[4] L. Volpe and M. Boudart; J. Phys. Chem.; 90 (1986) 4874.

[5] L. Volpe and M. Boudart; J. Solid State Chem.; 59 (1985) 332.

[6] J. G. Choi, R. L. Curl and L. T. Thompson; J. Catal.; 146 (1994) 218.

[7] D. A. King and F. J. Sebba; J. Catal.; 4 (1965) 253.

[8] N. Sengal and F. J. Sebba; J. Catal.; 8 (1967) 105.

[9] R. S. Wise, E. J. Markel; J. Catal.; 145 (1994) 335.

[10] M. Nagai, Y. Goto, A. Miyata, M. Kiyoshi, K. Hada, K. Oshikawa and S. Omi; J. Catal.; 182 (1999) 292.

[11] W. Zhaobin, X. Qin, P. Grange and B. Delmon; J. Catal.; 168 (1997) 176.

[12] S. W. Gong, H. K. Chen, W. Li, B. Q. Li and T. D. Hu; J. Mol. Catal. A; 225 (2005) 213.

[13] S. W. Gong, H. K. Chen, W. Li and B. Q, Li; Appl. Catal. A; 279 (2005) 257.

[14] S. W. Gong, H. K. Chen, W. Li and B. Q. Li; Catal. Comm.; 5 (2004) 621.

[15] B. R. Sahu and L. Klienman; Phys. Rev. B; 70 (2004) 073103.

[16] R. Marchand, F. Tessier and F. J. DiSalvo; J. Mater. Chem.; 9 (1999) 297.

[17] C. L. Bull, P. F. McMillan, E. Soignard and K. Leinenweber; J. Solid State Chem; 177 (2004) 1488.

[18] D.A. Evans and K.H. Jack; Acta Cryst.; 10 (1957) 83.

[19] D. Mckay; Catalysis over Molybdenum Containing Nitride Materials; PhD Thesis, University of Glasgow, 2007.

[20] A. Boultif and D. Louer; J. Appl. Cryst.; 37 (2004) 724.

[21] A. C. Larson and R. B. von Dreele; Generalized Structure Analysis System, MS-H805, Los Alamos, NM 87545 (1990).

[22] B. H. Toby; J. Appl. Crystallogr.; 34 (2001) 210.

[23] A-M. Alexander; unpublished results; 2010.

[24] M. R. Hillis, C. Kemball and M. W. Roberts; Trans. Faraday Soc.; 62 (1966) 3570.

[25] K.-I. Aika and A. Ozaki; J. Catal.; 14 (1969) 311.

4   Cobalt molybdenum nitride

4.1   *Introduction*

4.1.1   Cobalt molybdenum oxide (CoMoO₄)

Cobalt molybdenum oxide compounds have been investigated because of their structure[1,2], magnetic[3,4] and catalytic properties[5]. Cobalt molybdenum oxide is found in different forms depending on the synthetic route employed. There are currently three different compounds with the $CoMoO_4$ stoichiometry: a pale green low temperature α-phase (monoclinic space group C2/m)[6], a black high-pressure (hp-) phase (monoclinic space group P2/c)[4] and a pale violet high temperature β-phase (monoclinic space group C2/m)[2,7], additionally there exists a (dark) purple hydrated phase $CoMoO_4 \cdot 3/4H_2O$ (triclinic space group P-1)[8]. The structures of the phases have been well documented and single crystal diffraction has allowed accurate determination of the coordination environments within the crystals. Cobalt is octahedrally (CoO_6) coordinated to oxygen in all four compounds and both tetrahedral (MoO_4) and octahedral (MoO_6) coordination are observed for molybdenum with oxygen. MoO_6 octahedra are found in the α- and hp- phases whereas in the β- and hydrated phases MoO_4 tetrahedra are seen.

The focus during this project was on the use of hydrated cobalt molybdate ($CoMoO_4 \cdot nH_2O$) and the subsequently dehydrated form ($CoMoO_4$), which has been previously shown to produce cobalt molybdenum nitride (Co_3Mo_3N) via ammonolysis.

4.1.2   Cobalt molybdenum nitride (Co₃Mo₃N)

The synthesis of cobalt molybdenum nitride was first described in the late 1990s[9,10] Co_3Mo_3N forms a η-6 carbide structure based on that of Co_3Mo_3C, which was described by Newsam *et al.* in 1988[11]. Cobalt molybdenum nitride has been reported to be a highly active ammonia synthesis catalyst especially when doped with caesium.[12]

During studies performed by Mckay[13] it was observed by powder X-ray diffraction (PXRD) and microanalysis that the material changes when reduced under 3:1 H_2/Ar gas at elevated temperatures. Half of the nitrogen can be lost from the sample with a commensurate contraction in the unit cell parameter; which was proposed to be related to a change from an η-6 to an η-12 carbide structure. Due to limitations of PXRD in identifying the positions and exact occupancy of nitrogen this structural transformation had not been verified.

4.2 Experimental

4.2.1 Preparation

The methods used to synthesise cobalt molybdenum oxide were based on those described by Mckay[14] and Eda[8].

(i)   Using an ammonium molybdate precursor: stoichiometric amounts of both ammonium heptamolybdate $((NH_4)_6Mo_7O_{24}\cdot 4H_2O$, Sigma Aldrich, 81-83 % as MoO_3) and cobalt nitrate $(Co(NO_3)_2\cdot 6H_2O$, Sigma Aldrich, ≥ 98 %) were separately dissolved in 90 mL of distilled water and then added together. The resultant solution was stirred and heated to approximately 353 K in an oil bath. A purple precipitate was obtained after vacuum filtration and the precipitate was washed twice with distilled water and once with ethanol, then dried overnight at 423 K.

(ii)   Using a sodium molybdate precursor: A 150 mL, 0.66 M sodium molybdate hydrate solution $(Na_2MoO_4\cdot 2H_2O$, Sigma Aldrich, ≥ 99.5 %) was prepared in a flask to which a 400 mL, 0.25 M cobalt nitrate solution was added dropwise whilst stirring. After stirring for three hours, a dark purple precipitate was obtained by vacuum filtration. The precipitate was twice washed with distilled water and once with ethanol, then dried overnight at 423 K.

The resultant powders were analysed by PXRD before being calcined at 773 K in air for five hours and analysed again by PXRD to characterise the resultant phase.

Cobalt molybdenum nitride was formed by the ammonolysis of dehydrated cobalt molybdate $(CoMoO_4)$ under a strict heating regime as previously described. The reaction scheme as shown below shows how the ammonia reacts directly with the molybdate to form the nitride.

$$3\ CoMoO_4 + 8\ NH_3\ \rightarrow\ Co_3Mo_3N + \frac{7}{2}\ N_2 + 12\ H_2O$$

The heating regime described in Section 2.1.1 was employed. After reaction with ammonia, the sample was reduced in 3:1 H_2/N_2 gas for two hours at 973 K to complete the nitriding process. PXRD data were collected for the samples both after the ammonolysis and after the further reduction (3:1 H_2/N_2 gas) stage to confirm the phases present.

4.2.2   Characterisation

Powder X-ray diffraction (PXRD) data were collected using a Siemens D5000 diffractometer at room temperature, with Cu-K$_\alpha$ radiation. The patterns were collected using a step scan of 0.02° 2θ over a 5 – 85° 2θ range and a counting time per step of 0.8 seconds. Diffraction data used for Rietveld refinements employed step times and ranges of 11 seconds and 5 – 105° 2θ respectively.

In addition to the X-ray data, powder neutron diffraction (PND) data were collected on the POLARIS instrument at ISIS. Experiments were performed on the samples at room temperature and base temperature (4.2 K) using three banks of detectors. Samples were loaded into vanadium sample cans, to a maximum height of 40 mm and data collected as described in Section 2.4.1.2. Data were collected for approximately three hours in each case.

For *in-situ* variable temperature PND experiments a stainless steel cell was used, which had a collimator around the sample allowing only the 90° bank of detectors to be used. This is described in more detail in Section 2.4.1.2.1. The conditions used during the *in-situ* experiments were designed to mimic the reaction conditions used in the activity testing. 3:1 H$_2$/N$_2$ and 3:1 H$_2$/Ar gases were flowed through the system as required and the temperature varied (exact heating and gas regimes described at relevant points in this section).

Magnetic measurements were performed using a Quantum Design Model MPMS XL 5T Superconducting Quantum Interference Device (SQUID). In a standard experiment, ~50 mg of sample was loaded into an inverted gelatine-capsule (gel-cap) which was then firmly held centrally within a plastic straw holder. The straw was then attached to the SQUID probe ready for insertion into the SQUID. Measurements were defined by a software script, which controlled the temperature and magnetic field applied to the sample. All of the data were then analysed and evaluated using other software.

Thermal analysis was performed on the hydrated molybdate samples using a TA Instruments Q500 TGA. In a typical experiment, 20 – 50 mg of sample was loaded onto a pan balance and then heated to a set temperature at 1 K per minute, to investigate the dehydration of the molybdates. The required temperature of 773 K was held for 30 minutes to ensure any thermal events had occurred before cooling back to room temperature. Measurements were completed under air to mimic conditions of calcination.
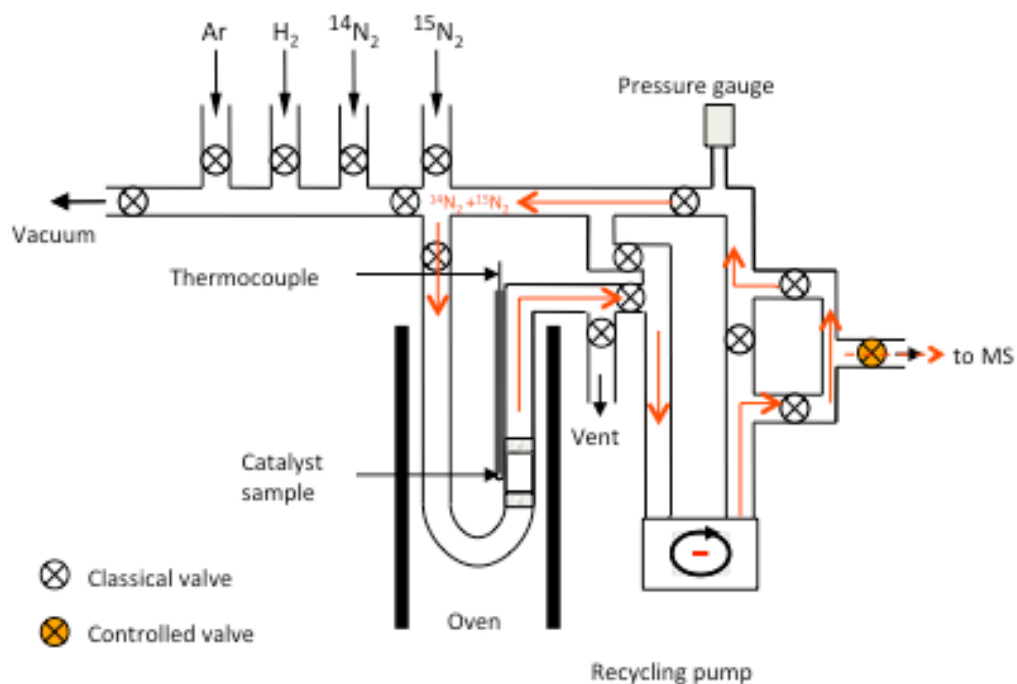
Figure 4-1: Isotopic Exchange reactor set-up

Isotopic exchange reactions were conducted on samples of cobalt molybdenum nitride and used a sealed system attached to a mass spectrometer (Figure 4-1). The reactor was held in a furnace which allowed for temperatures of 973 K to be obtained in the reactor bed whilst reaction gases were circulated around the system by a pump.

4.2.3   Activity testing

The samples were tested at ambient pressure for their potential as ammonia synthesis catalysts. The method employed used a fixed bed reactor through which reactant gas (60 mLmin^{-1}) of either 3:1 H_2/N_2 gas or 3:1 H_2/Ar gas was flowed. The production of ammonia was measured by the change in conductivity of a 200 mL, 0.00108 molL^{-1} sulfuric acid solution as effluent gas passes through the solution.

The reactions were conducted on 0.4 g of sample which was pre-treated at 973 K under 3:1 H_2/N_2 gas for two hours prior to the reaction being started. The reactions were conducted under either 3:1 H_2/N_2 gas at 673 K or under 3:1 H_2/Ar gas during which a variable temperature profile was employed.

4.3 Results and discussion

4.3.1 Cobalt molybdate

Samples were characterised by PXRD to determine phase purity and by TGA to ascertain the water content of the molybdates.

Hydrated cobalt molybdate was formed through solution methods using ammonium heptamolybdate and cobalt nitrate. Providing sufficient experimental care is taken, this process is highly reproducible with no side reactions or differing products. However, experiments showed that if a volume larger than 200 mL was used in a 500 mL flask then the reaction did not yield the hydrated form (deep violet powder) as expected (and as observed by Eda[8]) and a pale violet (powder) phase was obtained. By using the alternative synthesis method of sodium molybdate and cobalt nitrate the dark violet molybdate was formed without such problems.
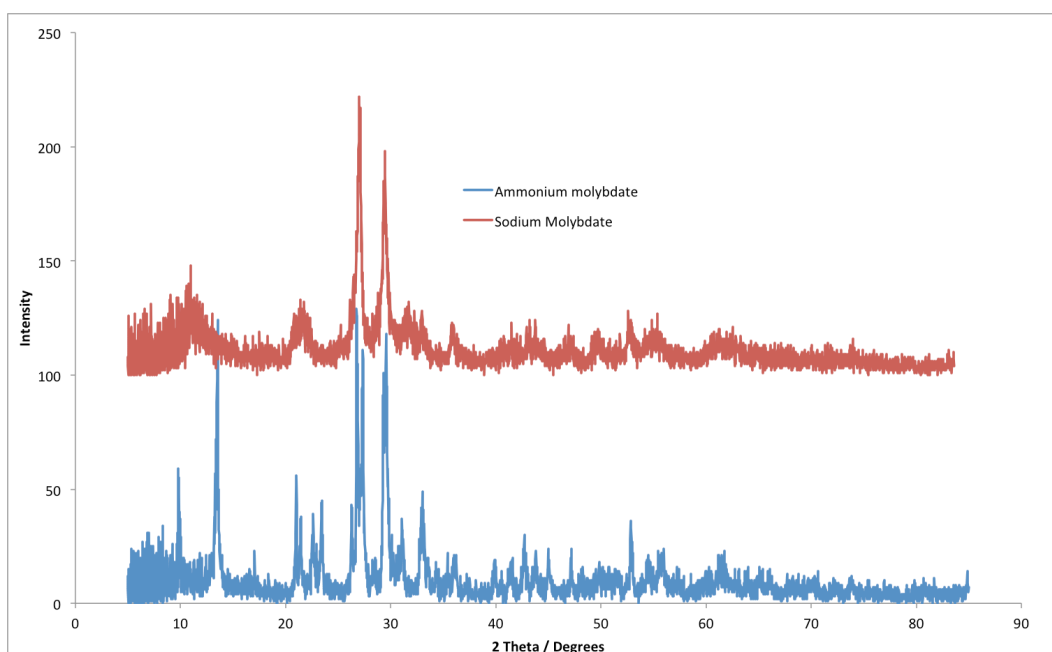
Figure 4-2: PXRD patterns of hydrated cobalt molybdates formed by both routes.

The initial PXRD patterns of the deep violet powders, taken after filtration and drying, (Figure 4-2) did not match to the powder patterns of the hydrated phase previously reported by Eda *et al.*[8] The two synthetic routes gave different PXRD patterns although the colour of the molybdates and water quantity present from TGA analysis (see below) were consistent.

Rietveld refinements were performed against the PXRD data. The refinement used a type 1 background function in GSAS (a shifted Chebyschev function). The lattice parameters were refined followed by the atomic parameters which, when stable, then allowed the peak profile to be refined. When the refinement had stabilised the thermal parameters were varied isotropically.

Attempted refinement against PXRD data using GSAS[15] and EXPGUI[16] indicated that the model phase proposed by Eda et al. used in the refinement does not produce a good fit to the data, which would indicate that the structure is not that of $CoMoO_4 \cdot 0.75H_2O$ as previously reported. This could relate to varying quantities of water present in the sample prior to calcination. The refinement was also limited by the quality of the PXRD data even when collected for extended durations. The results of the refinement are presented in the profile plot in Figure 4-3, Table 4-1 and Table 4-2.
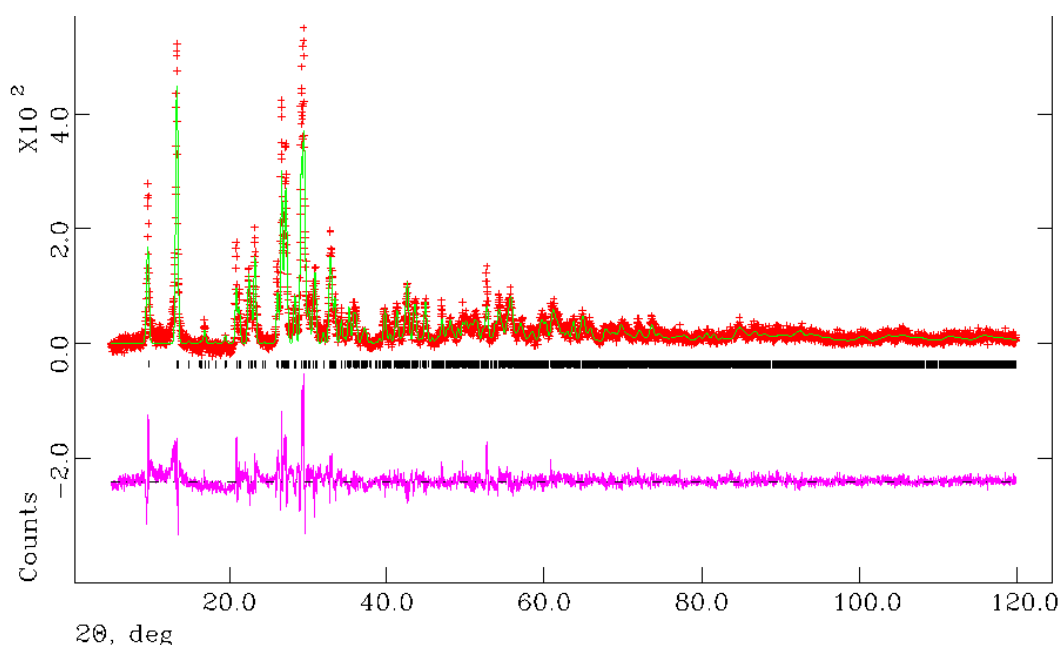
Figure 4-3: Final profile fit obtained from the refinement against PXRD for $CoMoO_4 \cdot nH_2O$.

The observed data are crosses, the calculated profile the solid line and lower continuous line the difference plot. Tick marks show allowed reflection positions.

Table 4-1: Crystallographic parameters for $CoMoO_4 \cdot nH_2O$ from PXRD data.

Parameter	Value
Crystal system	Triclinic
Space group	P-1
Formula mass / $gmol^{-1}$	966.035
Cell parameter, a / Å	6.8522(12)
Cell parameter, b / Å	6.9476(11)
Cell parameter, c / Å	9.3457(15)
α / °	76.594(10)
β / °	84.206(10)
γ / °	74.669(9)
Unit-cell volume / $Å^3$	417.01(12)
Calculated density ρ_x / gcm^{-3}	3.850
Number of observations	5750
Number of variables	63
R_p / %	18.43
R_{wp} / %	23.17
χ^2	2.336

Table 4-2: CoMoO$_4$·nH$_2$O PXRD refined parameters.

Atoms / Site	x	y	z	Occupancy	100× U$_{iso}$/U$_{eq}$ (Å^2)
Co 1 (2i)	0.1597(23)	0.6527(22)	0.7028(16)	1.000	0.50‡
Co 2 (2i)	0.2034(19)	0.8070(22)	0.9769(15)	1.000	0.50‡
Mo 1 (2i)	0.0006(13)	0.1992(13)	0.6752(8)	1.000	0.50‡
Mo 2 (2i)	0.2486(12)	0.2894(12)	0.0512(9)	1.000	0.50‡
O 1 (2i)	0.092(9)	-0.035(8)	0.7101(55)	1.000	0.50‡
O 2 (2i)	0.190(7)	0.378(8)	0.6919(55)	1.000	0.50‡
O 3 (2i)	-0.085(8)	0.242(9)	0.4577(54)	1.000	0.50‡
O 4 (2i)	-0.226(7)	0.317(9)	0.7710(48)	1.000	0.50‡
O 5 (2i)	0.185(8)	0.540(8)	0.9160(52)	1.000	0.50‡
O 6 (2i)	0.149(7)	0.140(8)	1.0045(54)	1.000	0.50‡
O 7 (2i)	0.153(8)	0.306(7)	0.2792(53)	1.000	0.50‡
O 8 (2i)	0.486(8)	0.187(7)	0.0823(49)	1.000	0.50‡
O 9 (2i)	0.485(6)	0.548(6)	0.6259(42)	1.489(63)	0.50‡
O 10 (2i)	-0.447(5)	-0.028(5)	0.5941(33)	1.342(60)	0.50‡

‡ - parameters fixed
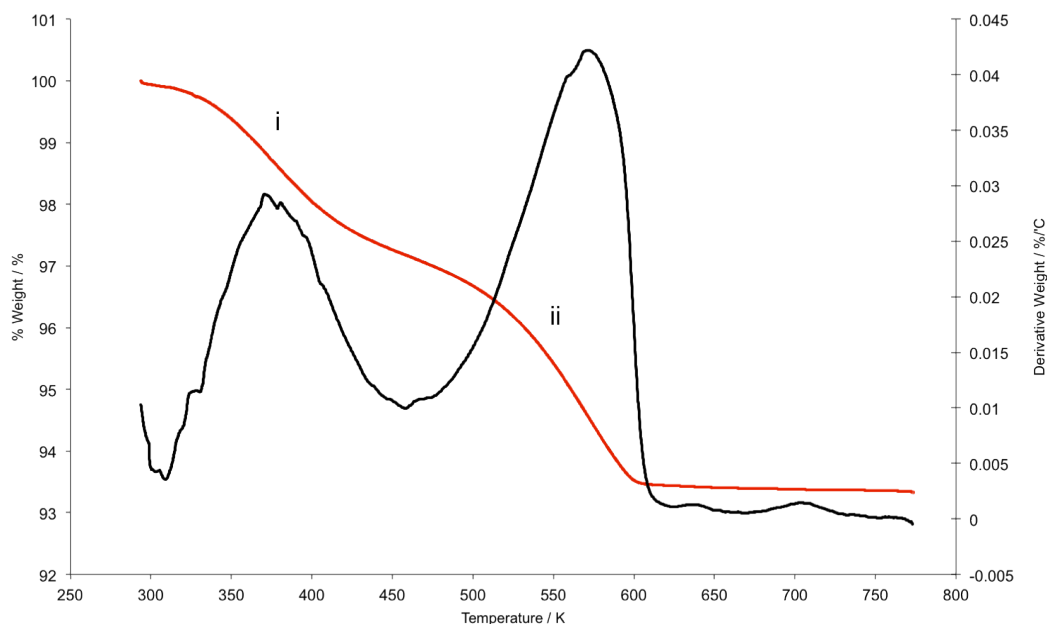
Figure 4-4: TGA trace of the calcination process for Co-Mo-O.

Region (i) – adsorbed water loss and (ii) – co-ordinated water.

The dehydration seen in Figure 4-4, indicated a total mass loss of 6.87 wt%, equivalent to that of 0.93 moles of water i.e. $CoMoO_4.0.93H_2O$. This is more than expected compared to previous results (0.75 equivalents of water). Using data from the TGA trace, it is possible to see two stages of weight loss (i) and (ii) these are both assigned to the loss of water from the sample. The first stage is of weight loss (i) is due to adsorbed water on the surface of the sample. This water is evolved up to 403 K, followed by a further weight loss that can be attributed to the loss of the co-ordinated water. The second weight loss accounts for 4 %.
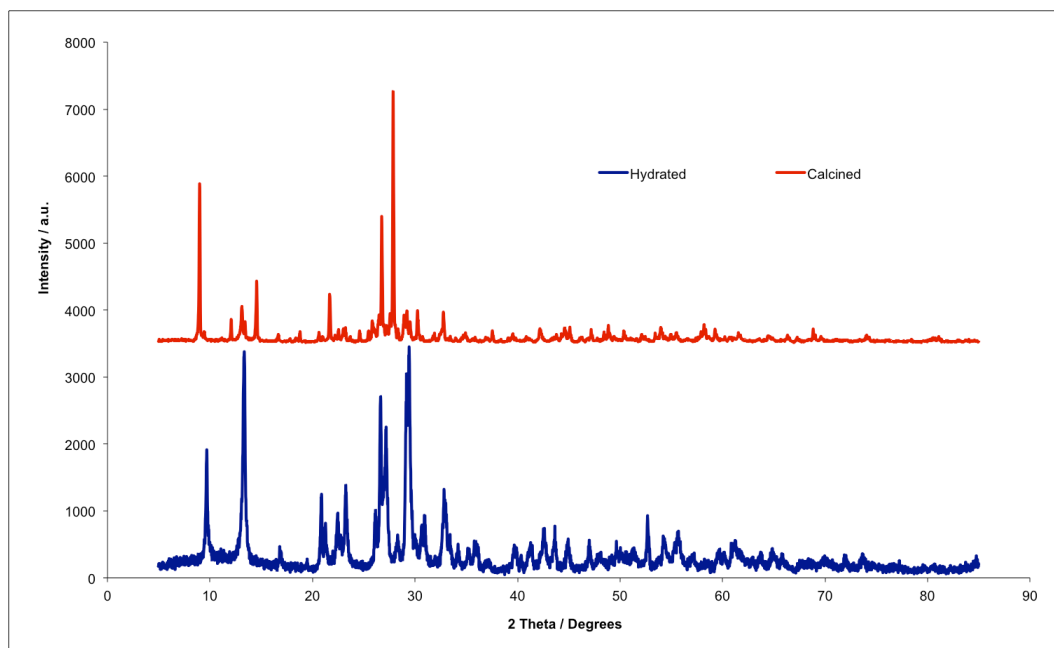
Figure 4-5: Comparison of PXRD patterns for hydrated and calcined cobalt molybdate.

The calcination process following heating in the TGA results in a definite colour change in the molybdate from a dark violet (hydrated phase) to a pale violet (dehydrated phase). The conversion is manifest in the PXRD patterns collected pre- and post- calcination (Figure 4-5).

An *in-situ* PXRD experiment was conducted, in order to follow the calcination process and observe any possible intermediate phases. The PXRD patterns (Figure 4-6) show that the structure of the molybdate changes from hydrated to dehydrated form between 573 and 623 K, this is effectively once all of the water has gone according to TGA, and no intermediate phases are observed. With no observable intermediate phases there is a direct change from hydrated to dehydrated form. This is confirmed by the TGA trace which shows dehydration to be completed by 673 K.
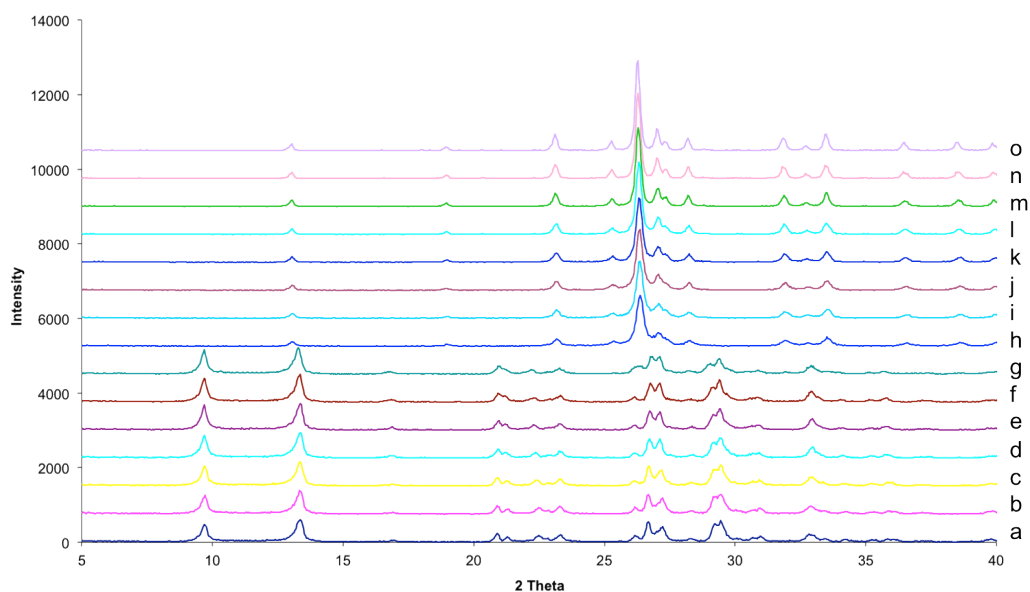
Figure 4-6: in-situ PXRD patterns of molybdate calcination.

a – 298 K, b - 323 K, c- 373 K, d- 423 K, e 473 K, f – 523 K, g – 573 K, h – 623 K, i – 673 K, j – 723 K, k – 773 K, l – 823 K, m – 873 K, n – 923 K, o – 973 K.

4.3.2 Cobalt molybdenum nitride

4.3.2.1 Co₃Mo₃N structural study

The preparation of the nitride from the cobalt molybdenum oxide precursor was performed by direct ammonolysis of the calcined hydrated oxide as described in Section 4.3.1. The result of PXRD analysis directly following the ammonolysis procedure is shown in Figure 4-7. A weakly diffracting powder pattern of a poorly crystalline nature is observed, which could not be matched to any phases present in the ICSD or the JCPDS databases.

From work previously conducted by Mckay[13] it was known that a further treatment stage at 973 K under 3:1 H_2/N_2 gas for two hours was required in order to obtain a crystalline cobalt molybdenum nitride (Co_3Mo_3N) phase. This stage of the synthetic process, was originally applied by Aika *et al.*[17] as a pre-treatment stage in studies of the ammonia synthesis efficacy of Co_3Mo_3N. The procedure was conducted at 873 K for six hours and promoted and stabilised the cobalt molybdenum nitride system. However, the pre-treatment stage employed by Mckay was shown to be effective after two hours at 973 K under a flowing 3:1 H_2/N_2 gas mixture. Given the success of the pre-treatment procedure shown by Mckay, this simpler method was applied here.
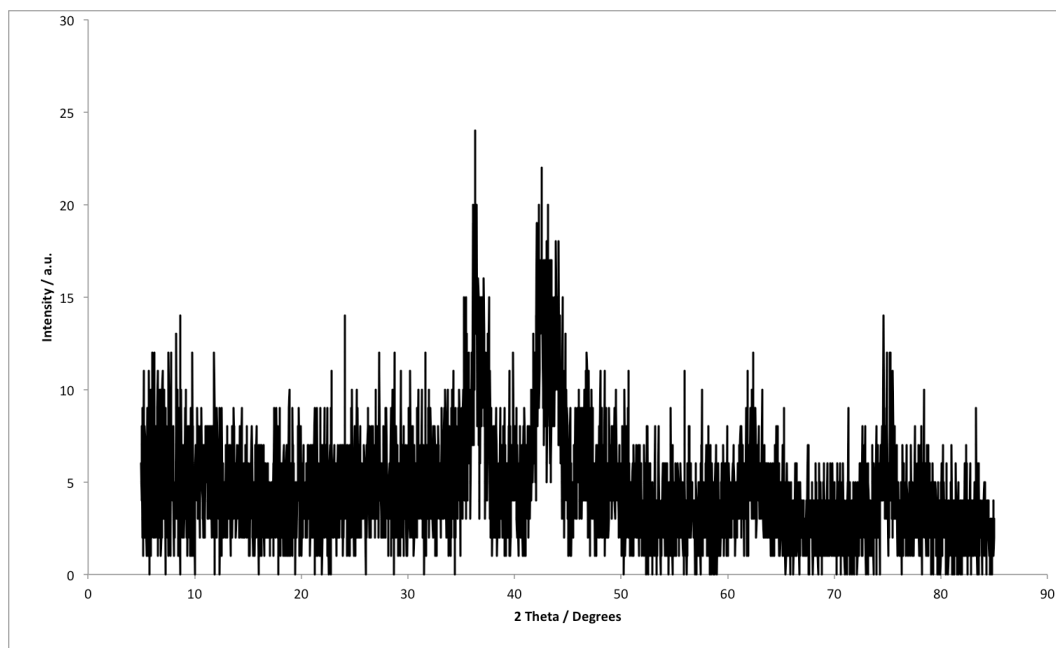
Figure 4-7: PXRD pattern of the product of ammonolysis of cobalt molybdenum oxide.

Thus, for all samples synthesised, the polycrystalline powder obtained from the ammonolysis stage was loaded into the test reactor and treated under a 60 mLmin^{-1} flow of 3:1 H$_2$/N$_2$ gas at 973 K for two hours to give a crystalline cobalt molybdenum nitride as shown in Figure 4-8.
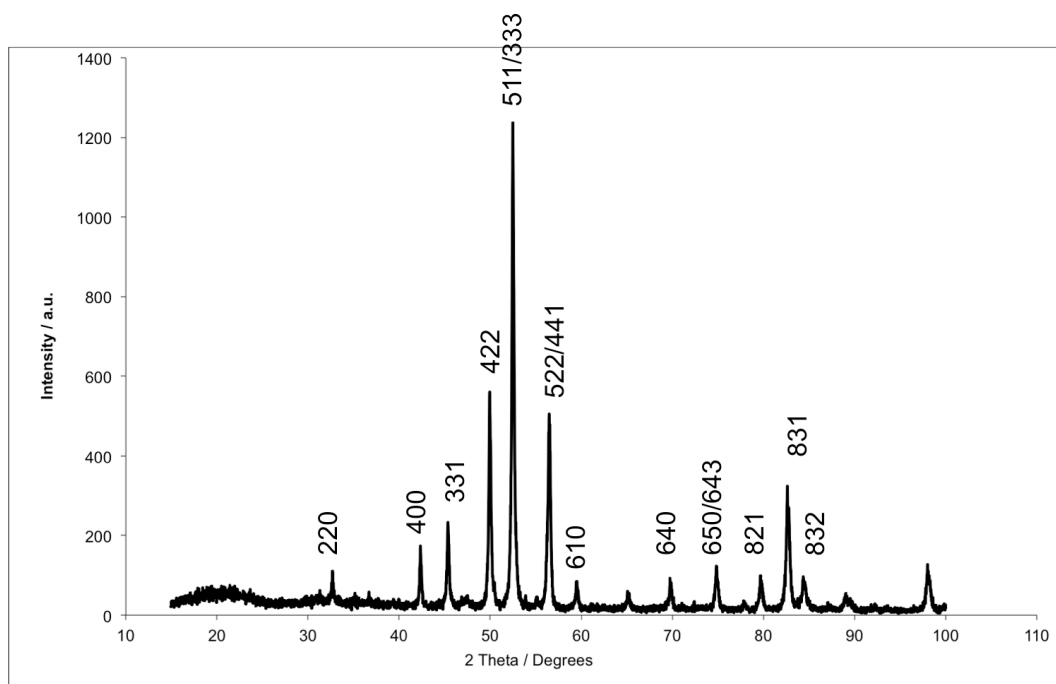
Figure 4-8: PXRD pattern of Co$_3$Mo$_3$N.

hkl labels for the main reflections of Co$_3$Mo$_3$N

The diffraction pattern shows that after the pre-treatment the sample is crystalline and indexing/least squares refinement procedures using Dicvol 04[18] matched to a cubic space group with a lattice parameter of $a = 11.023(6)$ Å. This is in good agreement to the published value for the structure of cobalt molybdenum nitride (Co_3Mo_3N).[10] Microanalysis indicates that there is a nitrogen content of 2.8(3) wt% which gives a stoichiometry of $Co_3Mo_3N_{0.9(1)}$.

The structure of the nitride is well known and various methods of synthesis have been reported in the literature. As first reported by Bem *et al.*[19], it is isostructural with η-Fe_3W_3C. The structure was further confirmed through refinements against X-ray and neutron data[10]. Literature unit cell details: Space group Fd-3m, a = 11.0270(4) Å, volume = 1340.8(1) Å^3.[10] One this basis, it has been possible to refine a model against the PXRD data collected against the literature model using GSAS and EXPGUI.

Refinement against PXRD data was performed on cobalt molybdenum nitride samples by first fitting the background to a shifted Chebyschev function (background function 1 in GSAS). Once the background was fitted, the lattice parameters were then refined followed by the atomic positions which when refined and stable, allowed the peak shape to be refined. When the refinement had stabilised, the thermal parameters were varied isotropically. Results of the refinement are shown in Figure 4-9, Table 4-3 and Table 4-4, which indicate that there is a good correlation between the observed and calculated patterns of Co_3Mo_3N.
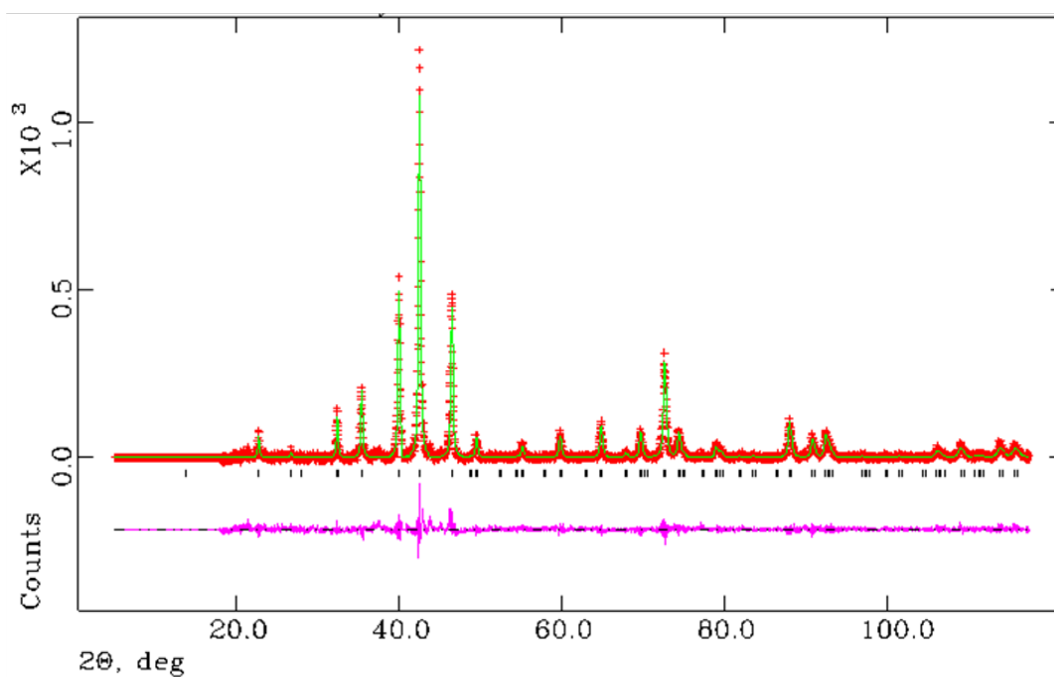
Figure 4-9: Final profile fit obtained from the refinement against the PXRD for Co$_3$Mo$_3$N.

The observed data are crosses, the calculated profile the solid line and lower continuous line the difference plot. Tick marks show allowed reflection positions.

Table 4-3: Crystallographic parameters for Co$_3$Mo$_3$N from PXRD data.

Parameter	Value
Formula	Co$_3$Mo$_3$N
Crystal system	Cubic
Space group	*Fd-3m*
Formula mass / gmol^{-1}	7658.016
Cell parameter, *a* / Å	11.0209(6)
Unit-cell volume / Å^3	1338.61(14)
Calculated density ρ_x / gcm^{-3}	9.500
Number of observations	4149
Number of variables	25
R$_p$ / %	20.69
R$_{wp}$ / %	14.77
χ^2	1.608

Table 4-4: PXRD refined parameters for Co$_3$Mo$_3$N.

Atoms / Site	x	y	z	Occupancy	100× U$_{iso}$ /U$_{eq}$ (Å^2)
Co 1 (32e)	0.29149(26)	0.29149(26)	0.29149(26)	1.00	1.25*
Co 2 (16d)	0.500000	0.500000	0.500000	1.00	1.02*
Mo (48f)	0.32444(26)	0.125000	0.125000	1.00	1.23*
N (16c)	0.000000	0.000000	0.000000	1.00	0.98*

* = Anisotropically measured – expansion is shown here:

Atoms	U$_{11}$ (Å^2)	U$_{22}$ (Å^2)	U$_{33}$ (Å^2)	U$_{12}$ (Å^2)	U$_{13}$ (Å^2)	U$_{23}$ (Å^2)
Co 1	1.25(17)	1.25(17)	1.25(17)	-0.06(15)	-0.06(15)	-0.06(15)
Co 2	1.02(28)	1.02(28)	1.02(28)	0.43(33)	0.43(33)	0.43(33)
Mo	1.23(18)	1.23(12)	1.23(12)	0.00	0.00	-0.61(18)
N	1.0(14)	1.0(14)	1.0(14)	2.3(18)	2.3(18)	2.3(18)

The nitride crystallises in cubic space group *Fd-3m*; this has two origin choices and origin setting 2 is used for the models. The structure is filled Ti$_2$Ni type and it is isotypic with the equivalent η-6 carbide Co$_3$Mo$_3$C.[11]

The refinement reached a minimum with the non-metal 16c site (0, 0, 0) fully occupied by nitrogen. During the refinement, the nitrogen occupancy was allowed to refine freely and the occupation of the site converged to 1.0 in agreement with the data obtained from the elemental analysis of the sample (2.8(3) wt%) and this is consistent with the stoichiometric Co$_3$Mo$_3$N.

In order to confirm the findings of the PXRD refinements, PND experiments were performed on the Co$_3$Mo$_3$N sample. This was necessary to confirm the nitrogen occupancy since the N only accounts for ~3% of the total electron density of the system, and therefore X-ray diffraction is limited in this respect. Room temperature (295 K) measurements were used to confirm the structure proposed from the PXRD refinements. Using the structure from the PXRD refinement as the starting model, the background was fitted with a reciprocal interpolation function (background function 8 in GSAS). In addition to parameters refined during the PXRD refinement absorption factors were also

refined. The results of the refinement are shown in Figure 4-10, Table 4-5 and Table 4-6.

Table 4-5: Crystallographic parameters for Co$_3$Mo$_3$N from (295 K) PND data.

Parameter	Value
Formula	Co$_3$Mo$_3$N
Space group	*Fd-3m*
Formula mass / gmol^{-1}	7658.016
Cell parameter, *a* / Å	11.01455(5)
Unit-cell volume / Å^3	1336.289(11)
Calculated density ρ_x / gcm^{-3}	9.516
Number of observations	7549
Number of variables	40
R$_p$ / %	1.93
R$_{wp}$ / %	2.83
χ^2	3.974

Table 4-6: 295 K PND refined parameters for Co$_3$Mo$_3$N.

Atoms / Site	x	y	z	Occupancy	100× U$_{iso}$ /U$_{eq}$ (Å^2)
Co 1 (32e)	0.29200(6)	0.29200(6)	0.29200(6)	1.00	0.51*
Co 2 (16d)	0.500000	0.500000	0.500000	1.00	0.35*
Mo (48f)	0.32398(3)	0.125000	0.125000	1.00	0.43*
N (16c)	0.000000	0.000000	0.000000	1.00	0.53*

* = Anisotropically measured – expansion is shown here:

Atoms	U$_{11}$ (Å^2)	U$_{22}$ (Å^2)	U$_{33}$ (Å^2)	U$_{12}$ (Å^2)	U$_{13}$ (Å^2)	U$_{23}$ (Å^2)
Co 1	0.512(22)	0.512(22)	0.512(22)	0.007(22)	0.007(22)	0.007(22)
Co 2	0.355(22)	0.355(22)	0.355(22)	-0.223(32)	-0.223(32)	-0.223(32)
Mo	0.585(15)	0.356(10)	0.356(10)	0.00	0.00	0.116(12)
N	0.532(10)	0.532(10)	0.532(10)	-0.007(9)	-0.007(9)	-0.007(9)
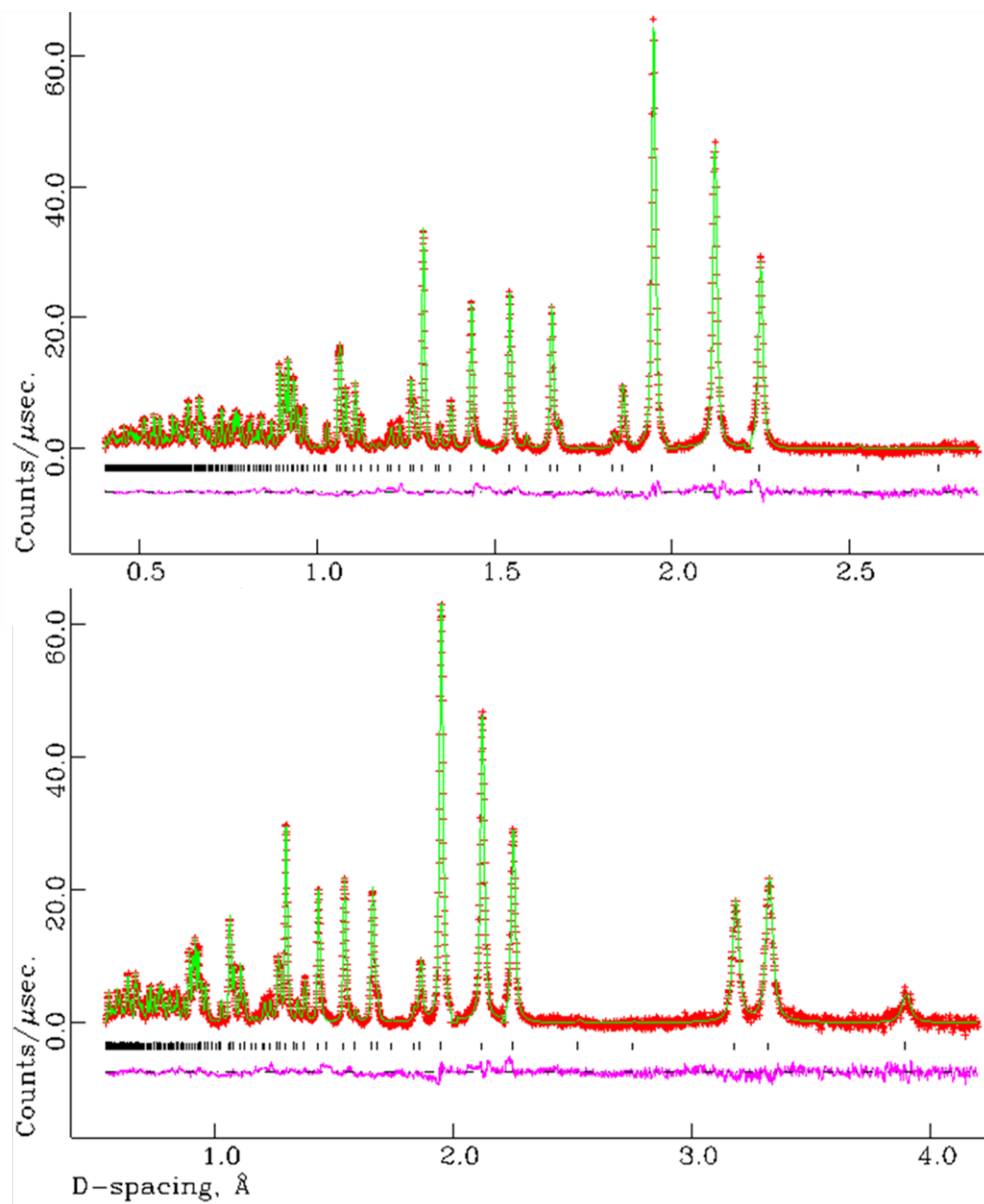
Figure 4-10: Final profile fit obtained from the refinement against PND at 295 K for Co_3Mo_3N.

The observed data are crosses, the calculated profile the solid line and lower continuous line the difference plot. Tick marks show allowed reflection positions. Top – Backscattering detector bank $\langle 2\theta \rangle = 145°$, Bottom - 90° detector bank.

The data from room temperature PND collected using the back-scattering and 90° bank of detectors on POLARIS show that the model from the PXRD refinements is correct. Selected interatomic distances and angles obtained from the refinement are shown in Table 4-7.

Table 4-7: Selected Interatomic Distances and Bond Angles for Co$_3$Mo$_3$N from PND data.

Temperature	290 K	4.2 K
Atomic Distance (Å)		
N – Mo ×6	2.1109(1)	2.1072(2)
Mo – Mo ×3	2.8659(1)	2.8543(2)
Mo – Mo ×3	3.1001(4)	3.1007(5)
Co(1) – Mo ×3	2.6275(7)	2.6216(9)
Co(1) – Mo ×3	2.7274(3)	2.7129(4)
Co(1) – Co(1) ×3	2.5805(16)	2.570(2)
Co(1) – Co(2) ×3	2.3816(3)	2.3737(4)
Co(2) – Mo ×6	2.7475(2)	2.7340(3)
Co(2) – Co(1) ×6	2.3816(3)	2.3737(4)
Bond Angle (°)		
N – Mo – N	134.56(2)	134.20(2)
Mo – N – Mo ×6	94.50(1)	94.74(1)
Mo – N – Mo ×6	85.50(1)	85.26(1)
Mo – N – Mo ×3	180.0	180.0

The Mo and N sub-lattices, are shown in Figure 4-11. The metal atoms (Co (x2) and Mo) occupy three special positions; with site symmetry of 32e, 16d and 48f respectively. The coordination environments for Co(1), Co(2), Mo, and N are depicted in more detail in Figure 4-12 and Figure 4-13. The occupation of the 16c site results in a slightly distorted octahedral coordination geometry for the NMo$_6$ octahedra, and the nitrogen is coordinated exclusively to the metal in the 48f site (Mo). The coordination environment of Mo-N is slightly distorted away from the ideal octahedral geometry by ±5°. The immediate environment of the cobalt in the 32e and 16d sites is unchanged, relative to the hypothetical alloy 'CoMo', whereas the coordination number of the molybdenum on the 48f site increases by 2.
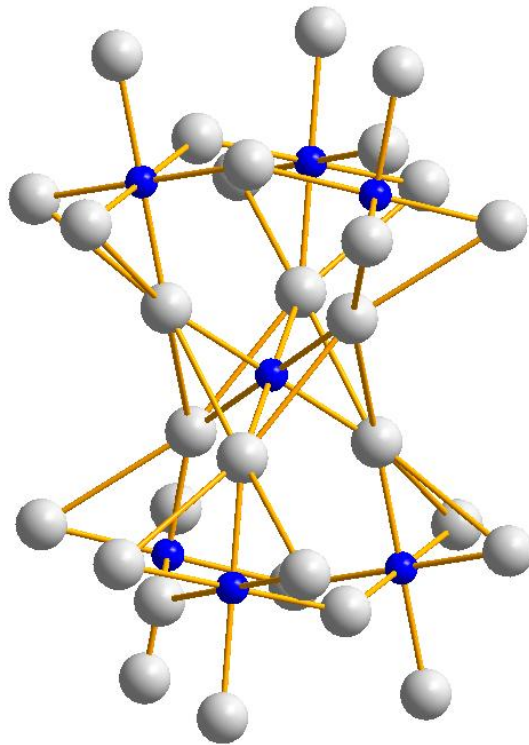
Figure 4-11: Mo-N sublattice in Co$_3$Mo$_3$N.

Mo – silver spheres, N – blue spheres.
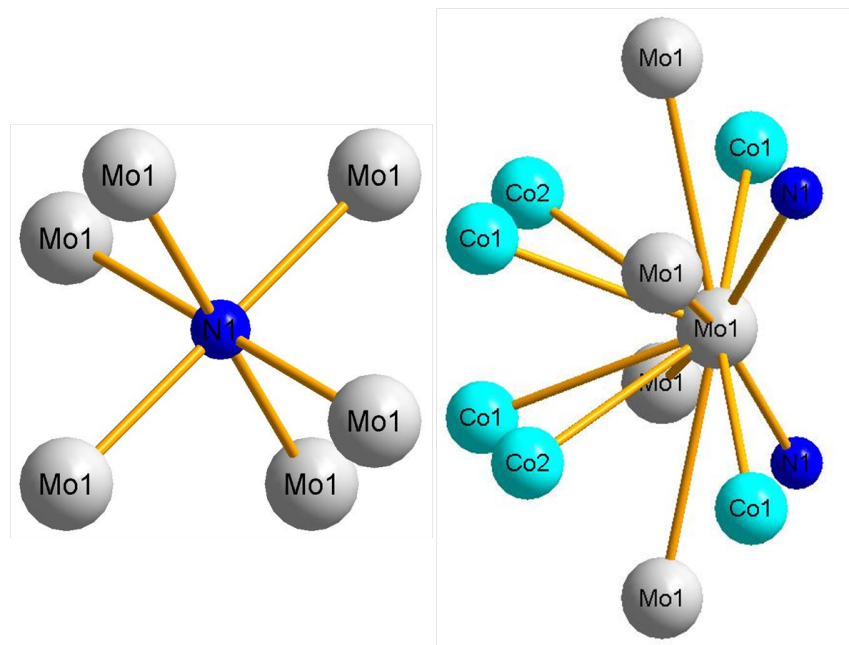
Figure 4-12: Co-ordination geometry at N (16c) site and Mo (48f) site.
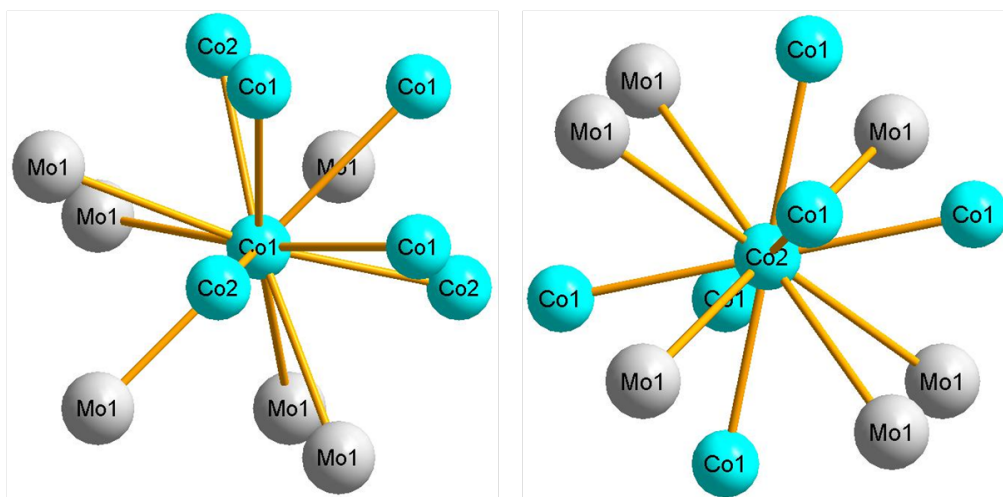
Figure 4-13: Co-ordination geometry at Co1 (32e) site and Co2 (16d) site.

The Co sublattice (composed of Co supertetrahedra; Co in the 32e positions forming tetrahedra capped on each face by Co in 16d sites) can be regarded as a metallic network, whereas the Mo-N vertex sharing octahedra can be regarded as relatively ionic. The interatomic distances of the Co and Mo-N sublattices resemble those reported in other work. The Co-Co distances are a good approximation to those in α-Co metal (2.51 Å)[20] and the Mo-N distances closely resemble those in the binary nitrides γ-Mo_2N and β-$Mo_2N_{0.8}$ and the ternary compound $LiMoN_2$ (2.095(4) Å)[21].

Low temperature (4.2 K) PND data were also collected and confirm the findings of the room temperature data. These measurements also demonstrated that no magnetic ordering was present in the patterns, which would be manifested by the appearance of additional magnetic reflections or enhanced peak intensities. The refinement results are shown in Table 4-8, Table 4-9 and Figure 4-14.

Table 4-8: Crystallographic parameters for Co$_3$Mo$_3$N from (4.2 K) PND data.

Parameter	Value
Formula	Co$_3$Mo$_3$N
Space group	*Fd-3m*
Formula mass / gmol^{-1}	7658.016
Cell parameter, *a* / Å	10.9808(2)
Unit-cell volume / Å^3	1324.05(4)
Calculated density ρ_x / gcm^{-3}	9.604
Number of observations	7549
Number of variables	63
R$_p$ / %	1.59
R$_{wp}$ / %	1.07
χ^2	2.64

Table 4-9: 4.2 K PND refined parameters for Co$_3$Mo$_3$N.

Atoms / Site	x	y	z	Occupancy	100× U$_{iso}$ /U$_{eq}$ (Å^2)
0.29221(7)	0.29221(7)	0.29221(7)	0.29221(7)	1.00	0.29*
Co 2 (16d)	0.500000	0.500000	0.500000	1.00	0.08*
Mo (48f)	0.32462(4)	0.125000	0.125000	1.00	0.12*
N (16c)	0.000000	0.000000	0.000000	1.00	0.29*

* = Anisotropically measured – expansion is shown here:

Atoms	U$_{11}$ (Å^2)	U$_{22}$ (Å^2)	U$_{33}$ (Å^2)	U$_{12}$ (Å^2)	U$_{13}$ (Å^2)	U$_{23}$ (Å^2)
Co 1	0.29(5)	0.29(5)	0.29(5)	-0.07(5)	-0.07(5)	-0.07(5)
Co 2	0.08(2)	0.08(2)	0.08(2)	-0.07(3)	-0.07(3)	-0.07(3)
Mo	0.112(15)	0.134(9)	0.134(9)	0.00	0.00	-0.017(12)
N	0.297(9)	0.297(9)	0.297(9)	-0.007(10)	-0.007(10)	-0.007(10)
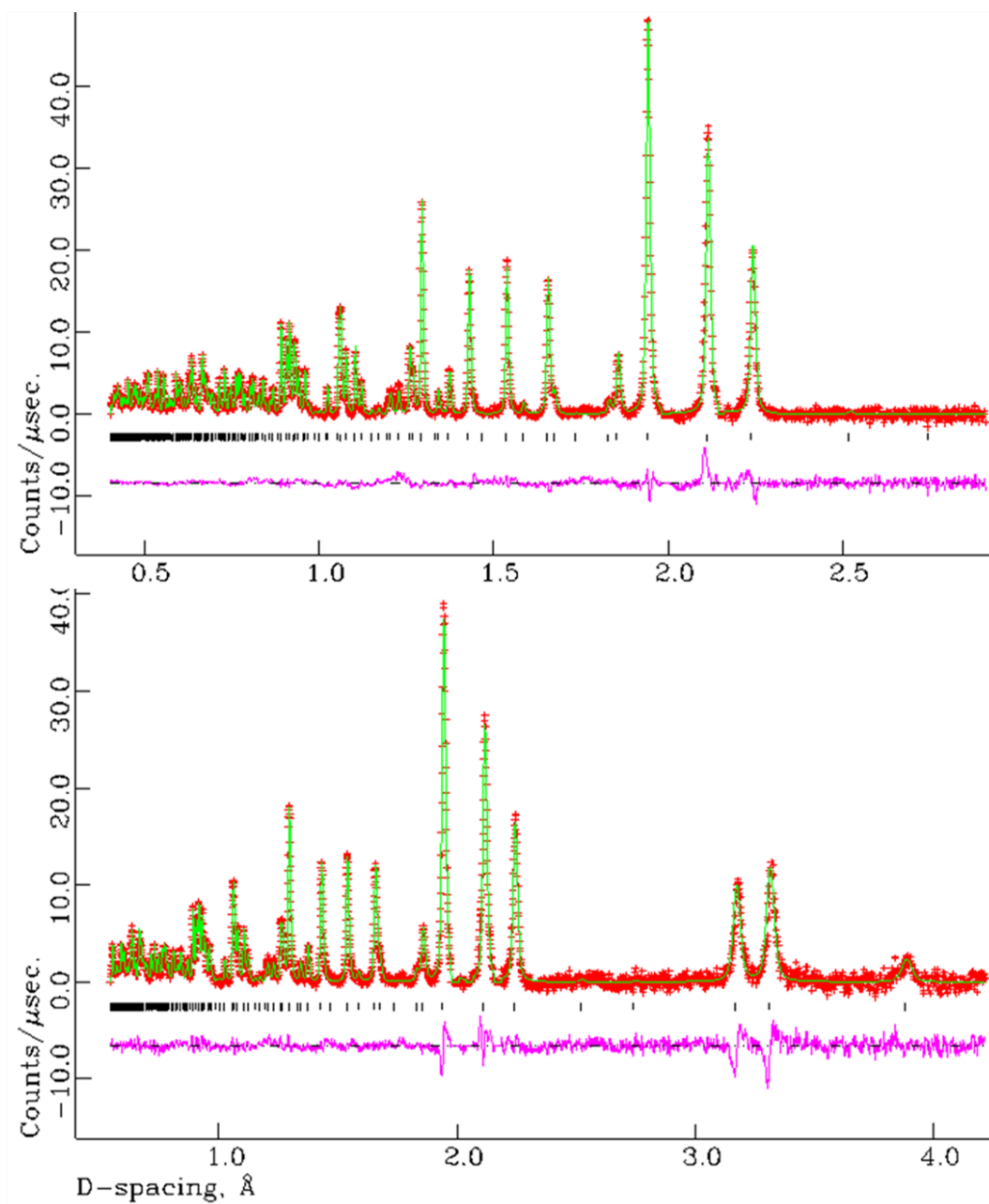
Figure 4-14: Final profile fit obtained from the refinement against PND at 4.2 K for Co₃Mo₃N.

The observed data are crosses, the calculated profile the solid line and lower continuous line the difference plot. Tick marks show allowed reflection positions. Top – Backscattering detector bank <2θ> = 145°, Bottom - 90° detector bank.

In addition to the diffraction and microanalysis results, magnetic measurements of Co_3Mo_3N were completed in order to compare with previous work completed by zur Loye *et al.*[10] which showed there was a small observable change in susceptibility below 100 K, suggesting that the compound is non-Curie-like. In order to confirm this, molar susceptibility was measured as a function of temperature at 5000 Oe, and yielded the plots shown in Figure 4-15. The susceptibility (and inverse susceptibility) is linear, with

only a gentle gradient for 100 K ≤ T ≤ 300 K, with a large increase in gradient below this temperature range.

The χ_M vs T data was fitted to a modified Curie-Weiss (C-W) expression, incorporating a temperature-independent term to represent the Pauli (P) paramagnetic component to the magnetism. Conversely, attempts to fit the perceived linear portion of the $1/\chi_M$ vs T plots (i.e., from the C-W only expression) were not successful. The P + C-W fits yield tentative values for C, θ, and χ^0 of 0.468(6) emu.mol^{-1}.K, 3.186(7) K, 0.011(1) emu.mol^{-1}.
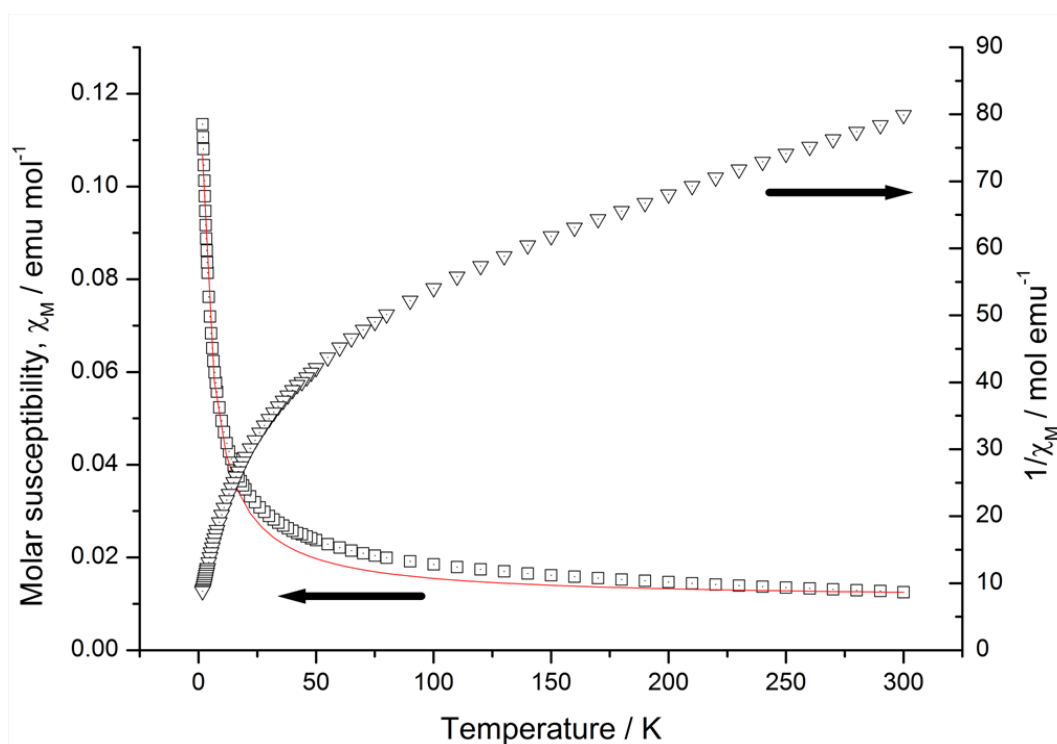
Figure 4-15: Plot of magnetic susceptibility measurements for Co$_3$Mo$_3$N.

(□) the molar magnetic susceptibility and (Δ) the inverse of the mass magnetic susceptibility against temperature (T). The red solid curves represent the best (P + C-W) fits to the χ_M vs T data.

Although a reasonable fit was obtained for a P + C-W model to the magnetic data, given the steep slope of the "Curie tail" at low temperature (with an approximate onset temperature of 90 K) and the precedent for deviation from paramagnetic behaviour in nitrides with the η-6 carbide structure,[23] examination of the magnetic behaviour as a function of field at 2 K was completed. The results of the M vs H measurements are shown in Figure 4-16.

The magnetisation plots show the Co$_3$Mo$_3$N exhibits a linear profile with applied field. Furthermore, it exhibits only a weak and almost negligible hysteresis manifested in a nominal coercive field (H$_c$ ≈ 20 Oe). Equally, however, the magnetisation of the sample does not saturate, even under a maximum applied field of 5 T.
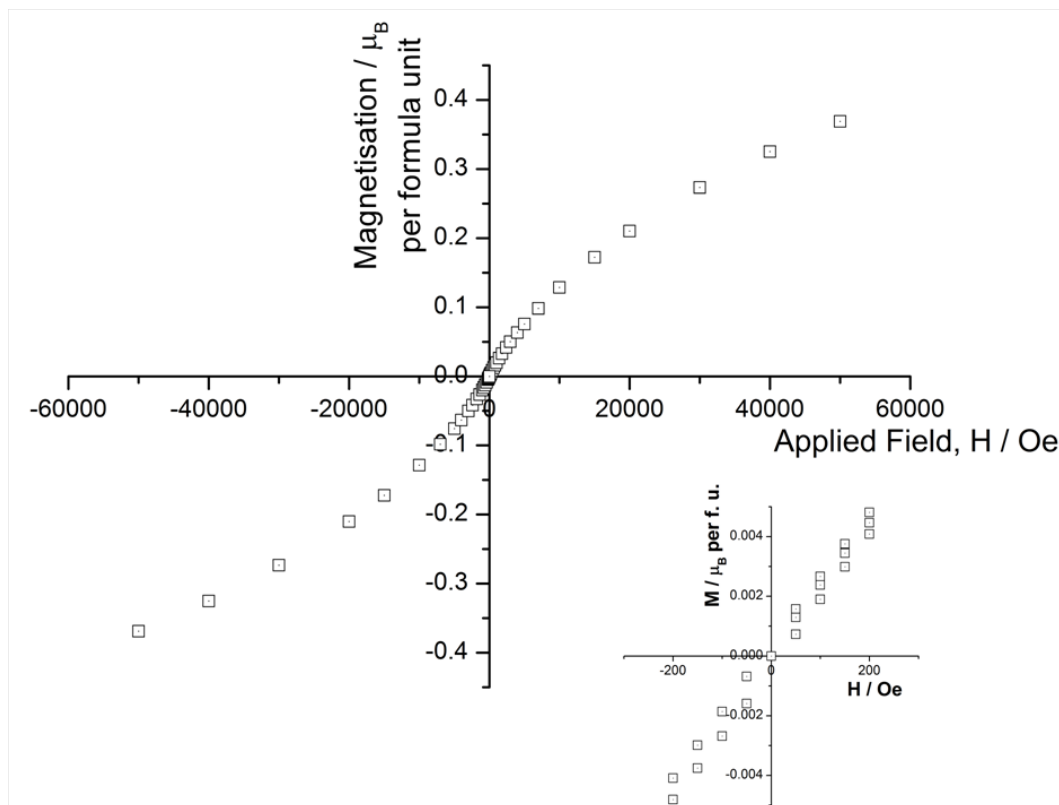
Figure 4-16: Magnetisation of Co$_3$Mo$_3$N as a function of applied field at 2 K.

Inset shows a closer view of the area around the origin.

4.3.2.2 Activity study

The ambient pressure ammonia synthesis efficacy of Co$_3$Mo$_3$N has been measured at 673 K for 12 hours using a 3:1 H$_2$/N$_2$ gas feed. Steady state production of ammonia was observed. This is shown in the reaction profile Figure 4-17, (the profile was fitted to a single axis for visual purposes). Limiting conductivity is reached below 400 μScm^{-1} and at this point a fresh reaction flask was used – the data relating to this is shown in the inset to Figure 4-17. The mass normalised ammonia synthesis rate determined for the experiment was 122 μmolh^{-1}g^{-1}.
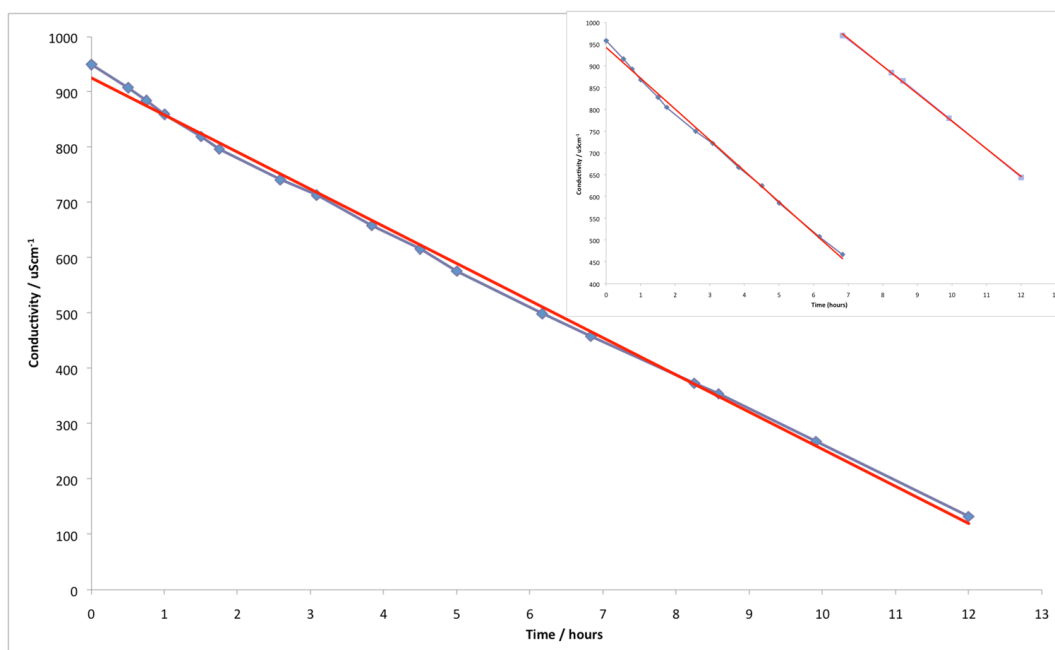
Figure 4-17: Reaction profile for Co$_3$Mo$_3$N under 3:1 H$_2$/N$_2$ gas at 673 K.

Inset shows reactivity data collected during the reaction.

Post-reaction microanalysis shows that there is no change in the nitrogen content upon reaction. The post-reaction PXRD analysis shows that there is also no change in the structure of the nitride during the reaction and indexing of the diffraction pattern of the post-reaction sample yields a unit cell parameter of $a = 11.032(1)$ Å. The surface area of the nitride prior to reaction was determined to be 17 m^{2}g^{-1}, although this value must be treated with caution, as it may not be truly representative due to the necessity of exposing the sample to air for its surface area determination, as Co$_3$Mo$_3$N is known to be air sensitive. The surface area determined is low compared to γ-Mo$_2$N (80 m^{2}g^{-1}), which is described previously. In order to test the reactivity of the lattice nitrogen present in Co$_3$Mo$_3$N, the feed gas was changed to 3:1 H$_2$/Ar gas.
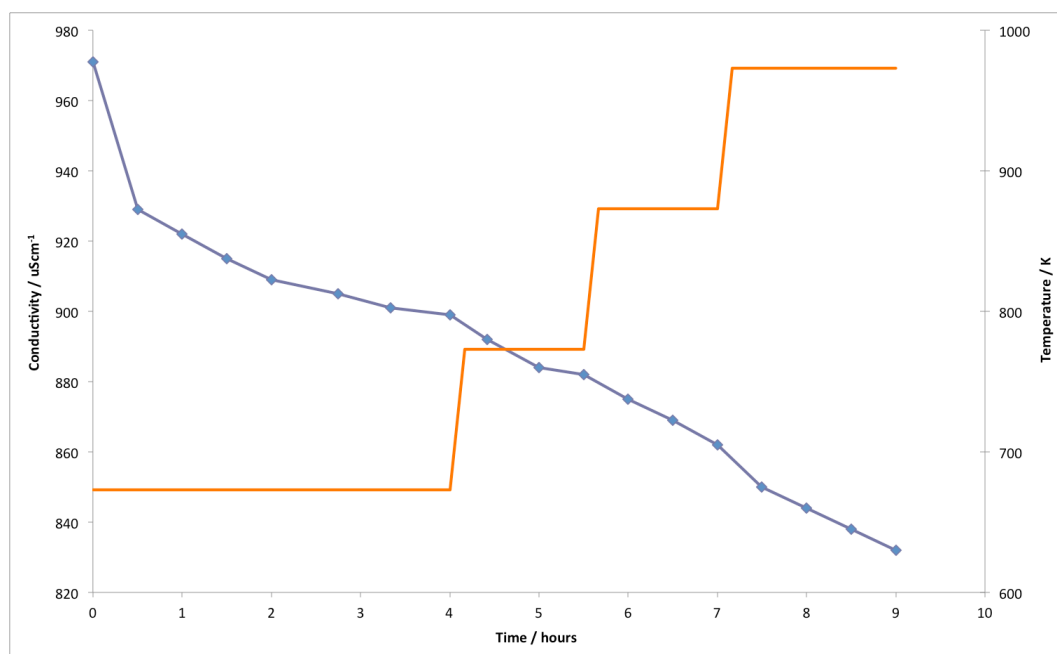
Figure 4-18: Reaction profile for Co_3Mo_3N under 3:1 H_2/Ar gas.

The reaction profile (Figure 4-18) shows an initial decrease in conductivity at 673 K, which quickly diminishes. After the first 30 minutes, the conductivity change slows and after four hours the production of ammonia production had ceased. Upon increasing the temperature to 773 K further limited production of ammonia was apparent. The temperature was subsequently further increased to 873 K and finally to 973 K, as shown in the temperature profile in Figure 4-18.

The post-H_2/Ar gas reaction PXRD pattern shows a shift to a higher angle 2θ, which is indicative of a decrease in the unit cell parameter. This can be seen clearly by comparison of the patterns presented in Figure 4-19. Indexing of the pattern gives a unit cell parameter of $a = 10.879(1)$ Å which is a significant reduction from the pre- reaction value of $a = 11.035(2)$ Å. In addition to these changes, microanalysis showed that there was a reduction in the nitrogen content of the sample to 1.50(3) wt%, which is close to half (46 %) of the nitrogen present prior to reaction. This gives a nominal stoichiometry of $Co_3Mo_3N_{0.5}$, which is in good agreement to results reported previously which proposed a new Co_6Mo_6N phase based on the η-12 carbide structure adopted by Co_6Mo_6C.[11]

The reduction in the nitrogen content of the nitride demonstrates unequivocally that nitrogen was lost from the bulk of the sample. However, the amount of ammonia produced only accounted for 18 % of the total nitrogen lost which may be a

consequence of the thermodynamics of the synthesis/decomposition of ammonia at higher temperatures where the formation of N_2 is favoured.
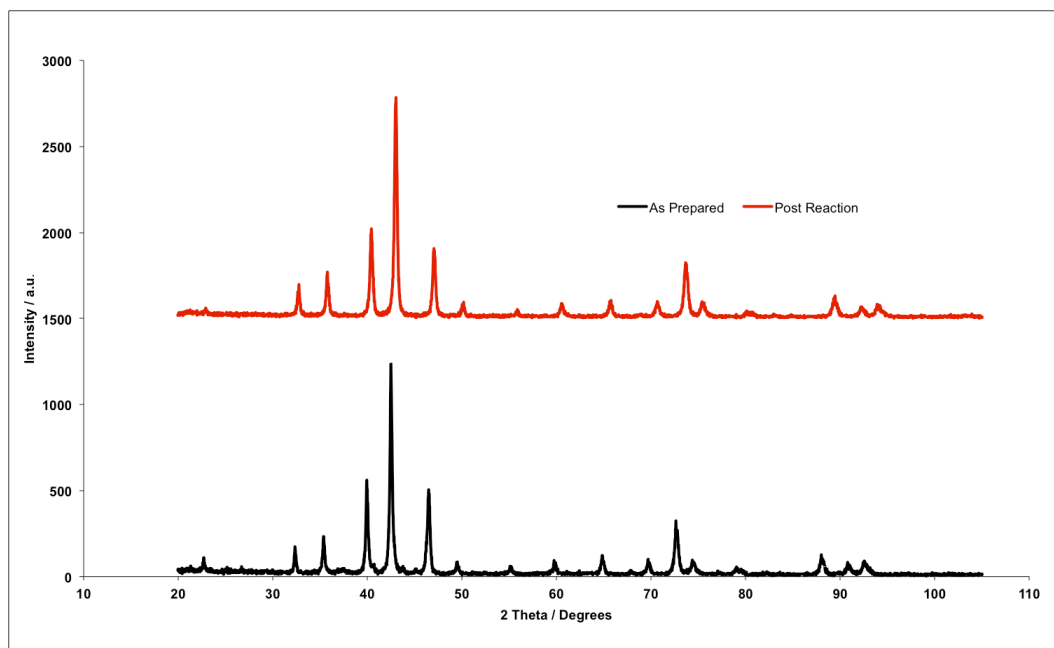
Figure 4-19: Comparison of PXRD patterns pre-reaction and post-reaction with 3:1 H_2/Ar gas.

4.3.2.3 Co_6Mo_6N structural study

As mentioned above, it is proposed that Co_6Mo_6N is isostructural to Co_6Mo_6C. Accordingly, Rietveld analysis was undertaken to test this. Various versions of the refinement were undertaken in order to determine the structure. The refinement against the PXRD data was performed by first fitting the background to a shifted Chebyschev function (background function 1 in GSAS). Once the background was fitted, the lattice parameters were then refined followed by variation of the atomic parameters which, when stable, then allowed the peak shape to be refined. When the refinement had stabilised, the thermal parameters were varied anisotropically.

The first model employed as the starting model for the refinement was the structure resulting from the refinement against the PND data for Co_3Mo_3N modified with the value for *a* taken from PXRD indexing, and the results of this refinement are shown in Table 4-10, Table 4-11 and Figure 4-20. The refined lattice parameters agree well to those found from indexing of the PXRD pattern. The occupancy of the 16c nitrogen position when allowed to freely vary, refined to 0.11(5), which is far below the value implied by the microanalysis; 1.50(3) wt% of N which would correspond to an occupancy of 0.5 on the non-metal 16c site (0, 0, 0).

Table 4-10: Crystallographic parameters for Co$_6$Mo$_6$N from PXRD data - 16c site freely occupied.

Parameter	Value
Formula	Co$_6$Mo$_6$N
Space group	*Fd-3m*
Formula mass / gmol^{-1}	7549.343
Cell parameter, *a* / Å	10.8828(18)
Unit-cell volume / Å^3	1288.9(4)
Calculated density ρ_x / gcm^{-3}	9.612
Number of observations	4749
Number of variables	22
R$_p$ / %	13.65
R$_{wp}$ / %	19.23
χ^2	1.215

Table 4-11: Co$_6$Mo$_6$N PXRD refined parameters - 16c site freely occupied.

Atoms / Site	x	y	z	Occupancy	100× U$_{iso}$/U$_{eq}$ (Å^2)
Co 1 (32e)	0.29267(19)	0.29267(19)	0.29267(19)	1.00	0.79(10)
Co 2 (16d)	0.500000	0.500000	0.500000	1.00	1.41(18)
Mo (48f)	0.32191(17)	0.125000	0.125000	1.00	0.79(10)
N (16c)	0.00000	0.00000	0.00000	0.11(5)	1.00‡

‡ - parameters fixed
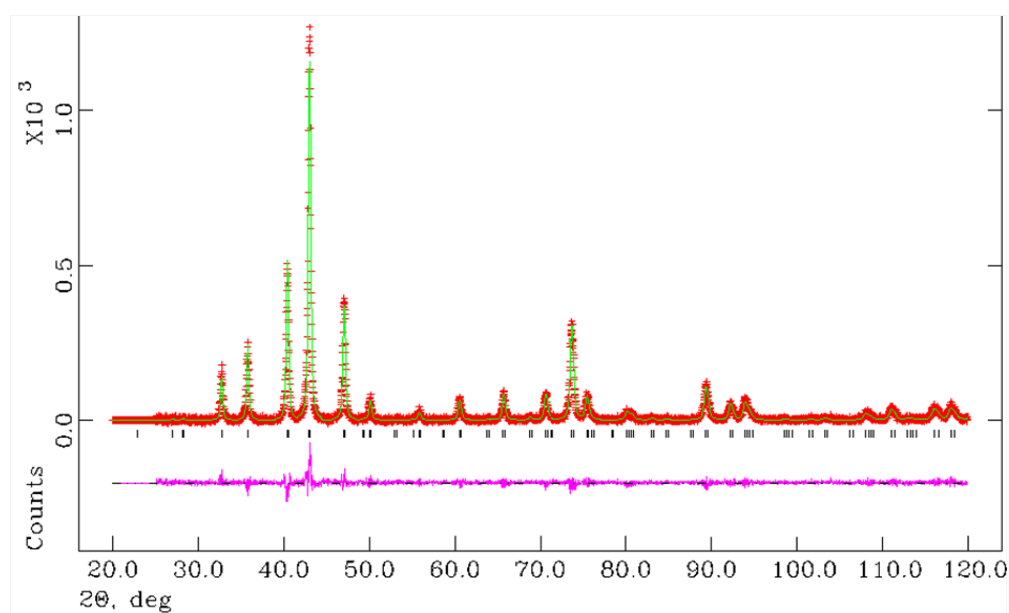
**Figure 4-20: Final profile fit obtained from the refinement against PXRD for Co₆Mo₆N –
16c site freely refining.**

The observed data are crosses, the calculated profile the solid line and lower
continuous line the difference plot. Tick marks show allowed reflection positions.

To be consistent with the microanalysis, the occupancy was fixed to 0.5 on the 16c site,
and the model tested, the results of which are shown in Table 4-12, Table 4-13 and
Figure 4-21.

Table 4-12: Crystallographic parameters for Co₆Mo₆N from PXRD data - 16c site fixed.

Parameter	Value
Formula	Co_6Mo_6N
Space group	*Fd-3m*
Formula mass / gmol^{-1}	7545.960
Cell parameter, *a* / Å	10.8823(14)
Unit-cell volume / Å^3	1288.72(30)
Calculated density ρ_x / gcm^{-3}	9.723
Number of observations	4749
Number of variables	21
R$_p$ / %	13.76
R$_{wp}$ / %	19.35
χ^2	1.229

Table 4-13: Co$_6$Mo$_6$N PXRD refined parameters – Fixed 16c site occupancy.

Atoms / Site	x	y	z	Occupancy	100× U$_{iso}$/U$_{eq}$ (Å^2)
Co 1 (32e)	0.29280(19)	0.29280(19)	0.29280(19)	1.00	0.85(10)
Co 2 (16d)	0.500000	0.500000	0.500000	1.00	1.52(18)
Mo (48f)	0.32166(17)	0.125000	0.125000	1.00	0.84(5)
N (16c)	0.00000	0.00000	0.00000	0.50‡	1.00‡

‡ - parameters fixed
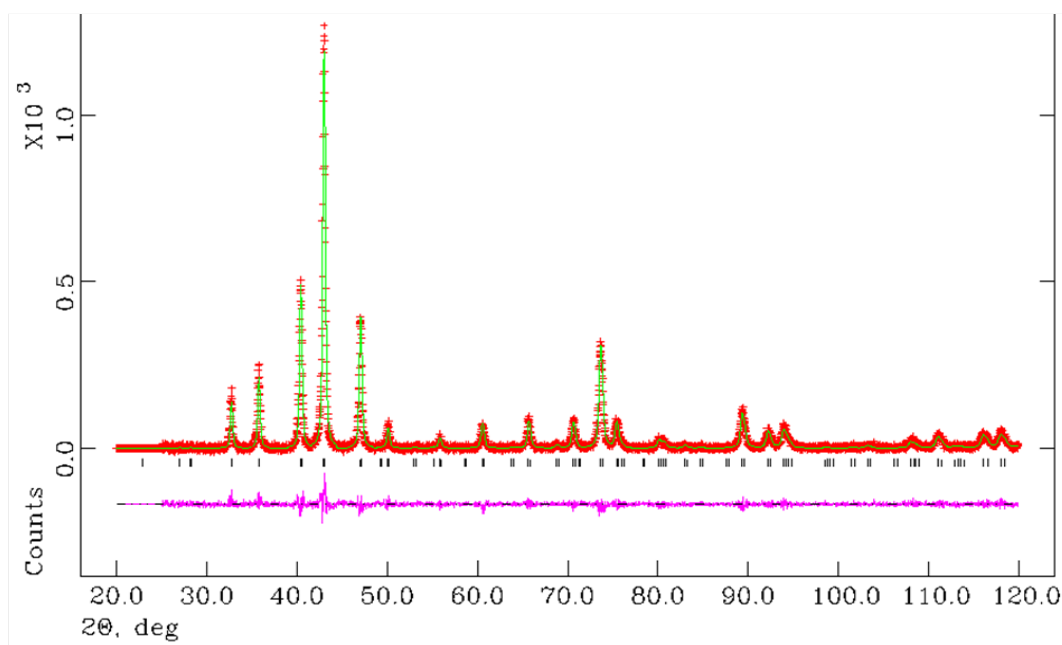
Figure 4-21: Final profile fit obtained from the refinement against PXRD for Co$_6$Mo$_6$N –16c sites occupation fixed to 0.5.

The observed data are crosses, the calculated profile the solid line and lower continuous line the difference plot. Tick marks show allowed reflection positions.

Although these refinement results gave a reasonable representation of the structure the possibility of the reduced Co$_6$Mo$_6$N analogous to the carbide needed to be evaluated. Refinements were therefore undertaken using the structural parameters of the carbide Co$_6$Mo$_6$C as the starting model in which the 8a site (1/8, 1/8, 1/8) is fully occupied. The results of the refinement are shown in Table 4-14, Table 4-15 and Figure 4-22.

Table 4-14: Crystallographic parameters for Co_6Mo_6N from PXRD data – 8a site wholly occupied.

Parameter	Value
Formula	Co_6Mo_6N
Space group	*Fd-3m*
Formula mass / $gmol^{-1}$	7545.960
Cell parameter, *a* / Å	10.8822(14)
Unit-cell volume / $Å^3$	1288.69(28)
Calculated density ρ_x / gcm^{-3}	9.723
Number of observations	4149
Number of variables	21
R_p / %	13.05
R_{wp} / %	18.95
χ^2	1.179

Table 4-15: Co_6Mo_6N – PXRD refined parameters – 8a site wholly occupied.

Atoms / Site	x	y	z	Occupancy	100× U_{iso} / U_{eq} ($Å^2$)
Co 1 (32e)	0.29215(19)	0.29215(19)	0.29215(19)	1.00	0.97(10)
Co 2 (16d)	0.500000	0.500000	0.500000	1.00	0.94(16)
Mo (48f)	0.32098(17)	0.125000	0.125000	1.00	0.81(5)
N (8a)	0.12500	0.12500	0.12500	0.97(8)	0.90‡

‡ - parameters fixed
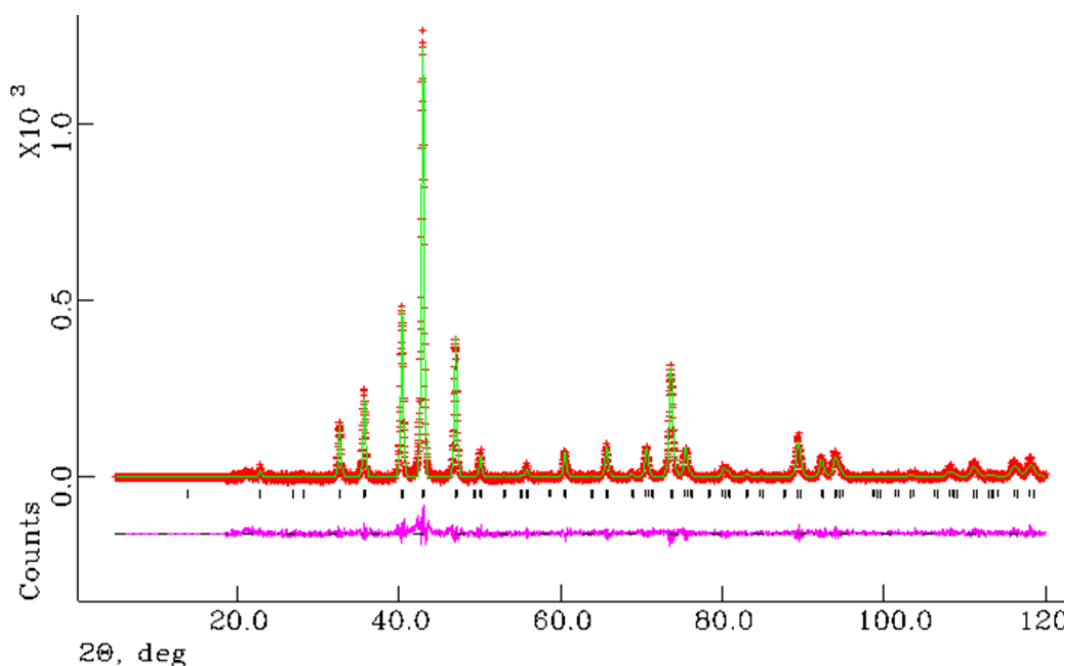
Figure 4-22: Final profile fit obtained from the refinement against PXRD for Co$_6$Mo$_6$N – 8a site wholly occupied.

> The observed data are crosses, the calculated profile the solid line and lower
> continuous line the difference plot. Tick marks show allowed reflection positions.

This produces a better fit than the previous models above. However, as a further test, refinement was also completed with both the 8a and 16c sites present and the nitrogen occupancy allowed to freely vary in order to see if any residual nitrogen remained on the 16c site. The results of this are shown in Table 4-16, Table 4-17 and Figure 4-23. This demonstrates that the refined occupancy for the 8a and 16c sites are 0.96(5) and 0.02(5) respectively, hence again suggesting that the 8a and 16c sites are fully occupied and vacant respectively in the post 3:1 H$_2$/Ar gas treated nitride.

Table 4-16: Crystallographic parameters for Co_6Mo_6N from PXRD data – 8a and 16c sites present.

Parameter	Value
Formula	Co_6Mo_6N
Space group	*Fd-3m*
Formula mass / $gmol^{-1}$	7549.484
Cell parameter, *a* / Å	10.8829(20)
Unit-cell volume / $Å^3$	1288.9(4)
Calculated density ρ_x / gcm^{-3}	9.728
Number of observations	4149
Number of variables	22
R_p / %	13.05
R_{wp} / %	18.95
χ^2	1.179

Table 4-17: Co_6Mo_6N PXRD refined parameters - 8a and 16c sites present.

Atoms / Site	x	y	z	Occupancy	$100 \times$ U_{iso}/U_{eq} $(Å^2)$
Co 1 (32e)	0.29217(19)	0.29217(19)	0.29217(19)	1.00	0.97(10)
Co 2 (16d)	0.500000	0.500000	0.500000	1.00	0.96(17)
Mo (48f)	0.32098(16)	0.125000	0.125000	1.00	0.81(5)
N (16c)	0.000	0.000	0.000	0.02(5)	1.00‡
N (8a)	0.12500	0.12500	0.12500	0.96(5)	1.00‡

‡ - parameters fixed
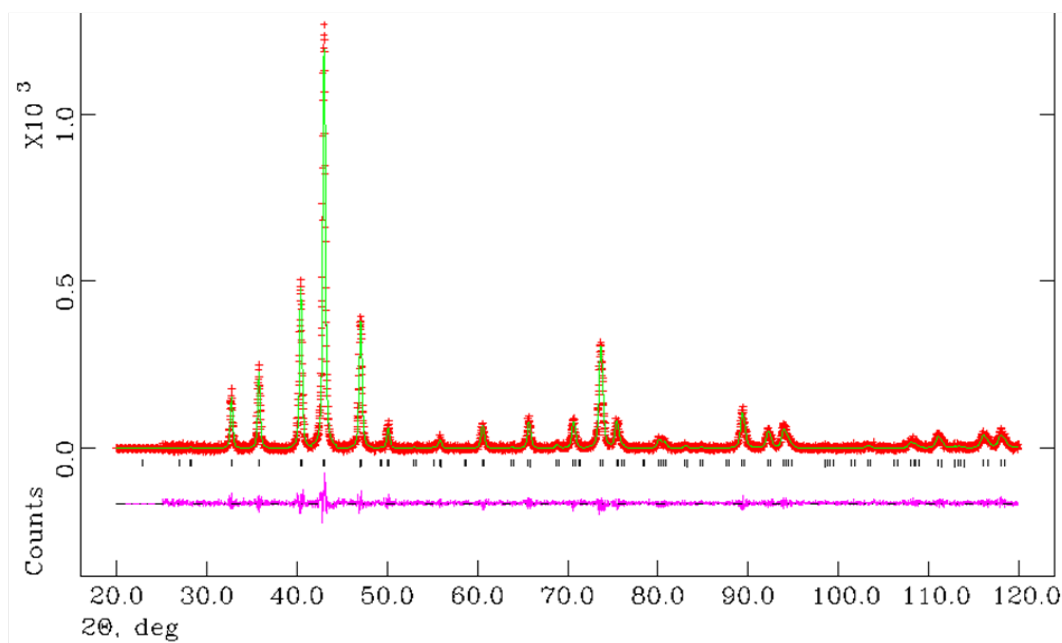
Figure 4-23: Final profile fit obtained from the refinement against PXRD for Co$_6$Mo$_6$N – 8a and 16c sites occupied to total N occupancy = 1.

The observed data are crosses, the calculated profile the solid line and lower continuous line the difference plot. Tick marks show allowed reflection positions.

Given the relatively small differences in the values of the R-factors and the goodness-of-fits for the various applied models in the PXRD refinements, it was important that the possible site distribution models for nitrogen in the reduced nitride phase were tested fully. Accordingly, for similar reasons to those detailed earlier, PND refinements were undertaken, in order to elucidate structure based on all of the alternative models proposed. For the refinement process the background was fitted to a reciprocal interpolation function (background function 8 in GSAS). In addition to the parameters refined during the PXRD refinement, absorption factors were also refined.
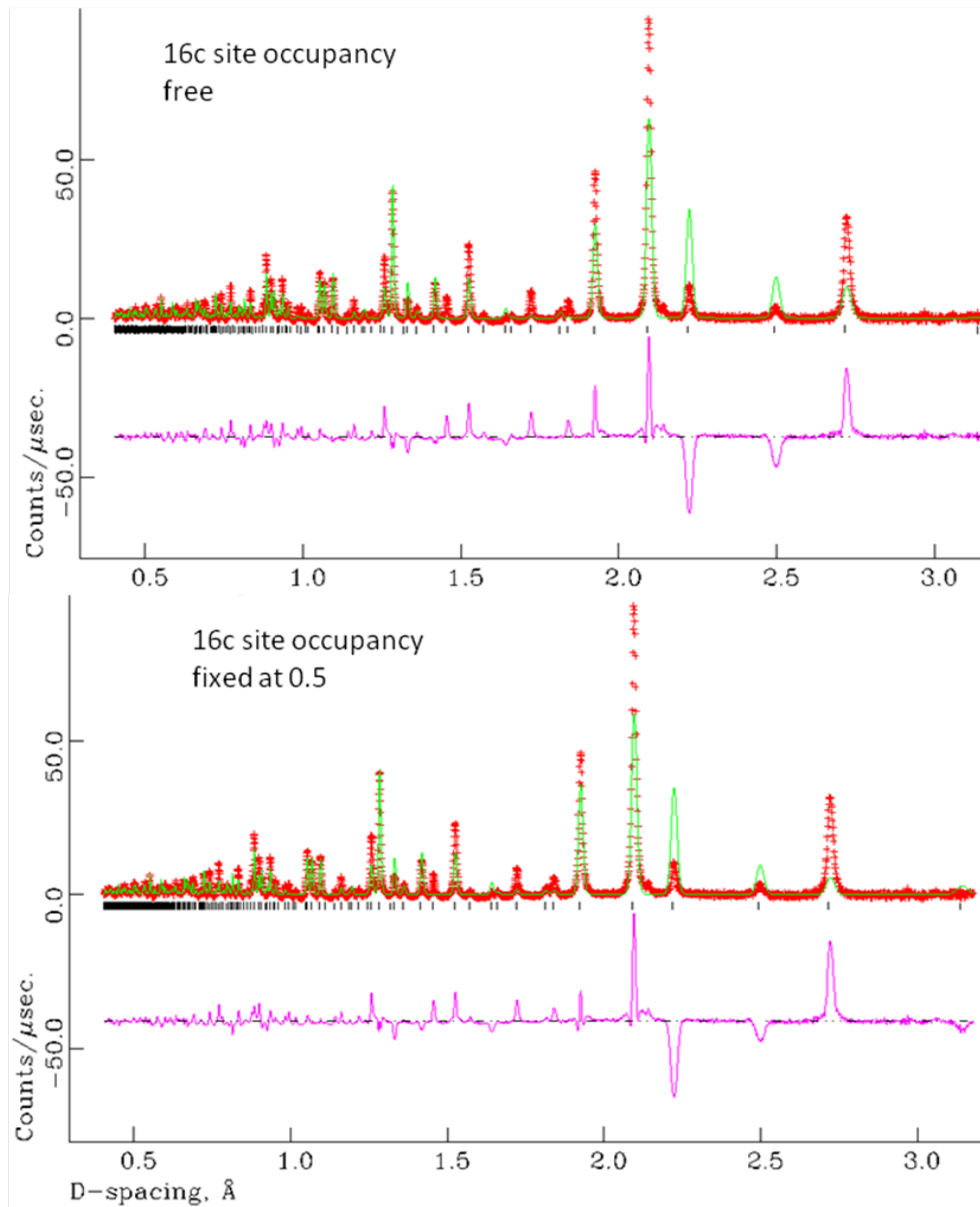
Figure 4-24: PND final profile fits of Co$_6$Mo$_6$N with 16c site present.

The observed data are crosses, the calculated profile the solid line and lower continuous line the difference plot. Tick marks show allowed reflection positions.

The results produced for a model with the 16c site occupied by N for example, could be readily assessed in terms of the quality of fits, the physical meaning of the figures obtained, and the errors associated with the refined parameters. Furthermore, the contrast in the difference profiles of the refinement plots presented an immediate and vivid indication of the relative value of the alternative models. (Figure 4-24) The best fit was obtained with a structure isotypic to the η-12 structured Co$_6$Mo$_6$C (space group Fd-3m) in which the 8a site is fully occupied by N, in the case of Co$_6$Mo$_6$N and the 16c site is vacant. The results are shown in Figure 4-25, Table 4-18 and Table 4-19.
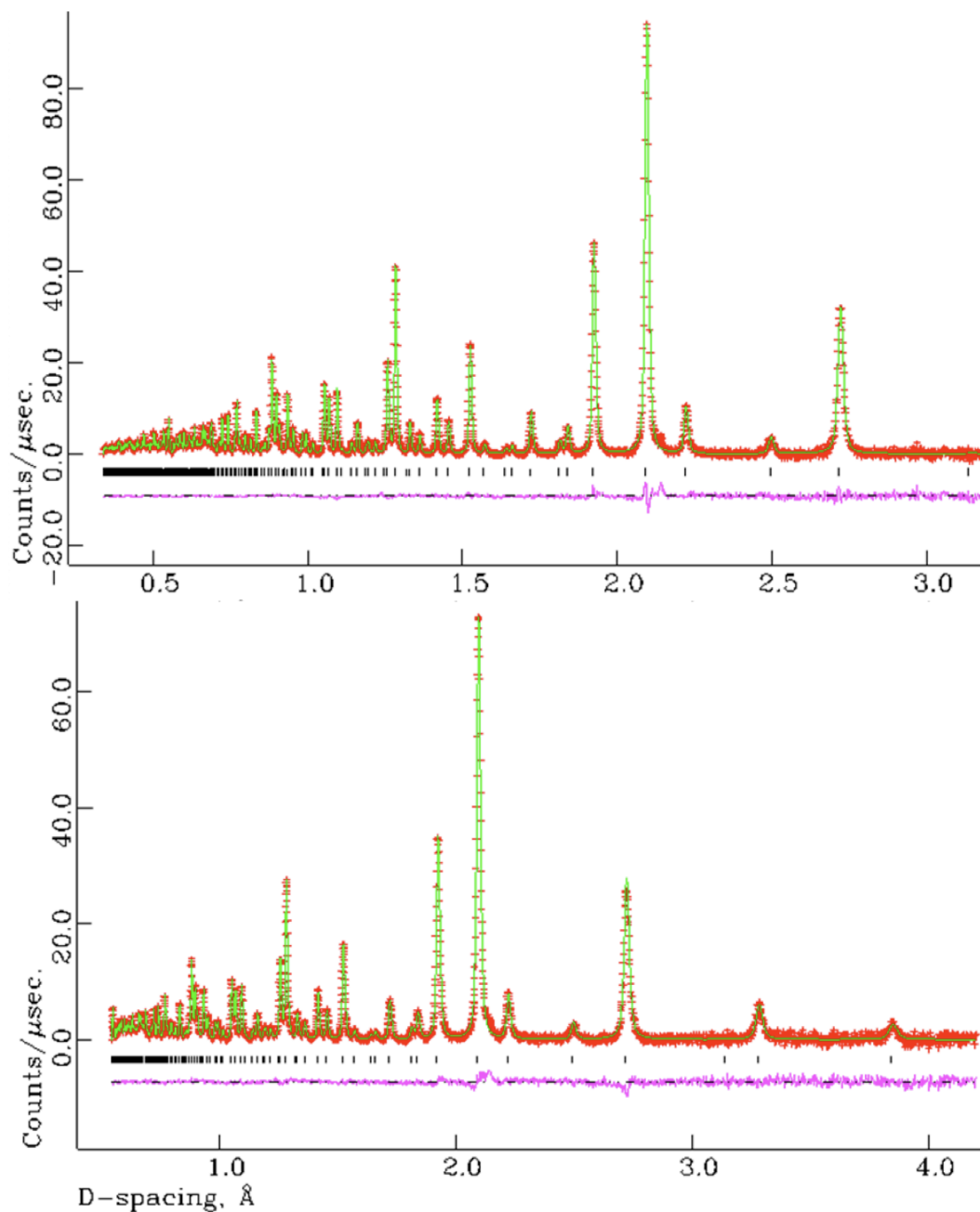
Figure 4-25: Final profile fit obtained from the refinement against PND at 295 K for Co_6Mo_6N.

The observed data are crosses, the calculated profile the solid line and lower continuous line the difference plot. Tick marks show allowed reflection positions. Top – Backscattering detector bank $\langle 2\theta \rangle = 145°$, Bottom - $90°$ detector bank.

Table 4-18: Crystallographic parameters for Co₆Mo₆N from PND data – 8a site wholly occupied.

Parameter	Value
Formula	Co_6Mo_6N
Space group	*Fd-3m*
Formula mass / $gmol^{-1}$	7543.242
Cell parameter, *a* / Å	10.87938(4)
Unit-cell volume / $Å^3$	1287.692(7)
Calculated density ρ_x / gcm^{-3}	9.727
Number of observations	8197
Number of variables	40
R_p / %	2.38
R_{wp} / %	1.28
χ^2	1.411

Table 4-19: Co₆Mo₆N PND refined parameters - 8a site.

Atoms / Site	x	y	z	Occupancy	100× U_{iso} /U_{eq} ($Å^2$)
Co 1 (32e)	0.29226(4)	0.29226(4)	0.29226(4)	1.00	0.48*
Co 2 (16d)	0.500000	0.500000	0.500000	1.00	0.45*
Mo (48f)	0.321289(20)	0.125000	0.125000	1.00	0.39*
N (8a)	0.125000	0.125000	0.125000	1.00	0.44*

* = Anisotropically measured – expansion is shown here:

Atoms	U_{11} ($Å^2$)	U_{22} ($Å^2$)	U_{33} ($Å^2$)	U_{12} ($Å^2$)	U_{13} ($Å^2$)	U_{23} ($Å^2$)
Co 1	0.480(12)	0.480(12)	0.480(12)	-0.051(14)	-0.051(14)	-0.051(14)
Co 2	0.451(14)	0.451(14)	0.451(14)	0.016(18)	0.016(18)	0.016(18)
Mo	0.355(9)	0.415(6)	0.415(6)	0.00	0.00	-0.047(9)
N	0.444(10)	0.444(10)	0.444(10)	0.00	0.00	0.00

The crystallographic information obtained from the refinement against the room temperature PND data (Table 4-20) shows that the co-ordination of the constituent atoms changes slightly from that described previously. The main changes occurred in the Co-Co sub-lattice and the Mo-N sub-lattice (Figure 4-26). The Co-Co intermetallic distances decrease which resulted in an overall contraction in the sub-lattice in the reduced nitride phase. The Mo-N sub-lattice change is manifested in an increase in the unique Mo-N distance which increases by ~1% and hence the Mo-N sub-lattice expands in the η-12 nitride. In addition the distortion of the NMo_6 octahedra seen in the η-6 nitride is removed.

Table 4-20: Selected Interatomic Distances and Bond Angles for Co_6Mo_6N from PND data.

Temperature	290 K	4.2 K
Atomic Distance (Å)		
N – Mo ×6	2.13550(22)	2.1361(4)
Mo – Mo ×3	2.84262(9)	2.8344(2)
Mo – Mo ×3	3.02006(32)	3.0210(5)
Co(1) – Mo ×3	2.5928(5)	2.5863(8)
Co(1) – Mo ×3	2.72028(19)	2.7095(3)
Co(1) – Co(1) ×3	2.5460(12)	2.5439(18)
Co(1) – Co(2) ×3	2.35174(24)	2.3474(4)
Co(2) – Mo ×6	2.73477(16)	2.7252(3)
Co(2) – Co(1) ×6	2.35174(24)	2.3474(4)
Bond Angle (°)		
N – Mo – N	162.716(5)	162.877(10)
Mo – N – Mo ×6	90.0	90.0
Mo – N – Mo ×6	90.0	90.0
Mo – N – Mo ×3	180.0	180.0

Both the Co-Mo and Mo-Mo distances decrease and, hence, although the Co(1)-Co(2) and Mo-N sublattices might still be regarded as "independent", the interaction between

them could be perceived as increasing as nitrogen is removed from the structure. The local environment of the atoms is shown in Figure 4-27 and Figure 4-28.
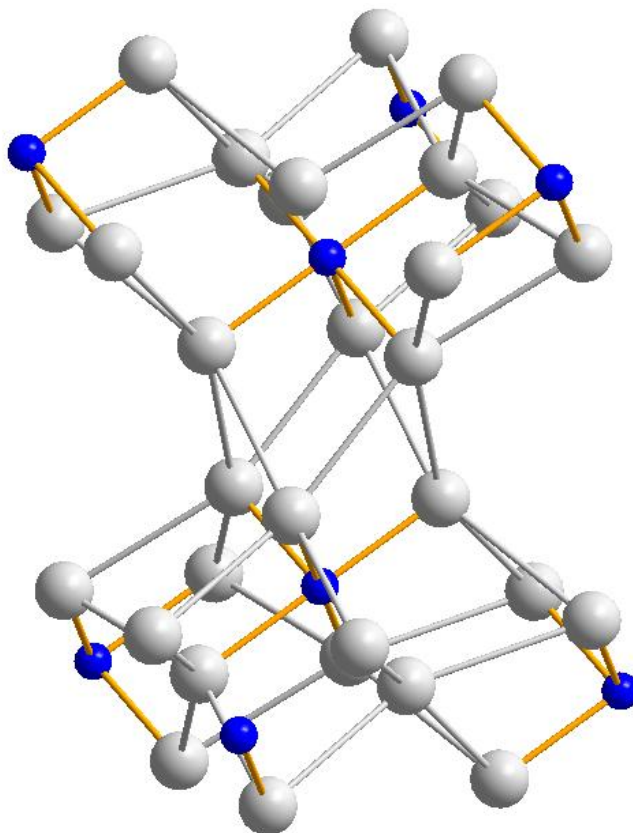
Figure 4-26: Mo-N sublattice in Co$_6$Mo$_6$N.

Mo – silver spheres, N – blue spheres.
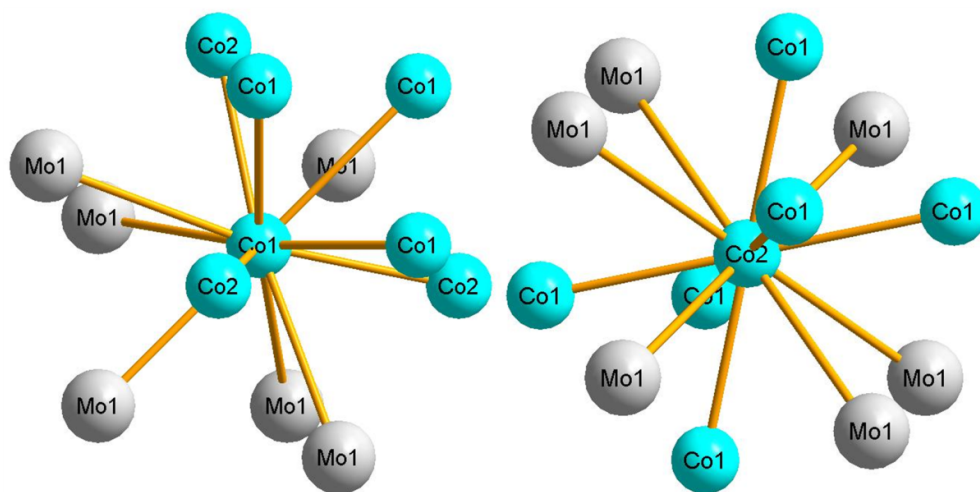
Figure 4-27: Co-ordination geometry at Co1 (32e) site and Co2 (16d) site in Co$_6$Mo$_6$N.
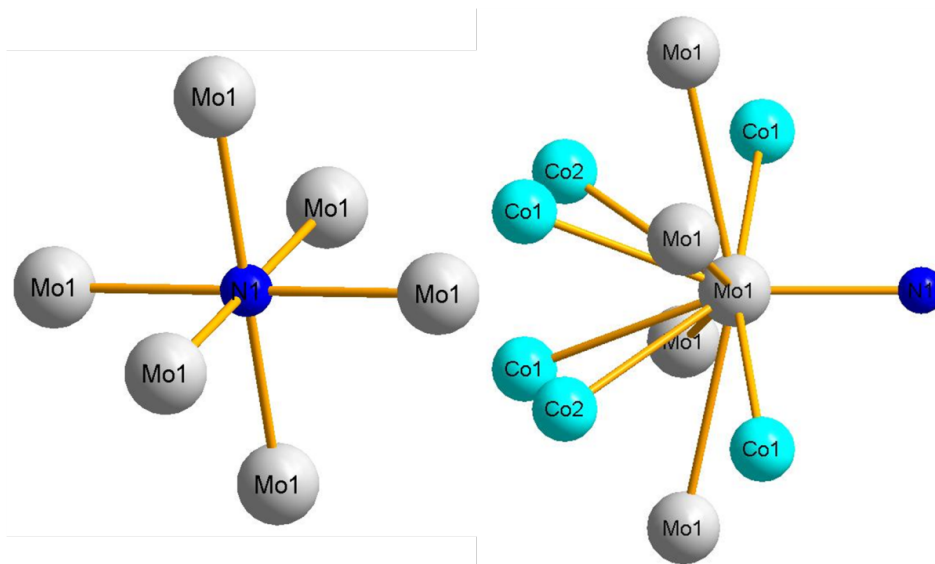
Figure 4-28: Co-ordination geometry at N (8a) site and Mo (48f) site in Co$_6$Mo$_6$N.

Low temperature (4.2 K) PND refinement data (Table 4-21,

Table 4-22 and Figure 4-29) are similar to the findings of the room temperature refinements and the hence the model of a cubic (Fd-3m) η-12 structured nitride in which nitrogen wholly occupies the 8a (1/8, 1/8, 1/8) site is also applicable at low temperature.

Table 4-21: Crystallographic parameters for Co$_6$Mo$_6$N from 4.2 K PND data.

Parameter	Value
Formula	Co$_6$Mo$_6$N
Space group	*Fd-3m*
Formula mass / gmol^{-1}	7658.016
Cell parameter, *a* / Å	10.8560(2)
Unit-cell volume / Å^3	1279.39(3)
Calculated density ρ_x / gcm^{-3}	9.794
Number of observations	7959
Number of variables	57
R$_p$ / %	1.42
R$_{wp}$ / %	0.85
χ^2	1.60

Table 4-22: Co$_6$Mo$_6$N PND refined parameters from 4.2 K data.

Atoms / Site	x	y	z	Occupancy	100× U$_{iso}$ /U$_{eq}$ (Å^2)
Co 1 (32e)	0.29215(6)	0.29215(6)	0.29215(6)	1.00	0.15*
Co 2 (16d)	0.500000	0.500000	0.500000	1.00	0.11*
Mo (48f)	0.32176(3)	0.125000	0.125000	1.00	0.09*
N (8a)	0.12500	0.12500	0.12500	1.00	0.39*

* = Anisotropically measured – expansion is shown here:

Atoms	U$_{11}$ (Å^2)	U$_{22}$ (Å^2)	U$_{33}$ (Å^2)	U$_{12}$ (Å^2)	U$_{13}$ (Å^2)	U$_{23}$ (Å^2)
Co 1	0.15(2)	0.15(2)	0.15(2)	-0.15(2)	-0.15(2)	-0.15(2)
Co 2	0.11(2)	0.11(2)	0.11(2)	0.11(3)	0.11(3)	0.11(3)
Mo	0.087(13)	0.098(8)	0.098(8)	0.00	0.00	0.007(13)
N	0.399(12)	0.399(12)	0.399(12)	0.00	0.00	0.00
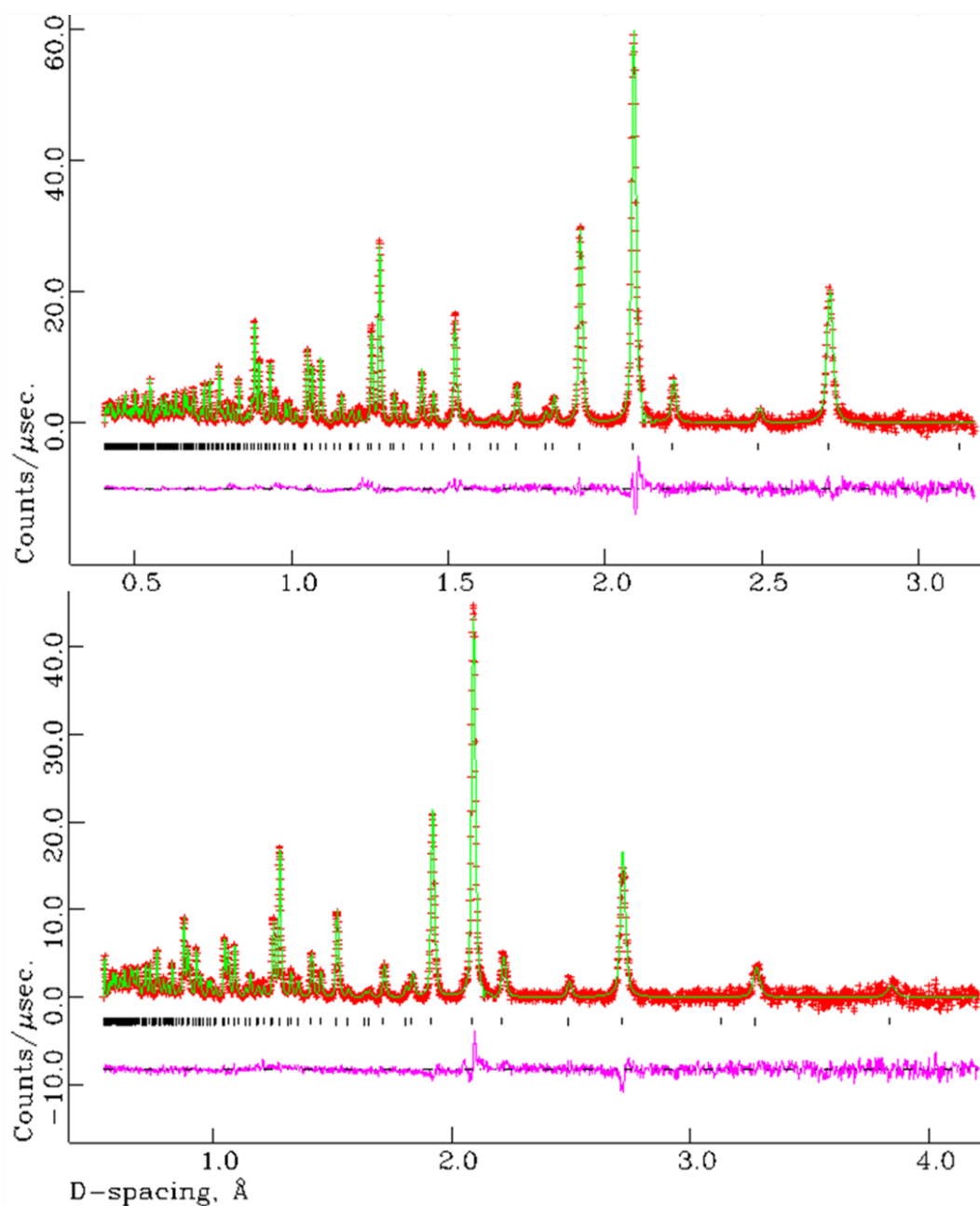
Figure 4-29: Final profile fit obtained from the refinement against PND at 4.2 K for Co_6Mo_6N.

The observed data are crosses, the calculated profile the solid line and lower continuous line the difference plot. Tick marks show allowed reflection positions. Top – Backscattering detector bank $<2\theta>$ = 145°, Bottom - 90° detector bank.

The relocation of the nitrogen within the system from the 16c site in Co_3Mo_3N to the 8a site in Co_6Mo_6N thus gives a new nitride phase. The Mo-N distances when the 8a site is filled increases from 2.111 Å to 2.135 Å, solely as a result of the migration of the N to the preferred 8a site. However, if the nitrogen did not relocate upon denitridation and remained on the 16c site at half occupation the bond length would be constrained by

symmetry of the N position to 2.07 Å (although this is longer than those found in ionic ternary molybdenum (VI) nitrides, e.g. $Ca(Ba)_3MoN_4$).[22]

Although no magnetic ordering was observed in the low temperature PND diffraction profiles, analogous magnetic measurements to those conducted previously on Co_3Mo_3N were conducted on Co_6Mo_6N for the purposes of comparison.
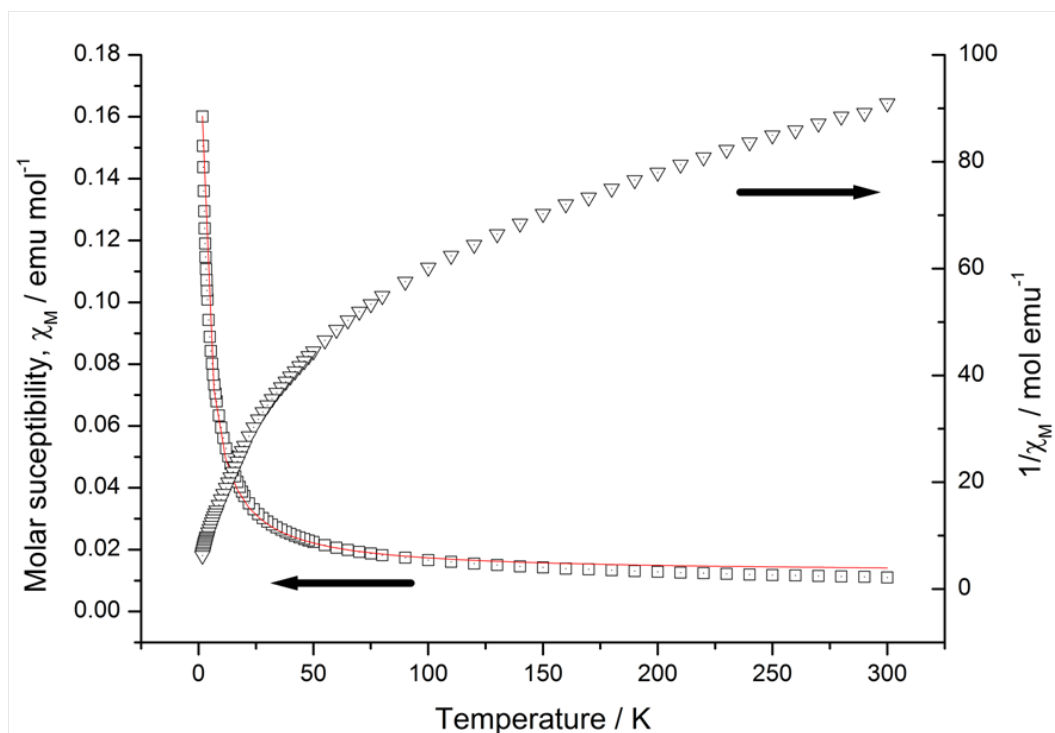
Figure 4-30: Plot of magnetic susceptibility measurements for Co_6Mo_6N.

(□) the molar magnetic susceptibility and (Δ) the inverse of the mass magnetic susceptibility against temperature (T). The red solid curves represent the best (P + C-W) fits to the χ_M vs T data.

The results, as shown in Figure 4-30 demonstrate, that a P + C-W fit yields values of 0.499(1) emu.mol^{-1}.K, 1.688(6) K, and 0.012(1) emu.mol^{-1} for C, θ, and χ^0. Co_6Mo_6N exhibits almost negligible hysteresis (Figure 4-31) yielding a coercive field of 4 Oe, which is lower than the 20 Oe coercive field shown previously for the Co_3Mo_3N sample.

The differences between the two phases are subtle, yet reproducible; indicating that the magnetism is intrinsic to the materials and therefore is more likely to be a function of the crystal chemistry than that of the microstructure of the samples. However the possibility of low levels of a ferromagnetic impurity (below the detection limits of diffraction – both PXRD and PND) cannot be discounted. The small positive Weiss constants from the fit to the temperature dependence of the susceptibility and the weak

hysteresis in the M vs H measurements, suggest localised ferromagnetic interactions within the Co(1)$_4$ tetrahedra. Assuming a similar magnetic structural model for the two Co-Mo-N phases to those for the magnetically ordered substituted phases described recently[23], then it could be expected that each Co(1) tetrahedron would couple anti-ferromagnetically to its nearest neighbours through the face-capping Co(2) atoms on the 16d sites.
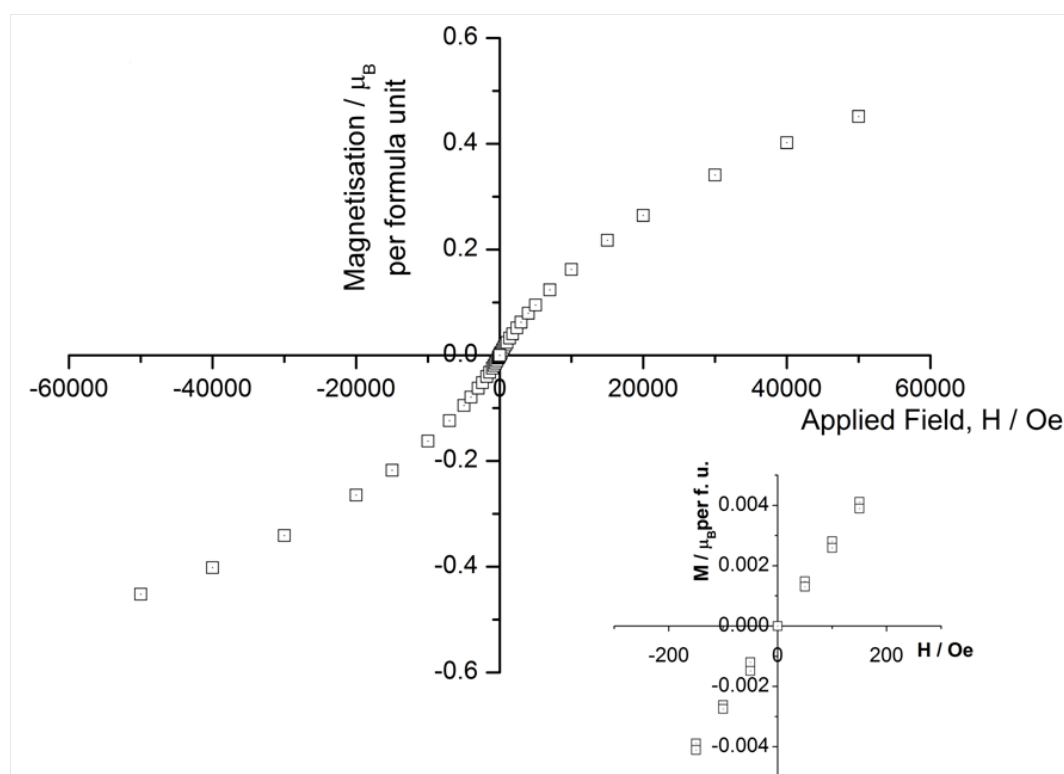
Figure 4-31: Magnetisation of Co$_6$Mo$_6$N as a function of applied field at 2 K.

Inset shows a closer view of the area around the origin.

4.3.2.4   Co$_3$Mo$_3$N – Co$_6$Mo$_6$N cycling

The loss of half the lattice nitrogen during the transformation of Co$_3$Mo$_3$N to Co$_6$Mo$_6$N raises the possibility that the Co$_3$Mo$_3$N could be viewed as a "reservoir" of activated nitrogen which could be of importance in the development of novel nitrogen-transfer chemistry. In order to validate this, it is necessary to obtain a detailed understanding of the denitridation and also to determine the conditions under which re-nitridation of Co$_6$Mo$_6$N to yield Co$_3$Mo$_3$N may occur. Probing of the system further through the use of more testing procedures and also *in-situ* PND allowed for greater understanding of how the Co-Mo-N system changes under varying conditions.

The system was shown to reduce under 3:1 H_2/Ar gas, with the limit of reduction being the Co_6Mo_6N phase. A set of reactions designed to see whether Co_3Mo_3N regeneration from Co_6Mo_6N is possible were undertaken. Reactions were initially conducted under 3:1 H_2/N_2 gas. In order to produce the Co_6Mo_6N sample required for this; Co_3Mo_3N was reacted at 973 K for five hours under 3:1 H_2/Ar gas yielding a pure phase Co_6Mo_6N which was then used for the regeneration testing.

The initial test was conducted at 973 K under 3:1 H_2/N_2 gas for six hours, and a separate test used a temperature of 673 K for six hours. The PXRD results are shown in Figure 4-32. Indexing of patterns prior to and after regeneration showed that the unit cell parameter increased from $a = 10.897(5)$ Å to $a = 11.012(7)$ Å and $a = 11.019(4)$ Å at 673 K and 973 K respectively. Microanalysis results (Table 4-23) this indicated that both the higher and lower temperature reactions were successful in regenerating the system to the original Co_3Mo_3N.
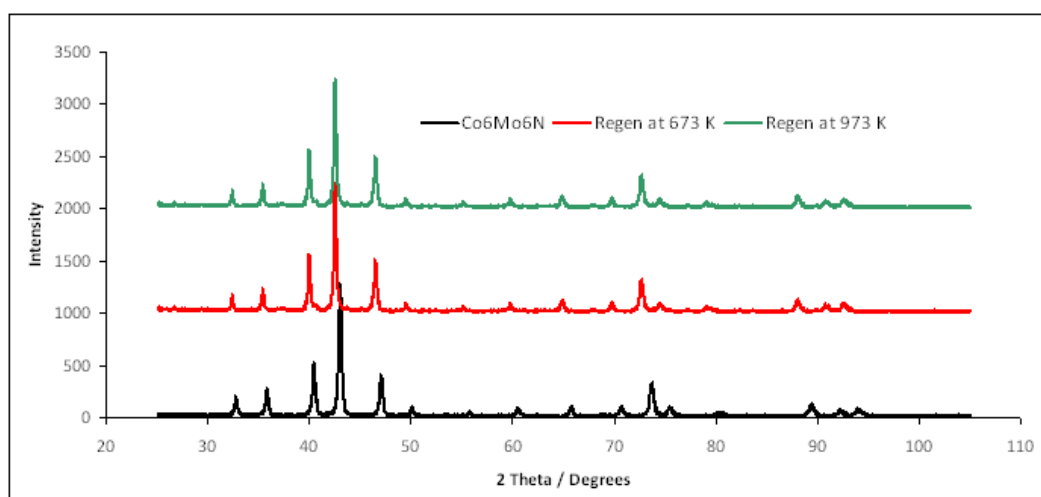
Figure 4-32: PXRD pattern showing regeneration of Co_6Mo_6N with 3:1 H_2/N_2 gas.

Table 4-23: Unit cell parameters and microanalysis results for regeneration.

Sample	Lattice parameter / Å	Nitrogen content / wt%
As prepared Co_3Mo_3N	11.025(4)	2.93(4)
Co_6Mo_6N	10.897(5)	1.50(3)
Restored Co_3Mo_3N with H_2/N_2 gas at 673 K	11.012(7)	2.91(4)
Restored Co_3Mo_3N with H_2/N_2 gas at 973 K	11.019(4)	2.84(6)

These results indicate that the system can be cycled between Co_3Mo_3N and Co_6Mo_6N. However the pathway through which the reduction and restoration proceeds is unknown. In order to observe any possible intermediate phases a time resolved PND experiment was undertaken, in which the reduction and regeneration processes were followed by *in-situ* diffraction.

Model structures were refined against room temperature PND data using GSAS. The starting model used in the refinement was taken from the *ex-situ* refinements performed previously (Section 4.3.2.1 and 4.3.2.3). The refinement confirms, as previously shown, that the fit to the Co_3Mo_3N phase reaches a minimum with the non-metal 16c (0, 0, 0) site fully occupied, as shown in Figure 4-33 and Table 4-24 and Table 4-25.
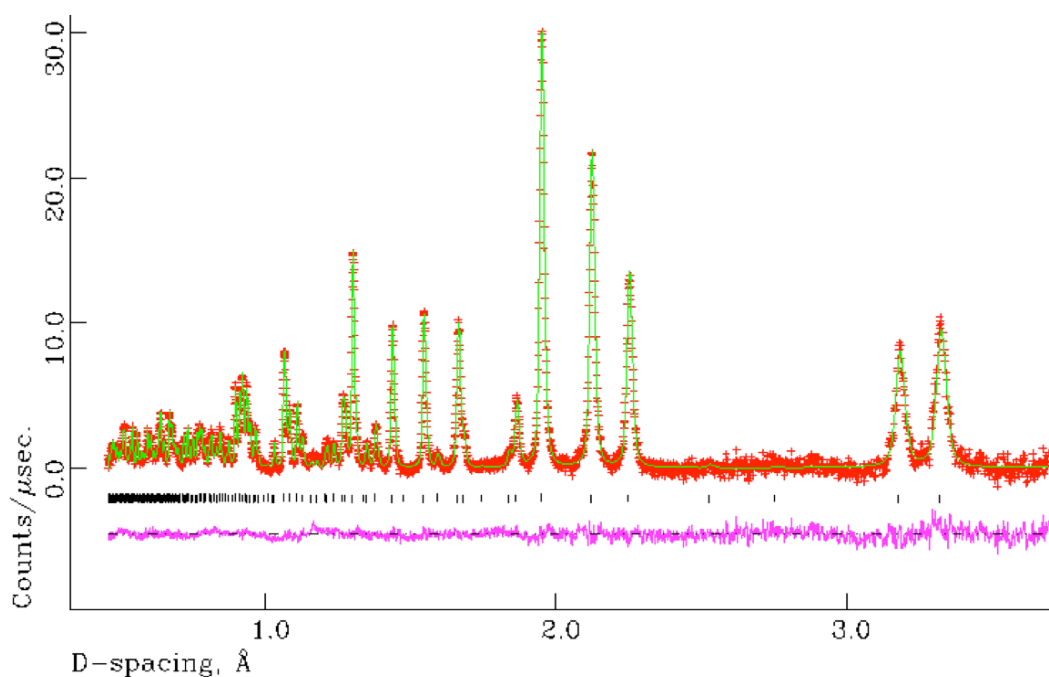
Figure 4-33: Final profile fit obtained from the refinement against *in-situ* PND at 295 K for Co_3Mo_3N.

The observed data are crosses, the calculated profile the solid line and lower continuous line the difference plot. Tick marks show allowed reflection positions.

Table 4-24: Crystallographic parameters for Co$_3$Mo$_3$N from *in-situ* PND data.

Parameter	Value
Formula	Co$_3$Mo$_3$N
Space group	*Fd-3m*
Formula mass / gmol^{-1}	7658.016
Cell parameter, *a* / Å	11.0253(4)
Unit-cell volume / Å^3	1340.20(9)
Calculated density ρ_x / gcm^{-3}	9.488
Number of observations	4172
Number of variables	32
R$_p$ / %	2.17
R$_{wp}$ / %	1.74
χ^2	1.247

Table 4-25: Co$_3$Mo$_3$N PND refined parameters from PND data.

Atoms / Site	x	y	z	Occupancy	100× U$_{iso}$ /U$_{eq}$ (Å^2)
Co 1 (32e)	0.29243(12)	0.29243(12)	0.29243(12)	1.00	0.29*
Co 2 (16d)	0.500000	0.500000	0.500000	1.00	0.42*
Mo (48f)	0.32387(7)	0.125000	0.125000	1.00	0.37*
N (16c)	0.000000	0.000000	0.000000	1.00	0.42*

* = Anisotropically measured – expansion is shown here:

Atoms	U$_{11}$ (Å^2)	U$_{22}$ (Å^2)	U$_{33}$ (Å^2)	U$_{12}$ (Å^2)	U$_{13}$ (Å^2)	U$_{23}$ (Å^2)
Co 1	0.29(5)	0.29(5)	0.29(5)	-0.07(5)	-0.07(5)	-0.07(5)
Co 2	0.42(6)	0.42(6)	0.42(6)	0.32(8)	0.32(8)	0.32(8)
Mo	0.516(33)	0.294(20)	0.294(20)	0.00	0.00	0.094(27)
N	0.417(20)	0.417(20)	0.417(20)	-0.005(20)	-0.005(20)	-0.005(20)

The room temperature measurement was used as the starting model for the Co_3Mo_3N phases and the *ex-situ* data from previous refinements was used as the model for the Co_6Mo_6N phase. The reaction conditions and stages are shown in Figure 4-34.
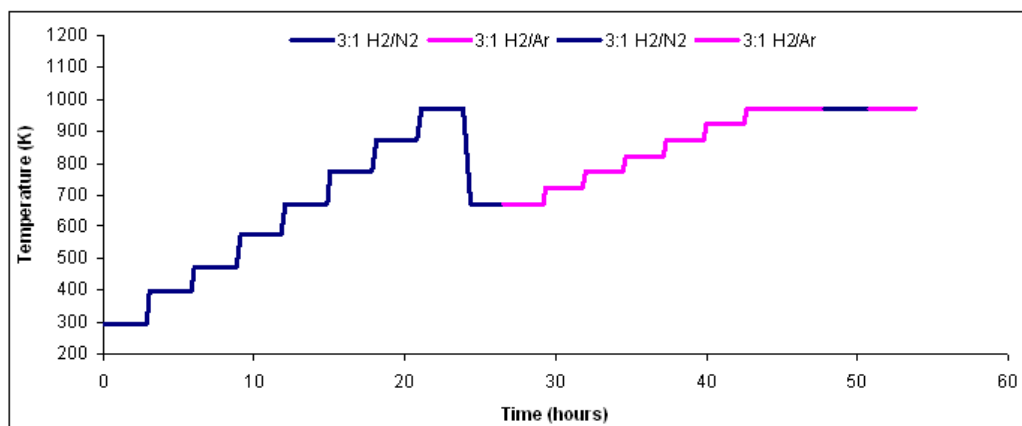
Figure 4-34: *In-situ* **reaction scheme and heating regime.**

Horizontal lines indicate times at which samples were analysed.

The initial stage of the reaction between 290 and 973 K under 3:1 H_2/N_2 gas, mimicked the conditions of the standard ammonia synthesis testing, with additional temperature increases up to 973 K, which removed any oxide species from the surface of the nitride.
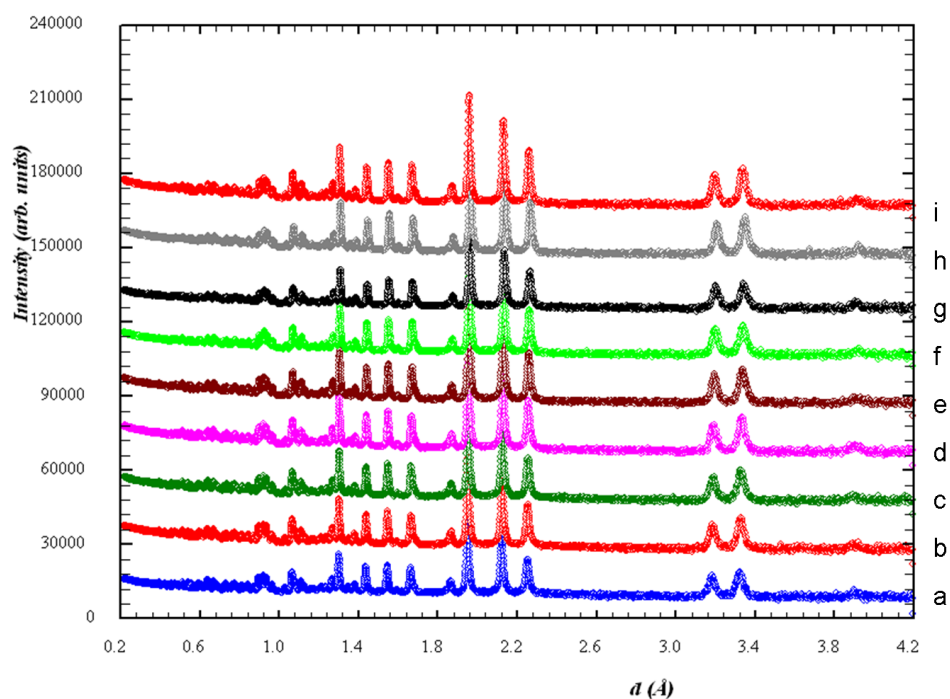
Figure 4-35: PND data for first stage of *in-situ* experiment.

a = as prepared, *b* = 373 K, *c* = 473 K, *d* = 573 K, *e* = 673 K, *f* = 773 K, *g* = 873 K, *h* = 973 K, *i* = 673 K (cooled)

The diffraction patterns (Figure 4-35) showed that there was no change in the structure, apart from an increase in lattice parameters upon heating due to lattice expansion as shown in Figure 4-36. Under these conditions, the only phase that could be observed was that of Co_3Mo_3N. The linear expansion coefficient for Co_3Mo_3N under flowing H_2/N_2 gas is 9.07 $x10^{-6}$ Å.K^{-1}.
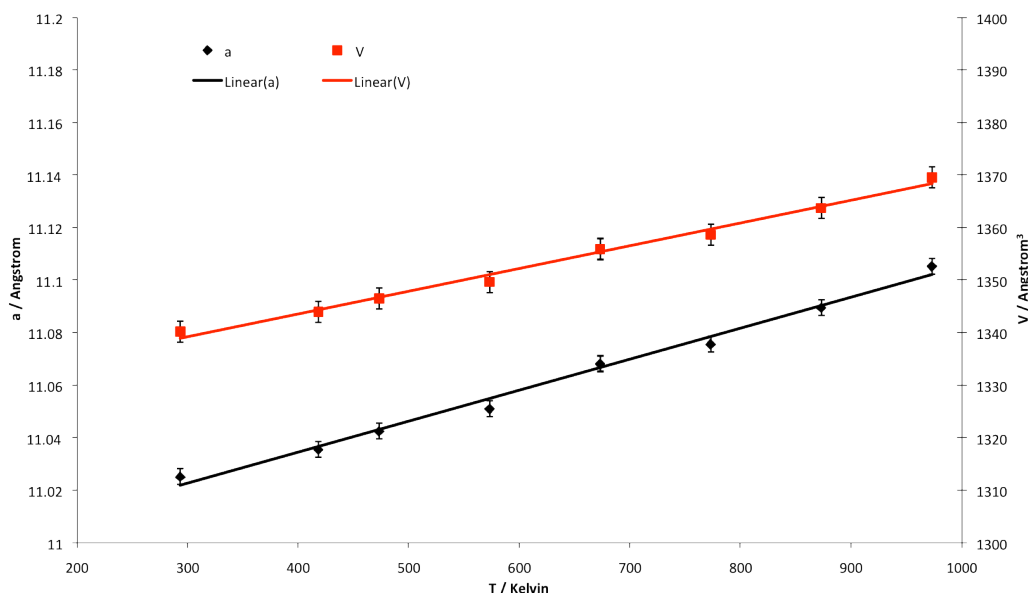
Figure 4-36: Plot indicating thermal expansion due to heating of Co$_3$Mo$_3$N.

> Lattice parameters taken from refined parameters taken from Reitveld refinements of in-situ PND data.

After cooling to 673 K the gas mixture was switched to 3:1 H_2/Ar gas, then the temperature was slowly increased to 973 K from 673 K in order to observe the anticipated removal of nitrogen and the corresponding changes in structure. The diffraction patterns were collected at set temperatures and, as can be seen in Figure 4-37, the profile begins to change between 873 K and 923 K. The Rietveld refinement of the pattern at 923 K shows that there is a mixture of the Co_3Mo_3N and Co_6Mo_6N nitrides present at this stage of the reaction. The PND pattern at 923 K clearly shows the Co_6Mo_6N phase at this temperature with the characteristic (400) peak at 2.75 Å.

(Structures of Co3Mo3N and Co6MO6N are described earlier in Sections 4.3.2.1 and 4.3.2.3).
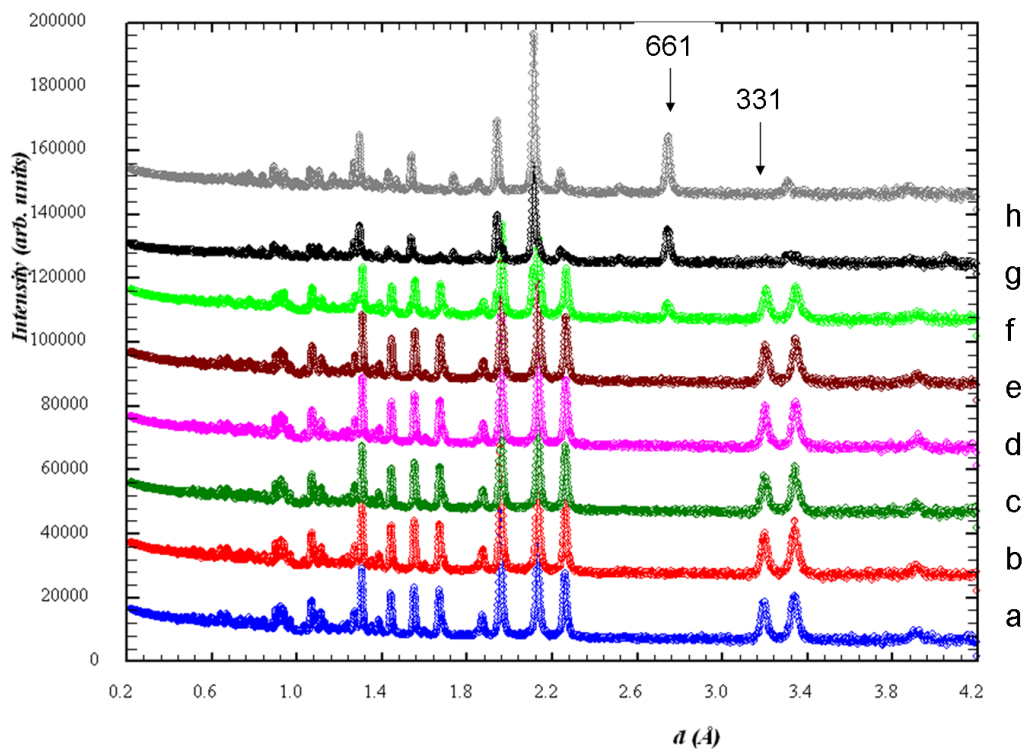
Figure 4-37: PND data for Co₃Mo₃N heated under 3:1 H₂/Ar gas.

a = 673 K, b = 723 K, c = 773 K, d = 823 K, e = 873 K, f = 923 K, g = 973 K (90 mins), h = 973 K (180 mins)

Table 4-26: Analysis of phase fractions of Co₃Mo₃N and Co₆Mo₆N present during the reaction profiles seen in Figure 4-37.

Temperature / K	Fraction of Co_3Mo_3N / %	Fraction of Co_6Mo_6N / %
673	100	0
723	100	0
773	100	0
823	100	0
873	100	0
923	75.59(45)	24.41
973 (90 mins)	16.32	83.68(53)
973 (180 mins)	0	100

The refinement data (Table 4-26) show that at 923 K the sample is composed of 75% Co_3Mo_3N and 25% Co_6Mo_6N respectively. The transformation therefore appears to be a direct one from the Co_3Mo_3N to Co_6Mo_6N phase with no intermediate phases being evident. Further there is no evidence in the variable temperature data for any additional new phases aside from the η-6 and η-12 nitrides. The diffraction data at 973 K after 90 minutes yielded a sample containing 16% Co_3Mo_3N and 84% Co_6Mo_6N respectively. Rietveld refinement against the data collected after three hours at 973 K (Table 4-27, Table 4-28 and Figure 4-38) yields single phase Co_6Mo_6N.

Table 4-27: Crystallographic parameters for Co₆Mo₆N from *in-situ* PND data.

Parameter	Value
Formula	Co_6Mo_6N
Space group	*Fd-3m*
Formula mass / gmol^{-1}	7545.960
Cell parameter, *a* / Å	10.9740(4)
Unit-cell volume / Å^3	1321.57(8)
Calculated density ρ_x / gcm^{-3}	9.481
Number of observations	4123
Number of variables	31
R_p / %	2.88
R_{wp} / %	2.05
χ^2	0.939

Table 4-28: Co$_6$Mo$_6$N PND refined parameters from PND data.

Atoms / Site	x	y	z	Occupancy	100× U_{iso}/U_{eq} (Å^2)
Co 1 (32e)	0.29231(15)	0.29231(15)	0.29231(15)	1.00	1.16*
Co 2 (16d)	0.500000	0.500000	0.500000	1.00	1.96*
Mo (48f)	0.32031(8)	0.125000	0.125000	1.00	1.29*
N (8a)	0.125000	0.125000	0.125000	1.00	1.46*

* = Anisotropically measured – expansion is shown here:

Atoms	U_{11} (Å^2)	U_{22} (Å^2)	U_{33} (Å^2)	U_{12} (Å^2)	U_{13} (Å^2)	U_{23} (Å^2)
Co 1	1.16(6)	1.16(6)	1.16(6)	0.19(7)	0.19(7)	0.19(7)
Co 2	1.96(10)	1.96(10)	1.96(10)	-0.75(10)	-0.75(10)	-0.75(10)
Mo	1.33(5)	1.267(35)	1.267(35)	0.00	0.00	-0.19(4)
N	1.46(4)	1.46(4)	1.46(4)	0.00	0.00	0.00
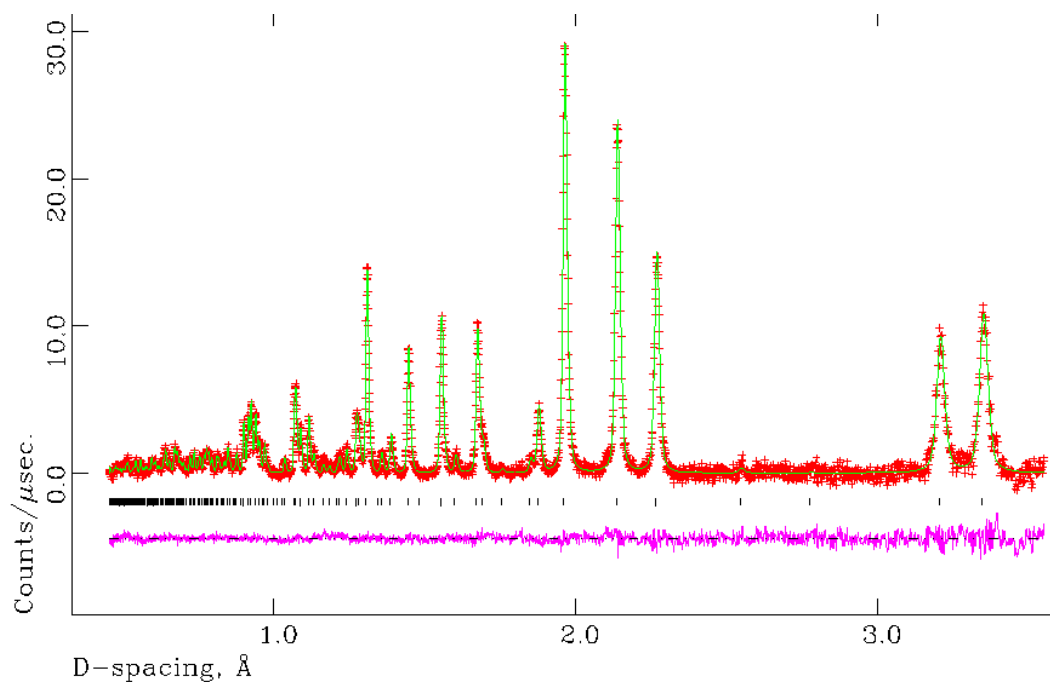
Figure 4-38: Final profile fit obtained from the refinement against *in-situ* PND data collected at 793 K under 3:1 H$_2$/Ar gas for 180 mins.

The observed data are crosses, the calculated profile the solid line and lower continuous line the difference plot. Tick marks show allowed reflection positions.

Previously, *ex-situ* studies had shown that the formation of the η-6 nitride from the η-12 nitride is reversible when the Co_6Mo_6N phase is treated under 3:1 H_2/N_2 gas. When the gas was changed to 3:1 H_2/N_2 gas, at 973 K, diffraction data were collected after 20 minutes of exposure. Under these conditions refinement revealed the sample was ~94% Co_3Mo_3N. Regeneration therefore appears to be very rapid with the Co_6Mo_6N phase having a large affinity for nitrogen. The sample was left for a total of 90 min at 973 K to complete regeneration. This is shown in Figure 4-39.
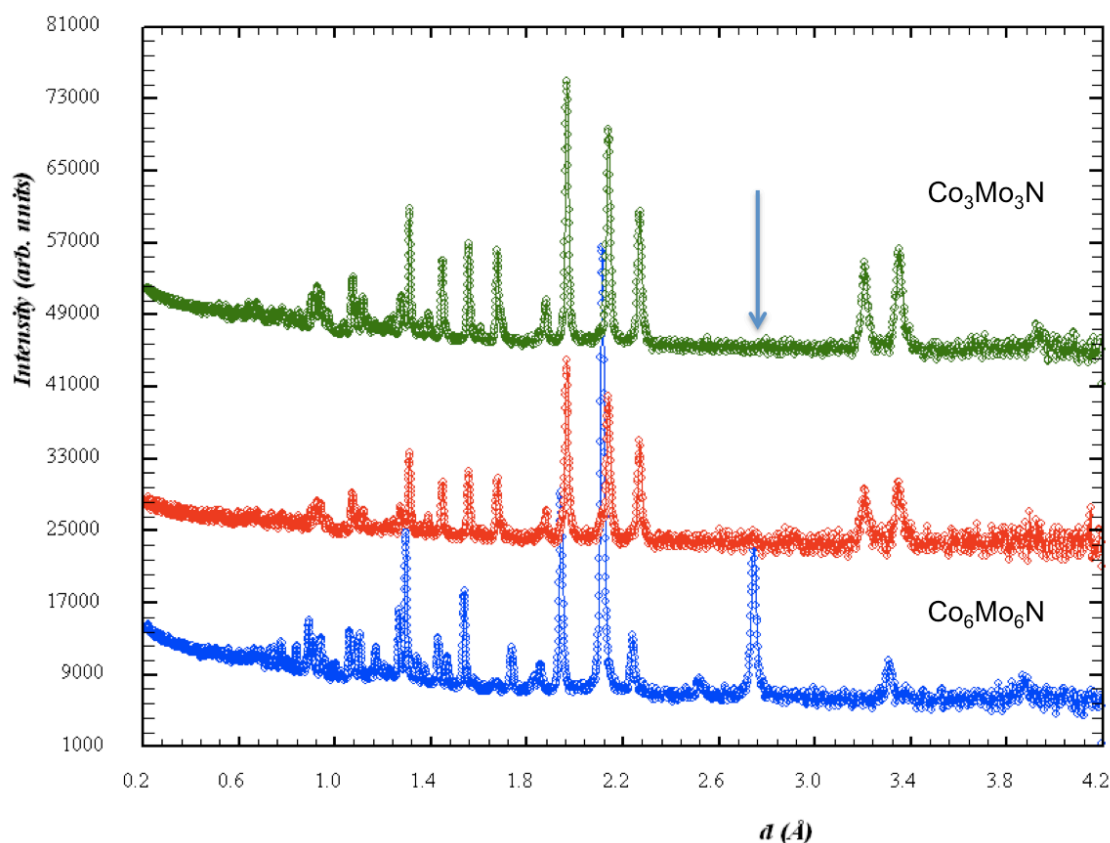
Figure 4-39: Regeneration at 973 K under 3:1 H_2/N_2 gas of Co_3Mo_3N.

Arrow indicates the 400 peak of Co_6Mo_6N

The complete reaction from Co_3Mo_3N to Co_6Mo_6N and back to Co_3Mo_3N shows that the process is a direct reaction which has no intermediate phase between the two members. The process by which the removal and replenishment occurs is at this stage unknown. However removal of nitrogen from the lattice requires the use of hydrogen. Significantly, in addition to the removal of half of the nitrogen from the lattice, the remaining half is relocated on a different site, (16c to 8a sites).

A time resolved PND experiment was conducted on a Co_3Mo_3N sample in order to observe the speed of reduction from the Co_3Mo_3N to Co_6Mo_6N and data were collected

at 20 minute intervals which is a compromise in order to indicate the timescale while still giving high quality data for analysis. Figure 4-40 shows the formation of the Co_6Mo_6N phase starts at ca. 40 minutes at a reaction temperature of 973 K. The formation of the Co_6Mo_6N phase occurs steadily with complete transformation from Co_3Mo_3N to the Co_6Mo_6N being observed after approximately three hours. Ratios of the refined phase fractions are seen in Table 4-29.
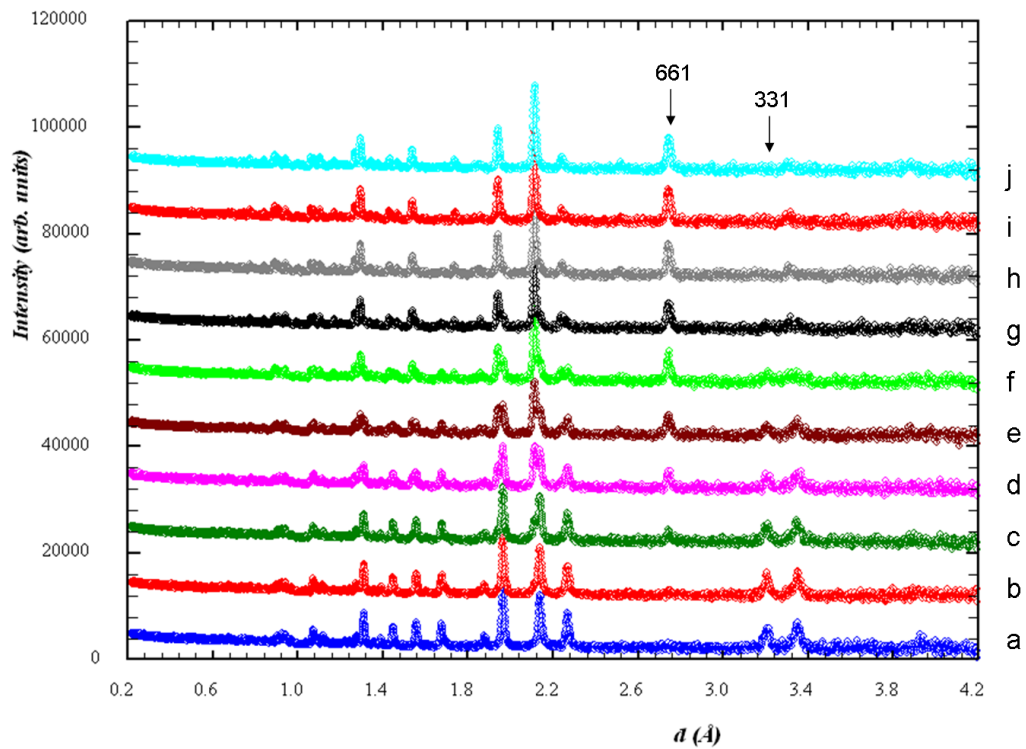
Figure 4-40: PND plots - showing *in-situ* time resolved patterns – 20 mins between patterns.

a = 0 mins, b = 20 mins, c = 40 mins, d= 60 mins, e = 80 mins, f = 100 mins,
g = 120 mins, h = 140 mins, i = 160 mins, j = 180 mins.

Table 4-29: Analysis of phase fractions of Co_3Mo_3N and Co_6Mo_6N present during the reaction profiles seen in Figure 4-40.

Time / mins	Fraction of Co_3Mo_3N / %	Fraction of Co_6Mo_6N / %
0	100	0
20	91.8(6)	8.2(6)
40	80.5(1)	19.5(1)
60	58.9(1)	41.1(1)
80	41.7(1)	58.3(1)
100	30.5(1)	69.5(1)
120	19.1(9)	80.9(9)
140	12.7(1)	87.3(1)
160	0	100
180	0	100

In order to potentially develop Co_3Mo_3N as a nitrogen storage material, it would be a significant advantage to be able to restore it with N_2 gas alone from Co_6Mo_6N rather than using 3:1 H_2/N_2 gas. Investigation of this process was undertaken using a 60 mLmin^{-1} flow rate of N_2 (BOC, OFN) in a fixed bed microreator.

Reactions performed at 673 K over a prolonged period (six hours) showed no regeneration to the Co_3Mo_3N. A series of experiments were performed at increasing temperatures, which showed that a degree of regeneration is evident after five hours at 773 K as presented in Figure 4-41 where the 2.0 wt% N content (as determined by microanalysis) is intermediate between that for Co_3Mo_3N and Co_6Mo_6N (2.8 and 1.5 wt% respectively).
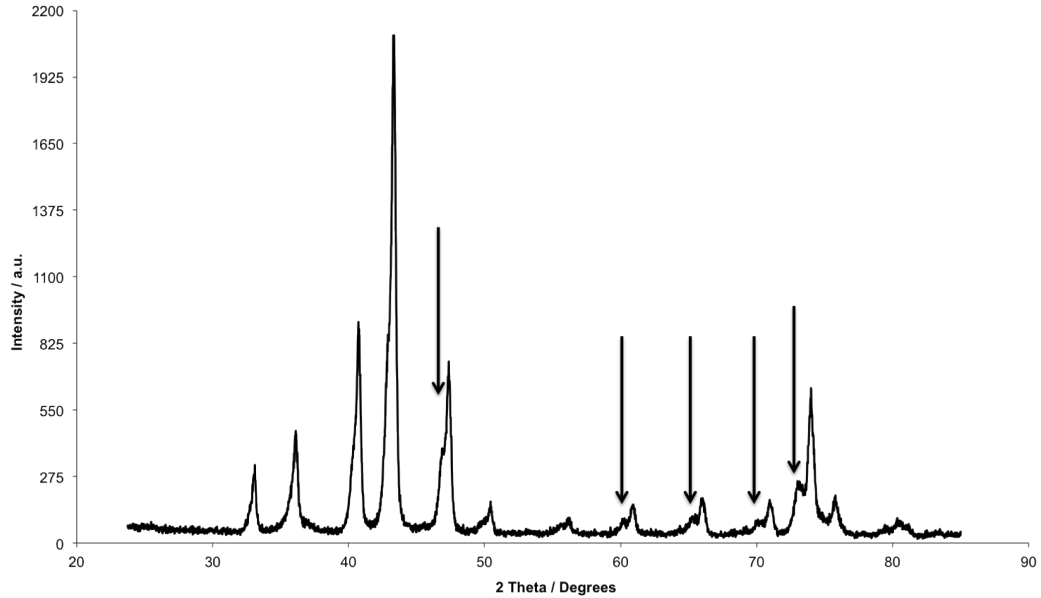
Figure 4-41: PXRD pattern of Co$_6$Mo$_6$N following treatment with 60 mLmin^{-1} N$_2$ at 773 K for five hours.

Identifiable 331 reflections marked with arrow.

The powder pattern, Figure 4-41, which was matched to a mixture of both Co$_3$Mo$_3$N and Co$_6$Mo$_6$N phases (estimated by Rietveld refinement to be 34.5 and 65.5% respectively), leads to the interesting implication that despite the nitride being subjected to a >3,500 fold excess of the quantity of nitrogen required to complete the regeneration of the Co$_6$Mo$_6$N phase, it was only partially regenerated. Under the conditions used in the reactor (the reaction bed was isothermal and the reaction was operated under a plug-flow regime) the observation of partial regeneration suggested that this mixed behaviour was intrinsic to the sample itself.

In order to follow the regeneration of the Co$_3$Mo$_3$N phase by treatment with N$_2$ alone, a temperature programmed *in-situ* PXRD experiment was performed, under the following conditions; nitrogen flow rate of 25 mLmin^{-1}, a temperature ramp rate of 12 Kmin^{-1}, a dwell time of two hours prior to the measurement, and a measurement time of 60 minutes. The results are shown in Figure 4-42, the patterns show that the proportion of Co$_3$Mo$_3$N in the sample increased as a function of reaction temperature/duration.
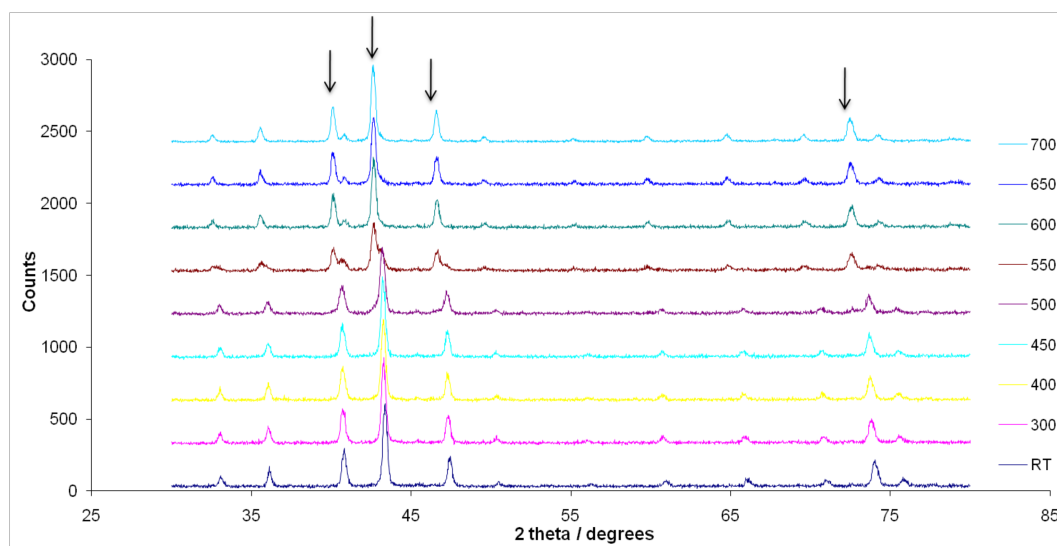
Figure 4-42: *In-situ* PXRD patterns of restoration of Co_3Mo_3N using N_2 from Co_6Mo_6N.

331 reflection positions marked with arrows

Quantitative analysis was performed on each dataset in order to analyse the phase composition at each temperature through Rietveld refinement using as the starting models the structures obtained by PND for Co_3Mo_3N and Co_6Mo_6N phases, the data for the refinements is reported in Table 4-30.

Table 4-30: Analysis of phase fractions of Co_3Mo_3N and Co_6Mo_6N present during *in-situ* PXRD measurements.

Temperature / K	Fraction Co_3Mo_3N / %	Fraction Co_6Mo_6N / %
303	0	100
573	0	100
673	0	100
723	0	100
773	15.4(4)	84.6(4)
823	75.3(2)	24.7(2)
873	87.8(3)	12.2(3)
923	95.2(5)	4.8(5)
973	98.1(9)	1.9(9)

At 973 K, the regeneration of Co_3Mo_3N was essentially complete. However, there was a very small amount of residual Co_6Mo_6N observable in the PXRD data. This has been quantified to approximately 2 wt%. A possible reason for the low levels of Co_6Mo_6N left at the end of the experiment is the *in-situ* set-up did not allow gas to permeate through to the whole sample and hence left some material in the reduced state.

In order to confirm that the regeneration is possible, corresponding microreactor experiments operating in the plug-flow regime demonstrate that complete conversion at 973 K is achieved after six hours exposure to N_2. (Figure 4-43)
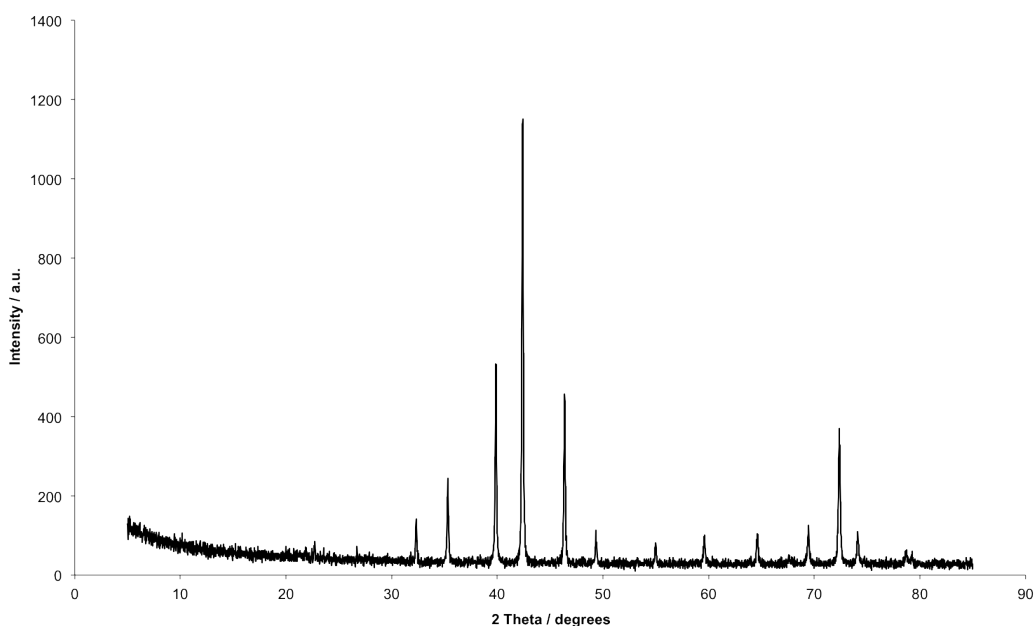
Figure 4-43: PXRD pattern of Co₃Mo₃N under plug-flow conditions after reaction at 973 K under N₂ gas.

These results indicate that the regeneration/restoration of the Co_3Mo_3N phase is possible under both 3:1 H_2/N_2 gas and pure N_2, although higher temperatures and a longer duration on stream is required when hydrogen is not present. This shows that the presence of hydrogen affects the restoration process enabling the nitrogen content to be restored to the lattice more easily. One explanation is that the hydrogen facilitates the migration of nitrogen onto the 16c site and hence allows – as for the depletion of nitrogen – a critical point to be reached after which the restoration process is very rapid. Another possibility is that restoration could be crystallite size dependent and that the result observed is reflective of the crystallite size distribution in the sample. Such phenomena are not unknown, with suggestions of crystallite size dependent variation of surface stoichiometry (and hence catalytic activity) having been published by Choi *et al.*

in different nitride and carbide systems[24]. The potential importance of the surface to bulk ratio in determining stoichiometry suggested that the surface composition could drive the phase transitions observed and that once a given composition is reached, a bulk phase change rapidly ensues. On the basis of this explanation it is possible to rationalise some observations made previously:

(i)   The Co_3Mo_3N – Co_6Mo_6N system consists of two line phases with no intermediate stoichiometries observed.

(ii)   Hydrogen is essential to drive the $Co_3Mo_3N \rightarrow Co_6Mo_6N$ phase transition, despite NH_3 being a very minor product (i.e. hydrogen is necessary to deplete the surface N content of Co_3Mo_3N to a critical value, beyond which N is eliminated from the bulk predominantly as N_2).

The ability to regenerate the system with both 3:1 H_2/N_2 gas and pure N_2 with no intermediate phases present gives the reaction scheme detailed below (Figure 4-44) this shows the removal of nitrogen as either NH_3 or N_2 and the restoration with both gases.
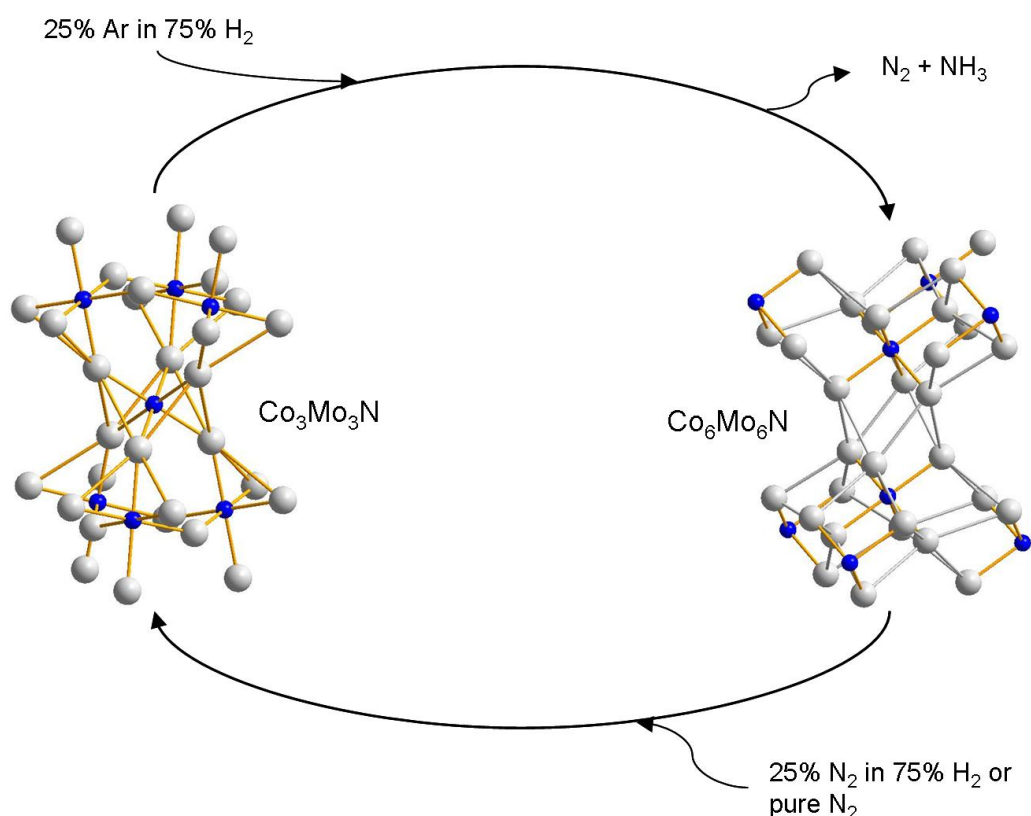
Figure 4-44: Cycle between Co₃Mo₃N and Co₆Mo₆N.

Grey spheres – Molybdenum, Blue Spheres – Nitrogen.

4.3.2.5   Isotopic exchange study

From studies in previous sections, it has not been possible to differentiate between the proportion of NH_3 generated by hydrogenation of lattice N species from the hydrogenation of surface NH_x species[13,25] with confidence. Surface NH_x species are known to be generated by ammonolysis and 3:1 H_2/N_2 gas pre-treatment[26,27]. However, the possibility of generating Co_3Mo_3N by treatment of Co_6Mo_6N formed *in-situ* by reduction under 3:1 H_2/Ar gas and then restored using N_2 gas alone (i.e. a non-hydrogen containing feed) affords the opportunity of preparing materials free from NH_x residues. For means of comparison between nitrides with and without a surface coating of NH_x species, a conventionally prepared (ammonolysis and 3:1 H_2/N_2 gas pre-treatment) Co_3Mo_3N was used as a standard.

The two samples were tested as previously described in Section 2.3 and the resulting reaction profiles shown on the same axis in Figure 4-45, indicating that the total amount of ammonia produced from a Co_3Mo_3N sample regenerated from Co_6Mo_6N by N_2 is much lower (31 % reduction in NH_3 produced) than that of the conventionally prepared sample. The quantity of ammonia produced by the regenerated sample, although reduced, is significant and indicates that direct reaction pathways, of lattice N to yield NH_3 are accessible.
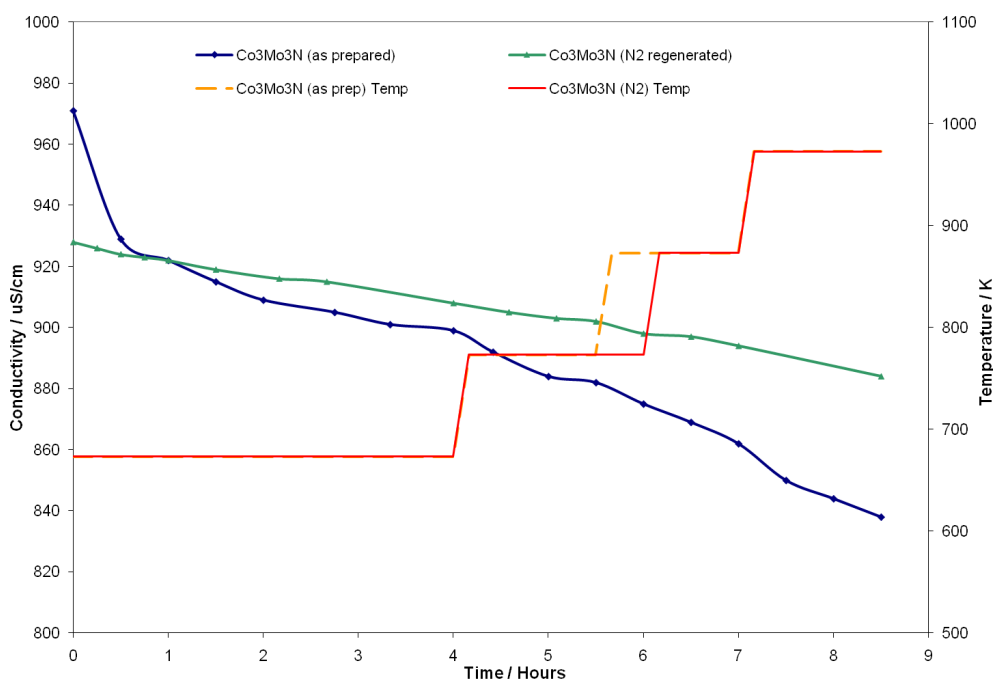
Figure 4-45: Comparison of reaction profiles for Co$_3$Mo$_3$N.

Green line - regenerated by N_2 and Blue line - prepared by conventional methods.

In order to explain and understand the findings previously discussed, $^{15}N_2$ isotopic exchange reactions were performed allowing the reaction pathway to be probed through the use of mass spectrometry observing the gases evolved during the reactions performed.

The system used is detailed in Section 4.2. A mixture of gases can be introduced into the reactor and the system sealed to allow measurements of the nitrogen exchanged with the lattice of the sample, through mass spectrometry. In this system there is no co-fed hydrogen in the exchange gas, this means that the reactions were not able to be directly compared to the reactions previously shown for activity studies.

Samples were initially pre-treated under 3:1 H_2/N_2 gas at 973 K to remove any surface oxide species present. The resultant product remaining after the pre-treatment procedure was assumed to be Co_3Mo_3N. Initial reactions were carried out on pure Co_3Mo_3N after treatment with 3:1 H_2/N_2 gas at 973 K for two hours, the reaction was conducted as a temperature programmed experiment under a gaseous mixture of $^{14}N_2$ and $^{15}N_2$ and starting at a temperature of 673 K increasing to 973 K.

The result of this is shown in Figure 4-46, which clearly demonstrates the occurrence of exchange. However, exchange did not start until the temperature had exceeded 723 K, (see Figure 4-47). Evidence for exchange is seen in the formation of $^{14}N^{15}N$, since $^{15}N_2$ was only present in the feed gas.
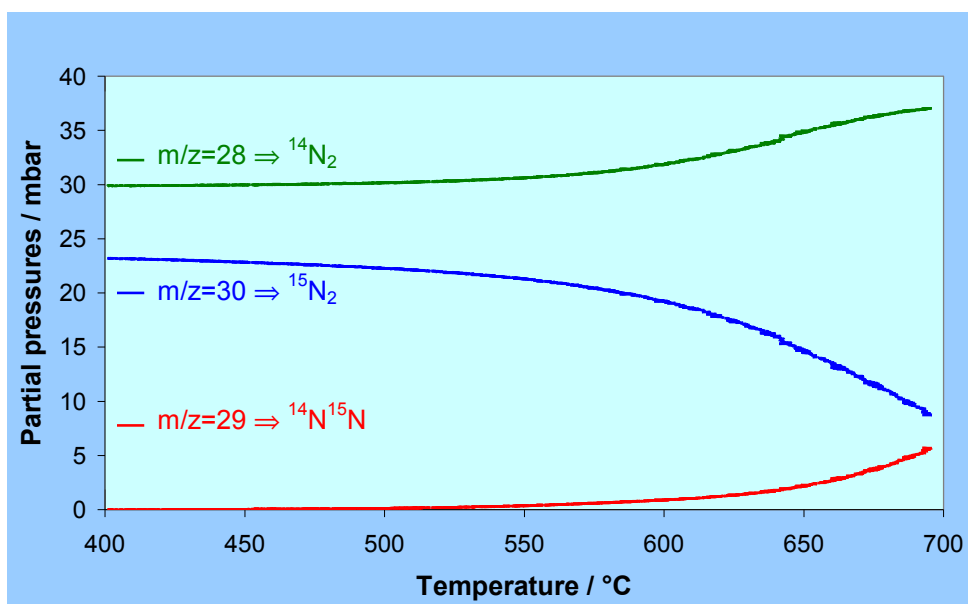
Figure 4-46: Temperature programmed isotopic exchange reaction under mixed $^{14}N_2$ and $^{15}N_2$.
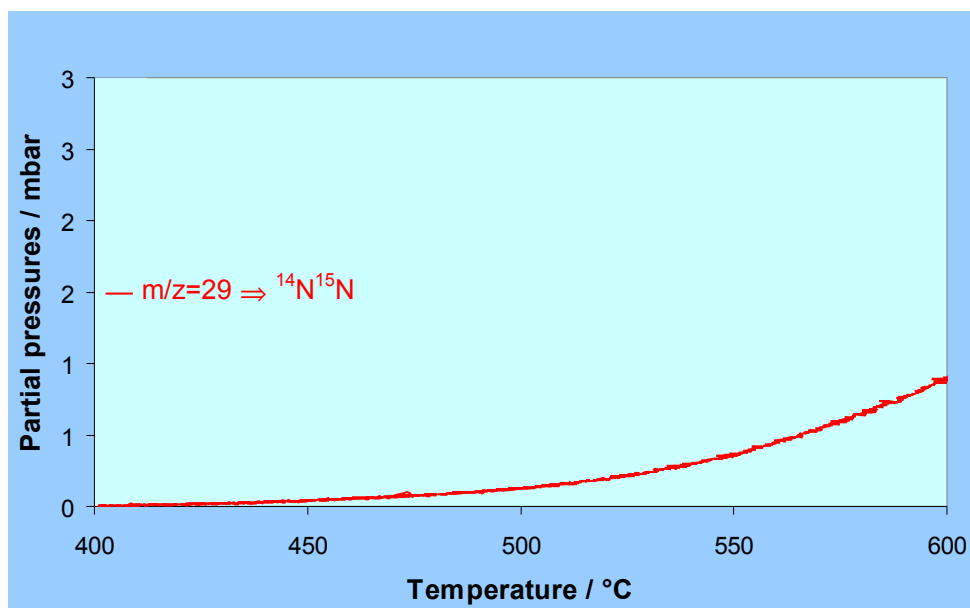
Figure 4-47: Close inspection of exchange start point seen in Figure 4-46.

The exchange observed occurs above 723 K although the nature of the exchange is either:

(i)   homomolecular exchange (exchange in the gas phase)

$$^{14}N_{2\ (g)} + {}^{15}N_{2\ (g)} \rightarrow 2\,{}^{14}N^{15}N_{(g)}$$
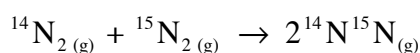
(ii)   heterolytic exchange (exchange with the lattice)

$$^{15}N_{2\ (g)} + {}^{14}N_{(s)} \rightarrow {}^{14}N^{15}N_{(g)} + {}^{15}N_{(s)}$$
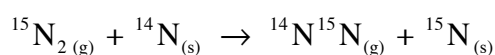
In order to ascertain the exchange route, a complementary isothermal experiment was conducted at 723 K. The experiment shows exchange occurs through the formation of $^{14}N^{15}N$. Here only $^{15}N_2$ gas was introduced into the system and to confirm the route of exchange the concentration of ^{15}N in the gas phase was analysed.

As seen in Figure 4-48 the atomic fraction of ^{15}N in the gas phase is reduced during the reaction, indicating that the nitrogen is taken into the sample. Hence the exchange was shown to proceed via a heteroexchange pathway in the case of Co_3Mo_3N at 723 K.
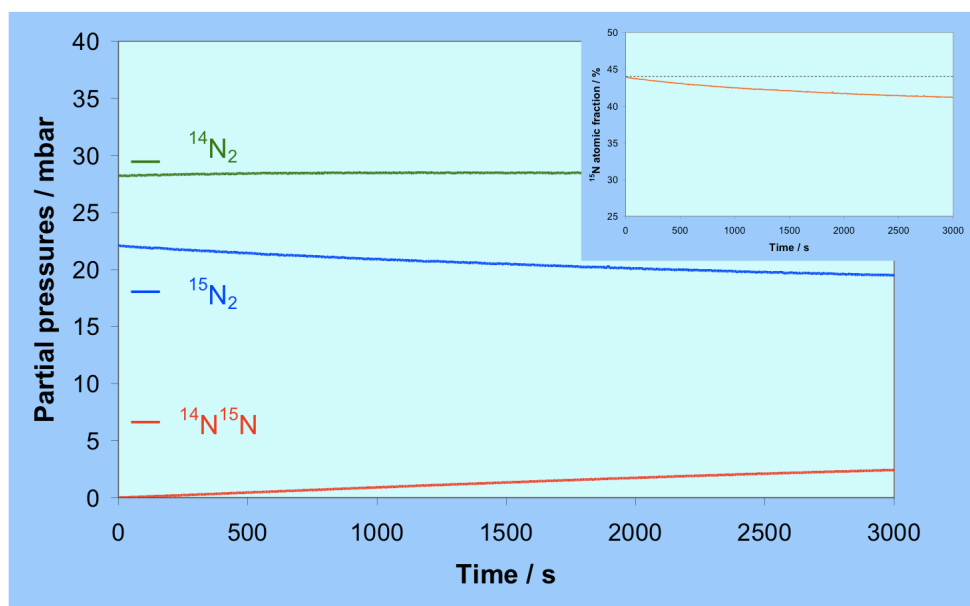
Figure 4-48: Isothermal exchange reaction at 723 K.

Inset shows variation of atomic fraction of ^{15}N.

This result indicates that exchange of nitrogen in Co_3Mo_3N is possible, however as previously proposed, there is surface NH_x species on the Co_3Mo_3N samples.
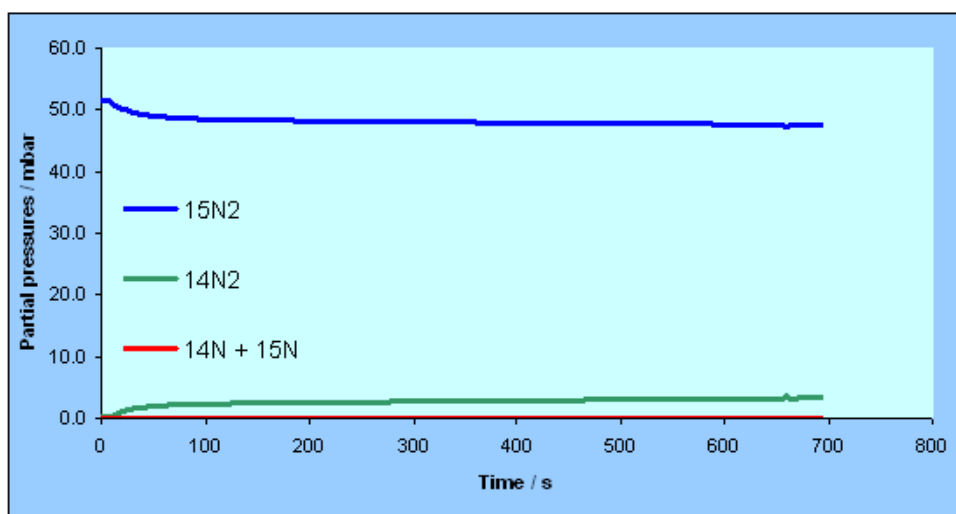
Figure 4-49: Isothermal Exchange reaction at 973 K on an Ar gas purged Co_3Mo_3N sample.

In order to evaluate the exchange possible in the bulk of Co_3Mo_3N, the surface was cleared of NH_x species through an Ar purge of the system at 973 K prior to $^{15}N_2$ being introduced.

The result of the exchange is seen in Figure 4-49, in which $^{15}N_2$ consumption, offset by $^{14}N_2$ production is observed. The level of nitrogen exchange in this purged sample is

less than that observed for in Figure 4-48. After an intial decreased in $^{15}N_2$ partial pressure, the value remains almost constant with time. This indicates that the exchange previously shown is not with the nitrogen in the lattice of the nitride but with the surface NH_x species present during the reaction. This result cannot be correlated to the ammonia testing previously shown as the absence of hydrogen in the feed gas does not allow for nitrogen to be removed from the system and then replaced.

The ability for Co_3Mo_3N to undergo nitrogen exchange is therefore limited under pure N_2 gas, and the exchange observed is with the surface NH_x species. However from the results discussed earlier, Co_6Mo_6N is able to uptake nitrogen very rapidly and thus the exchange of nitrogen with the reduced Co_6Mo_6N phase should be possible under the conditions of the nitrogen exchange experiment. To observe this exchange a pre-treatment stage at 973 K under 3:1 H_2/Ar gas was performed on a Co_3Mo_3N sample for 90 minutes, which was assumed to partially reduce the nitride to a mixed Co_3Mo_3N/Co_6Mo_6N phase. Subsequently, $^{15}N_2$ was introduced to the system at 973 K resulting in a rapid loss in $^{15}N_2$ and formation of $^{14}N^{15}N$ as shown in Figure 4-50. This behaviour is very hard to explain as the overall pressure of the system remains at ~50 mbar. Further analysis and experiments are required to understand the behaviour exhibited by Co_6Mo_6N.
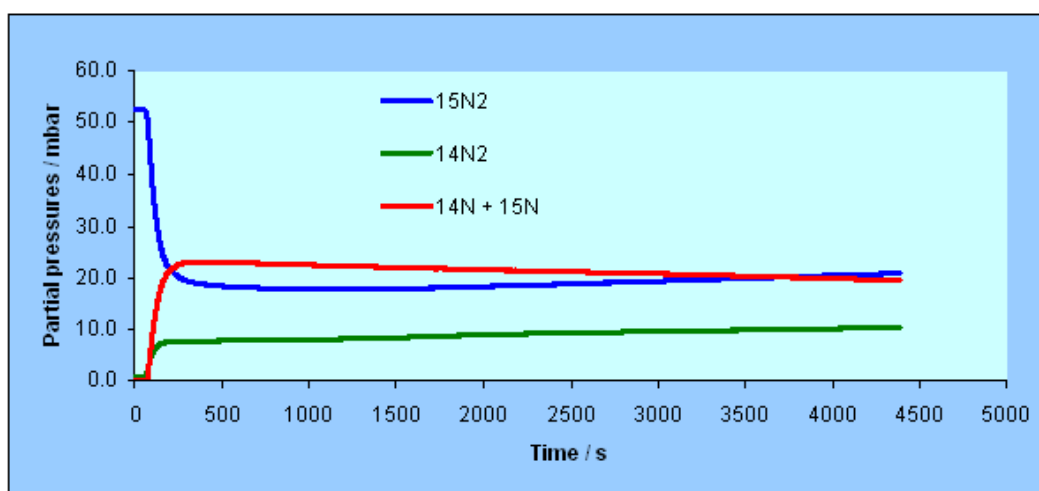
Figure 4-50: Isothermal exchange conducted at 973 K on a partially reduced Co_3Mo_3N sample.

4.4 Summary

This chapter details the Co-Mo-N system both in terms of structural and reactivity studies. The literature had previously dealt in great detail with the structure and activity of Co_3Mo_3N which has been reported to be an effective ammonia synthesis catalyst. Mckay *et al.* had previously proposed a new Co_6Mo_6N phase. This phase was confirmed through the work presented in this thesis. The possibility that Co-Mo-N could be used as a possible "reservoir" of activated nitrogen had not been previously investigated.

Work completed has determined a structure for the new Co_6Mo_6N phase (cubic Fd-3m) and analysis of the crystallographic information has shown that up to 50 % of the nitrogen in Co_3Mo_3N can be released in the presence of hydrogen and the remaining nitrogen migrates within the Mo-N sub-lattice.

N_2 release has been shown in the production of ammonia and nitrogen under 3:1 H_2/Ar gas. The system has been shown to be fully restorable by reaction with 3:1 H_2/N_2 gas and under harsher conditions with pure N_2, which allows even greater possibilities as to the use of Co_3Mo_3N as a store of activated nitrogen. The ability to regenerate the system with nitrogen is economically and environmentally preferred.

Work conducted on the samples showed that the nitride had NH_x species remaining on the surface from the synthesis. These could be be readily removed through treatment with Ar at higher temperatures. However experiments showed that the ability for the nitride to release nitrogen and in turn itself reduce, requires the presence of hydrogen in the gas to create vacancies which can then be restored by nitrogen.

Even with no surface NH_x species Co_3Mo_3N can be seen as a store of nitrogen. Evidence presented in this chapter shows that the nitride retains an ability to produce ammonia, although the amount of ammonia produced is only 30% of that obtainable otherwise.

4.5 References

[1] A. P. Young and C. M. Schwartz; Science; 141 (1963) 348.

[2] A. W. Sleight and B. L. Chamberland; Inorg. Chem.; 7 (1968) 1672.

[3] M. Wiesmann, H. Ehrenberg, G. Wltschek, P. Zinn, H. Weitzel, H. Fuess; J. Magn. Magn. Mater.; 150 (1995) L1.

[4] C. Livage, A. Hynaux, J. Marrot, M. Nogues and G. Férey; J. Mater. Chem.; 12 (2002) 1423.

[5] J.L. Brito, A.L. Barbosa; J. Catal.; 171 (1997) 467.

[6] G. W. Smith and J. A. Ibers; Acta. Cryst.; 19 (1965) 269.

[7] P. Courtine, P. P. Cord, G. Pannetier, J. C. Daumas, R. Montarnal; Bull. Soc. Chim. Fr.; (1968) 4816.

[8] K. Eda, Y. Uno, N. Nagai, N. Sotani, M. S. Whittingham; J. Solid State Chem.; 178 (2005) 2791.

[9] S. Alconchel, F. Sapina, D. Beltrán and A. Beltrán; J. Mater. Chem.; 8 (1998) 1901.

[10] S. K. Jackson, R. C. Layland and H-C. zur Loye; J. Alloys and Comps.; 291 (1999) 94.

[11] J. M. Newsam, A. J. Jacobson, L. E. McCandlish, R. S. Polizzotti; J. Solid State Chem.; 75 (1988) 296.

[12] J. S. J. Hargreaves and D. Mckay; Specialsit Periodical Reports in Catalysis, RSC Cambridge; 19 (2006) 84.

[13] D. Mckay, D. H. Gregory, J. S. J. Hargreaves, S. M. Hunter and X. L. Sun; Chem. Commun.; (2007) 3051.

[14] D. Mckay; Catalysis over Molybdenum Containing Nitride Materials; PhD Thesis; University of Glasgow, 2007.

[15] A. C. Larson and R. B. von Dreele; Generalized Structure Analysis System, MS-H805, Los Alamos, NM 87545 (1990).

[16] B. H. Toby; J. Appl. Crystallogr.; 34 (2001) 210.

[17] R. Kojima and K-I. Aika; *Appl. Catal. A: Gen.*; 215 (2001) 149.

[18] A. Boultif and D. Louer; J. Appl. Cryst.; 37 (2004) 724.

[19] D. S. Bem, C. P. Gibson and H.-C. zur Loye; Chem. Mater.; 5 (1993) 397.

[20] A. Taylor and R. Floyd; Acta Crystallogr.; 3 (1950) 285.

[21] S. H. Elder, L. H. Doerrer, F. J. DiSalvo, J. B. Parise, D. Guyomard and J. M. Tarascon; Chem. Mater.; 4 (2002) 928.

[22] C. F. Baker, M. G. Barker, A. J. Blake, C. Wilson and D. H. Gregory; Dalton Trans.; (2003) 1065.

[23] L. A. Sviridov, P. D. Battle, F. Grandjean, G. J. Long and T. J. Prior; Inorg. Chem.; 49 (2010) 1133.

[24] J-G. Choi, J. Ha and J-W. Hong; Appl. Catal. A: Gen.; 168 (1998) 47.

[25] D. Mckay, J. S. J. Hargreaves, J. L. Rico, J. L. Rivera and X-L. Sun; J. Solid. State. Chem.; 181 (2008) 235.

[26] G. W. Haddix, D. H. Jones, J. A. Reimer and A. T. Bell; J. Catal.; 112 (1988) 556.

[27] Z. Wei, Q. Xin, P. Grange and B. Delmon; J. Catal. 168 (1997) 176.

5   Iron and nickel molybdenum nitrides

5.1   *Introduction*

The reactivity and structure of iron and nickel molybdenum nitrides (M_nMo_3N (M = Fe, n = 3, M = Ni, n = 2)) is discussed fully in this chapter. Iron molybdenum nitride was first synthesised by Bem et al.[1] by ammonolysis of oxide precursor and the nitride was reported to be isostrucutral with η-Fe_3W_3C.[1] It has also been prepared by heating alkanolamine complexed precursors in ammonia[2] or by reaction between Fe–Mo and gaseous N_2 or NH_3.[3]

The structure of Ni_2Mo_3N was determined to be a filled β-manganese type structure by Alconchel et al.[4] Previously, there had been conflicting reports on the structure of the nitride, with it originally being described as of η-carbide type which was indexed to an orthorhombic unit cell.[1] However, Weil and Kumta, who used different synthetic conditions, presented an entirely different diffraction pattern from that previously reported.[5]

In relation to magnetism, ternary nitrides with η-carbide or filled β-manganese structures are some of the most interesting materials reported recently. In these systems, long range magnetic order can be switched on with an appropriate choice of transition metal and valence electron count.[6,7,8]

5.2   *Experimental*

5.2.1   Preparation

5.2.1.1   *Iron molybdenum nitride*

Iron molybdenum oxide was the starting compound for the synthesis of the resultant ternary nitride. The oxide was synthesised through one of two ways:

(i)   Dropwise addition of a 0.25M aqueous solution of iron (III) nitrate ($Fe(NO_3)_3 \cdot 9H_2O$) to a 0.66M solution of sodium molybdate ($Na_2MoO_4 \cdot 2H_2O$).

(ii)   Dropwise addition of 0.25M iron (II) chloride ($FeCl_2 \cdot 2H_2O$) to a 0.66M solution of sodium molybdate ($Na_2MoO_4 \cdot 2H_2O$).

In both cases the resultant precipitate is filtered, washed and dried. The oxides were then calcined under a 60 mLmin^{-1} flow of nitrogen at 773 K before reacting under ammonia following the same procedure as described for the cobalt system (4.2.1).

5.2.1.2   *Nickel molybdenum nitride*

Ternary nickel compounds were synthesised from nickel molybdate through dropwise addition of 0.25M solution of nickel nitrate (Ni(NO$_3$)$_2$·6H$_2$O) to a 0.66M solution of sodium molybdate (Na$_2$MoO$_4$·2H$_2$O). The resulting solution was heated to around 323 K in order to aid the crystallisation of the molybdate. The oxide was reacted with a 3:1 H$_2$/N$_2$ gas mixture at a flow rate of 60 mLmin^{-1} at 973 K for three hours to form the nitride.

5.2.2   Characterisation

Powder X-ray diffraction (PXRD) data were collected for the samples after nitridation. Data collection was conducted at room temperature on a Siemens D5000 diffractometer, utilising Cu-K$_\alpha$ radiation. The samples were prepared as previously described in Section 2.4.1.1. The patterns were collected using a step scan of 0.02 °2θ over a 5 – 85 °2θ range and a time per step of 0.8 seconds. Diffraction data used for Rietveld refinements employed step times and ranges of 11 seconds and 5 – 105 °2θ respectively.

In addition to the X-ray data, powder neutron diffraction (PND) data were collected on the POLARIS instrument at ISIS. Experiments were performed on the samples at room temperature and base temperature (4.2 K) using three banks of detectors. Samples were loaded into vanadium sample cans, to a maximum height of 40 mm. Data were collected for approximately three hours in each case. For the variable temperature experiments, a special *in-situ* stainless steel cell was employed, that had a collimator around the sample which only allowed the 90° bank of detectors to be used. This is described in more detail in Section 2.4.1.2.1.

To probe the dehydration stages of the molybdate precursors, thermal analysis was performed on the hydrated molybdate samples using a TA Instruments Q500 TGA. In a typical experiment, 20 – 50 mg of sample was loaded onto a pan balance and then heated at 1 K per minute. The temperature was held for 30 minutes to ensure any thermal events had occurred before cooling back to room temperature. Measurements were completed under a flow of air to mimic conditions of calcination.

CHN (Carbon, Hydrogen and Nitrogen) analysis was performed using a CE-440 elemental analyser. Analysis was conducted via combustion of samples under pure oxygen. The combustion products were carried through the system by helium gas and the mixture was analysed using high-precision thermal conductivity detection.

5.2.3   Activity testing

The samples were tested at ambient pressure for their activity as ammonia synthesis catalysts. The method employed used a fixed bed reactor through which reactant gas (60 mLmin^{-1}) of either 3:1 H_2/N_2 gas or 3:1 H_2/Ar gas was flowed. The production of ammonia was measured by the change in conductivity of a 200 mL, 0.00108 molL^{-1} sulfuric acid solution.

The reactions were conducted on 0.4 g of sample which was pre-treated at 973 K under 3:1 H_2/N_2 gas for two hours prior to the reaction being started. The reactions were conducted under either 3:1 H_2/N_2 gas at 673 K or 3:1 H_2/Ar gas during which a variable temperature profile was employed.

5.3   Results and discussion

5.3.1   Iron molybdate precursor

The preparative method was found to be very important in the formation of iron molybdate; the formation of ferrous molybdate ($FeMoO_4$) from the iron (III) nitrate involved a change in the oxidation state of the iron from +3 to +2 in the resultant molybdate; however when using iron (II) chloride there was no change in oxidation state of the iron in the transformation to the molybdate.

Prior to calcination, a non-crystalline pattern was collected for samples prepared from both of routes (i) and (ii) in Section 5.2.1.1. However post calcination at 773 K, the pattern can be matched to known molybdate phases. The PXRD pattern of the molybdate formed through the use of iron nitrate gives a mixed phase product of both ferrous molybdate ($FeMoO_4$) and ferric molybdate ($Fe_2(MoO_4)_3$), which is shown in Figure 5-1. The PXRD pattern (Figure 5-2) of the molybdate formed using iron (II) chloride gives single phase ferrous molybdate, $FeMoO_4$.
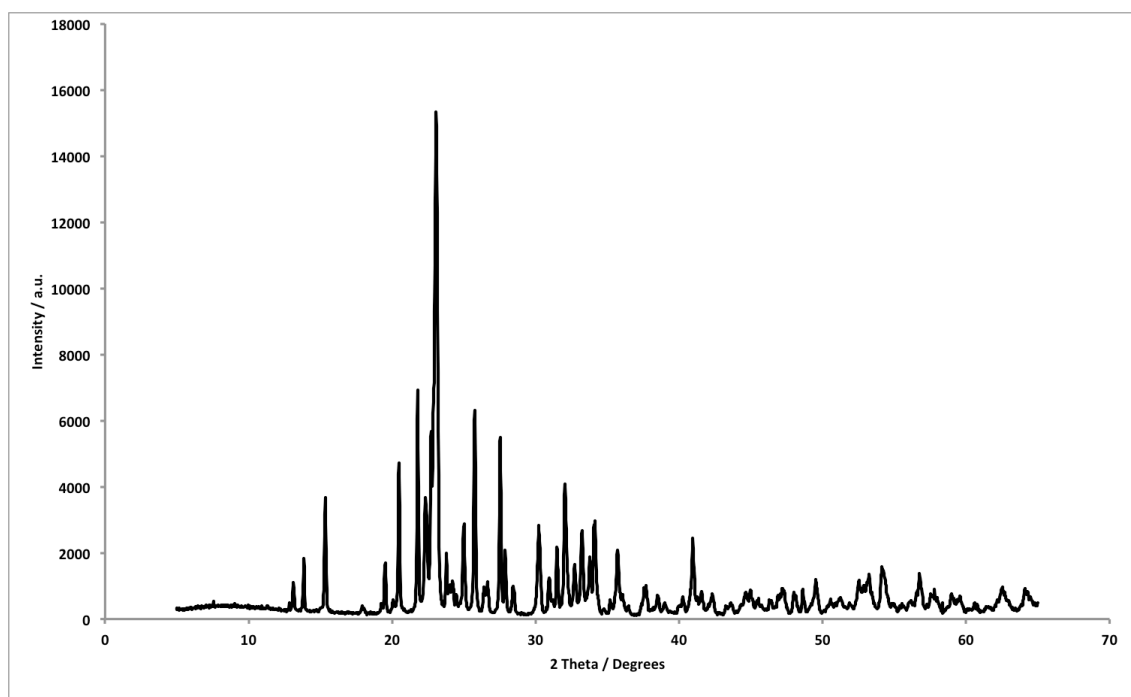
Figure 5-1: PXRD pattern of iron molybdate formed via iron nitrate solution.
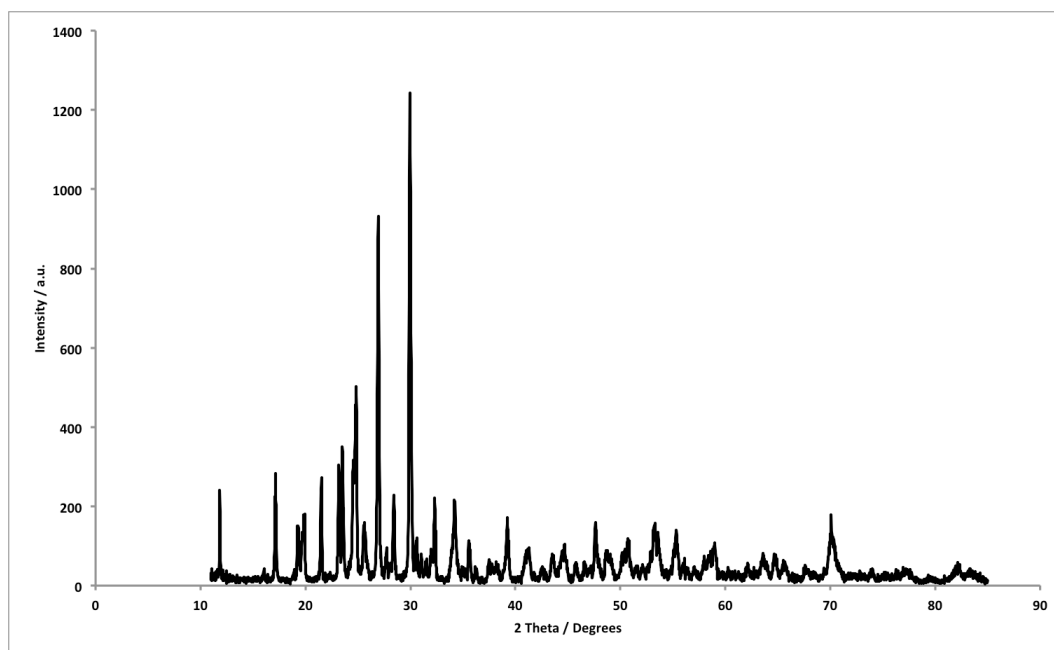
Figure 5-2: PXRD pattern of iron molybdate formed via iron chloride solution.

The results of TGA (plot not shown here) show that there was a total weight loss of 12.56 % which is equivalent to 1.72 moles of water which would give a stoichiometry of $FeMoO_4·1.72H_2O$ for the precursor. The nature of the water could not be easily determined due to the TGA trace showing no distinct transition areas, therefore the amount of water co-ordinated to the iron molybdate is not possible to be confirmed.

5.3.2 Iron molybdenum nitride (Fe$_3$Mo$_3$N)

5.3.2.1 Nitride synthesis and characterisation

The iron molybdates (formed via both routes, as previously described) were nitrided using ammonia at 1058 K followed by a pre-treatment stage under 3:1 H$_2$/N$_2$ gas at 973 K. This was related to the preparative route used in the formation of cobalt molybdenum nitride.

Initial experiments were performed on molybdate mixtures prepared from iron (II) nitrate. Figure 5-3 presents the resultant PXRD pattern following nitridation.
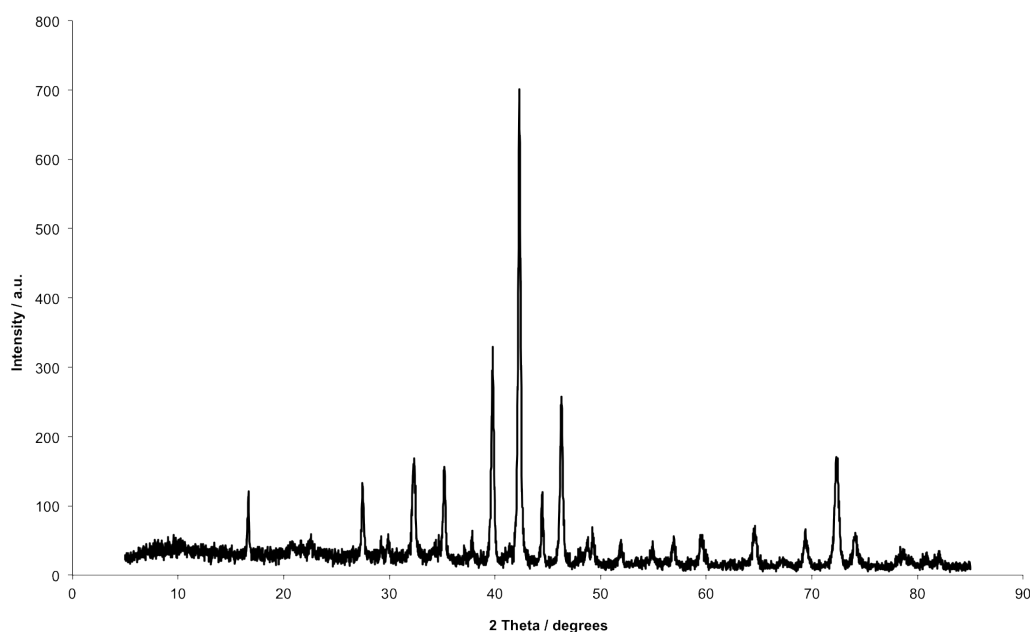
Figure 5-3: PXRD pattern of Fe$_3$Mo$_3$N synthesised via iron nitrate.

The pattern contains reflections which can be related to both Fe$_3$Mo$_3$N and γ-Mo$_2$N. The sets of reflections were indexed and lattice parameters of $a = 11.091(3)$ Å and $a = 4.161(2)$ Å were found for Fe$_3$Mo$_3$N and γ-Mo$_2$N respectively. Both were in good agreement to the literature values for the ternary[9] and binary nitrides detailed previously in Section 3.3.2.

On the basis of the indexing, it has been possible to refine the literature model against the PXRD data collected using GSAS and EXPGUI. Refinement against PXRD data was performed for samples by first fitting the background to a shifted Chebyschev function (background function 1 in GSAS). Once the background was fitted, the lattice parameters were then refined followed by the atomic positions which once stable,

allowed the peak shape to be refined. When the refinement had again stabilised, the thermal parameters were varied isotropically. Results of the refinement are shown in Table 5-1, Table 5-2 and Figure 5-4 which indicate that there is a good correlation between the observed and calculated pattern of Fe_3Mo_3N.

Table 5-1: Crystallographic parameters for Fe_3Mo_3N PXRD data synthesised via iron nitrate.

Parameter	Value
Formula	Fe_3Mo_3N
Crystal system	Cubic
Space group	Fd-3m
Formula mass / $gmol^{-1}$	7509.888
Cell parameter, a / Å	11.0546(11)
Unit-cell volume / $Å^3$	1350.90(24)
Calculated density ρ_x / gcm^{-3}	9.231
Number of observations	4099
Number of variables	20
R_p / %	20.21
R_{wp} / %	27.87
χ^2	2.273

Table 5-2: Refined atomic parameters for Fe_3Mo_3N synthesised via iron nitrate from PXRD data.

Atoms / Site	x	y	z	Occupancy	$100\times$ U_{iso} /U_{eq} ($Å^2$)
Fe 1 (32e)	0.2952(5)	0.2952(5)	0.2952(5)	1.00	0.40(12)
Fe 2 (16d)	0.5000	0.5000	0.5000	1.00	1.29(28)
Mo (48f)	0.3242(4)	0.1250	0.1250	1.00	3.27(57)
N (16c)	0.0000	0.0000	0.0000	1.00	1.50‡

‡ - parameters fixed
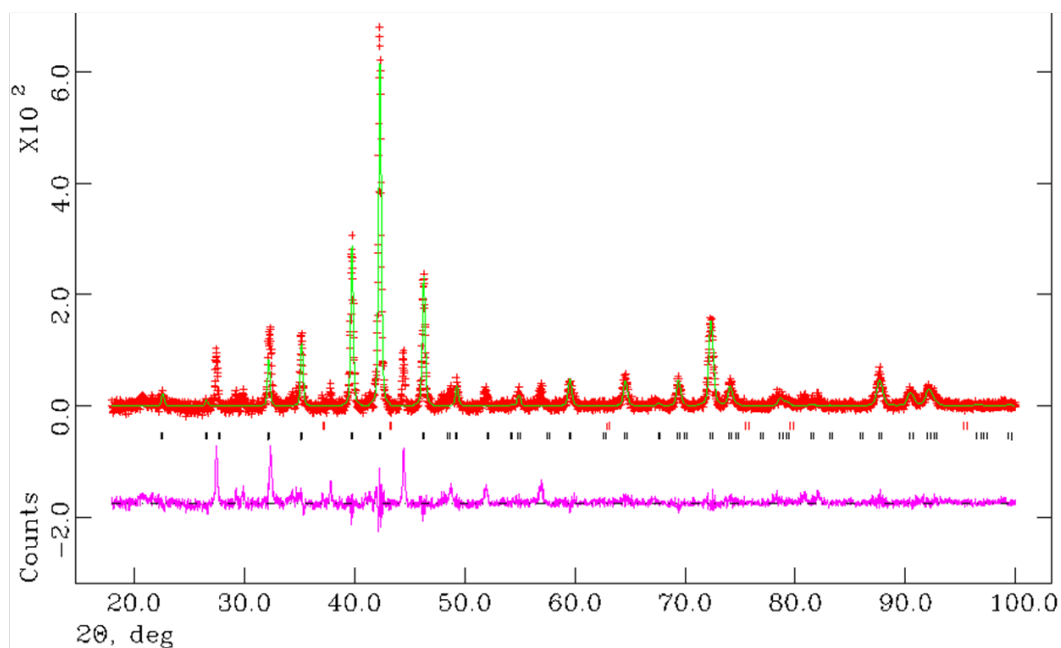
Figure 5-4: Final profile fit obtained from the refinement against PND data for Fe₃Mo₃N synthesised from iron (II) nitrate.

The observed data are crosses, the calculated profile the solid line and lower continuous line the difference plot. Tick marks show allowed reflection positions. Red Tick-marks – γ-Mo$_2$N$_{0.8}$, Black tick-marks – Fe$_3$Mo$_3$N.

The refined models are in good agreement with those reported for the two phases in the literature. The iron molybdenum nitride crystallises in cubic space group Fd-3m (using origin setting 2) as was found to be the case for the corresponding Co$_3$Mo$_3$N system. The molybdenum nitride crystallises in cubic space group, Fm-3m. The refinement indicated that the Fe$_3$Mo$_3$N was not the only product of the reaction; the expected γ-Mo$_2$N could not be refined along with the ternary nitride.

The microanalysis results for the nitride however indicated that there was only 3.0(2) wt% of nitrogen present in the sample. This result is close to the theoretical value of 2.98 wt% for pure Fe$_3$Mo$_3$N. The amount of γ-Mo$_2$N present in the sample was unable to be obtained from the refinement due to the poor data. For example a sample containing a ratio of 80:20 Fe$_3$Mo$_3$N:Mo$_2$N would have a nitrogen content of 3.36 wt%. PND experiments were performed on the same sample. The structures from the PXRD refinement were used as the starting model. The background was fitted to a reciprocal interpolation function (background function 8 in GSAS). In addition to the parameters refined during the PXRD refinement, absorption factors were also varied. The results of

the refinement are shown in Table 5-3, Table 5-4 and Figure 5-5. The data collected from the PND experiments are in good agreement with the PXRD fits.

Table 5-3: Crystallographic parameters for Fe$_3$Mo$_3$N from PND data.

Parameter	Value
Formula	Fe$_3$Mo$_3$N
Crystal system	Cubic
Space group	Fd-3m
Formula mass / gmol^{-1}	7494.889
Phase Fraction	70.5
Cell parameter, a / Å	11.09099(15)
Unit-cell volume / Å^3	1364.305(33)
Calculated density ρ_x / gcm^{-3}	9.142
Formula	γ-Mo$_2$N
Crystal system	Cubic
Space group	Fm-3m
Formula mass / gmol^{-1}	406.767
Phase Fraction	29.5
Cell parameter, a / Å	4.1596(5)
Unit-cell volume / Å^3	71.973(16)
Calculated density ρ_x / gcm^{-3}	9.388
Number of observations	4426
Number of variables	35
R$_p$ / %	4.61
R$_{wp}$ / %	2.98
χ^2	1.132

Table 5-4: Refined atomic parameters for Fe₃Mo₃N and γ-Mo₂N from PND data.

Fe$_3$Mo$_3$N

Atoms / Site	x	y	z	Occupancy	100× U_{iso}/U_{eq} (Å^2)
Fe 1 (32e)	0.29364(7)	0.29364(7)	0.29364(7)	1.00	0.41*
Fe 2 (16d)	0.500000	0.500000	0.500000	1.00	0.46*
Mo (48f)	0.3221(1)	0.125000	0.125000	1.00	0.39*
N (16c)	0.000000	0.000000	0.000000	0.933(8)	0.48*

* = Anisotropically measured – expansion is shown here:

Atoms	U_{11} (Å^2)	U_{22} (Å^2)	U_{33} (Å^2)	U_{12} (Å^2)	U_{13} (Å^2)	U_{23} (Å^2)
Fe 1	0.456(32)	0.456(32)	0.456(32)	-0.017(25)	-0.017(25)	-0.017(25)
Fe 2	0.386(28)	0.386(28)	0.386(28)	0.075(37)	0.075(37)	0.075(37)
Mo	0.47(6)	0.37(4)	0.37(4)	0.00	0.00	0.08(5)
N	0.48(5)	0.48(5)	0.48(5)	0.02(5)	0.02(5)	0.02(5)

γ-Mo$_2$N$_{0.8}$

Atoms / Site	x	y	z	Occupancy	100× U_{iso}/U_{eq} (Å^2)
Mo (4a)	0.000000	0.000000	0.000000	1.00	1.00
N (4b)	0.500000	0.500000	0.500000	0.41(2)	0.9(2)
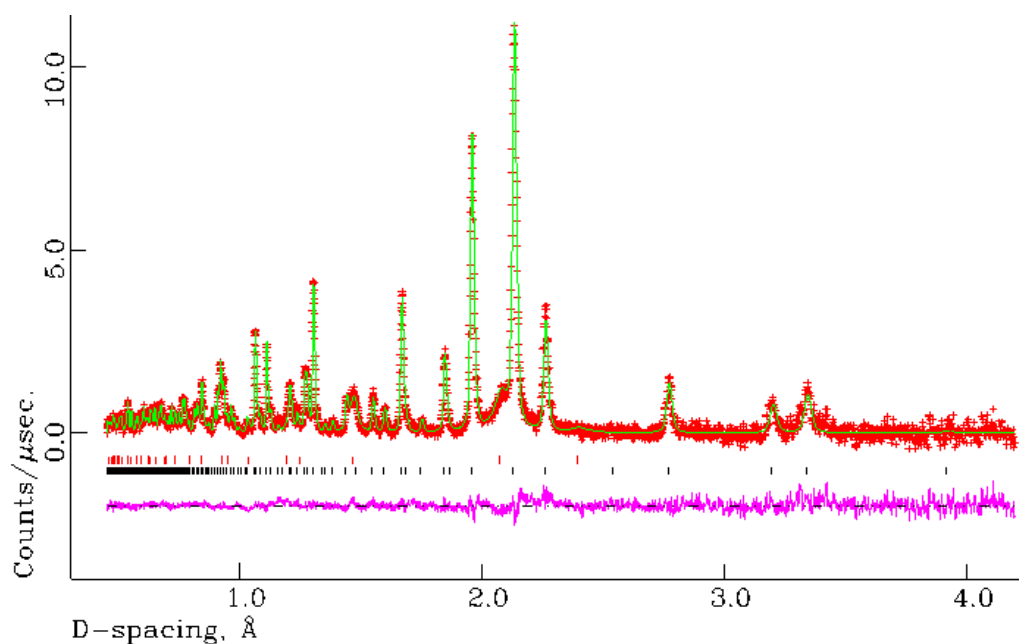
Figure 5-5: Final profile fit obtained from the refinement against PND data for Fe₃Mo₃N synthesised from iron (II) nitrate.

The observed data are crosses, the calculated profile the solid line and lower continuous line the difference plot. Tick marks show allowed reflection positions.
Red tick-marks – γ-Mo₂N₀.₈, Black tick-marks – Fe₃Mo₃N

A sample of iron molybdenum nitride was prepared via iron (II) chloride and sodium molybdate as described in Section 5.2.1.1. This method produced a single phase sample which was analysed by PXRD and indexed to yield lattice parameters of $a = 11.069(5)$ Å. (Figure 5-6).
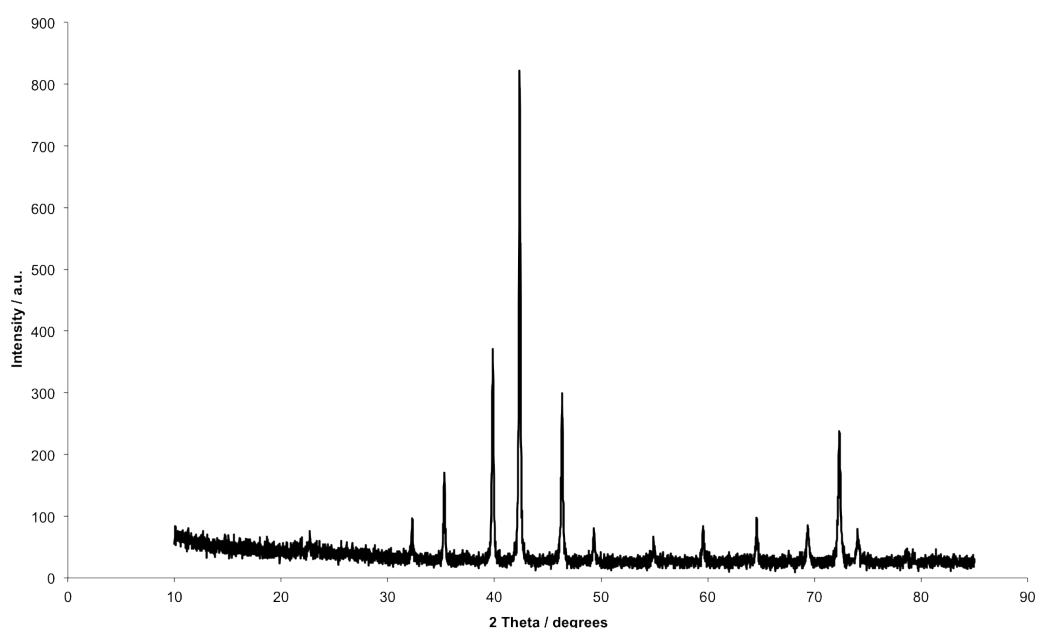
Figure 5-6: PXRD pattern of Fe₃Mo₃N prepared via iron (II) chloride.

CHN microanalysis for this sample gave a value of 2.94(5) wt% nitrogen which is in good agreement to the theoretical value of 2.98 wt% for Fe_3Mo_3N. In order to confirm the resultant structure and phase purity, a refinement against PXRD data was undertaken with the starting model for the refinement taken from the PND structure. The results of the refinement are presented in Table 5-5, Table 5-6 and Figure 5-7.

Table 5-5: Crystallographic parameters for Fe_3Mo_3N synthesised from iron (II) chloride for PXRD data.

Parameter	Value
Formula	Fe_3Mo_3N
Crystal system	Cubic
Space group	Fd-3m
Formula mass / $gmol^{-1}$	7577.579
Cell parameter, a / Å	11.0767(28)
Unit-cell volume / $Å^3$	1359.1(6)
Calculated density ρ_x / gcm^{-3}	9.259
Number of observations	4189
Number of variables	24
R_p / %	15.22
R_{wp} / %	19.05
χ^2	1.356

Table 5-6: Refined atomic parameters for Fe_3Mo_3N synthesised from iron (II) chloride from PXRD data.

Atoms / Site	x	y	z	Occupancy	$100 \times$ U_{iso}/U_{eq} $(Å^2)$
Fe 1 (32e)	0.2938(4)	0.2938(4)	0.2938(4)	1.00	0.82(34)
Fe 2 (16d)	0.500000	0.500000	0.500000	1.00	1.35(50)
Mo (48f)	0.3212(4)	0.125000	0.125000	1.00	0.88(15)
N (16c)	0.000000	0.000000	0.000000	1.00	1.23(4)
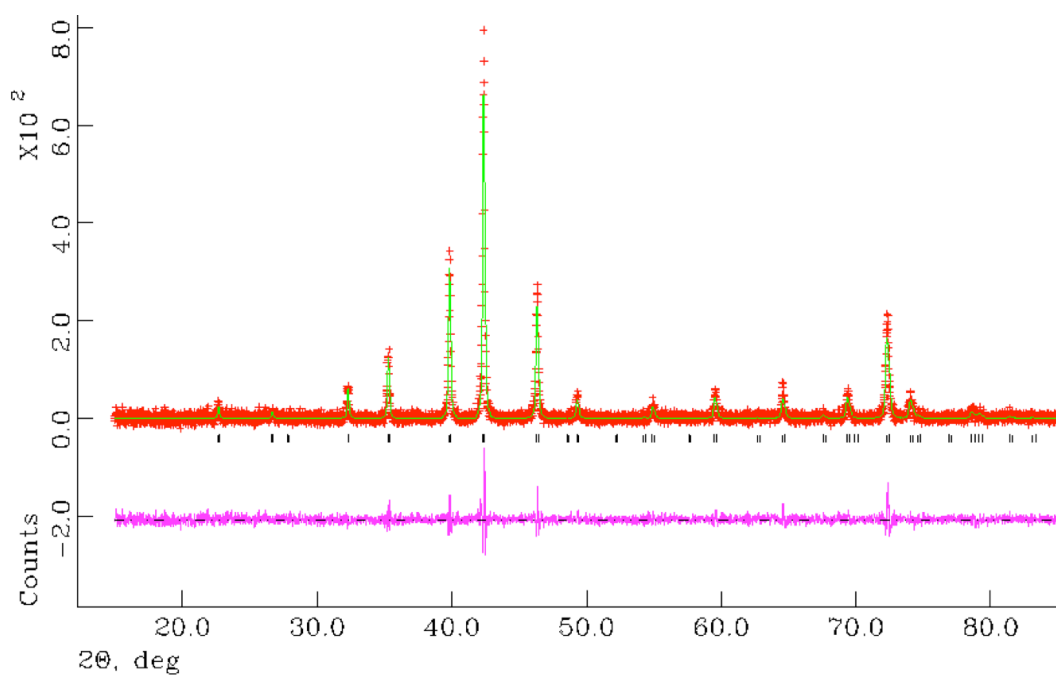
Figure 5-7: Final profile fit obtained from the refinement against PXRD data for Fe$_3$Mo$_3$N.

The observed data are crosses, the calculated profile the solid line and lower continuous line the difference plot. Tick marks show allowed reflection positions.

Ex-situ PND data were collected and a structural refinement was performed using the PXRD model as the starting model. The results of the refinement are shown in Table 5-7, Table 5-8 and Figure 5-8.

Table 5-7: Crystallographic parameters for Fe₃Mo₃N synthesised from iron (II) chloride for PND data collected at room temperature.

Parameter	Value
Formula	Fe_3Mo_3N
Crystal system	Cubic
Space group	Fd-3m
Formula mass / $gmol^{-1}$	7504.486
Cell parameter, a / Å	11.06788(9)
Unit-cell volume / $Å^3$	1355.79(2)
Calculated density ρ_x / gcm^{-3}	9.191
Number of observations	7878
Number of variables	45
R_p / %	3.08
R_{wp} / %	1.85
χ^2	1.477

Table 5-8: Refined atomic parameters for Fe₃Mo₃N from PND data.

Atoms / Site	x	y	z	Occupancy	$100\times$ U_{iso}/U_{eq} ($Å^2$)
Fe 1 (32e)	0.29382(2)	0.29382(2)	0.29382(2)	1.00	0.36*
Fe 2 (16d)	0.500000	0.500000	0.500000	1.00	0.42*
Mo (48f)	0.32175(3)	0.125000	0.125000	1.00	0.49*
N (16c)	0.000000	0.000000	0.000000	0.976(2)	0.41*

* = Anisotropically measured – expansion is shown here:

Atoms	U_{11} ($Å^2$)	U_{22} ($Å^2$)	U_{33} ($Å^2$)	U_{12} ($Å^2$)	U_{13} ($Å^2$)	U_{23} ($Å^2$)
Fe 1	0.424(6)	0.424(6)	0.424(6)	-0.018(5)	-0.018(5)	-0.018(5)
Fe 2	0.489(6)	0.489(6)	0.489(6)	-0.025(8)	-0.025(8)	-0.025(8)
Mo	0.454(11)	0.316(7)	0.316(7)	0.00	0.00	0.009(9)
N	0.407(9)	0.407(9)	0.407(9)	-0.002(8)	-0.002(8)	-0.002(8)
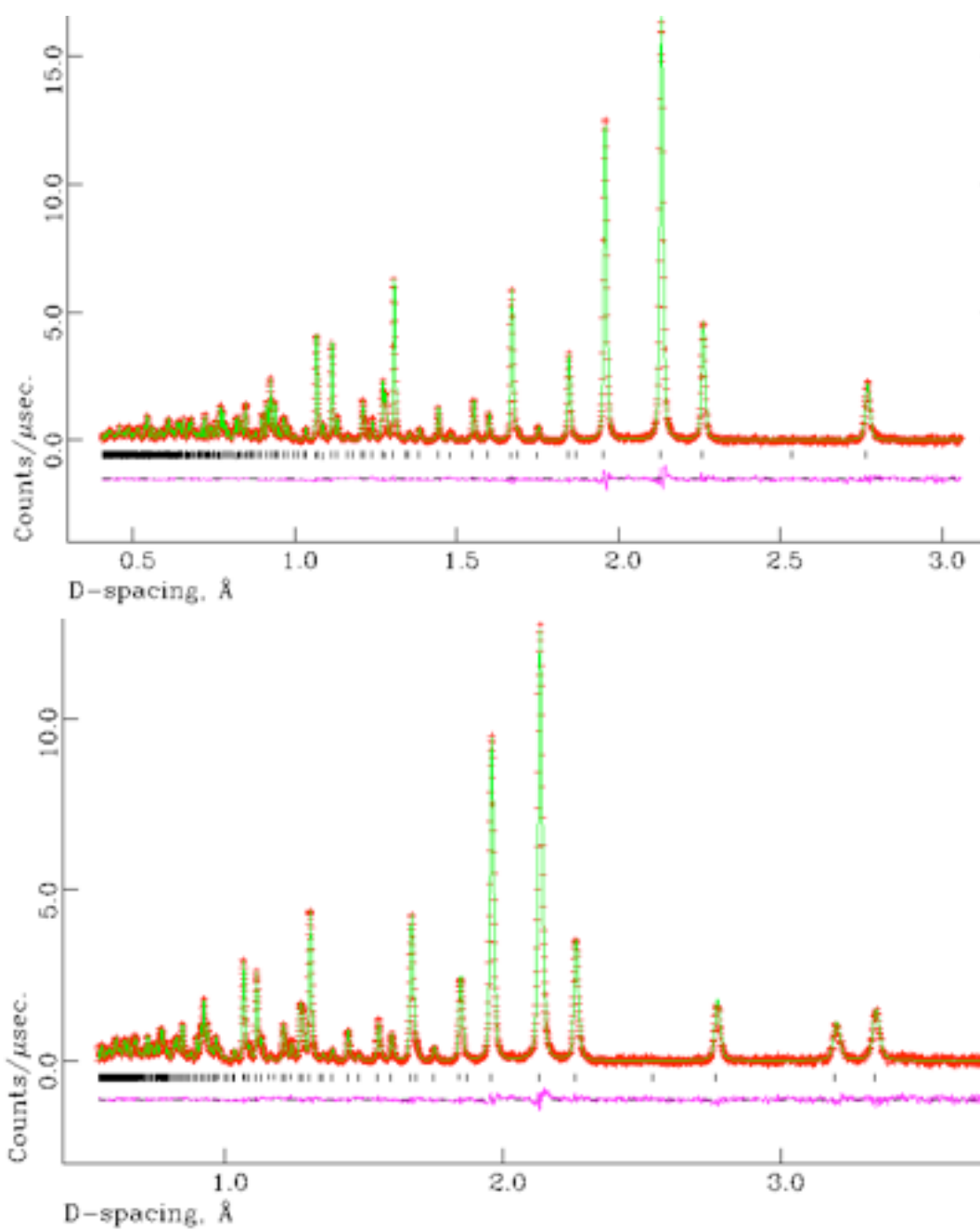
Figure 5-8: Final profile fit obtained from the refinement against PND data for Fe$_3$Mo$_3$N.

The observed data are crosses, the calculated profile the solid line and lower
continuous line the difference plot. Tick marks show allowed reflection positions.
Top – Backscattering detector bank <2θ> = 145°, Bottom - 90° detector bank.

The crystallographic information obtained for the 331 phase from the single phase sample agrees well with that obtained from the Fe_3Mo_3N/γ-Mo_2N mixed sample, with the iron molybdenum nitride crystallising with the η–carbide structure in which the 16c site is occupied wholly by nitrogen as observed in the analogous cobalt compound (Section 4.3.2.1). The interatomic distances and angles obtained from the refinement of the single phase sample are shown in Table 5-9.

Table 5-9: Selected Interatomic Distances and Bond Angles for Fe_3Mo_3N from PXRD and PND data.

	PXRD	PND
Atomic Distance (Å)		
N – Mo ×6	2.1113(17)	2.1110(18)
Mo – Mo ×4	2.8942(19)	2.8946(20)
Mo – Mo ×4	3.075(6)	3.073(7)
Fe(1) – Mo ×3	2.661(6)	2.661(7)
Fe(1) – Mo ×3	2.773(4)	2.774(4)
Fe(1) – Fe(1) ×3	2.546(14)	2.545(14)
Fe(1) – Fe(2) ×3	2.3852(27)	2.3851(27)
Fe(2) – Mo ×6	2.7844(32)	2.7851(33)
Fe(2) – Fe(1) ×6	2.3852(27)	2.3851(27)
Bond Angle (°)		
N – Mo – N	136.08(23)	136.12(23)
Mo – N – Mo ×6	93.47(16)	93.43(16)
Mo – N – Mo ×6	86.53(16)	86.57(16)
Mo – N – Mo ×3	180.0	180.0

The Mo and N sub-lattice, shown in Figure 5-9 is similar to that seen for Co_3Mo_3N with bond lengths shown above in Table 5-9. The individual atomic coordination environments for Fe(1), Fe(2), Mo and N are shown in Figure 5-10 and Figure 5-11. These show that there is a distorted arrangement of the atoms as in Co_3Mo_3N.
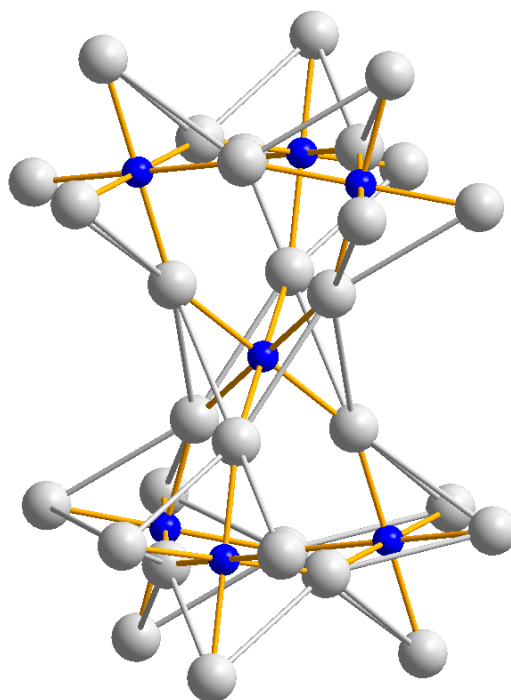
Figure 5-9: Mo-N sublattice in Fe₃Mo₃N.

Mo - silver spheres, N – blue spheres.
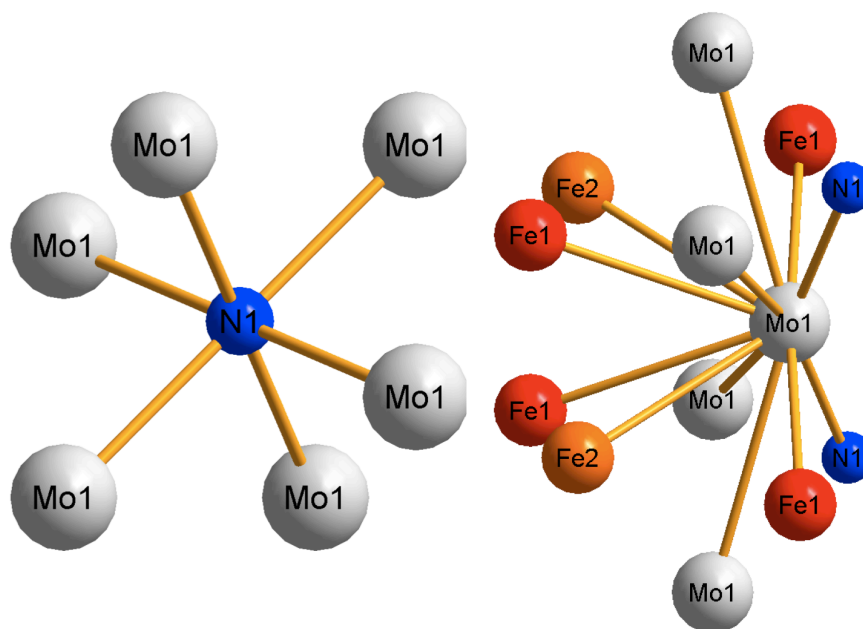
Figure 5-10: Co-ordination geometry at N (16c) site and Mo (48f) site.
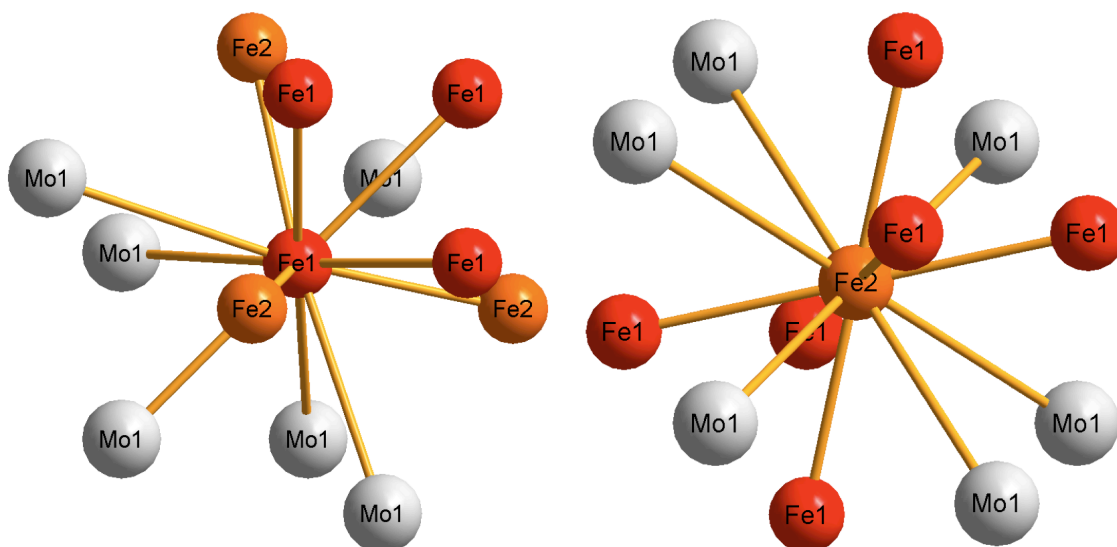
Figure 5-11: Co-ordination environment at Fe1 (32e) site and Fe2 (16d) site.

5.3.2.2 Activity Study

The ambient pressure ammonia synthesis efficacy of Fe_3Mo_3N had previously been studied by Mckay who demonstrated that Fe_3Mo_3N was active for ammonia production at 673 K. However it would be expected that the presence of γ-Mo_2N - known to be a good ammonia synthesis catalyst - in the tested sample would almost certainly have an effect on the ammonia production efficacy. Therefore reactivity tests were undertaken on the single phase Fe_3Mo_3N material only. Ammonia synthesis testing was conducted at 673 K for 330 mins under 3:1 H_2/N_2 gas and results are shown in Figure 5-12.
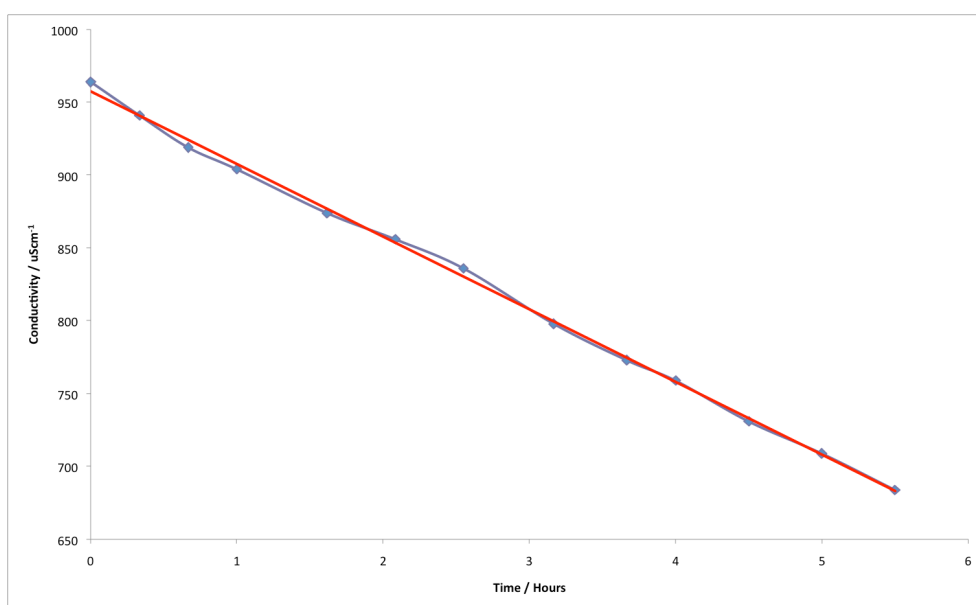
Figure 5-12: Reaction profile for Fe₃Mo₃N under 3:1 H₂/N₂ gas at 673 K.

The profile demonstrates steady state ammonia production. The mass normalised rate was 91 $\mu molh^{-1}g^{-1}$. This is in good agreement with the work of Mckay, although it is lower than that seen for Co_3Mo_3N which gave a mass normalised rate of 136 $\mu molh^{-1}g^{-1}$. The reaction had no overall effect on the nitrogen composition of the nitride sample, the post-reaction microanalysis result for the sample was 2.96(6) wt%.
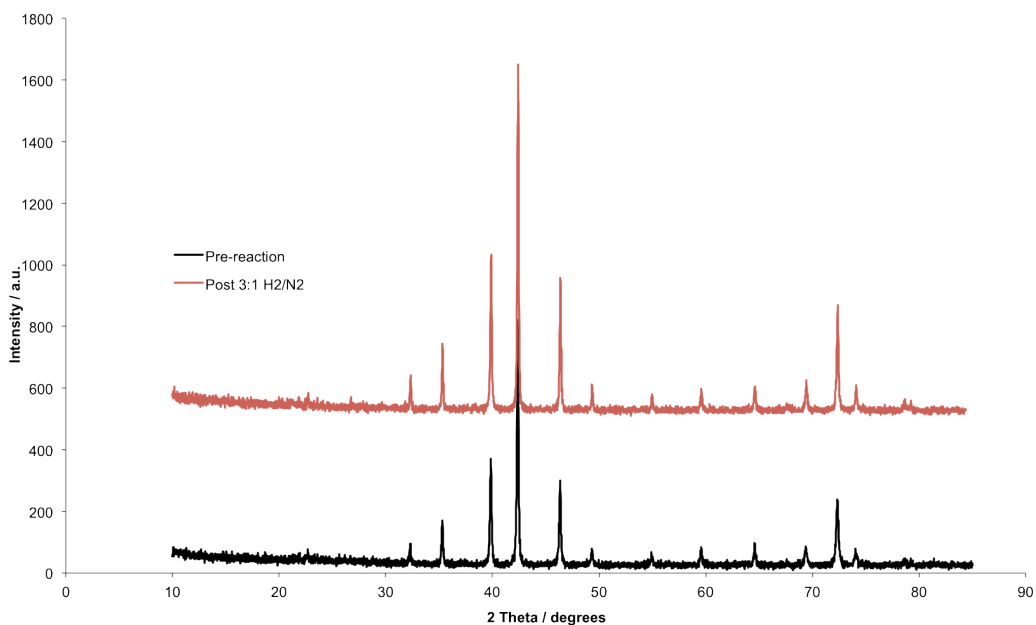
Figure 5-13: Post reaction PXRD pattern for Fe$_3$Mo$_3$N under 3:1 H$_2$/N$_2$ gas.

Pre-reaction PXRD pattern in Black, Post-reaction PXRD pattern in red.

The post-reaction PXRD analysis shows no change in the structure of the sample and the pattern can be indexed to give $a = 11.0724(5)$ Å compared to $a = 11.0767(3)$ Å prior to reaction.

The surface area of the Fe_3Mo_3N sample was 8 m^2g^{-1}, which is approximately half that of the Co_3Mo_3N samples in Section 4.3.2.2. However it must be borne in mind that the surface area measurements are collected on air sensitive samples that had been exposed to the atmosphere.

In order to investigate the lability of the lattice nitrogen, the samples were tested under 3:1 H$_2$/Ar gas. The reaction profile seen in Figure 5-14 shows that, as with the cobalt system, there is a decrease in the conductivity upon reaction at 673 K, which then ceases after an extended period on stream (180 mins). Once the reaction temperature is increased the conductivity decreases further.
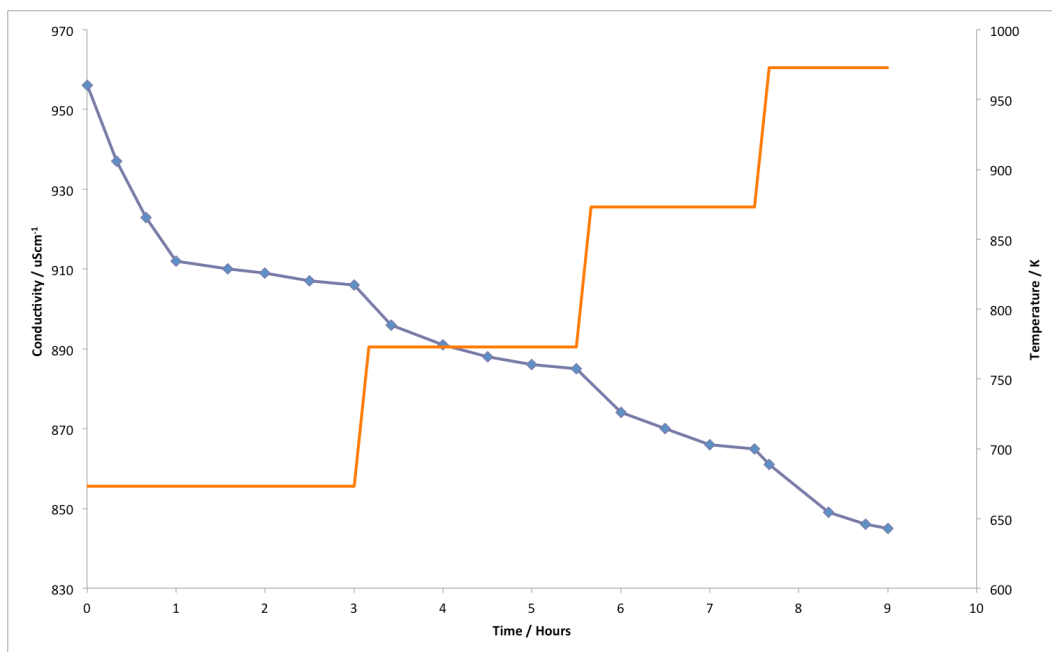
Figure 5-14: Reaction profile for Fe$_3$Mo$_3$N under 3:1 H$_2$/Ar gas.

The total reduction in conductivity over the course of the temperature programmed reaction is similar to that seen in the cobalt system (Section 4.2.3). However in stark contrast to the cobalt system the post-reaction PXRD (Figure 5-15) and microanalysis results show no change in the structure or nitrogen composition. Microanalysis results giving a value of 2.89(5) wt% nitrogen, which indicated that no nitrogen is removed from the sample.
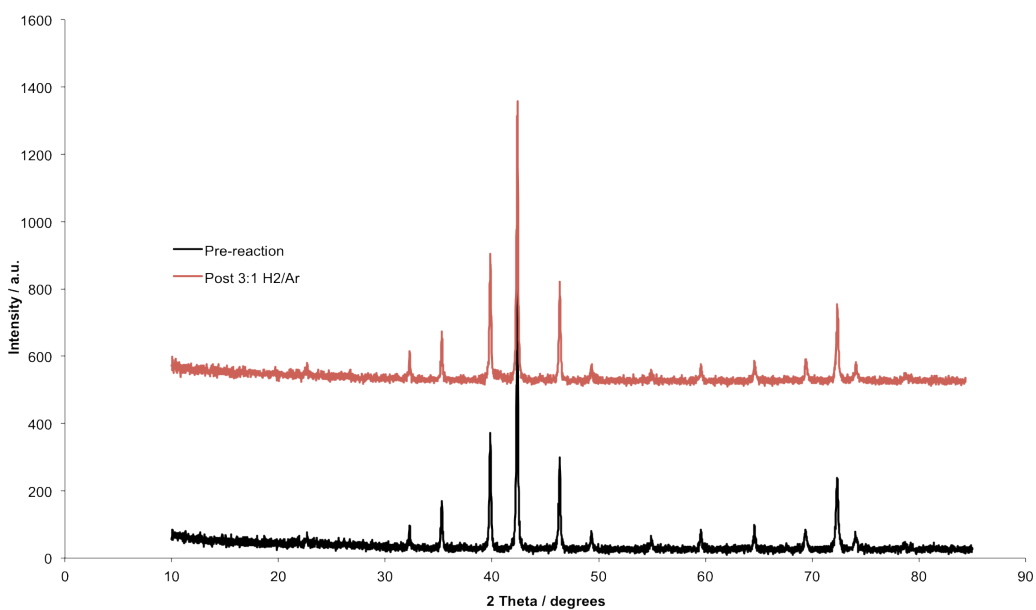
Figure 5-15: Post reaction PXRD pattern for Fe$_3$Mo$_3$N under 3:1 H$_2$/Ar gas.

Pre-reaction PXRD pattern in Black, Post-reaction PXRD pattern in red.

5.3.2.3   Further structural study

Work previously conducted on iron molybdenum nitride samples by Mckay (containing an impurity γ-Mo$_2$N phase) showed that there was a 22 % reduction in the nitrogen content post-reaction with 3:1 H$_2$/Ar gas at 973 K.[10] This was attributed to the partial reduction of γ-Mo$_2$N to Mo metal.

An *in-situ* PND experiment was undertaken on the mixed phase sample, in order to understand the processes which the ternary nitride undergoes during the testing procedure. The material was exposed to an analogous heating regime to that employed for the cobalt system as shown in Section 4.3.2.3

The first stage of the *in-situ* experiment between 290 and 973 K under 3:1 H$_2$/N$_2$ gas, mimicked the standard ammonia synthesis testing procedure. This also removed any surface oxides present on the sample.
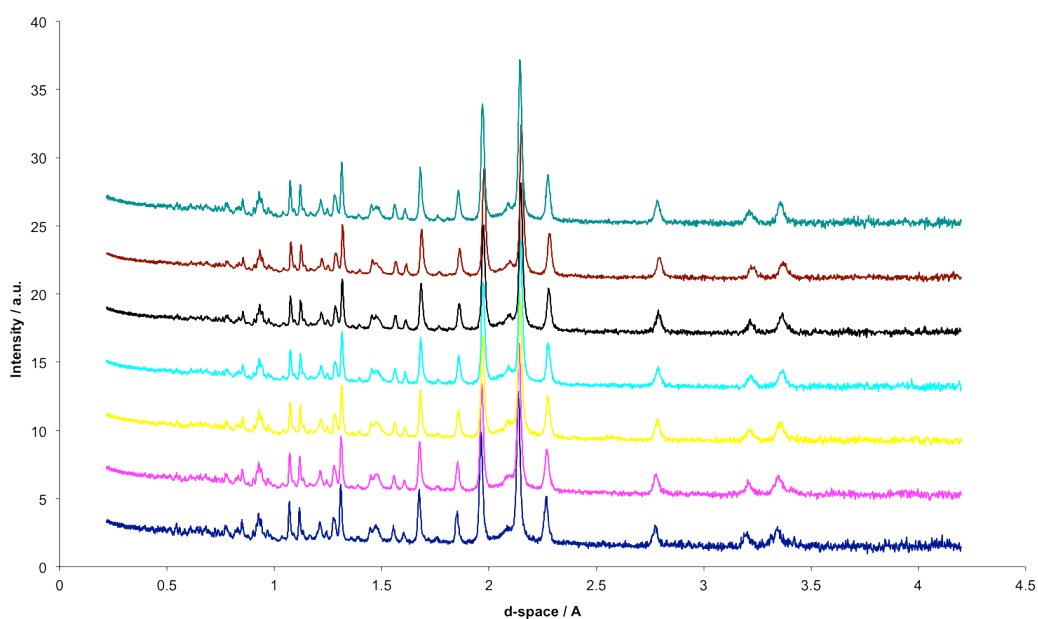
Figure 5-16: PND data for the first stage of *in-situ* experiment.

The diffraction patterns taken during the initial 3:1 H$_2$/N$_2$ gas treatment of the reaction showed no change in the structure of the sample as shown in Figure 5-16. However thermal expansion effects were evident as shown in Figure 5-17. The only phases observed during this procedure were Fe$_3$Mo$_3$N and γ-Mo$_2$N.
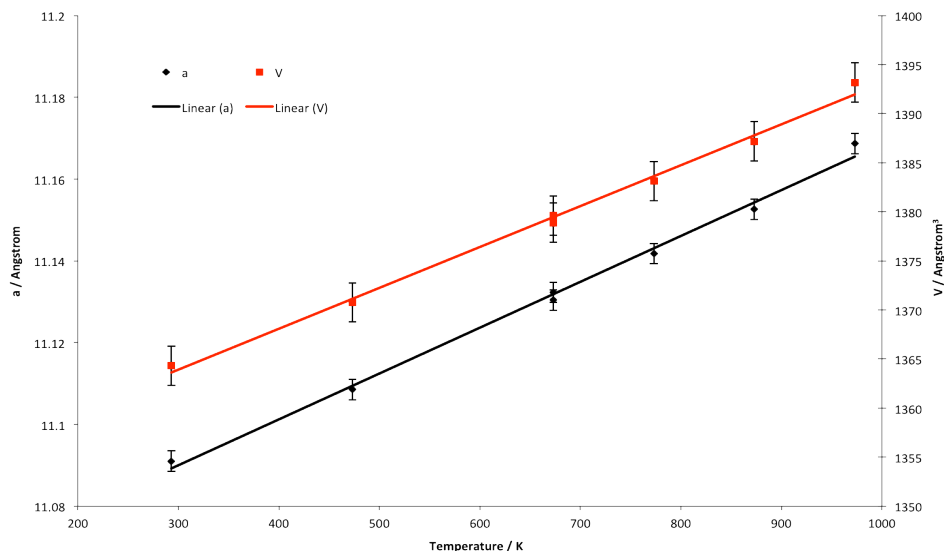
Figure 5-17: Lattice expansion for Fe$_3$Mo$_3$N under 3:1 H$_2$/N$_2$ gas.

These results are analogous to those seen in the cobalt system (Section 4.3.2.3) where no observable change occurs during reaction under 3:1 H$_2$/N$_2$ gas.

The feed gas was switched to 3:1 H$_2$/Ar gas and the temperature was increased initially to 923 K. The model, used to analyse the resultant diffraction pattern, was refined to show that the system contained Fe$_3$Mo$_3$N, γ-Mo$_2$N and, additionally Mo metal, indicating that the reduction at this point is of the binary phase rather than the ternary phase. The results of the refinement are shown in Table 5-10, Table 5-11 and Figure 5-18.

Table 5-10: Crystallographic parameters for Fe$_3$Mo$_3$N and γ-Mo$_2$N from *in-situ* PND experiment collected at 923 K under 3:1 H$_2$/Ar gas.

Parameter	Value
Formula	Fe$_3$Mo$_3$N
Crystal system	Cubic
Space group	Fd-3m
Formula mass / gmol^{-1}	7496.282
Phase Fraction	80.3
Cell parameter, *a* / Å	11.16402(11)
Unit-cell volume / Å^3	1391.431(25)
Calculated density ρ$_x$ / gcm^{-3}	8.946

156

Formula	γ-Mo_2N
Crystal system	Cubic
Space group	Fm-3m
Formula mass / gmol^{-1}	399.705
Phase Fraction	12.2
Cell parameter, *a* / Å	4.1494(13)
Unit-cell volume / Å^3	71.44(4)
Calculated density ρ_x / gcm^{-3}	9.290
Formula	Mo
Crystal system	Cubic
Space group	Im-3m
Formula mass / gmol^{-1}	191.880
Phase Fraction / %	7.5
Cell parameter, *a* / Å	3.1538(5)
Unit-cell volume / Å^3	31.369(9)
Calculated density ρ_x / gcm^{-3}	10.157
100x U_{iso} /U_{eq} / Å^2	1.42(18)
Number of observations	4426
Number of variables	38
R_p / %	3.82
R_{wp} / %	2.53
χ^2	1.383

Table 5-11: Refined atomic parameters for Fe$_3$Mo$_3$N and γ-Mo$_2$N from the *in-situ* PND experiment performed at 923 K under 3:1 H$_2$/Ar gas.

Fe3Mo3N

Atoms / Site	x	y	z	Occupancy	100× U$_{iso}$/U$_{eq}$ (Å^2)
Fe 1 (32e)	0.29283(6)	0.29283(6)	0.29283(6)	1.00	1.25*
Fe 2 (16d)	0.500000	0.500000	0.500000	1.00	1.29*
Mo (48f)	0.32081(10)	0.125000	0.125000	1.00	1.20*
N (16c)	0.000000	0.000000	0.000000	0.939(6)	1.26*

* = Anisotropically measured – expansion is shown here:

Atoms	U$_{11}$ (Å^2)	U$_{22}$ (Å^2)	U$_{33}$ (Å^2)	U$_{12}$ (Å^2)	U$_{13}$ (Å^2)	U$_{23}$ (Å^2)
Fe 1	1.25(4)	1.25(4)	1.25(4)	-0.056(25)	-0.056(25)	-0.056(25)
Fe 2	1.29(4)	1.29(4)	1.29(4)	-0.093(40)	-0.093(40)	-0.093(40)
Mo	1.44(7)	1.08(5)	1.08(5)	0.00	0.00	0.06(5)
N	1.26(5)	1.26(5)	1.26(5)	0.07(4)	0.07(4)	0.07(4)

γ-Mo$_2$N

Atoms / Site	x	y	z	Occupancy	100× U$_{iso}$/U$_{eq}$ (Å^2)
Mo (4a)	0.000000	0.000000	0.000000	1.00	1.03(15)
N (4b)	0.500000	0.500000	0.500000	0.285(15)	1.37(34)
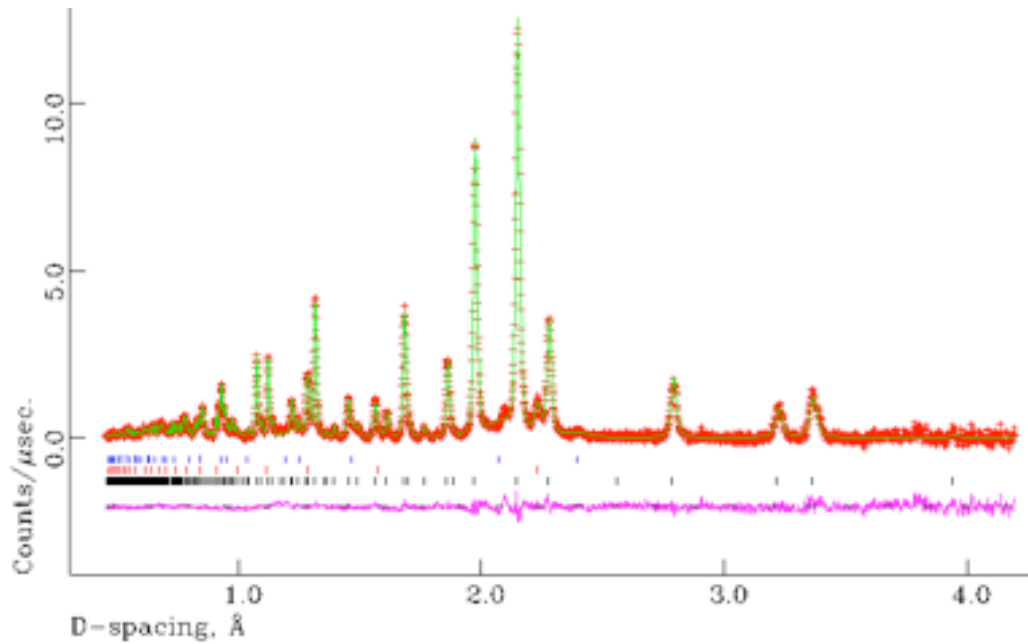
Figure 5-18: Final profile fit obtained from the refinement against *in-situ* PND data at 923 K for Fe$_3$Mo$_3$N under 3:1 H$_2$/Ar gas.

> The observed data are crosses, the calculated profile the solid line and lower
> continuous line the difference plot. Tick marks show allowed reflection positions.
> Blue tick-marks – Mo, Red tick-marks - γ-Mo$_2$N, Black tick-marks – Fe$_3$Mo$_3$N.

Further heating to 973 K showed complete reduction of the binary phase to molybdenum metal which is in good agreement with the observations of Mckay. The system was then further heated to 1073 K in order to determine if the ternary phase was reduced. The results of this refinement are shown in Table 5-12, Table 5-13 and Figure 5-19.

Table 5-12: Crystallographic parameters for Fe$_3$Mo$_3$N and Mo from the *in-situ* PND experiment performed at 1073 K under 3:1 H$_2$/Ar gas.

Parameter	Value
Formula	Fe$_3$Mo$_3$N
Crystal system	Cubic
Space group	Fd-3m
Formula mass / gmol^{-1}	7498.765
Phase Fraction	79.1
Cell parameter, *a* / Å	11.1856(1)
Unit-cell volume / Å^3	1399.51(2)
Calculated density ρ_x / gcm^{-3}	8.897
Formula	Mo
Crystal system	Cubic
Space group	Im-3m
Formula mass / gmol^{-1}	191.880
Phase Fraction / %	20.1
Cell parameter, *a* / Å	3.16033(10)
Unit-cell volume / Å^3	31.5644(18)
Calculated density ρ_x / gcm^{-3}	10.094
100x U$_{iso}$ /U$_{eq}$ / Å^2	1.12(6)
Number of observations	4426
Number of variables	33
R$_p$ / %	4.11
R$_{wp}$ / %	2.64
χ^2	1.325

Table 5-13: Refined atomic parameters for Fe$_3$Mo$_3$N and Mo from *in-situ* PND experiment collected at 1073 K.

Atoms / Site	x	y	z	Occupancy	100× U$_{iso}$ /U$_{eq}$ (Å^2)
Fe 1 (32e)	0.29297(6)	0.29297(6)	0.29297(6)	1.00	1.38*
Fe 2 (16d)	0.500000	0.500000	0.500000	1.00	1.33*
Mo (48f)	0.32050(10)	0.125000	0.125000	1.00	1.43*
N (16c)	0.000000	0.000000	0.000000	0.950(4)	1.43*

* = Anisotropically measured – expansion is shown here:

Atoms	U$_{11}$ (Å^2)	U$_{22}$ (Å^2)	U$_{33}$ (Å^2)	U$_{12}$ (Å^2)	U$_{13}$ (Å^2)	U$_{23}$ (Å^2)
Fe 1	1.33(4)	1.33(4)	1.33(4)	-0.026(25)	-0.026(25)	-0.026(25)
Fe 2	1.43(4)	1.43(4)	1.43(4)	-0.248(40)	-0.248(40)	-0.248(40)
Mo	1.48(7)	1.33(5)	1.33(5)	0.00	0.00	-0.11(5)
N	1.43(4)	1.43(4)	1.43(4)	-0.10(5)	-0.10(5)	-0.10(5)
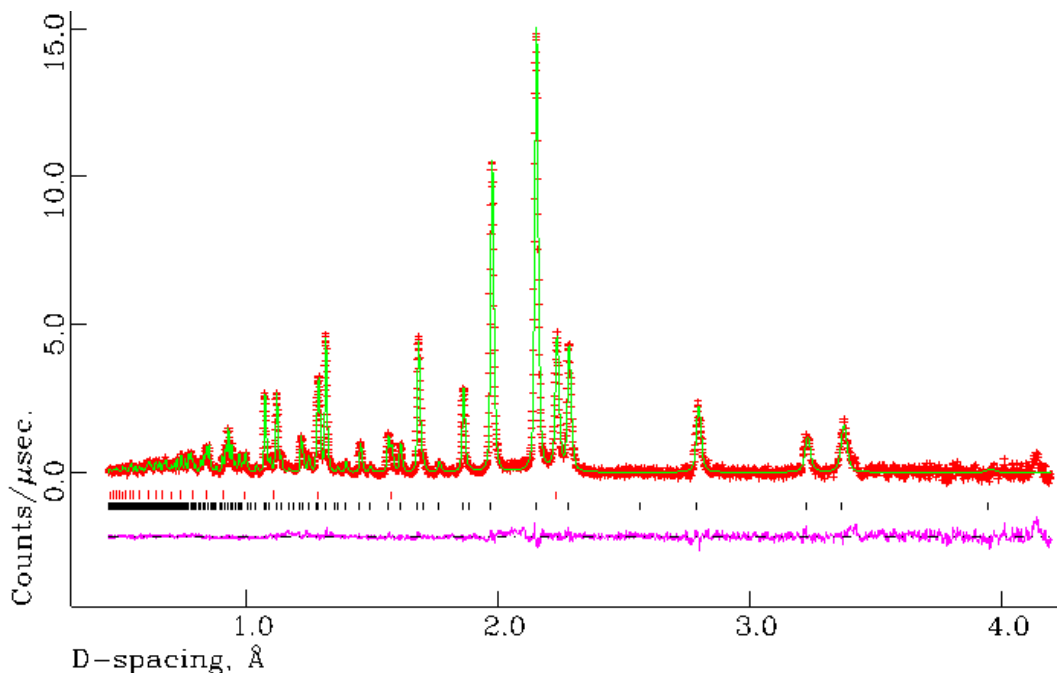
Figure 5-19: Final profile fit obtained from the refinement against *in-situ* PND at 1073 K for Fe$_3$Mo$_3$N.

The observed data are crosses, the calculated profile the solid line and lower continuous line the difference plot. Tick marks show allowed reflection positions. Red tick-marks - Mo, Black tick-marks – Fe$_3$Mo$_3$N.

As anticipated, the results demonstrate that at 1073 K the γ-Mo_2N is completely reduced to Mo under 3:1 H_2/Ar gas, whereas the ternary phase remains fully nitrogenated. The data thus indicated that under 3:1 H_2/Ar gas conditions the ternary nitride does not generate nitrogen for use in the production of ammonia. The reduction of the binary system, which is known to be active for ammonia synthesis and to reduce to molybdenum metal, may have contributed to the activity for the Fe_3Mo_3N phase previously seen by Mckay.[10]

However, in order to demonstrate this conclusively, the pure phase sample was investigated. The detail of the structure of the nitride after reaction with 3:1 H_2/Ar gas was determined by refinement against PXRD data (Table 5-14, Table 5-15 and Figure 5-20).

Table 5-14: Crystallographic parameters for Fe_3Mo_3N for PXRD data post 3:1 H_2/Ar gas reaction.

Parameter	Value
Colour of powder	Black
Formula	Fe_3Mo_3N
Crystal system	Cubic
Space group	Fd-3m
Formula mass / $gmol^{-1}$	7597.720
Cell parameter, a / Å	11.0725(31)
Unit-cell volume / $Å^3$	1357.5(7)
Calculated density ρ_x / gcm^{-3}	9.294
Number of observations	4189
Number of variables	23
R_p / %	15.85
R_{wp} / %	20.61
χ^2	1.645

Table 5-15: Refined atomic parameters for Fe$_3$Mo$_3$N from PXRD data following reaction under 3:1 H$_2$/Ar gas.

Atoms / Site	x	y	z	Occupancy	100× U$_{iso}$/U$_{eq}$ (Å^2)
Fe 1 (32e)	0.2930(5)	0.2930(5)	0.2930(5)	1.00	0.8(4)
Fe 2 (16d)	0.500000	0.500000	0.500000	1.00	1.1(5)
Mo (48f)	0.3219(5)	0.125000	0.125000	1.00	1.2(3)
N (16c)	0.000000	0.000000	0.000000	1.00	1.5(5)
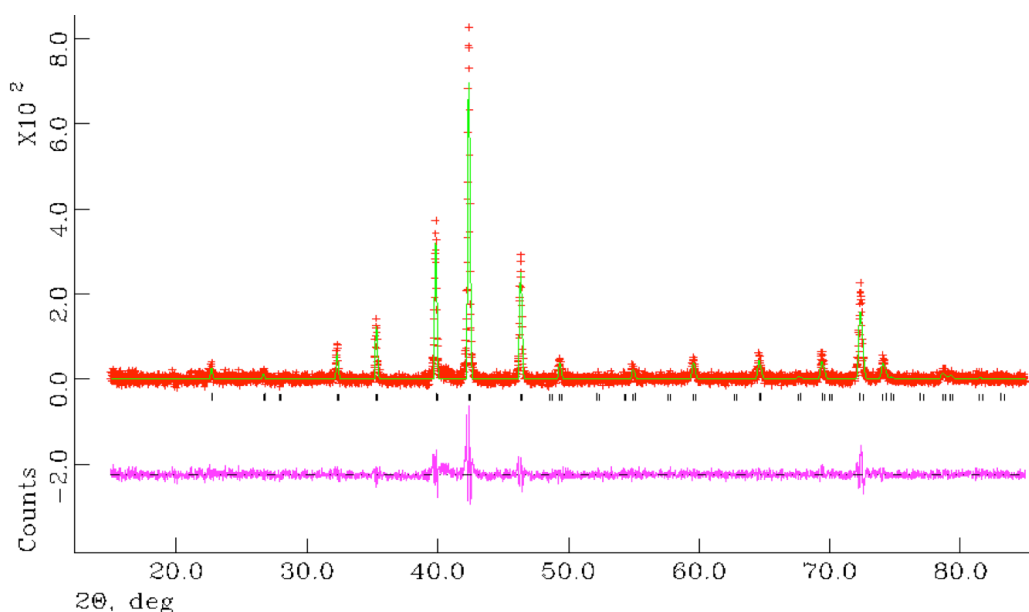
Figure 5-20: Final profile fit obtained from the refinement against PXRD data following reaction under 3:1 H$_2$/Ar gas.

The observed data are crosses, the calculated profile the solid line and lower continuous line the difference plot. Tick marks show allowed reflection positions.

Subsequent PND data collected on the post reaction sample was used to obtain a definitive structure and determine whether the nitrogen content of the sample was unchanged following reaction at 973 K under 3:1 H$_2$/Ar gas. The results of the refinement are shown in Table 5-16, Table 5-17 and Figure 5-21.

Table 5-16: Crystallographic parameters for Fe$_3$Mo$_3$N for PND data post 3:1 H$_2$/Ar gas reaction.

Parameter	Value
Formula	Fe$_3$Mo$_3$N
Crystal system	Cubic
Space group	Fd-3m
Formula mass / gmol^{-1}	7503.868
Cell parameter, a / Å	11.06553(4)
Unit-cell volume / Å^3	1354.929(9)
Calculated density ρ_x / gcm^{-3}	9.196
Number of observations	8894
Number of variables	41
R$_p$ / %	4.54
R$_{wp}$ / %	2.38
χ^2	1.489

Table 5-17: Refined atomic parameters for Fe$_3$Mo$_3$N from post 3:1 H$_2$/Ar gas reaction PND data.

Atoms / Site	x	y	z	Occupancy	100× U$_{iso}$ /U$_{eq}$ (Å^2)
Fe 1 (32e)	0.29377(2)	0.29377(2)	0.29377(2)	1.00	0.38*
Fe 2 (16d)	0.500000	0.500000	0.500000	1.00	0.41*
Mo (48f)	0.32169(3)	0.125000	0.125000	1.00	0.49*
N (16c)	0.000000	0.000000	0.000000	0.973(3)	0.44*

* = Anisotropically measured – expansion is shown here:

Atoms	U$_{11}$ (Å^2)	U$_{22}$ (Å^2)	U$_{33}$ (Å^2)	U$_{12}$ (Å^2)	U$_{13}$ (Å^2)	U$_{23}$ (Å^2)
Fe 1	0.412(6)	0.412(6)	0.412(6)	-0.002(6)	-0.002(6)	-0.002(6)
Fe 2	0.493(7)	0.493(7)	0.493(7)	-0.036(9)	-0.036(9)	-0.036(9)
Mo	0.373(13)	0.383(8)	0.383(8)	0.00	0.00	-0.030(11)
N	0.44(1)	0.44(1)	0.44(1)	-0.02(1)	-0.02(1)	-0.02(1)
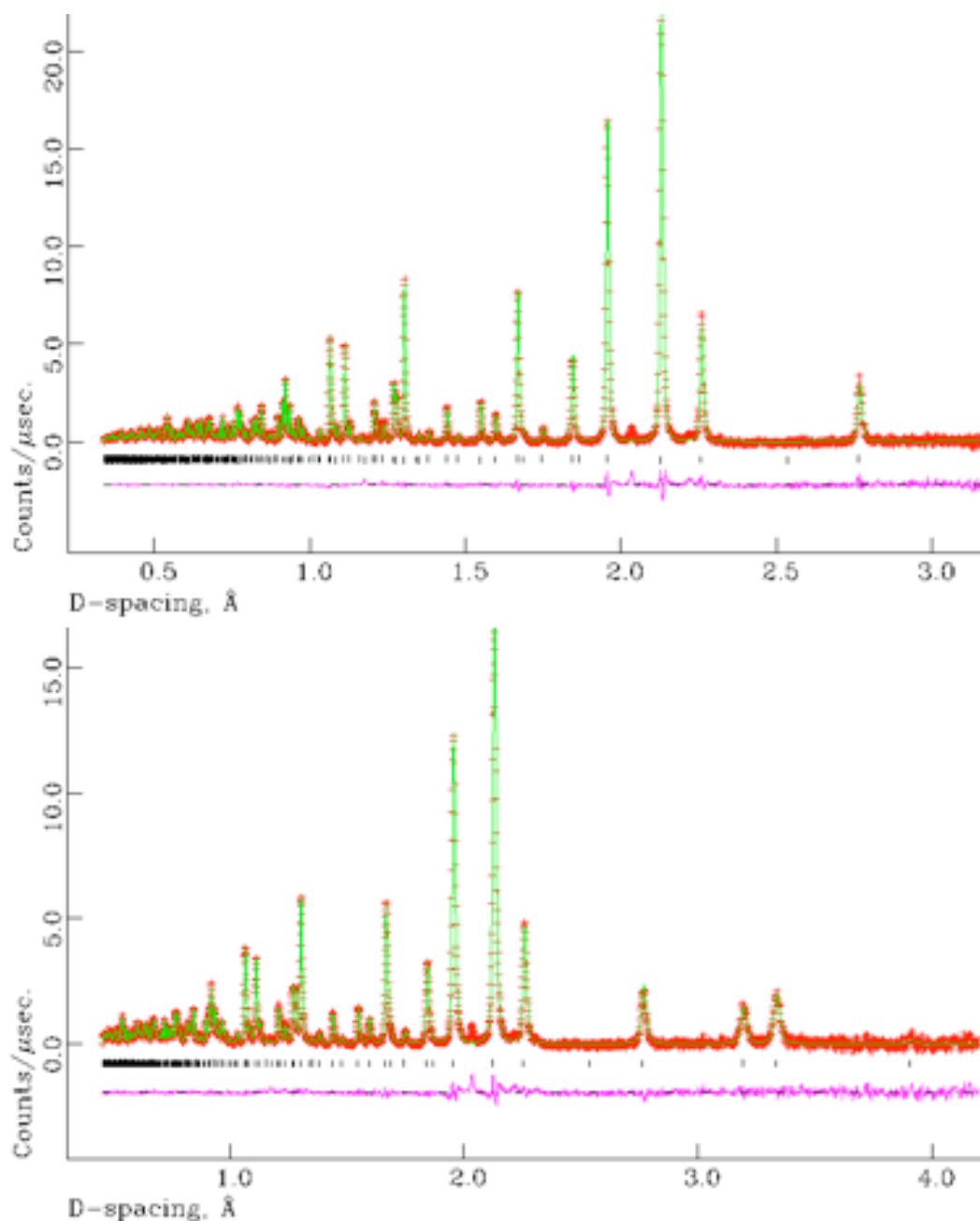
Figure 5-21: Final profile fit obtained from the refinement against PND data following reaction under 3:1 H_2/Ar gas.

> The observed data are crosses, the calculated profile the solid line and lower
> continuous line the difference plot. Tick marks show allowed reflection positions.
> Top – Backscattering detector bank <2θ> = 145°, Bottom - 90° detector bank.

Despite evidence suggesting that there is no change in the lattice nitrogen content following 3:1 H_2/Ar gas treatment at 973 K, catalytic testing data indicate that ammonia is produced during the reaction. A possible explanation is that the system is loaded with surface NH_x species during the two hour pre-treatment at 973 K which are adsorbed onto the surface and then released over the course of the reaction.

The differences between the iron and cobalt system under reaction with 3:1 H_2/Ar gas show that although the structure of the compounds at the outset is the same (η-6 carbide, space group Fd-3m), the chemistry which the samples undergo is very different. Whereas the cobalt compound reduces to a η-12 carbide structured nitride, Co_6Mo_6N, no change was observed in the iron system even when the temperature was increased to 1073 K under 3:1 H_2/Ar gas. The difference in the chemical reactivity therefore must be related to the effect of iron on the Mo-N sub-lattice. In the case of cobalt, the nitrogen migrates to the 8a site which gives a more regular octahedral geometry. By contrast, apparently the iron present in the Fe_3Mo_3N system affects the local binding of the nitrogen and does not allow the nitrogen to be removed or relocated to the 8a from 16c site.

5.3.3   Nickel molybdenum nitride (Ni_2Mo_3N)

5.3.3.1   Structural study

It was observed that Ni_2Mo_3N could be prepared via the direct reaction of $NiMoO_4 \cdot nH_2O$ with 3:1 H_2/N_2 gas at 973 K for three hours. This direct route was used to form the nickel molybdenum nitride for further studies. This contrasts to the method employed by Alconchel, who used higher temperatures to form the nitride under ammonia.[4] In previous work a range of impurities co-existed with Ni_2Mo_3N including, Mo_2N, MoN, $Ni_{0.2}Mo_{0.8}N$ and Ni_3N along with a cubic impurity phase which was not identified. Literature unit cell details: Space group P4$_1$32, a = 6.634(2) Å, volume = 292.22(2) Å^3.[4] The PXRD pattern obtained from the nitridation procedure employed here (Figure 5-22) indicated a biphasic sample containing Ni_2Mo_3N and a nickel metal phase. The presence of Ni in Ni_2Mo_3N sample had been shown previously by Mckay[10] and is expected from the experimental procedure, reflecting the 1:1 Ni to Mo ratio in the nickel molybdate precursor.

Indexing the pattern using Dicvol 04[11] gives lattice parameters for the Ni_2Mo_3N phase of a = 6.631(5) Å. This is in good agreement to the literature value of 6.634(2) Å.
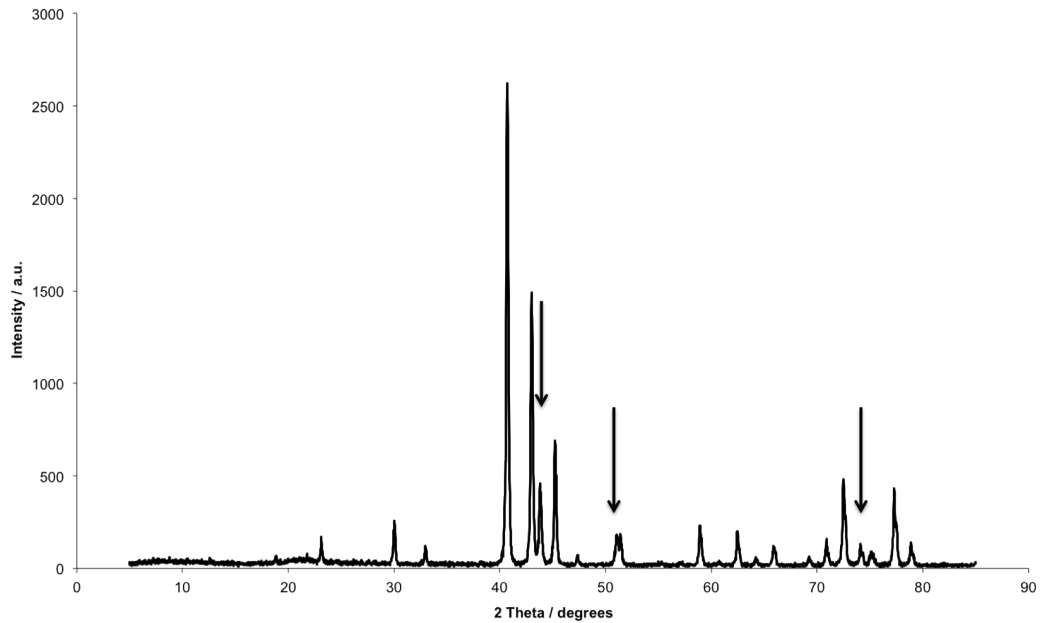
Figure 5-22: PXRD pattern of Ni-Mo-N.

Ni reflections marked with arrow

The microanalysis results for the nitride gave a nitrogen content of 1.98 wt% which is lower than expected from the theoretical stoichiometry. In order to confirm the amount of the Ni impurity present, a refinement was undertaken against the PXRD data. The results are shown in Table 5-18, Table 5-19 and Figure 5-23. Refinement against PXRD data was performed for samples by first fitting the background to a shifted Chebyschev function (background function 1 in GSAS). Once the background was fitted, the lattice parameters were then refined prior to the atomic positions followed by variation of the peak profile parameters. When the refinement had stabilised, the thermal parameters were varied anisotropically.

Table 5-18: Crystallographic parameters for Ni_2Mo_3N for PXRD data.

Parameter	Value
Formula	Ni_2Mo_3N
Crystal system	Cubic
Space group	$P4_132$
Formula mass / $gmol^{-1}$	1676.908
Phase Fraction / %	86.5
Cell parameter, a / Å	6.636(3)
Unit-cell volume / $Å^3$	292.22(2)
Calculated density ρ_x / gcm^{-3}	9.529
Formula	Ni
Crystal system	Cubic
Space group	Fm-3m
Formula mass / $gmol^{-1}$	234.800
Phase Fraction / %	13.5
Cell parameter, a / Å	3.57095(29)
Unit-cell volume / $Å^3$	45.536(6)
Calculated density ρ_x / gcm^{-3}	8.562
100x U_{iso} /U_{eq} ($Å^2$)	0.69(20)
Number of observations	5750
Number of variables	36
R_p / %	12.30
R_{wp} / %	17.75
χ^2	1.427

Table 5-19: Refined atomic parameters for Ni_2Mo_3N from PXRD data.

Atoms / Site	x	y	z	Occupancy	$100\times$ U_{iso}/U_{eq} ($Å^2$)
Ni (8c)	0.06764(30)	0.06764(30)	0.06764(30)	1.00	0.29*
Mo (12d)	0.125000	0.20148(14)	0.45148(14)	1.00	0.37*
N (4a)	0.375000	0.375000	0.375000	1.00	0.42*

* = Anisotropically measured – expansion is shown here:

Atoms	U_{11} ($Å^2$)	U_{22} ($Å^2$)	U_{33} ($Å^2$)	U_{12} ($Å^2$)	U_{13} ($Å^2$)	U_{23} ($Å^2$)
Ni	0.53(9)	0.53(9)	0.53(9)	-0.01(9)	-0.01(9)	-0.01(9)
Mo	0.45(9)	0.48(6)	0.48(6)	-0.10(5)	-0.10(5)	-0.07(7)
N	0.3(5)	0.3(5)	0.3(5)	-1.2(6)	-1.2(6)	-1.2(6)
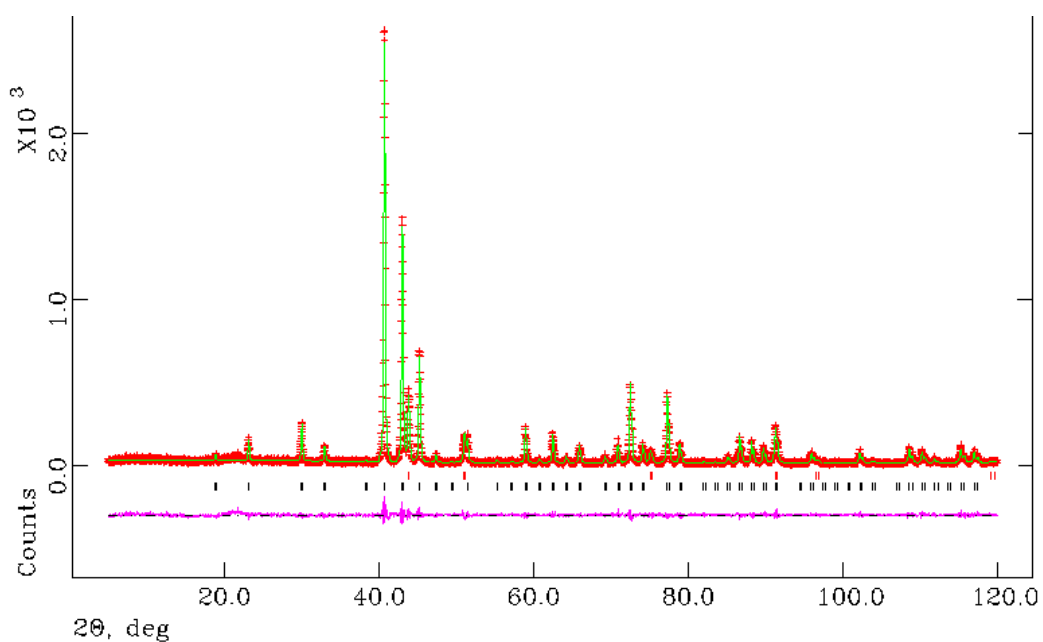
Figure 5-23: Final profile fit obtained from the refinement against PXRD data for Ni_2Mo_3N.

The observed data are crosses, the calculated profile the solid line and lower
continuous line the difference plot. Tick marks show allowed reflection positions.
Red tick-marks - Ni, Black tick-marks – Ni_2Mo_3N.

Rietveld refinement against the PXRD data confirmed that Ni_2Mo_3N crystallises in
cubic space group $P4_132$ and conforms to the β-Mn model proposed by Alchonel *et al.*[4]
The ratio of Ni_2Mo_3N to Ni is approximately 85:15, which indicates there is an excess

of Ni over the amount expected (nitrogen content of 2.77 wt%). This result indicates that the microanalysis results do not fully account for the expected nitrogen content. Therefore there is an expectation that there was an impurity phase which is not visible in the PXRD data or that the material did not combust sufficiently for accurate nitrogen analysis

PND experiments were conducted to obtain a definitive model and N stoichiometry for Ni_2Mo_3N and also to identify any possible additional phases. The refinement results are shown in Figure 5-24, Table 5-20 and Table 5-21. Ternary nitride was confirmed along with the presence of Ni as the only observable impurity phase. The refined model demonstrates that the Ni_2Mo_3N phase is almost completely stoichiometric with N occupying the 4a (3/8, 3/8, 3/8) site. The ratio of the phases was 86.5:13.5 %, not accounting for the inconsistencies in the microanalysis results. If there were extra phases present in the system then these are undetectable by PXRD or PND. It is possible that amorphous phases could be present in the sample, but the relatively flat background profile would suggest that this is unlikely.
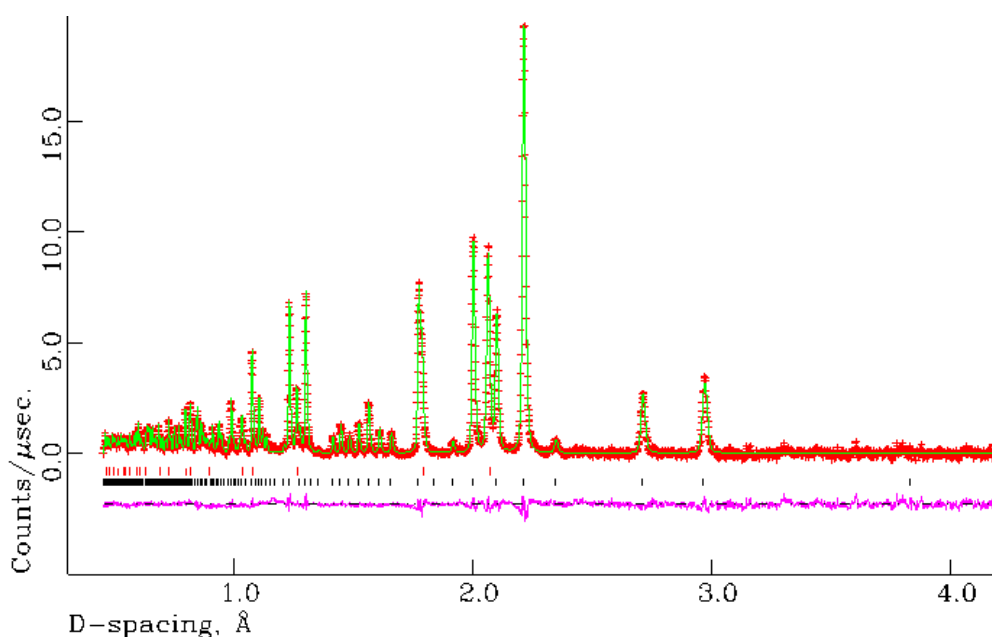
Figure 5-24: Final profile fit obtained from the refinement against PND data collected at room temperature for Ni_2Mo_3N.

The observed data are crosses, the calculated profile the solid line and lower continuous line the difference plot. Tick marks show allowed reflection positions. Red tick-marks - Ni, Black tick-marks – Ni_2Mo_3N.

Table 5-20: Crystallographic parameters for Ni$_2$Mo$_3$N for PND data collected at room temperature.

Parameter	Value
Formula	Ni$_2$Mo$_3$N
Crystal system	Cubic
Space group	P4$_1$32
Formula mass / gmol^{-1}	1676.908
Phase Fraction / %	86.5
Cell parameter, *a* / Å	6.6457(2)
Unit-cell volume / Å^3	293.51(1)
Calculated density ρ_x / gcm^{-3}	9.487
Formula	Ni
Crystal system	Cubic
Space group	Fm-3m
Formula mass / gmol^{-1}	234.800
Phase Fraction / %	13.5
Cell parameter, *a* / Å	3.57708(6)
Unit-cell volume / Å^3	45.7704(14)
Calculated density ρ_x / gcm^{-3}	8.518
100x U$_{iso}$/U$_{eq}$ (Å^2)	0.366(15)
Number of observations	4426
Number of variables	25
R$_p$ / %	3.69
R$_{wp}$ / %	2.81
χ^2	1.665

Table 5-21: Refined atomic parameters for Ni₂Mo₃N for PND data collected at room temperature.

Atoms / Site	x	y	z	Occupancy	$100 \times$ U_{iso}/U_{eq} (Å^2)
Ni (8c)	0.06692(9)	0.06692(9)	0.06692(9)	1.00	0.36*
Mo (12d)	0.125000	0.2015(1)	0.4515(1)	1.00	0.23*
N (4a)	0.375000	0.375000	0.375000	0.978(6)	0.28*

* = Anisotropically measured – expansion is shown here:

Atoms	U_{11} (Å^2)	U_{22} (Å^2)	U_{33} (Å^2)	U_{12} (Å^2)	U_{13} (Å^2)	U_{23} (Å^2)
Ni	0.36(2)	0.36(2)	0.36(2)	0.001(20)	0.001(20)	0.001(20)
Mo	0.46(2)	0.46(2)	0.46(2)	0.04(3)	-0.04(3)	-0.14(4)
N	0.27(3)	0.27(3)	0.27(3)	-0.10(3)	-0.10(3)	-0.10(3)

Selected bond lengths and angles are shown in Table 5-22 and a representation of the structure of Ni₂Mo₃N is shown in Figure 5-25.

Table 5-22: Selected Interatomic Distances and Angles for Ni₂Mo₃N from PND Data.

Parameter	Value
Atomic Distance / Å	
N–Mo ×6	2.0855(2)
Mo-Mo ×5	2.734(1)
Mo-Mo ×5	2.746(1)
Mo-Mo ×5	2.8216(3)
Ni-Ni ×3	2.4732(4)
Bond Angle / °	
N-Mo-N	154.70(5)
Mo-N-Mo ×6	83.57(4)
Mo-N-Mo ×3	85.30(5)
Mo-N-Mo ×3	111.426(8)
Mo-N-Mo ×3	160.17(3)
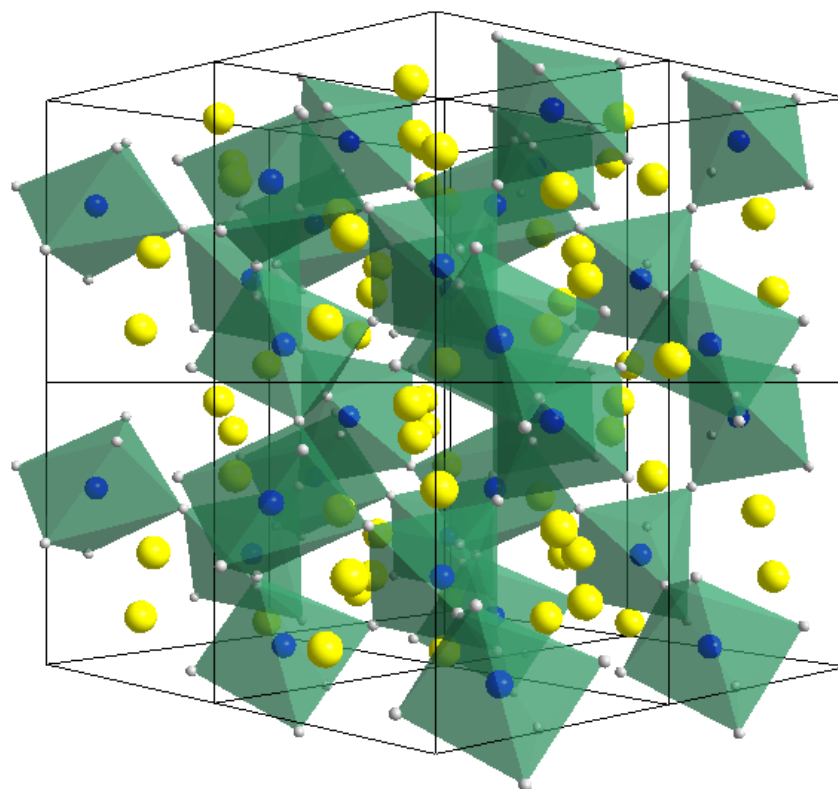
Figure 5-25: Structural image of Ni$_2$Mo$_3$N showing a 2x2x2 unit cell.

Mo - Grey spheres, N - Blue spheres, Ni - Yellow spheres.
2x2x2 unit cell used for comparison of like for like sizes with unit cells of Fe$_3$Mo$_3$N and Co$_3$Mo$_3$N.

The Ni$_2$Mo$_3$N structure has a very distorted NMo$_6$ octahedral arrangement, which can be seen in Figure 5-26. The Mo-N bond is slightly contracted compared to those seen in Co$_3$Mo$_3$N (Section 4.3.2.1).
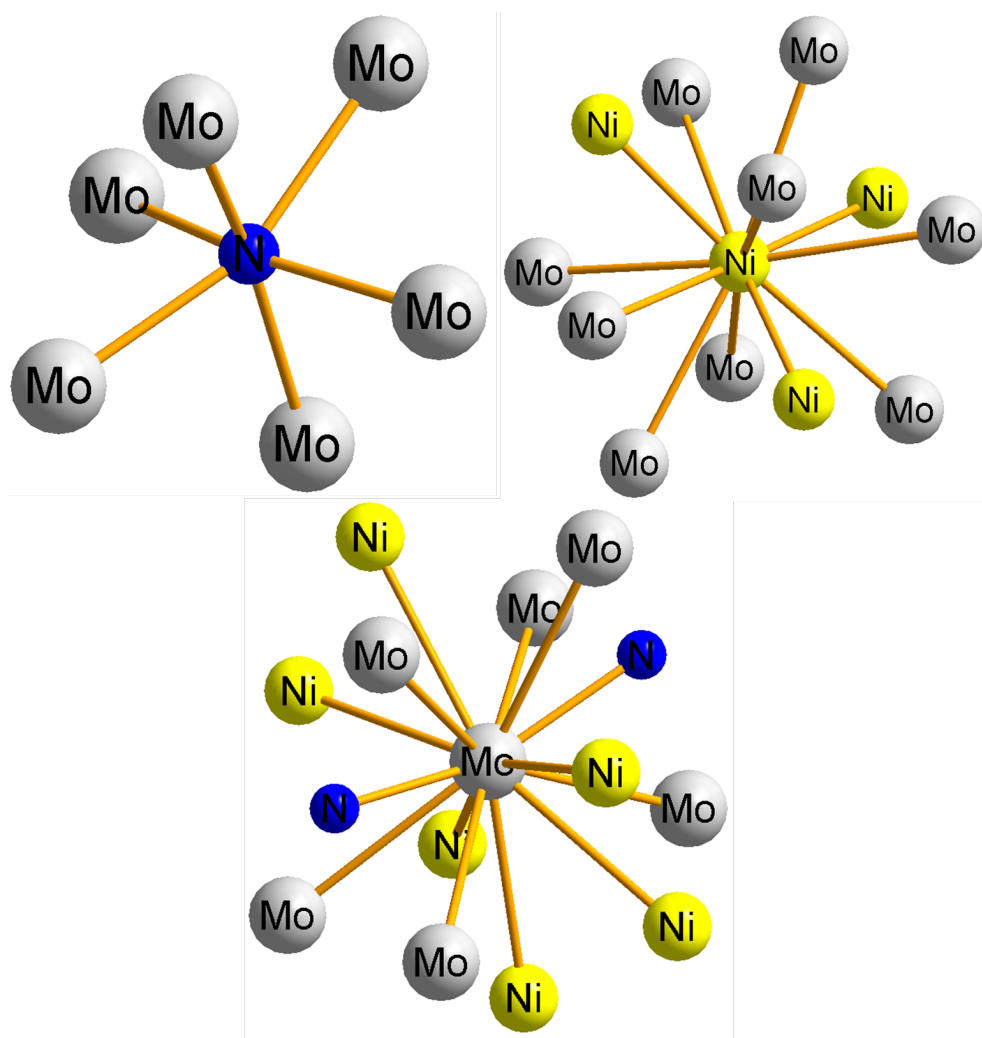
Figure 5-26: Co-ordination environments for Ni, Mo and N in Ni$_2$Mo$_3$N.

5.3.3.2   Activity study

The ambient pressure ammonia synthesis efficacy of Ni$_2$Mo$_3$N has been measured at 673 K for five hours using a 3:1 H$_2$/N$_2$ gas feed. Steady state production of ammonia was observed, as shown in the reaction profile in Figure 5-27.
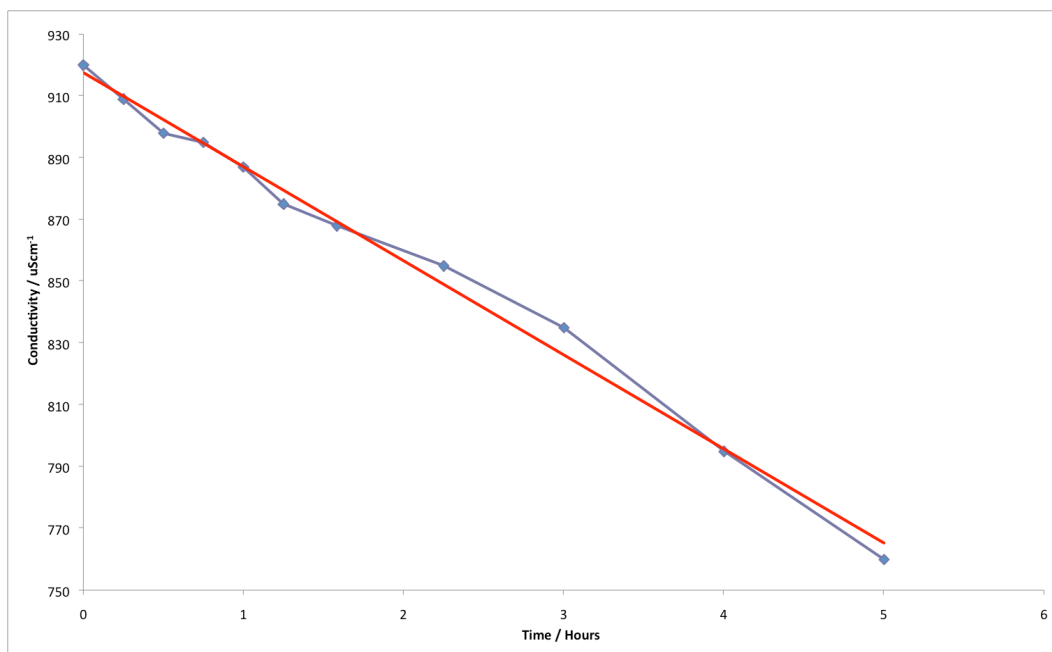
Figure 5-27: Reaction profile for Ni$_2$Mo$_3$N under 3:1 H$_2$/N$_2$ gas at 673 K.

The catalytic activity of the Ni$_2$Mo$_3$N system gives a reaction rate of 97.3 μmolh^{-1}g^{-1} which is lower than that of the Co$_3$Mo$_3$N system (Section 4.3.2.2).

The post-reaction analysis of the sample shows no change in the PXRD data with indexing giving a lattice parameter of a = 6.6315(4) Å. The microanalysis results show no reduction of nitrogen content upon reaction. (Table 5-23).
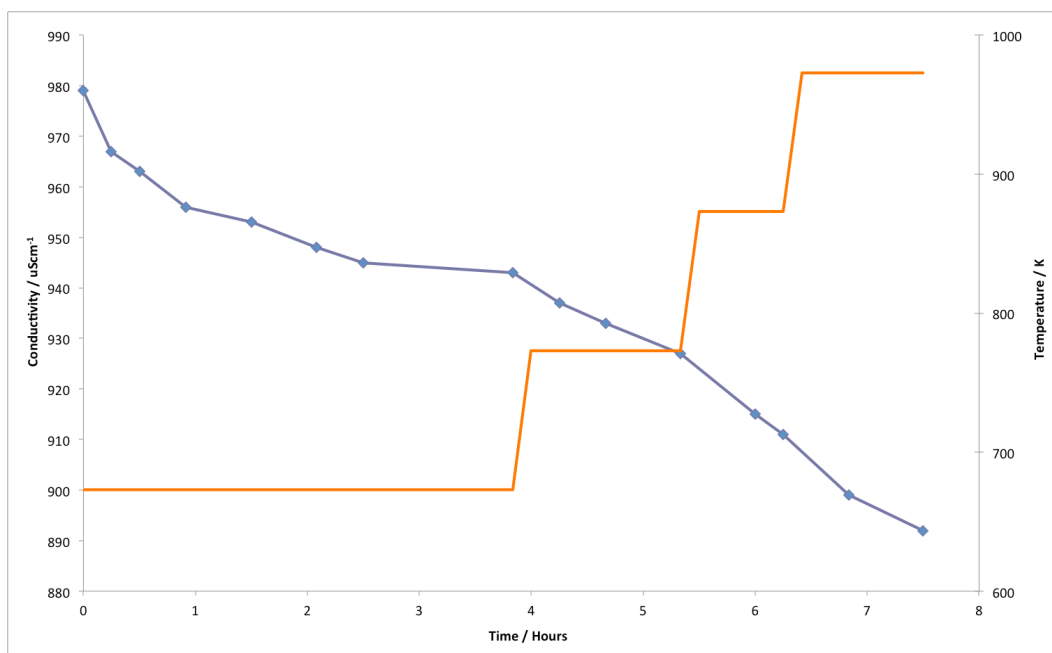
Figure 5-28: Reaction profile for Ni$_2$Mo$_3$N under 3:1 H$_2$/Ar gas.

The reactivity of the lattice nitrogen present in the β-Mn structured Ni_2Mo_3N was tested, by changing the feed gas to 3:1 H_2/Ar gas. The reaction profile is shown in Figure 5-28, which shows an initial decrease in the conductivity at 673 K, which quickly diminishes and after two hours conductivity becomes constant showing no further production of ammonia. After the temperature was increased to 773 K, the rate of ammonia production increased although further increases in temperature was necessary to sustain the production of ammonia.

Table 5-23: Microanalysis results for Ni_2Mo_3N.

Conditions	As prepared	Post Reaction / 3:1 H_2/N_2 gas	Post Reaction / 3:1 H_2/Ar gas	Regeneration / 3:1 H_2/N_2 gas
N content / wt%	1.98 (2)	2.00 (2)	1.92 (4)	1.94 (5)

Post-reaction analysis shows no significant change in the nitrogen content of the sample (Table 5-23). The post-reaction PXRD pattern also showed no change with respect to the pre-reaction pattern, indicating that there was no change in the structure of the nitride.

In order to confirm the findings of the reactivity study an *in-situ* PND experiment was undertaken to follow any possible changes in the system with time and temperature .
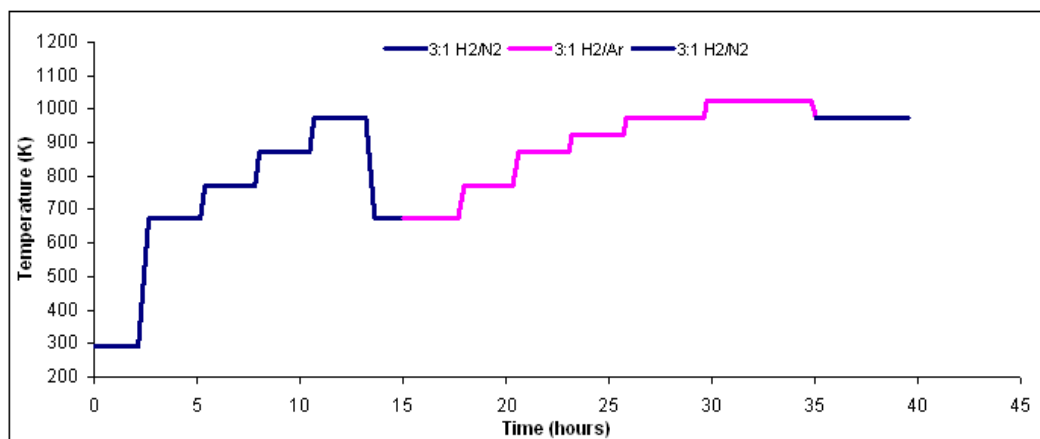
Figure 5-29: Heating regime for *in-situ* PND reaction of Ni_2Mo_3N.

The *in-situ* PND experiment conditions followed the heating regimes shown in Figure 5-29, these mimicked the test reactions under both 3:1 H_2/N_2 gas and 3:1 H_2/Ar gases. A regeneration stage was then applied at 973 K under 3:1 H_2/N_2 gas. The experiment was designed to see if any changes occurred in the system under any of the conditions applied.
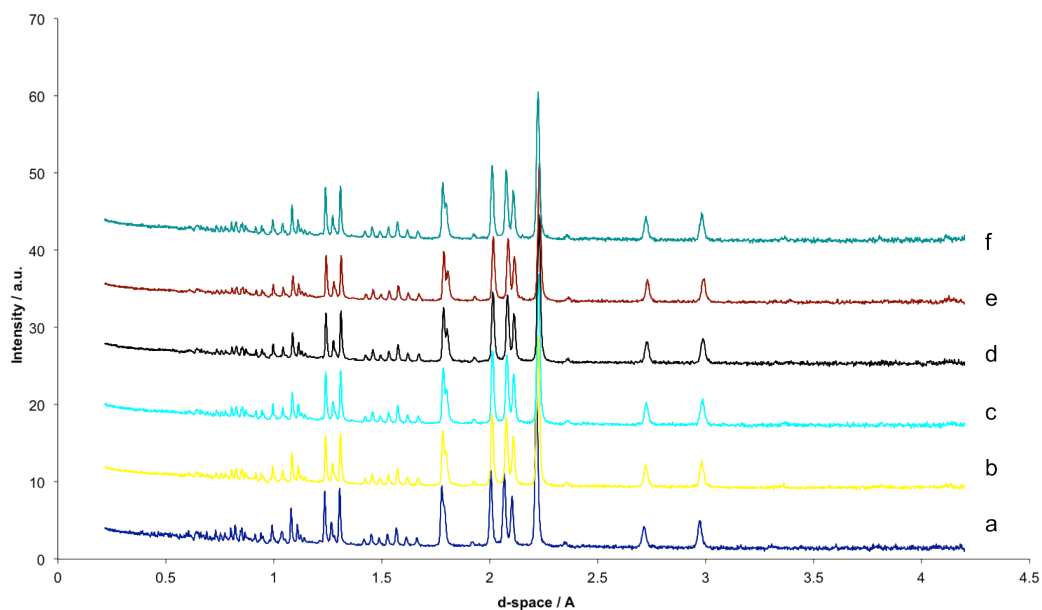
Figure 5-30: PND data for initial heating stage of *in-situ* experiment.

a = 290 K, b = 673 K, c = 773 K, d = 873 K, e = 973 K, f = 673 K (cooled).

The initial stage of the reaction under 3:1 H_2/N_2 gas showed no change in the Ni-Mo-N structure (Figure 5-30), with only thermal expansion being evident. The expansion is shown in Figure 5-31.
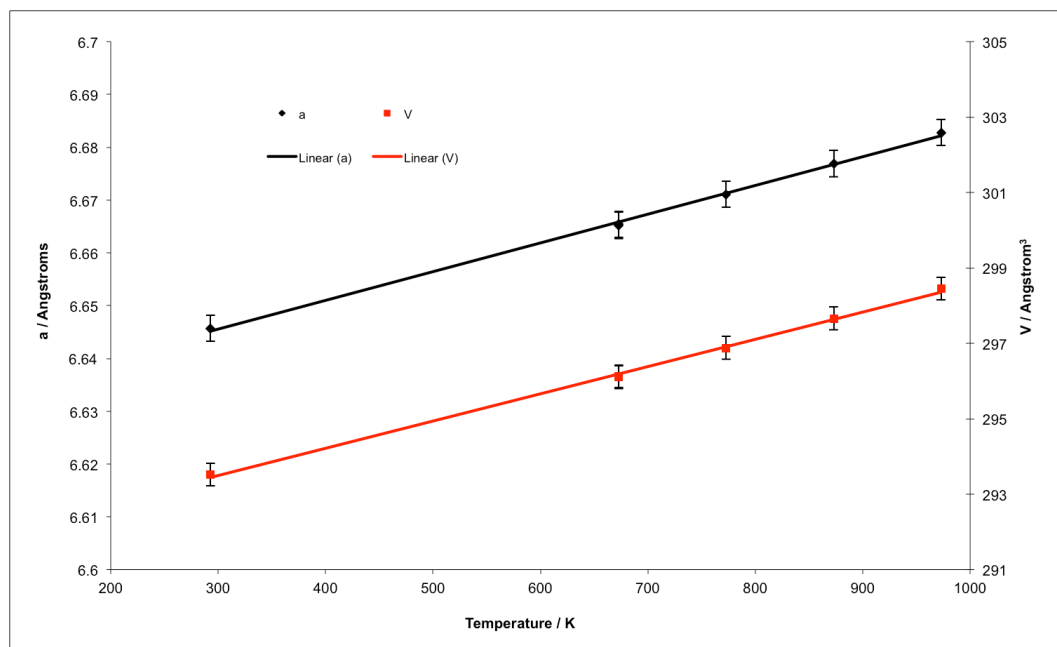
Figure 5-31: Plot showing lattice expansion of Ni_2Mo_3N.

From the patterns collected, it is possible to conclude that ratio of Ni_2Mo_3N to Ni remains constant (86:14 %) throughout heating.

After cooling to 673 K, the feed gas was switched to 3:1 H_2/Ar gas, and the temperature increased. Patterns were collected at set temperatures as presented in Figure 5-32. These show no change in the structure upon heating. When the temperature reaches 973 K the ratio of Ni_2Mo_3N to Ni is 85:15. The temperature was then increased further to 1023 K and Figure 5-32 shows there was no change to either of the phases present during the experiment. Details of the refinement against data collected at 1023 K is presented in Table 5-24, Table 5-25 and Figure 5-33.
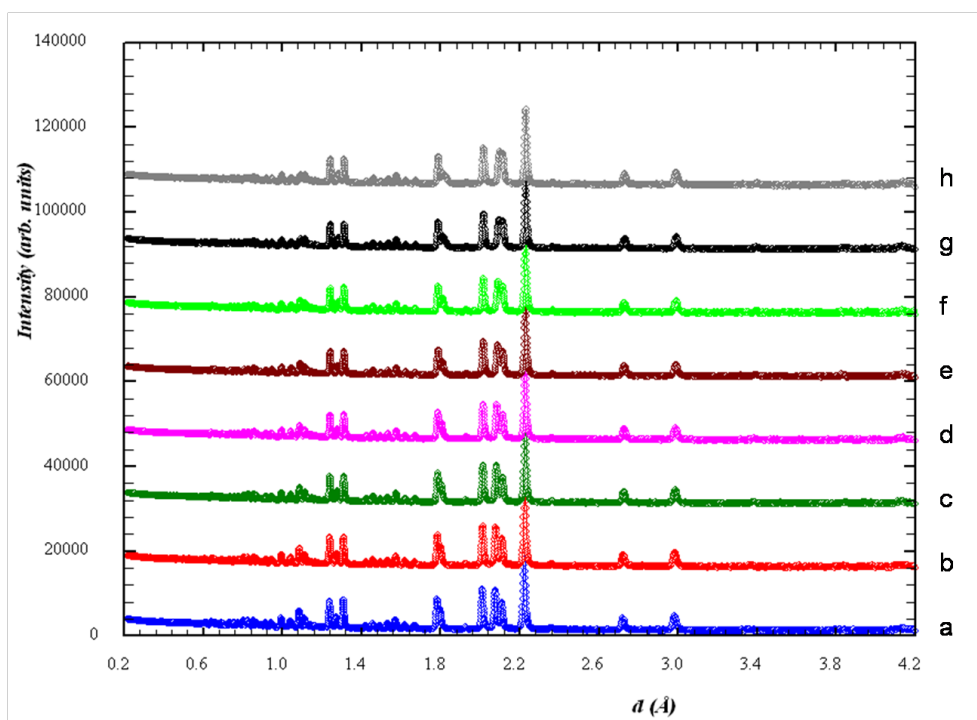
Figure 5-32: PND data for Ni$_2$Mo$_3$N under 3:1 H$_2$/Ar gas.

(a) 673 K, (b) 773 K, (c) 873 K, (d) 923 K, (e) 973 K (90 mins), (f) 973 K (180 mins), (g) 1023 K (120 mins), (h) 1023 K (240 mins).

Table 5-24: Crystallographic parameters for Ni$_2$Mo$_3$N for PND data collected at 1023 K.

Parameter	Value
Formula	Ni$_2$Mo$_3$N
Crystal system	Cubic
Space group	P4$_1$32
Formula mass / gmol^{-1}	1675.230
Phase Fraction / %	84.9(3)
Cell parameter, *a* / Å	6.68617(7)
Unit-cell volume / Å^3	298.904(5)
Calculated density ρ_x / gcm^{-3}	9.307
Formula	Ni
Crystal system	Cubic
Space group	Fm-3m
Formula mass / gmol^{-1}	234.800
Phase Fraction / %	15.1(3)
Cell parameter, *a* / Å	3.6288(1)
Unit-cell volume / Å^3	47.783(3)
Calculated density ρ_x / gcm^{-3}	8.160
100x U$_{iso}$ /U$_{eq}$ (Å^2)	1.22(4)
Number of observations	4426
Number of variables	32
R$_p$ / %	4.03
R$_{wp}$ / %	2.99
χ^2	2.304

Table 5-25: Refined atomic parameters for Ni₂Mo₃N for PND data collected at 1023 K.

Atoms / Site	x	y	z	Occupancy	$100\times$ U_{iso}/U_{eq} (Å²)
Ni (8c)	0.0672(1)	0.0672(1)	0.0672(1)	1.00	1.34*
Mo (12d)	0.125000	0.2028(2)	0.4528(2)	1.00	1.10*
N (4a)	0.375000	0.375000	0.375000	0.970(8)	1.05*

* = Anisotropically measured – expansion is shown here:

Atoms	U_{11} (Å²)	U_{22} (Å²)	U_{33} (Å²)	U_{12} (Å²)	U_{13} (Å²)	U_{23} (Å²)
Ni	1.34(4)	1.34(4)	1.34(4)	-0.02(3)	-0.02(3)	-0.02(3)
Mo	1.43(9)	0.93(5)	0.93(5)	0.04(4)	-0.04(4)	-0.21(6)
N	1.05(6)	1.05(6)	1.05(6)	-0.26(4)	-0.26(4)	-0.26(4)
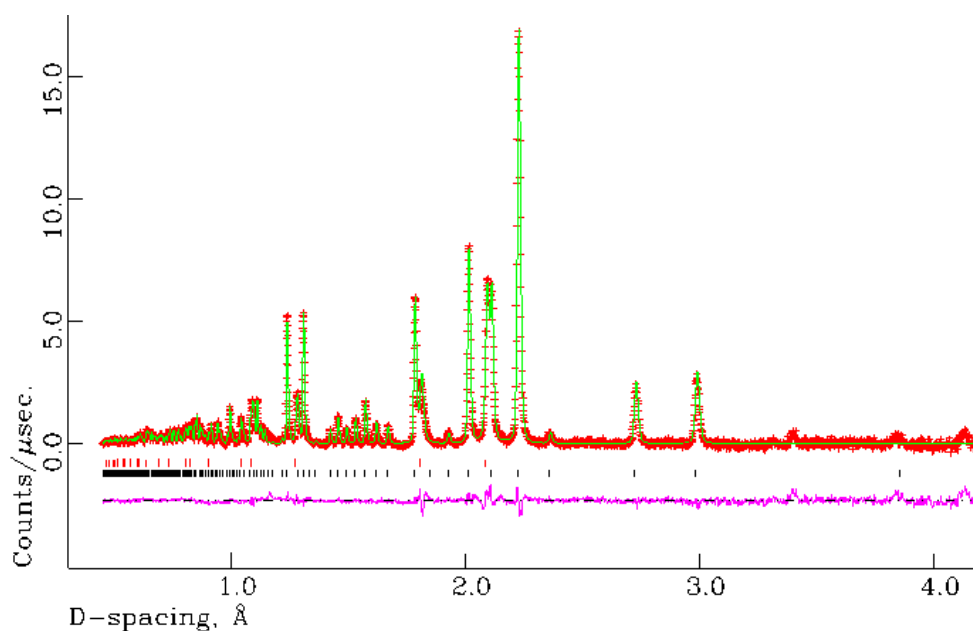
Figure 5-33: Final profile fit obtained from the refinement against *in-situ* PND data collected at 1023 K for Ni₂Mo₃N.

The observed data are crosses, the calculated profile the solid line and lower
continuous line the difference plot. Tick marks show allowed reflection positions.
Red tick-marks - Ni, Black tick-marks – Ni₂Mo₃N.

The *in-situ* experiment showed that there was no change to the structure or composition in the ternary nitride sample. The reduced nitrogen content apparent in the microanalysis results cannot be attributed to a crystalline impurity phase. Therefore, incomplete combustion of the samples within the CHN analyser during analysis or the presence of an amorphous impurity phase remains the only likely explanation for this observation.

5.4   Summary

The work presented in this chapter shows that the ternary systems of iron and nickel molybdenum nitride behave very differently to those seen for cobalt molybdenum nitride with no reduction and regeneration pathway observable in either case.

In the iron molybdenum nitride it has been shown that the ternary phase can be formed as a single phase product through the use of iron (II) chloride as the iron source for the ternary molybdate precursor. In addition the used of iron (III) nitrate gives a biphasic product of iron molybdenum nitride and γ-Mo_2N. In both cases the ternary phase is able to be identified and refined to give identical structures. The data collected from both PXRD and PND experiments were used to confirm the structure previously reported.

The reactivity of the iron phase was shown to be less than that seen previously for the Co_3Mo_3N system, however during the reaction under 3:1 H_2/Ar gas, it was observed that no change occurred to the Fe_3Mo_3N unlike the cobalt system. In the mixed phase system there is evidence of the reduction of the binary Mo-N phase present to Mo metal.

The formation of nickel molybdenum nitride was shown to be possible from the hydrated nickel molybdate, this process is highly reproducible and although this has an impurity phase present of nickel metal, the formation of the nitride is facile. The structure of the nitride was confirmed using PXRD and PND data against which the reported structure was refined. The level of Ni impurity remained constant throughout the study of the nitride and although this is present the structure could still be confirmed by diffraction. However the microanalysis gives a figure for the amount of nitrogen present which is higher than expected and even taking into account the Ni impurity phase present, other phases must be present to give such a reading for the nitrogen content, as such this phase or phases must be amorphous as they do not show up in the diffraction data collected.

Reactivity for the nickel phase is the lowest of the three ternary nitrides studied during this work giving a reactivity series of $Ni_2Mo_3N < Fe_3Mo_3N < Co_3Mo_3N$. This could be related to the mobility of the nitrogen within the structure of the nitrides with the Ni_2Mo_3N crystallising into a β-Mn structure which has very constrained geometry which does not allow the nitrogen to move. However the differences seen in the η-carbide structures of Co_3Mo_3N and Fe_3Mo_3N must be related to the interactions between the transistion metal and the nitrogen as the co-ordination geometry for the Mo-N sublattices are almost identical for the two systems. This would lead to the postulation that the iron has a stronger binding effect on the nitrogen than the cobalt making it unwilling to allow the nitrogen to migrate from the 16c to 8a site.

5.5   References

[1] D S. Bem, C. P. Gibson and H-C zur Loye; Chem. Mater.; 5 (1993) 397.

[2] K. S. Weil and P. N. Kumta: Mater. Sci. Eng. B; 38 (1996) 109.

[3] X. Z. Chen, J. L. Dye, H. A. Eick, S. H. Elder and K.-L Tsai; Chem. Mater.; 9 (1997) 1172.

[4] S. Alconchel, F. Sapina, D. Beltran and A. Beltran; J. Mater. Chem.; 9 (1999) 749.

[5] K. S. Weil, P. N. Kumta and J. Grins; J. Solid State Chem.; 146 (1999) 22.

[6] T. J. Prior and P. D. Battle; J. Solid State Chem.; 172 (2003) 138.

[7] T. J. Prior and P. D. Battle; J. Mater. Chem.; 14(2004) 3001.

[8] T. J. Prior S. E. Oldham, V. J. Couper and P. D. Battle; Chem. Mater.; 17 (2005) 1867.

[9] S. K. Jackson, R. C. Layland and H-C zur Loye; J. Alloys and Compds.; 219 (1999) 94.

[10] D. Mckay; Catalysis over Molybdenum Containing Nitride Materials; PhD Thesis; University of Glasgow, 2007.

[11] A. Boultif and D. Louer; J. Appl. Cryst.; 37 (2004) 724.

6   Quaternary Nitrides – Iron cobalt molybdenum nitride

6.1   Introduction

Quaternary nitrides with the eta-carbide structure have been studied in detail in terms of variation of their properties as the electron concentration on the 32e and 16d changes. This work has focussed on the $Fe_{3-x}Co_xMo_3N$ family and Ni_2GaMo_3N.[1] The study has shown that the synthesis of the iron and cobalt family is facile under the solid state preparative conditions used however the addition of gallium to the Ni_2Mo_3N phase resulted in mixed phase products containing both filled β–Mn and η–carbide structures.

The ability to form the η–carbide structured quaternary nitrides is of interest as the difference in the reactivity and subsequent phase changes seen for the ternary iron and cobalt systems allows for a study to investigate what effect the addition of both iron and cobalt has on the reactivity and also to what extent there maybe is a structural change dependent on compostion.

The addition of germanium into the η–carbide structured nitrides was investigated following the reduction of germanium (VI) oxide by Barker et al. when preparing the germanide $FeMo_4Ge_3$.[2] Other quaternary systems with the η–carbide structure such as Co_2GeMo_3N and the nickel and iron substituted variants of these have also been investigated.[3]

A complete examination and discussion of the synthetic routes and structures of various quaternary nitrides has been shown by Kift.[4]

6.2   Experimental

6.2.1   Preparation

A series of iron cobalt molybdenum oxides were the starting compounds for the synthesis of the resultant quaternary nitrides. The oxides were synthesised using methods similar to those used for the preparation of the ternary nitrides of cobalt and iron (Sections 4.2.1 and 5.2.1.1).

Hence, the mixed metal molybdates were the starting point for the formation of the quaternary nitrides. The molybdates were formed by dropwise addition of iron chloride $(FeCl_2\cdot 2H_2O)$ and cobalt nitrate $(Co(NO_3)_2\cdot 6H_2O)$ to a 0.66 M solution of sodium molybdate $(Na_2MoO_4\cdot 2H_2O)$. The resultant precipitate was filtered, washed and dried,

calcined in air at 773 K and then reacted under ammonia following the same procedure as described for the cobalt system (Section 4.2.1). A two hour pre-treatment procedure was subsequently employed at 973 K under 3:1 H_2/N_2 gas.

In order to obtain a range of compounds throughout the iron-cobalt series, a variety of molybdate phases were synthesised. The target iron cobalt molybdate stoichiometries are presented in Table 6-1.

Table 6-1: Conditions for synthesis of molybdates used to form quaternary nitrides.

Sample	Nominal Stoichiometry	Mass of material / g		
		$Na_2MoO_4 \cdot 2H_2O$	$FeCl_2 \cdot 2H_2O$	$Co(NO_3)_2 \cdot 6H_2O$
1	$Fe_{0.2}Co_{0.8}MoO_4$		0.745	4.729
2	$Fe_{0.4}Co_{0.6}MoO_4$	4.839	1.491	3.638
3	$Fe_{0.6}Co_{0.4}MoO_4$		2.485	2.183
4	$Fe_{0.8}Co_{0.2}MoO_4$		3.231	1.091

The series encompasses a broad range of Co/Fe ratios. This allowed for a complete picture to be obtained for the structural and reactivity differences in the phases as more iron was doped into the system.

6.2.2 Characterisation

Powder X-ray diffraction (PXRD) data were collected for the samples after the respective nitridation stages described above. Data collection was conducted on a Panalytical Xpert diffractometer, utilising Cu-K_α radiation at room temperature. The samples were prepared as previously described in Section 2.4.1.1. The patterns were collected using a step scan of 0.02 °2θ over a 5 – 85 °2θ range and a time per step of 0.8 seconds. Diffraction data used for Rietveld refinements employed step times and ranges of 11 seconds and 5 – 105 °2θ respectively.

In addition to the X-ray data, powder neutron diffraction (PND) data were collected on the POLARIS instrument at ISIS. Experiments were performed on the samples at room temperature using three banks of detectors. Samples were loaded into vanadium sample cans, to a maximum height of 40 mm and data collected as described in Section 2.4.1.2.1. Data were collected for approximately three hours in each case.

6.2.3   Activity testing

The samples were tested at ambient pressure for their potential as ammonia synthesis catalysts. The method employed used a fixed bed reactor through which reactant gas (60 mLmin^{-1}) of either 3:1 H_2/N_2 gas or 3:1 H_2/Ar gas was flowed. The production of ammonia was measured by the change in conductivity of a 200 mL, 0.00108 molL^{-1} sulfuric acid solution as reactor gases passed through the solution.

The reactions were conducted on 0.4 g of sample which was pre-treated at 973 K under 3:1 H_2/N_2 gas flowing at 60 mLmin^{-1} for two hours prior to the reaction being started. The reactions were conducted under either 3:1 H_2/N_2 gas at 673 K or under 3:1 H_2/Ar gas during which a variable temperature profile was employed.

6.3   Results and Discussion

6.3.1   Structural study

The same general method as applied to the formation of the ternary phase nitrides, was used for the quaternary systems. Iron (II) chloride was employed as an iron source in order to obtain a single phase nitride and sodium molybdate was used as the molybdenum source as it is known to be a suitable precursor for the ternary phases of both cobalt and iron.

The molybdates were all red-brown in colour and upon calcination turned deeper red colour. Molybdate formation was not studied further as nitride formation was successfully achieved. The nitrides were analysed through PXRD and the patterns collected showed a single phase system in all four cases. The patterns were matched to those from ternary phase analogues.

Indexing of the patterns collected gave lattice parameters which are shown in Table 6-2. These are in good agreement with values for the ternary end member phases and also to values for the related quaternary phases as reported by Prior et al.[1] The differences between those previously reported and the nitrides synthesised here are compared after each stage of the reaction.

Table 6-2: Lattice parameters for quaternary systems.

	Actual stoichiometry	Lattice parameter / Å
Sample 1	$Fe_{0.6}Co_{2.4}Mo_3N$	11.0451(5)
Sample 2	$Fe_{1.2}Co_{1.8}Mo_3N$	11.0552(7)
Sample 3	$Fe_{1.8}Co_{1.2}Mo_3N$	11.0560(4)
Sample 4	$Fe_{2.4}Co_{0.6}Mo_3N$	11.0607(4)

Since the X-ray scattering from Fe and Co is almost identical there is an inability to derive comparative structures of quaternary phases via PXRD experiments. Hence a series of PND experiments were undertaken. Room temperature (295 K) measurements were used to confirm the structure of the proposed nitrides. The initial model used a single quaternary nitride phase, based on the structures reported by Prior et al.[1] The background was fitted to a reciprocal interpolation function (background function 8 in GSAS). Lattice parameters were then refined, followed by the atomic positions which when refined until stable, allowed the peak shape to be refined. When the refinement had stabilised, the thermal parameters were varied anisotropically. In addition, absorption factors were refined. Constraints were placed on the occupancy of the shared atomic positions and the thermal parameters for the iron and cobalt sites constraining the atom sharing sites to be identical to each other. The results for the refinement against the PND data for Sample 1 are shown in Figure 6-1, Table 6-3and Table 6-4.
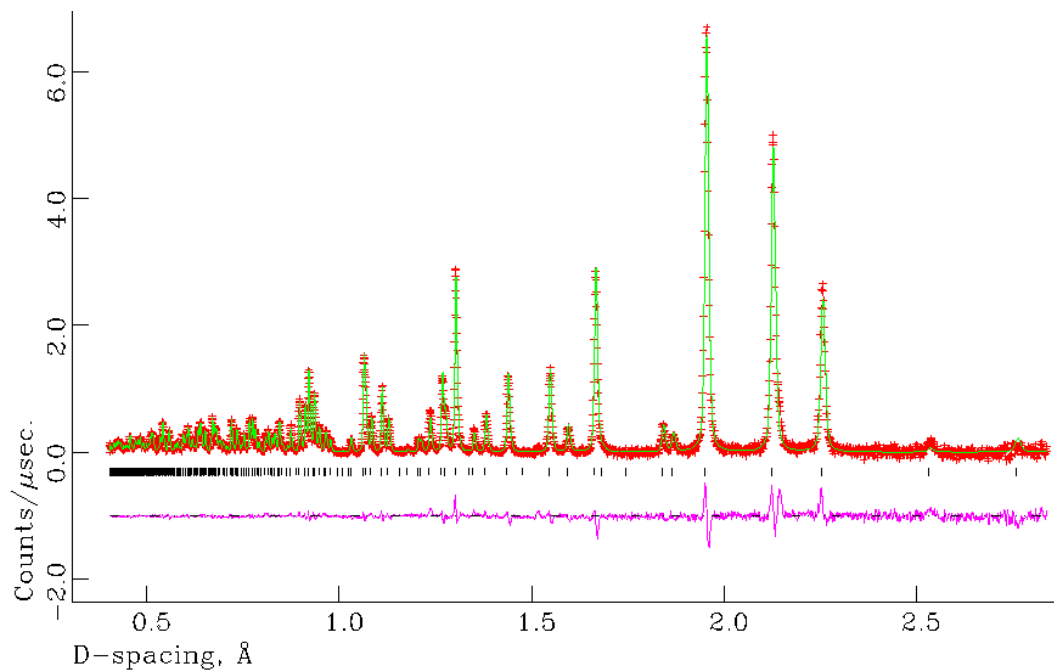
Figure 6-1: Final profile fit obtained from the refinement against *in-situ* PND at 295 K for Sample 1 - one quaternary phase only. Nominal one single 331 phase.

The observed data are crosses, the calculated profile the solid line and lower continuous line the difference plot. Tick marks show allowed reflection positions.

Table 6-3: Crystallographic parameters for Sample 1 from PND data.

Parameter	Value
Formula [$Fe_xCo_yMo_3N$]	$Fe_{1.084}Co_{1.916}Mo_3N$
Crystal system	Cubic
Space group	Fd-3m
Formula mass / $gmol^{-1}$	7604.444
Cell parameter, a / Å	11.04737(8)
Unit-cell volume / Å^3	1348.27(2)
Calculated density ρ_x / gcm^{-3}	9.366
Number of observations	7786
Number of variables	35
R_p / %	3.76
R_{wp} / %	2.40
χ^2	2.78

Table 6-4: Refined atomic parameters for Sample 1 from PND data.

Atoms / Site	x	y	z	Occupancy	100× U_{iso} /U_{eq} (Å^2)
Fe 1 (32e) Co 1 (32e)	0.29333(7)	0.29333(7)	0.29333(7)	0.232(5) 0.768(5)	0.612(37)
Fe 2 (16d) Co2 (16d)	0.500000	0.500000	0.500000	0.620(4) 0.380(4)	0.380(24)
Mo (48f)	0.32282(6)	0.125000	0.125000	1.00	0.307(11)
N (16c)	0.000000	0.000000	0.000000	1.00	0.649(20)

As can be seen from the difference plots the model does not provide a completely convincing fit to the data. The broadening of the 331 phase reflections led to a two phase model being investigated. The results for the refinements are shown in Table 6-5 – Table 6-9 and Figure 6-2 – Figure 6-5.

Table 6-5: Crystallographic parameters for quaternary nitrides from PND data.

Parameter	Value			
	Sample 1	**Sample 2**	**Sample 3**	**Sample 4**
Formula [$Fe_xCo_yMo_3N$]	$Fe_{1.052}Co_{1.948}$	$Fe_{1.619}Co_{1.381}$	$Fe_{2.291}Co_{0.709}$	$Fe_{2.682}Co_{0.318}$
Crystal system	Cubic			
Space group	Fd-3m			
Phase Fraction / %	54	51	88	100
Formula mass / gmol^{-1}	7606.066	7578.120	7544.840	7530.930
Cell parameter, *a* / Å	11.0315(2)	11.0407(2)	11.0599(2)	11.0634(3)
Unit-cell volume / Å^3	1342.45(5)	1345.84(5)	1352.85(4)	1354.15(6)
Calculated density ρ_x / gcm^{-3}	9.408	9.350	9.261	9.235
Formula [$Fe_xCo_yMo_3N$]	$Fe_{1.064}Co_{1.936}$	$Fe_{1.61}Co_{1.39}$	$Fe_{1.22}Co_{1.78}$	
Crystal system	Cubic			
Space group	Fd-3m			
Phase Fraction / %	46	49	12	
Formula mass / gmol^{-1}	7605.481	7578.463	7598.010	
Cell parameter, *a* / Å	11.0588(3)	11.0697(2)	11.052(1)	
Unit-cell volume / Å^3	1352.46(5)	1356.46(5)	1350.0(3)	
Calculated density ρ_x / gcm^{-3}	9.338	9.277	9.346	
Number of observations	4017	3585	3585	4004
Number of variables	29	29	30	22
R_p / %	3.95	3.68	2.44	3.29
R_{wp} / %	1.98	1.97	1.57	1.58
χ^2	2.871	2.907	2.217	0.900

Only one phase was refined in the case of Sample 4.

Table 6-6: Refined atomic parameters for Sample 1 from PND data.

Atoms / Site	x	y	z	Occupancy	$100\times$ U_{iso}/U_{eq} (Å^2)
Fe 1 (32e)	0.2933(2)	0.2933(2)	0.2933(2)	0.225(15)	0.55(9)
Co 1 (32e)				0.775(15)	
Fe 2 (16d)	0.500000	0.500000	0.500000	0.602(12)	0.30(6)
Co2 (16d)				0.398(12)	
Mo (48f)	0.3229(2)	0.125000	0.125000	1.00	0.34(2)
N (16c)	0.000000	0.000000	0.000000	1.00	0.66(5)
Atoms / Site	**x**	**y**	**z**	**Occupancy**	$100\times$ U_{iso}/U_{eq} (Å^2)
Fe 1 (32e)	0.2931(2)	0.2931(2)	0.2931(2)	0.211(16)	0.51(10)
Co 1 (32e)				0.789(16)	
Fe 2 (16d)	0.500000	0.500000	0.500000	0.642(14)	0.56(7)
Co2 (16d)				0.358(14)	
Mo (48f)	0.32271(17)	0.125000	0.125000	1.00	0.31(2)
N (16c)	0.000000	0.000000	0.000000	1.00	0.61(5)
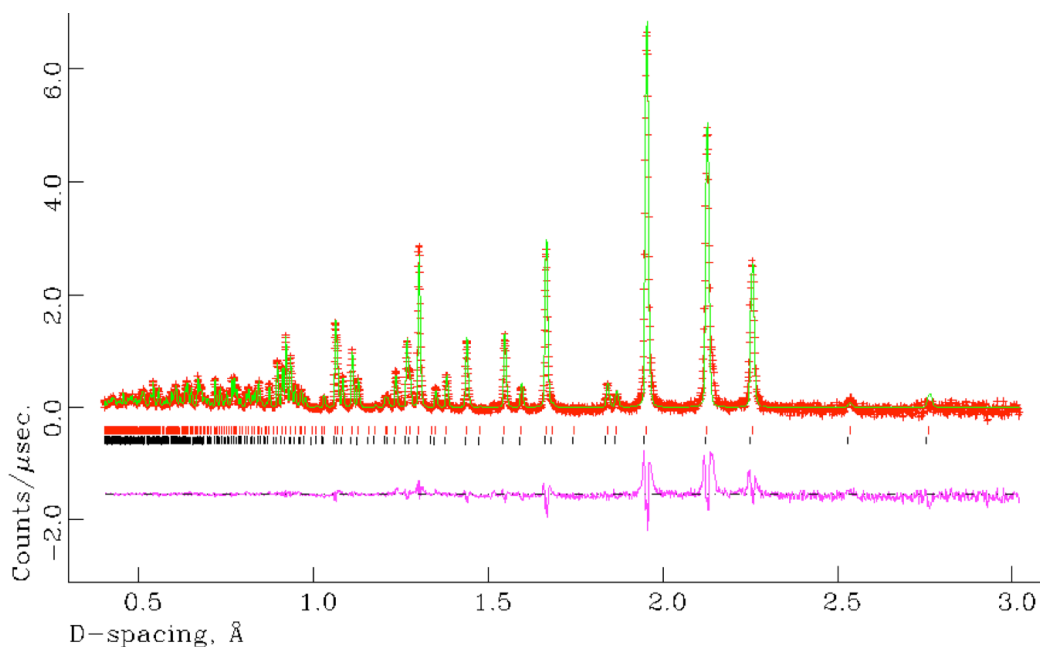
Figure 6-2: Final profile fit obtained from the refinement against PND data at 295 K for Sample 1.

The observed data are crosses, the calculated profile the solid line and lower continuous line the difference plot. Tick marks show allowed reflection positions. Red Tick-marks - $Fe_{1.064}Co_{1.936}$, Black tick-marks - $Fe_{1.052}Co_{1.948}$.

Table 6-7: Refined atomic parameters for Sample 2 from PND data.

Atoms / Site	x	y	z	Occupancy	100× U_{iso} /U_{eq} (Å^2)
Fe 1 (32e) Co 1 (32e)	0.2938(2)	0.2938(2)	0.2938(2)	0.398(17) 0.602(17)	0.55(8)
Fe 2 (16d) Co2 (16d)	0.500000	0.500000	0.500000	0.823(16) 0.177(16)	0.57(6)
Mo (48f)	0.3222(2)	0.125000	0.125000	1.00	0.34(3)
N (16c)	0.000000	0.000000	0.000000	1.00	0.45(4)
Atoms / Site	x	y	z	Occupancy	100× U_{iso} /U_{eq} (Å^2)
Fe 1 (32e) Co 1 (32e)	0.2935(2)	0.2935(2)	0.2935(2)	0.389(17) 0.611(17)	0.37(7)
Fe 2 (16d) Co2 (16d)	0.500000	0.500000	0.500000	0.832(17) 0.168(17)	0.53(6)
Mo (48f)	0.3223(2)	0.125000	0.125000	1.00	0.31(3)
N (16c)	0.000000	0.000000	0.000000	1.00	0.61(5)
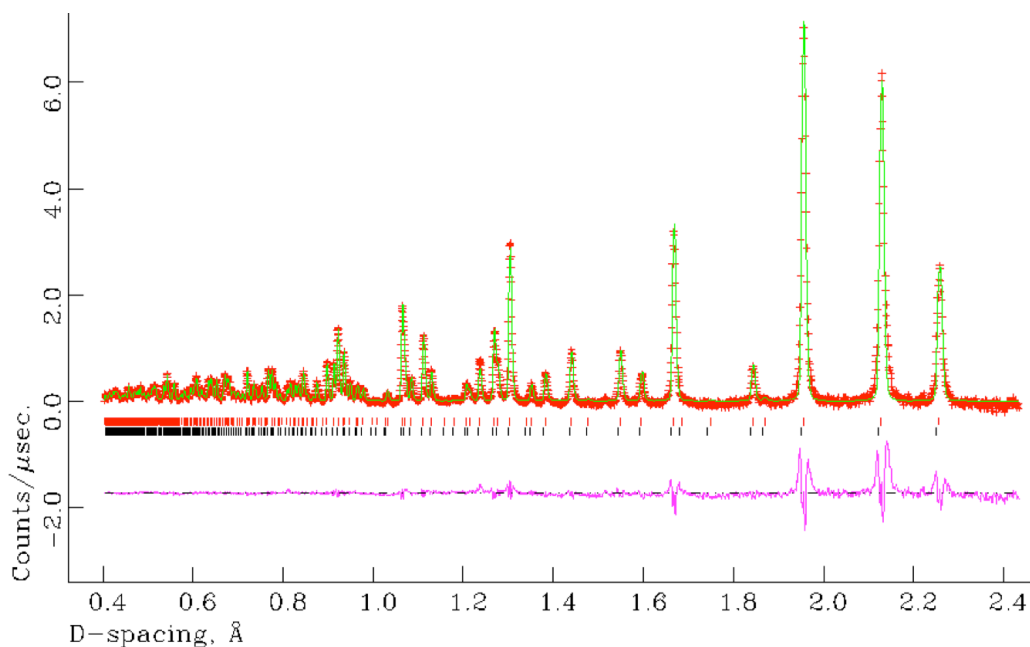
Figure 6-3: Final profile fit obtained from the refinement against PND data at 295 K for Sample 2.

The observed data are crosses, the calculated profile the solid line and lower continuous line the difference plot. Tick marks show allowed reflection positions. Red Tick-marks - $Fe_{1.61}Co_{1.39}$, Black tick-marks - $Fe_{1.619}Co_{1.81}$.

Table 6-8: Refined atomic parameters for Sample 3 from PND data.

Atoms / Site	x	y	z	Occupancy	100× U_{iso}/U_{eq} (Å²)
Fe 1 (32e)	0.29357(8)	0.29357(8)	0.29357(8)	0.690(12)	0.44(3)
Co 1 (32e)				0.310(12)	
Fe 2 (16d)	0.500	0.500	0.500	0.911(11)	0.42(3)
Co2 (16d)				0.089(11)	
Mo (48f)	0.3224(1)	0.125	0.125	1.00	0.27(2)
N (16c)	0.000	0.000	0.000	1.00	0.45(3)
Atoms / Site	x	y	z	Occupancy	100× U_{iso}/U_{eq} (Å²)
Fe 1 (32e)	0.301(2)	0.301(2)	0.301(2)	0.16(9)	1.50‡
Co 1 (32e)				0.84(9)	
Fe 2 (16d)	0.500	0.500	0.500	0.90(10)	1.9(6)
Co2 (16d)				0.10(10)	
Mo (48f)	0.312(2)	0.125	0.125	1.00	0.83(19)
N (16c)	0.000	0.000	0.000	1.00	0.50(25)

‡ - parameter fixed.
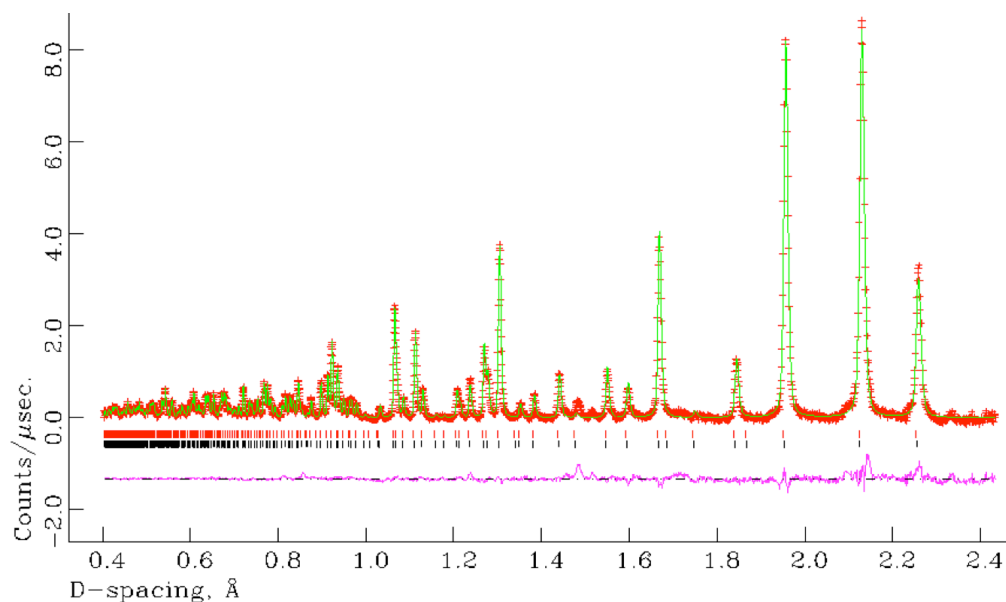
Figure 6-4: Final profile fit obtained from the refinement against PND data at 295 K for Sample 3.

The observed data are crosses, the calculated profile the solid line and lower continuous line the difference plot. Tick marks show allowed reflection positions.
Red Tick-marks – $Fe_{2.291}Co_{0.709}$, Black tick-marks - $Fe_{1.22}Co_{1.78}$.

Table 6-9: Refined atomic parameters for Sample 4 from PND data.

Atoms / Site	x	y	z	Occupancy	$100\times$ U_{iso}/U_{eq} (Å^2)
Fe 1 (32e) Co 1 (32e)	0.29385(5)	0.29385(5)	0.29385(5)	0.841(8) 0.159(8)	0.401(23)
Fe 2 (16d) Co2 (16d)	0.500	0.500	0.500	1.00 0.00	0.529(18)
Mo (48f)	0.32171(8)	0.125	0.125	1.00	0.294(15)
N (16c)	0.000	0.000	0.000	1.00	0.369(19)
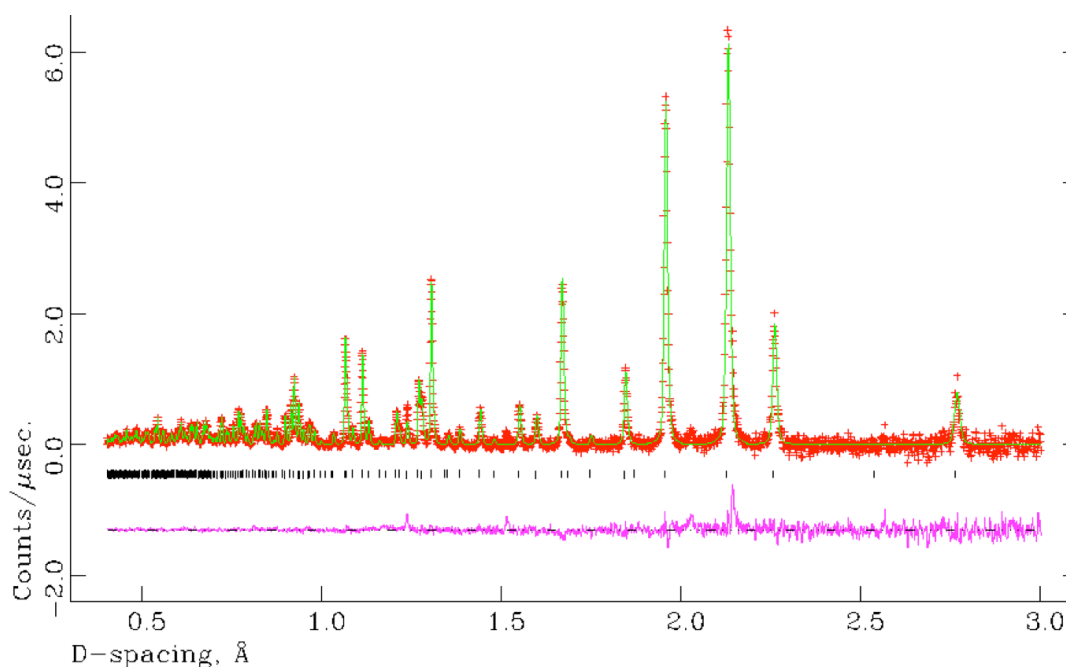
Figure 6-5: Final profile fit obtained from the refinement against PND data at 295 K for Sample 4.

The observed data are crosses, the calculated profile the solid line and lower continuous line the difference plot. Tick marks show allowed reflection positions.

Although the data for samples 1 and 2 allowed both phases to be modelled, this was not possible for sample 3 as the profile parameters could not be refined successfully for the second phase. This could be attributed to the relatively low levels of the second phase present in the sample. In the case of sample 4, the presence of a second phase could not be ascertained, the quality of the fit would indicate that sample 4 maybe a single phase sample.

Analysis of the refined parameters to those shown previous by Prior and Battle, shows that the parameters and stoichiometries obtained are different to those previously shown which is indicated in Figure 6-6.
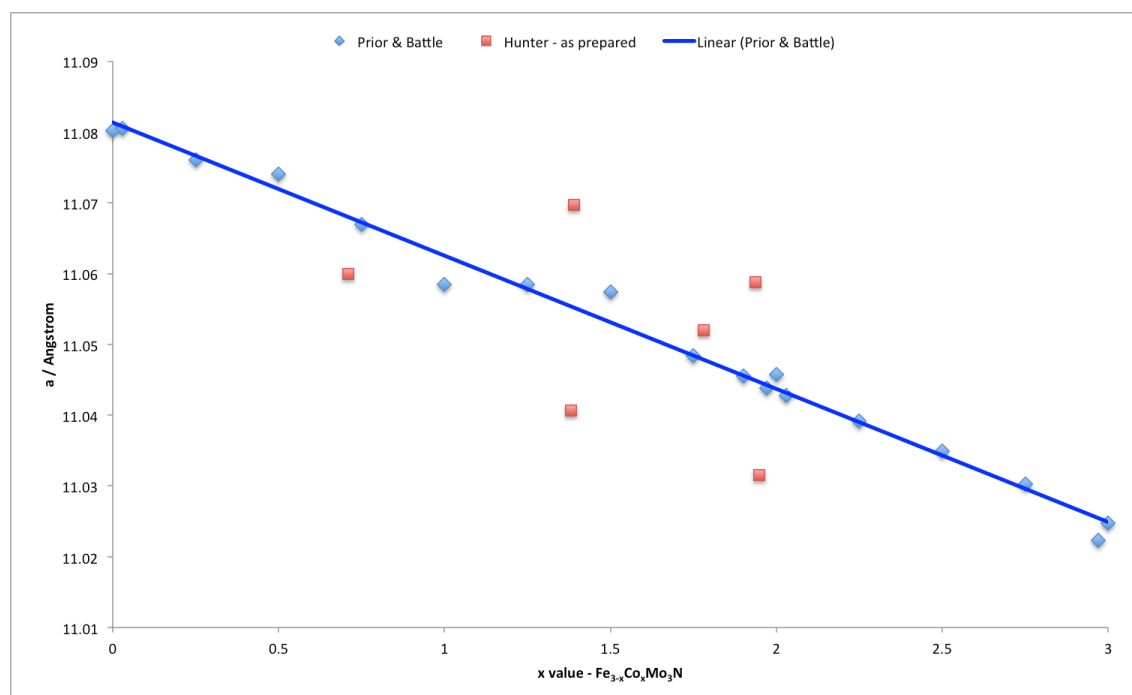
Figure 6-6: Comparison of lattice parameters and stoichiometry of quaternary nitrides as prepared.

The differences in the stoichiometry between those seen by Prior and those synthesised here may be related to the synthetic procedure, which is strictly controlled by Prior who uses a solid solution of the oxides compared with the molybdate ammonolysis used in this study.

6.3.2   Activity Study

In order to measure the activity of the quaternary nitrides and make comparison with the related ternary systems, ambient pressure ammonia synthesis efficacy was measured.

Two samples were tested, samples 1 and 4, to allow comparison of both iron rich and cobalt rich systems. Given the fact that the synthesis of single phase quaternary compounds was not achieved, attributing the activity of a single stoichiometry is obviously not possible.

The activity of the two systems under 3:1 H_2/N_2 gas at 673 K is shown in Figure 6-7. These have very different activities and the rates of reaction are 148 $\mu molh^{-1}g^{-1}$ and 65 $\mu molh^{-1}g^{-1}$ for samples 1 and 4 respectively. Sample 1 has a slightly greater efficacy for the formation of ammonia under 3:1 H_2/N_2 gas than the ternary cobalt system previously discussed in Section 4.3.2.2.
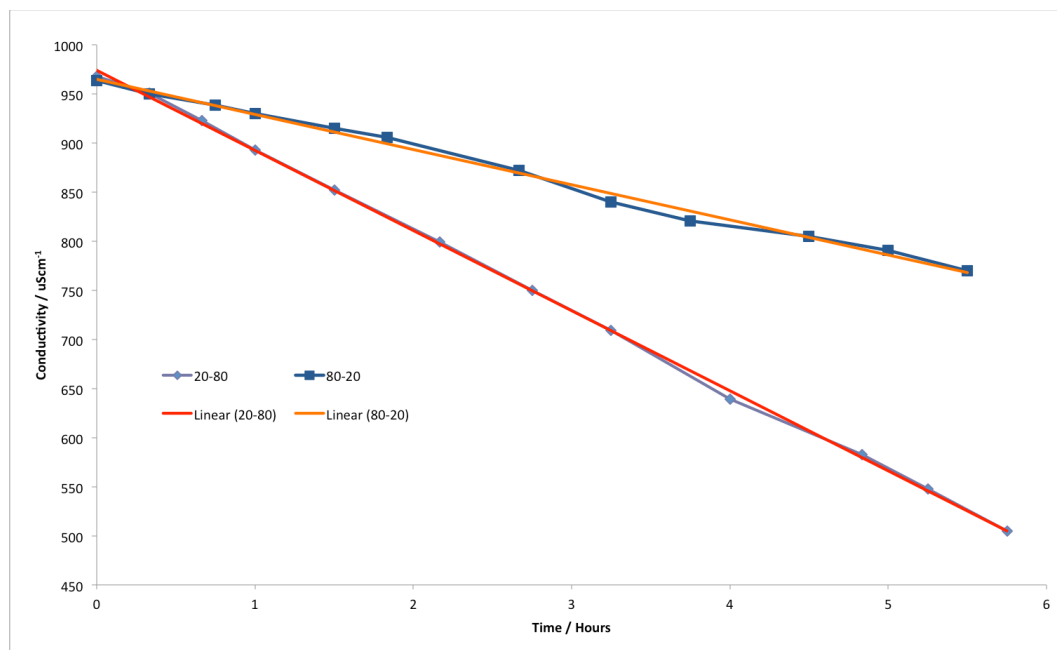
Figure 6-7: Reaction profiles for the quaternary nitride systems under 3:1 H_2/N_2 gas at 673 K.

The post-reaction microanalysis of the samples has shown that there is no change in the nitrogen content of the systems upon reaction as shown in Table 6-10. This is consistent with the results seen previously for the two end members of the series, i.e. Co_3Mo_3N and Fe_3Mo_3N.

Table 6-10: Microanalysis results for quaternary nitrides post 3:1 H_2/N_2 gas.

Sample	As prepared	Post Rxn 3:1 H_2/N_2 gas @ 673 K for 6 hrs
1	2.95(2)	3.01(6)
2	2.98(3)	2.93(8)
3	3.02(4)	2.99(3)
4	2.98(3)	2.97(4)

The post-reaction PXRD patterns showed no change from those collected prior to reaction. The data leads to the conclusion that the quaternary phases behave in a similar way to the ternary systems under 3:1 H_2/N_2 gas and that a proposed reaction pathway is via surface NH_x species which can be removed and replaced at 673 K under 3:1 H_2/N_2 gas.

The quaternary systems were reacted under 3:1 H_2/Ar gas to test the activity of the nitrogen within the lattice and to determine if the nitrogen would relocate as in the Co-Mo-N system or if it is immobile as in the Fe-Mo-N system.

The reaction profiles for the two samples are shown in Figure 6-8 and Figure 6-9. Both profiles show similar features to those seen previously for the ternary nitrides, with a decrease in conductivity initially which is attributed to surface NH_x species being removed from the sample and then a gradual slowing in the production of ammonia. On further heating, additional production of ammonia occurs as indicated by the decrease in conductivity measured. This is similar to the behaviour of the other systems tested as described in Sections 4.3.2.2 and 5.3.2.2.
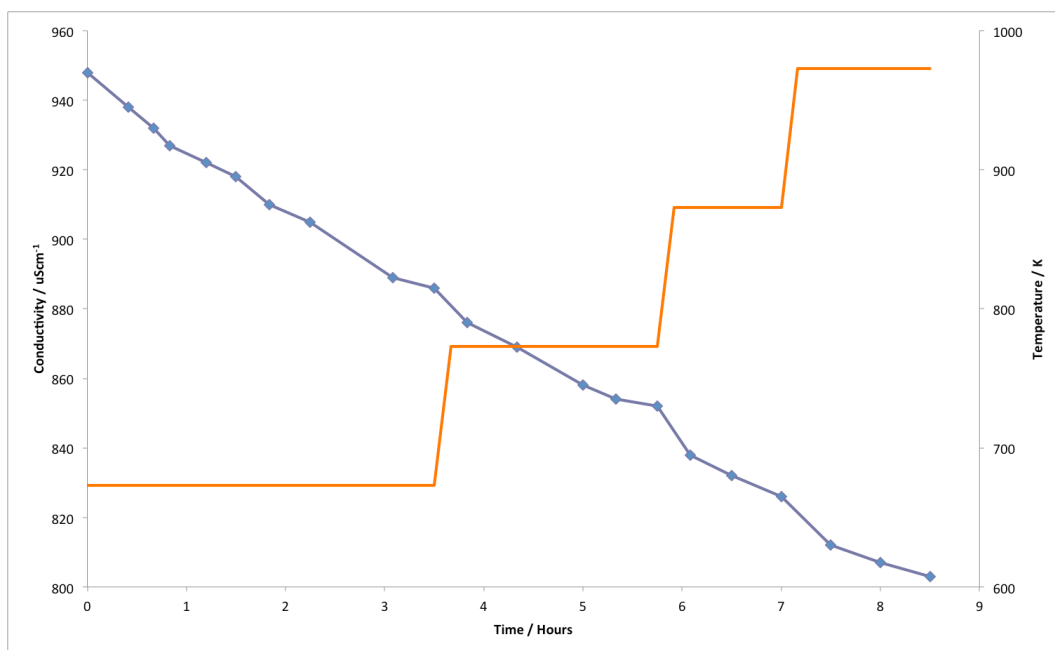
Figure 6-8: Reaction profile for Sample 1 under 3:1 H$_2$/Ar gas.
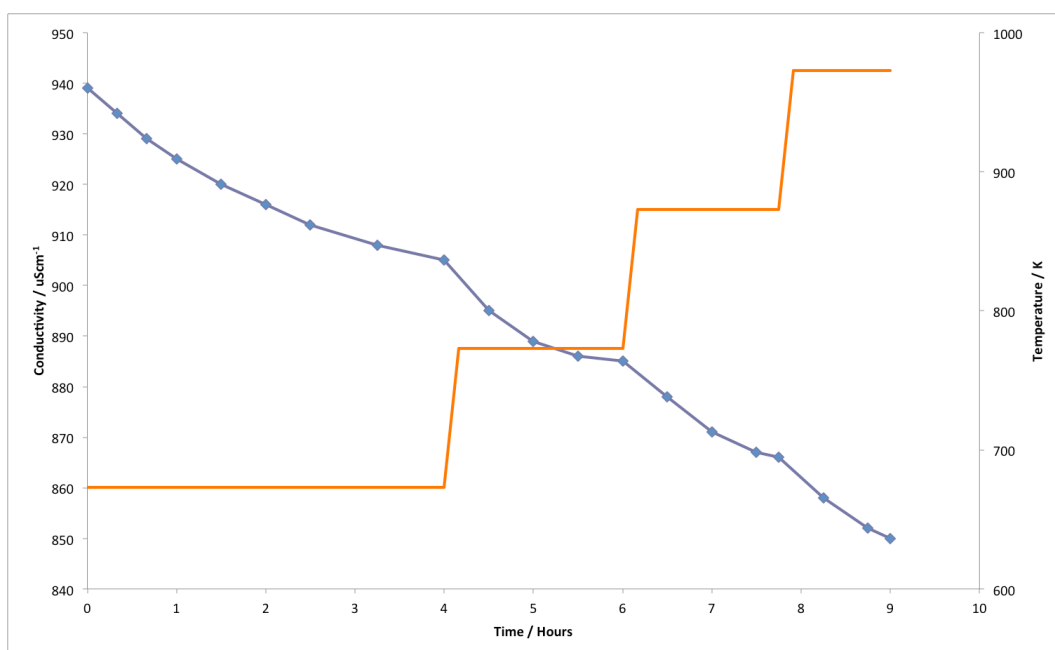
Figure 6-9: Reaction profile for Sample 4 under 3:1 H$_2$/Ar gas.

The results of testing show that sample 1 is more active than sample 4. The sample is also slightly more active than the ternary cobalt phase (Co$_3$Mo$_3$N) as described previously. The results indicate that the low levels of iron present had a positive effect on the activity of the system.

The post-reaction PXRD and microanalysis results showed distinct differences between the two samples. Sample 1 showed signs of splitting into at least two distinct phases whereas sample 4 shows no change from the pattern collected prior to the reaction. The splitting in sample 1 could be accounted for by one of the quaternary phases reducing to

a '661' phase as seen in Co_3Mo_3N system while the other phase remains unchanged, as seen in the Fe_3Mo_3N system.

The differences in the microanalysis results are seen in Table 6-11, they indicate that sample 1 has lost about 30 % of its nitrogen, whereas sample 4 has retained almost all of its nitrogen.

Table 6-11: Microanalysis results for quaternary nitrides.

Sample	Nitrogen wt%		
	As prepared	Post Rxn 3:1 H_2/N_2 gas @ 673 K for 6 hrs	Post Rxn 3:1 H_2/Ar gas @ 973 K for 6 hrs
1	2.95(2)	3.01(6)	2.03(4)
4	2.98(3)	2.97(4)	2.90(3)
2*	2.98(3)	2.93(8)	2.45(7)
3*	3.02(4)	2.99(3)	2.89(6)

* Results for samples 2 and 3 taken from preparative procedure for PND samples, no reactivity tests were conducted on these samples – see below.

As previously discussed the quaternary systems are hard to quantify by refinement against the PXRD data and so data collected from *ex-situ* PND experiments were used for refining of structures. The limited time available on the POLARIS diffractometer allowed for data from only part of the series to be collected. The results of the refinements against samples 1, 2 and 3 reacted under 3:1 H_2/Ar gas at 973 K for six hours are presented below. The refinement results are shown in Table 6-12 – Table 6-15 and Figure 6-10 – Figure 6-12.

Table 6-12: Crystallographic parameters for quaternary nitrides treated under 3:1 H_2/Ar gas from PND data.

Parameter	Value		
	Sample 1	Sample 2	Sample 3
Formula [$Fe_xCo_yMo_zN$]	$Fe_{2.146}Co_{3.854}Mo_6$	$Fe_{3.244}Co_{2.756}Mo_6$	$Fe_{2.124}Co_{0.876}Mo_3$
Crystal system	Cubic		
Space group	Fd-3m		
Phase Fraction / %	85	25	53
Formula mass / $gmol^{-1}$	7492.950	7465.874	7553.126
Cell parameter, a / Å	10.90587(9)	10.9101(2)	11.0498(2)
Unit-cell volume / Å^3	1297.12(2)	1298.63(4)	1349.15(3)
Calculated density ρ_x / gcm^{-3}	9.592	9.547	9.296
Formula [$Fe_xCo_yMo_3N$]	$Fe_{1.271}Co_{1.729}$	$Fe_{1.691}Co_{1.309}$	$Fe_{2.482}Co_{0.518}$
Crystal system	Cubic		
Space group	Fd-3m		
Phase Fraction / %	15	75	47
Formula mass / $gmol^{-1}$	7595.229	7574.568	7535.430
Cell parameter, a / Å	11.0635(5)	11.05671(8)	11.07230(22)
Unit-cell volume / Å^3	1354.2(1)	1351.69(2)	1357.42(5)
Calculated density ρ_x / gcm^{-3}	9.313	9.305	9.218
Number of observations	4119	3950	3950
Number of variables	33	34	28
R_p / %	2.90	2.42	4.21
R_{wp} / %	1.46	1.29	2.09
χ^2	1.638	1.325	4.210

Top half of the table relates to the shifted phase, the bottom half relates to the unshifted phase.

Table 6-13: Refined atomic parameters for sample 1 post 3:1 H$_2$/Ar gas from PND data.

Atoms / Site	x	y	z	Occupancy	100× U$_{iso}$/U$_{eq}$ (Å^2)
Fe 1 (32e)	0.29340(8)	0.29340(8)	0.29340(8)	0.217(6)	0.44(4)
Co 1 (32e)				0.783(6)	
Fe 2 (16d)	0.500000	0.500000	0.500000	0.639(6)	0.74(3)
Co2 (16d)				0.361(6)	
Mo (48f)	0.32058(7)	0.125000	0.125000	1.00	0.35(1)
N (8a)	0.125000	0.125000	0.125000	1.00	0.50(2)
Atoms / Site	**x**	**y**	**z**	**Occupancy**	**100× U$_{iso}$/U$_{eq}$ (Å^2)**
Fe 1 (32e)	0.2935(5)	0.2935(5)	0.2935(5)	0.235(26)	0.75‡
Co 1 (32e)				0.765(26)	
Fe 2 (16d)	0.500000	0.500000	0.500000	0.801(38)	0.89(16)
Co2 (16d)				0.199(38)	
Mo (48f)	0.3206(4)	0.125000	0.125000	1.00	0.29(5)
N (16c)	0.000000	0.000000	0.000000	1.00	0.53(11)

‡ - parameter fixed.
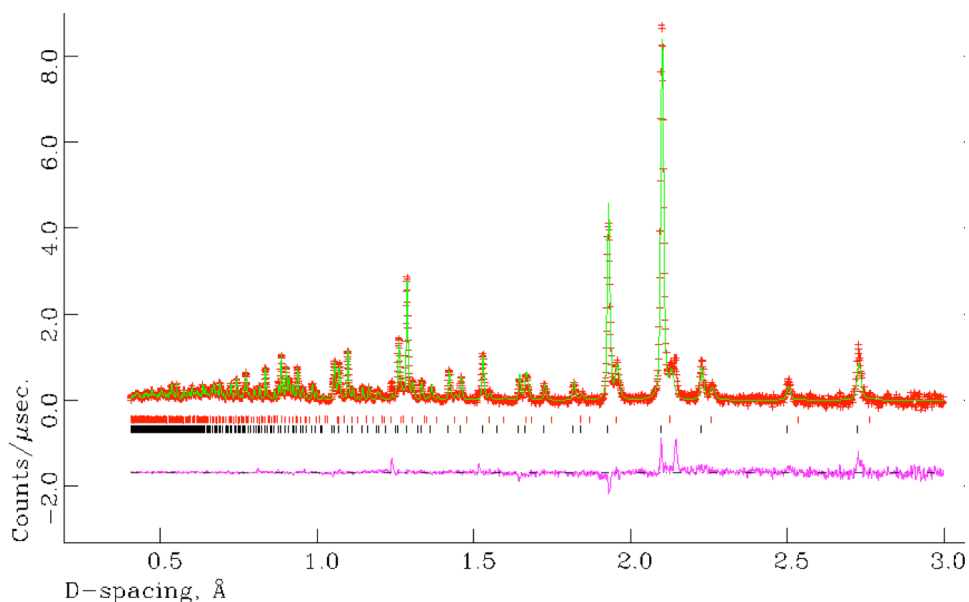
Figure 6-10: Final profile fit obtained from the refinement against PND data at 295 K for sample 1 post 3:1 H$_2$/Ar gas.

The observed data are crosses, the calculated profile the solid line and lower continuous line the difference plot. Tick marks show allowed reflection positions. Red Tick-marks – Fe$_{1.271}$Co$_{1.729}$Mo$_3$N, Black tick-marks – Fe$_{2.416}$Co$_{3.854}$Mo$_6$N.

Table 6-14: Refined atomic parameters for sample 2 post 3:1 H$_2$/Ar gas from PND data.

Atoms / Site	x	y	z	Occupancy	100× U$_{iso}$/U$_{eq}$ (Å^2)
Fe 1 (32e)	0.2938(2)	0.2938(2)	0.2938(2)	0.440(19)	0.61(8)
Co 1 (32e)				0.560(19)	
Fe 2 (16d)	0.500000	0.500000	0.500000	0.742(18)	0.65(8)
Co2 (16d)				0.258(18)	
Mo (48f)	0.3208(2)	0.125000	0.125000	1.00	0.28(3)
N (8a)	0.125000	0.125000	0.125000	1.00	0.32(5)
Atoms / Site	**x**	**y**	**z**	**Occupancy**	**100× U$_{iso}$/U$_{eq}$ (Å^2)**
Fe 1 (32e)	0.29397(7)	0.29397(7)	0.29397(7)	0.423(7)	0.45(3)
Co 1 (32e)				0.577(7)	
Fe 2 (16d)	0.500000	0.500000	0.500000	0.845(7)	0.49(2)
Co2 (16d)				0.155(7)	
Mo (48f)	0.32206(7)	0.125000	0.125000	1.00	0.28(1)
N (16c)	0.000000	0.000000	0.000000	1.00	0.44(2)
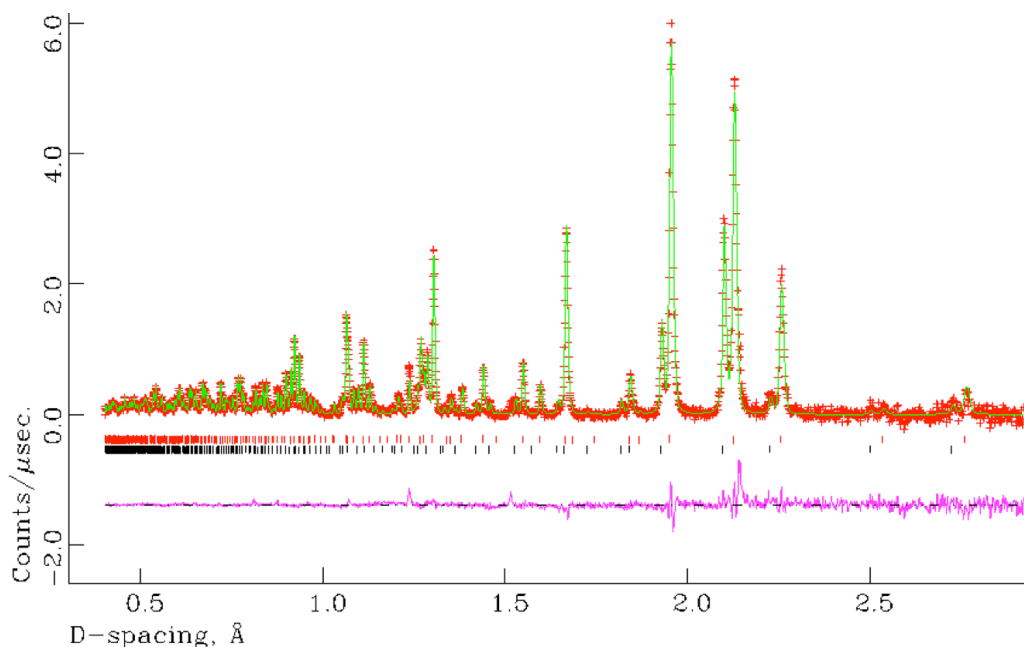
Figure 6-11: Final profile fit obtained from the refinement against PND data at 295 K for Sample 2 post 3:1 H$_2$/Ar gas.

The observed data are crosses, the calculated profile the solid line and lower continuous line the difference plot. Tick marks show allowed reflection positions. Red Tick-marks – Fe$_{3.244}$Co$_{2.756}$Mo$_6$N, Black tick-marks – Fe$_{1.691}$Co$_{1.309}$Mo$_3$N.

Table 6-15: Refined atomic parameters for sample 3 post 3:1 H_2/Ar gas from PND data.

Atoms / Site	x	y	z	Occupancy	$100\times$ U_{iso} /U_{eq} (Å^2)
Fe 1 (32e)	0.2940(2)	0.2940(2)	0.2940(2)	0.605(18)	0.41(5)
Co 1 (32e)				0.395(18)	
Fe 2 (16d)	0.500000	0.500000	0.500000	0.914(13)	0.55(5)
Co 2 (16d)				0.086(13)	
Mo (48f)	0.3220(2)	0.125000	0.125000	1.00	0.44(3)
N (16c)	0.000000	0.000000	0.000000	1.00	0.52(5)
Atoms / Site	x	y	z	Occupancy	$100\times$ U_{iso} /U_{eq} (Å^2)
Fe 1 (32e)	0.301(2)	0.301(2)	0.301(2)	0.741(17)	0.39(5)
Co 1 (32e)				0.259(17)	
Fe 2 (16d)	0.500000	0.500000	0.500000	1.00‡	0.53(4)
Co 2 (16d)				0.00‡	
Mo (48f)	0.312(2)	0.125000	0.125000	1.00	0.20(3)
N (16c)	0.000000	0.000000	0.000000	1.00	0.29(4)

‡ - parameter fixed – based on statistic refining to > 1 for Fe 2 and < 0 for Co 2.
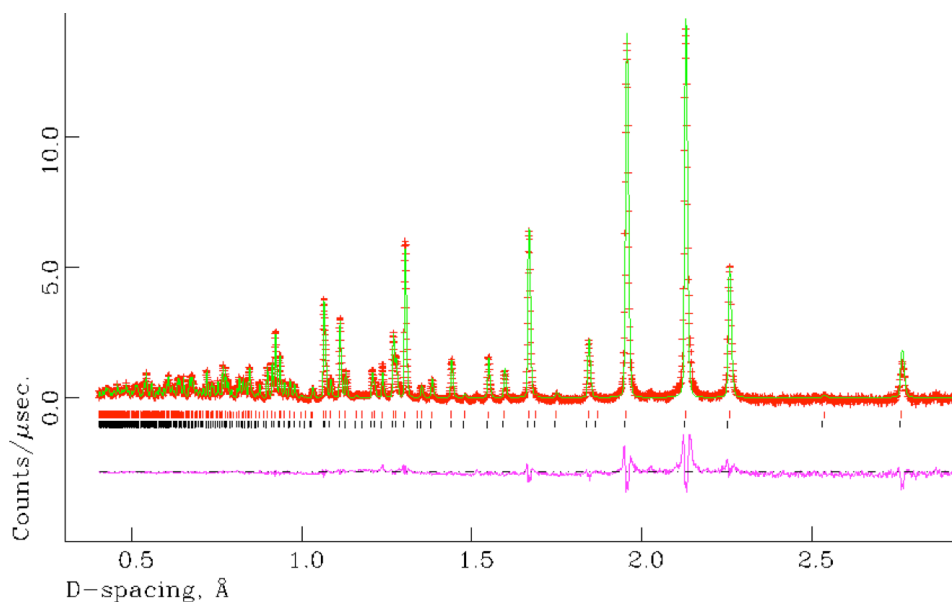
Figure 6-12: Final profile fit obtained from the refinement against PND data at 295 K for sample 3 post 3:1 H_2/Ar gas.

The observed data are crosses, the calculated profile the solid line and lower continuous line the difference plot. Tick marks show allowed reflection positions. Red Tick-marks – $Fe_{2.124}Co_{0.876}Mo_3N$, Black tick-marks – $Fe_{2.482}Co_{0.518}Mo_3N$.

The data shows that two phases were present in all of the samples following reaction. In samples 1 and 2 there was a confirmed reduced '661' phase and an invariant '331' phase; sample 3 showed no presence of a reduced '661' phase and two invariant '331' phases were observed. This behaviour suggested that the quantity of iron present was important in preventing a structural transition and associated loss of N. This is in good agreement with the results for the ternary iron system, Fe_3Mo_3N, which remains unchanged under 3:1 H_2/Ar gas. Therefore the efficacy for reduction is based on the content of the cobalt within the sample; with a cobalt rich sample there is a loss of nitrogen and migration of the remaining nitrogen to the 8a site.

Comparing the stoichiometry and structure of the nitrides to the single phase nitride samples shown by Prior once again show the relationship to those previously seen. This is highlighted in Figure 6-13, in this case the comparison between those prepared here and those prepared by Prior show a better relationship between the two studies. With two of the phases agreeing with the trend seen in the work previously undertaken and reported.
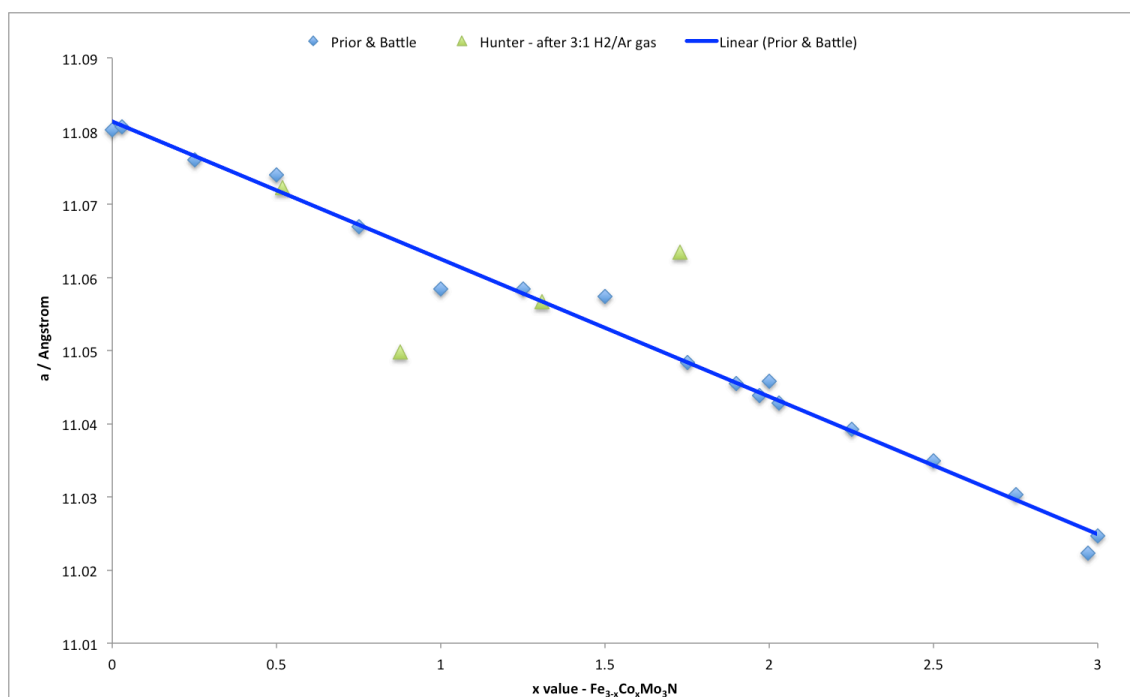
Figure 6-13: Comparison of lattice parameter and stoichiometry post 3:1 H_2/Ar gas reaction.

6.3.3   Nitrogen cycling

As shown above, the reduction of quaternary nitrides to a '661' phase is possible under 3:1 H_2/Ar gas at 973 K although the amount of iron present has a limiting effect on this. The regeneration of reduced compounds was therefore investigated to show whether the system could be cycled, as seen in the Co-Mo-N system. The use of *ex-situ* PND experiments to probe the samples allowed for an accurate determination of the phases present in the system following treatment at 973 K under 3:1 H_2/N_2 gas.

The PXRD patterns for the four samples (Figure 6-14 – Figure 6-17) show that samples 1 and 2 are reducible and can be subsequently regenerated. The nitrogen content of the samples is seen to be reduced from ca. 3 wt% to 2.03(4) and 2.45(7) wt% in the case of sample 1 and 2 respectively, these values as determined by microanalysis add to the findings of the PND diffraction which indicates a mixed phase of '331' and '661' quaternary nitrides which upon regeneration give a nitrogen content of 3.00(4) and 2.95(3) wt% respectively.
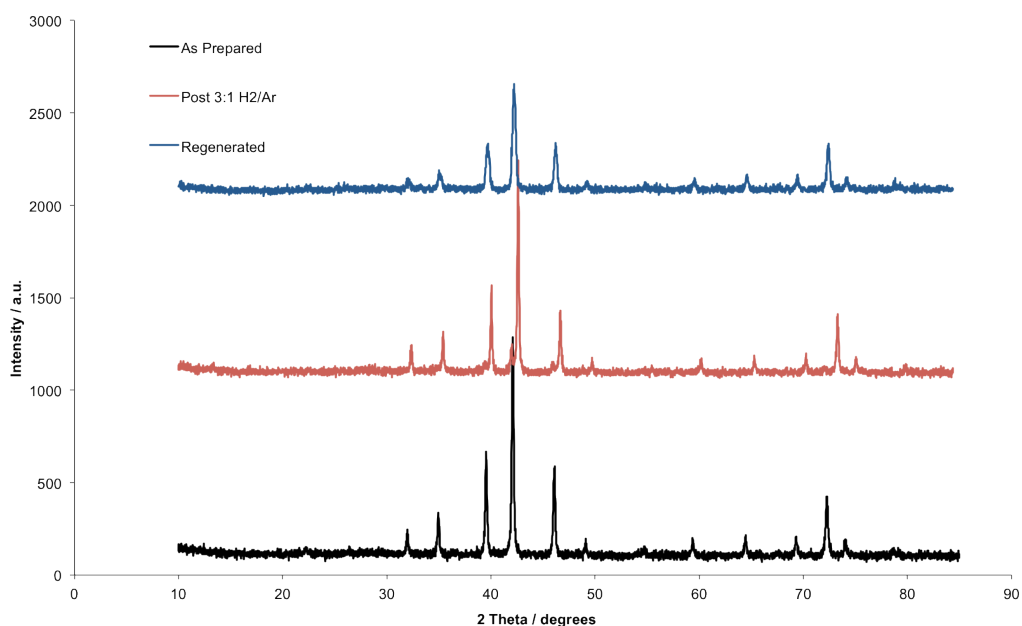
Figure 6-14: PXRD patterns for Sample 1.
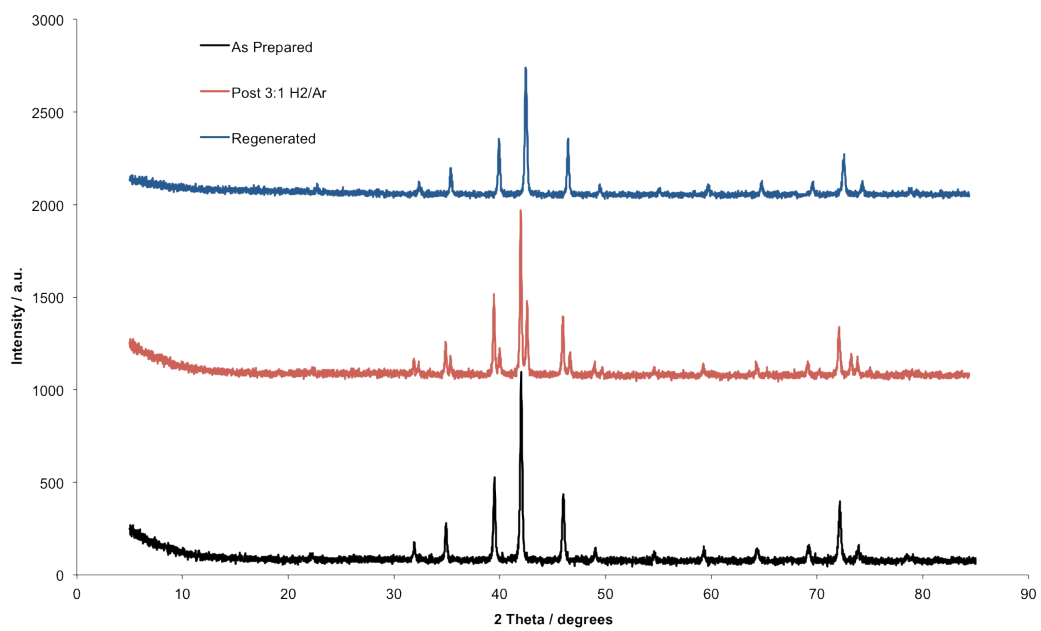
Figure 6-15: PXRD patterns for sample 2.
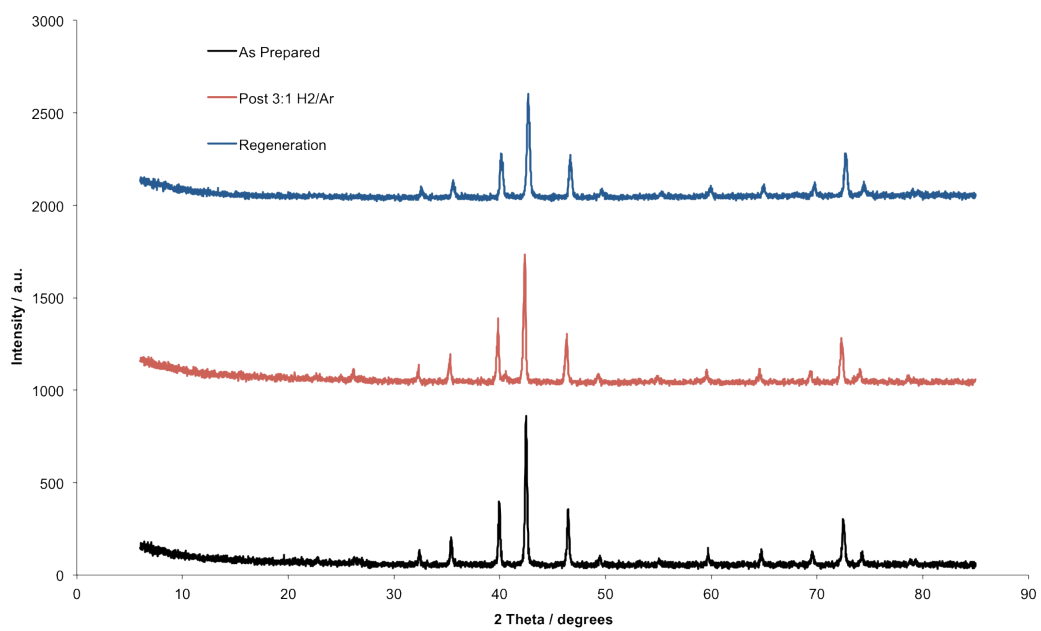
Figure 6-16: PXRD patterns for sample 3.
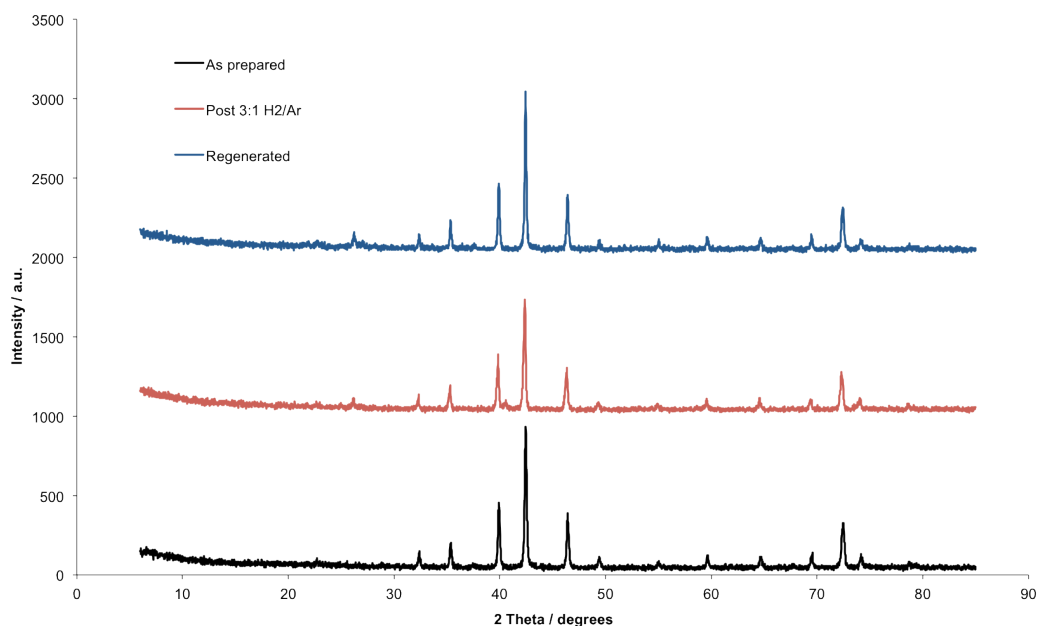
Figure 6-17: PXRD patterns for sample 4.

Table 6-16: Microanalysis results for quaternary nitrides

Sample	Nitrogen / wt%			
	As prepared	**Post Rxn 3:1 H_2/N_2 gas @ 673 K for 6 hrs**	**Post Rxn 3:1 H_2/Ar gas @ 973 K for 6 hrs**	**Regenerated 3:1 H_2/N_2 gas @ 973 K**
1	2.95(2)	3.01(6)	2.03(4)	3.00(4)
2	2.98(3)	2.93(8)	2.45(7)	2.95(3)
3	3.02(4)	2.99(3)	2.89(6)	2.98(6)
4	2.98(3)	2.97(4)	2.89(3)	2.94(5)

As previously noted PXRD data could not be used for accurate determination of the structures of the quaternary nitrides. As discussed in Section 6.3.1, the nitride as prepared consists of two quaternary phases. Upon heating under 3:1 H_2/Ar gas a reduced '661' quaternary phase along with a non-reduced quaternary phase exists.

From the PXRD data and microanalysis results (Table 6-16) it appears that after regeneration at 973 K under 3:1 H_2/N_2 gas the samples are regenerated to a single phase quaternary nitride. To confirm the structure of the samples post-regeneration, PND experiments were performed. The results of the refinements are shown in Table 6-17 – Table 6-20 and Figure 6-18 – Figure 6-20.

Table 6-17: Crystallographic parameters for regenerated quaternary nitrides from PND data.

Parameter	Value		
	Sample 1	Sample 2	Sample 3
Formula [$Fe_xCo_yMo_3N$]	$Fe_{1.08}Co_{1.92}Mo_3N$	$Fe_{1.674}Co_{1.326}Mo_3N$	$Fe_{2.208}Co_{0.792}Mo_3N$
Crystal system	Cubic		
Space group	Fd-3m		
Formula mass / $gmol^{-1}$	7604.628	7575.415	7548.975
Cell parameter, a / Å	11.04214(8)	11.05264(7)	11.05875(4)
Unit-cell volume / $Å^3$	1346.36(2)	1350.20(2)	1352.440(7)
Calculated density ρ_x / gcm^{-3}	9.379	9.317	9.269
Number of observations	3893	3585	3950
Number of variables	22	22	23
R_p / %	2.45	2.38	2.28
R_{wp} / %	1.38	1.53	1.20
χ^2	1.467	1.668	1.386

Table 6-18: Refined atomic parameters for regenerated sample 1 from PND data

Atoms / Site	x	y	z	Occupancy	100× U_{iso} /U_{eq} (Å^2)
Fe 1 (32e) Co 1 (32e)	0.29336(9)	0.29336(9)	0.29336(9)	0.227(7) 0.773(7)	0.57(4)
Fe 2 (16d) Co2 (16d)	0.500000	0.500000	0.500000	0.626(6) 0.374(6)	0.39(3)
Mo (48f)	0.32281(7)	0.125000	0.125000	1.00	0.27(1)
N (8a)	0.125000	0.125000	0.125000	1.00	0.610(2)
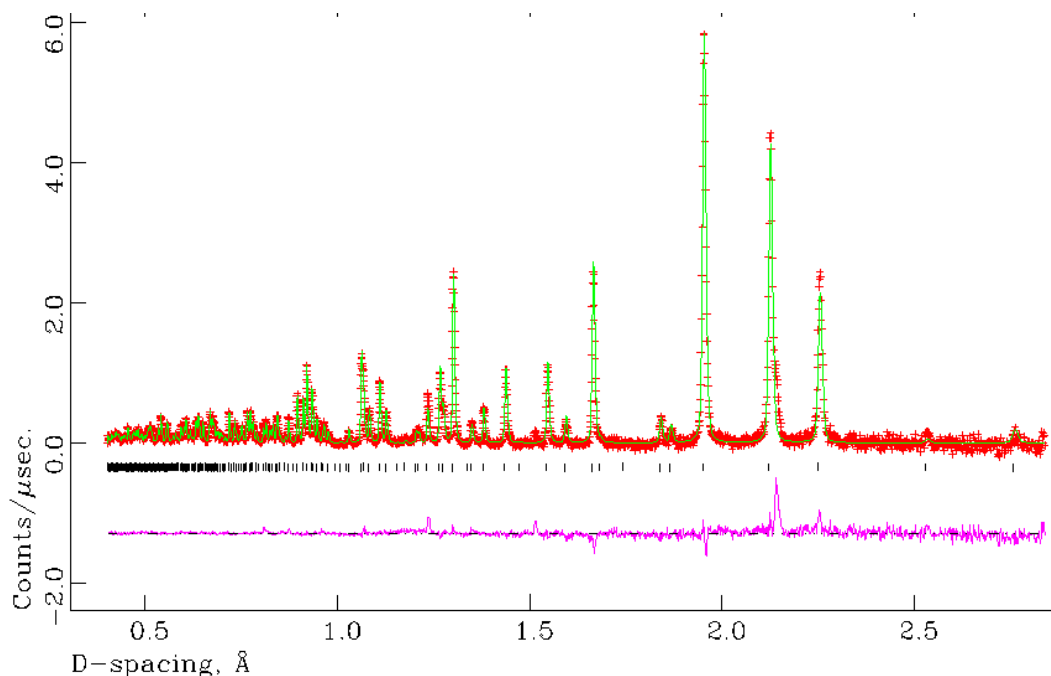
Figure 6-18: Final profile fit obtained from the refinement against PND data at 295 K for sample 1 regenerated with 3:1 H_2/N_2 gas.

The observed data are crosses, the calculated profile the solid line and lower continuous line the difference plot. Tick marks show allowed reflection positions.

Table 6-19: Refined atomic parameters for regenerated sample 2 from PND data.

Atoms / Site	x	y	z	Occupancy	100× U_{iso}/U_{eq} (Å^2)
Fe 1 (32e) Co 1 (32e)	0.29376(6)	0.29376(6)	0.29376(6)	0.416(6) 0.584(6)	0.46(3)
Fe 2 (16d) Co2 (16d)	0.500000	0.500000	0.500000	0.842(6) 0.158(6)	0.53(2)
Mo (48f)	0.32250(6)	0.125000	0.125000	1.00	0.28(1)
N (8a)	0.125000	0.125000	0.125000	1.00	0.44(2)
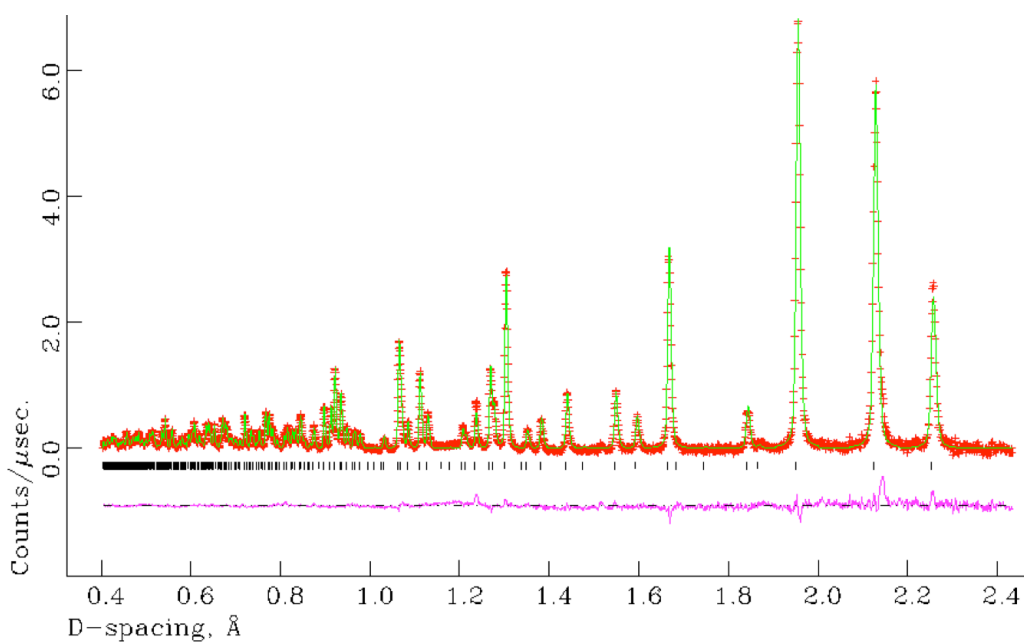
Figure 6-19: Final profile fit obtained from the refinement against PND data at 295 K for sample 2 regenerated with 3:1 H_2/N_2 gas.

The observed data are crosses, the calculated profile the solid line and lower continuous line the difference plot. Tick marks show allowed reflection positions.

Table 6-20: Refined atomic parameters for regenerated sample 3 from PND data.

Atoms / Site	x	y	z	Occupancy	$100\times$ U_{iso} /U_{eq} (Å²)
Fe 1 (32e) Co 1 (32e)	0.29397(2)	0.29397(2)	0.29397(2)	0.642(3) 0.358(3)	0.44(1)
Fe 2 (16d) Co2 (16d)	0.500000	0.500000	0.500000	0.924(3) 0.076(3)	0.488(9)
Mo (48f)	0.32209(3)	0.125000	0.125000	1.00	0.338(6)
N (8a)	0.125000	0.125000	0.125000	1.00	0.610(2)
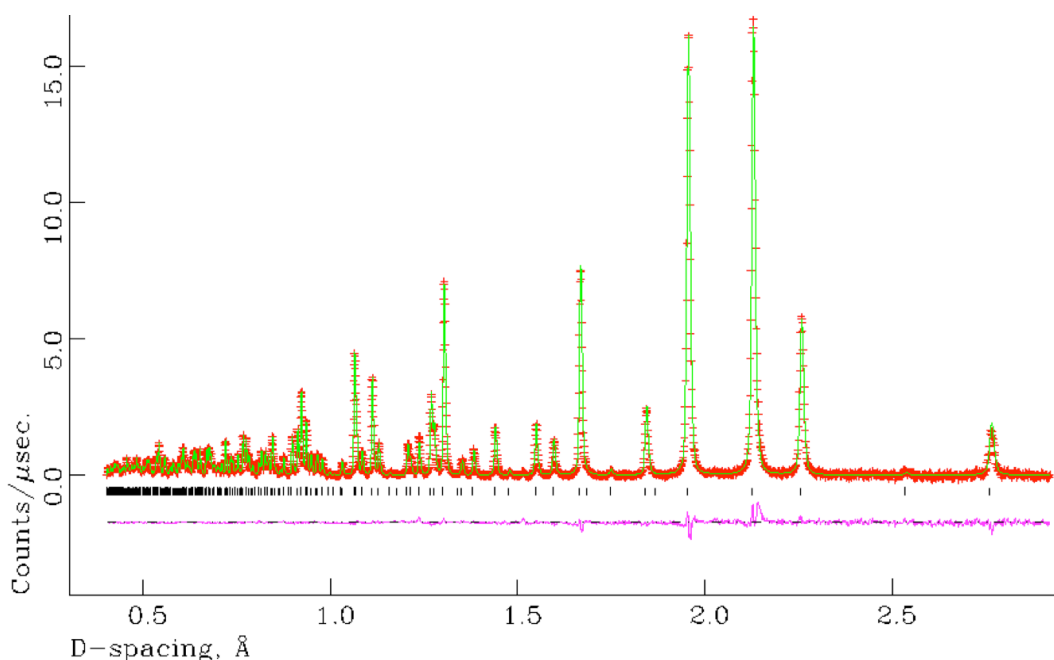
Figure 6-20: Final profile fit obtained from the refinement against PND data at 295 K for sample 3 regenerated with 3:1 H$_2$/N$_2$ gas.

The observed data are crosses, the calculated profile the solid line and lower
continuous line the difference plot. Tick marks show allowed reflection positions.

In contrast to the materials prior to the regeneration which contained two quaternary phases, the results of the refinements strongly suggest that single phase nitrides are formed after regeneration. The structures of the quaternary nitrides are in good agreement with those of nitrides of similar stoichiometry formed from the reduction-nitridation of the oxides as shown by Prior and Battle.[1] The ability to synthesise nitrides via reduction and nitridation shown by Prior and Battle, leads to the proposal that the reduction and re-nitridation stages of the reactions shown above could

be a method to produce single-phase quaternary nitrides for further study – although accurate phase composition of the quaternary nitride is not possible via this method.

Final comparison with the study of Prior and Battle shows that there is a good relationship between those and the nitrides which form after the regeneration stage of the reaction. This relationship is shown in Figure 6-21. This relationship shows that the reduction and regeneration stages of the reaction produces a series of nitrides with lattice parameters and stoichiometries which are in good agreement to those seen from the direct nitridation of the oxides.
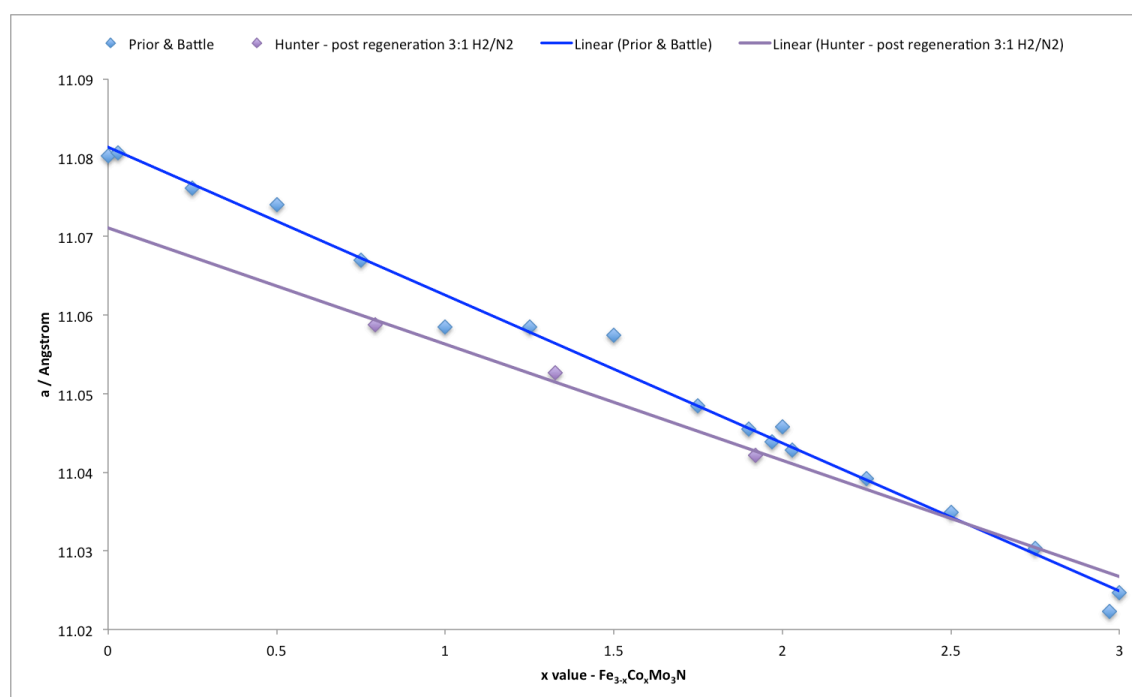
Figure 6-21: Comparison of lattice paramters and stoichiometry of quaternary nitrides post regeneration.

6.4 Summary

This chapter details the synthesis and structure of the quaternary nitrides formed from combining cobalt nitrate and iron (II) chloride with sodium molybdate to yield suitable precursors. It was observed that the route using cobalt nitrate and iron (II) chloride produced two phases, unlike the solid solution method employed by Prior and Battle which produced a pure, single phase samples. Both phases present in the study described in the chapter were quaternary phases, however the ability to control precisely the stoichiometry of the nitride was not possible via the synthetic method used. It may be possible to form single phase samples by altering the heating regime to give a longer

heating stage or applying higher temperatures. Unfortunately, the presence of two phases in the sample does not allow for conclusive determination of the reactivity of each of the quaternary nitride.

The ability to reduce the cobalt rich quaternary nitrides under 3:1 H_2/Ar gas to a 661 system is analogous to the Co_3Mo_3N system. However, the existence of 331 phases which are unchanged after 3:1 H_2/Ar gas treatment is analogous to the Fe_3Mo_3N system. The regeneration process changed the system to a single phase quaternary nitride, the opportunity to explore the properties in relation to reduction or activity was not completed. The structures agree with those previously shown by Prior and Battle and allow for the possibility - although not confirmed - that they are reducible to a single '661' phase. Thus after initial' homogenisation' of the reaction mixture, it might be possible to cycle individual '331' phases (to'661' and back).

6.5   *References*

[1] T. J. Prior and P. D. Battle; J. Mater. Chem.; 14 (2004) 3001.

[2] P. J. Baker, P. D. Battle, S. J. Blundell, F. Grandjean, T. Lancaster, G. J. Long, S. E. Oldham and T. J. Prior; Phys. Rev. B: Condens. Matter; 77 (2008) 134405.

[3] L. A. Sviridov, P. D. Battle, F. Grandjean, G. J. Long and T. J. Prior; Inorg. Chem.; 49 (2010) 1133.

[4] R. L. Kift; Intermetallic Compounds by Reductive Annealing; PhD Thesis, University of Hull, 2010.

7   Conclusions and future work

7.1   Conclusions

In this thesis the structure and reactivity of a series of binary, ternary and quaternary molybdenum containing nitrides have been investigated. The experimental work conducted during this project identified the structural characteristics and the activity of the nitrides. For structural analysis, a combination of powder X-ray and neutron diffraction (PXRD and PND) and microanalysis results were utilised. Reactivity testing employed the use of a standard reaction producing ammonia as a method of comparing the phases.

The work completed on the binary systems focussed on structural investigations of the three phases of molybdenum nitride; beta, delta and gamma. Previous investigations on the binary nitrides had given a complete reactivity study, hence the structural information collected during this project was used in an attempt to correlate the reactivity with structure, stoichiometry and phase compositions.

The beta molybdenum nitride structure was confirmed – crystallising in tetragonal space group $I4_1/amd$ with a stoichiometry of $Mo_2N_{0.8}$. The stoichiometry, which had been reported in several variants in previous work, has been shown to be invariant when reacted under 3:1 H_2/N_2 gas and 3:1 H_2/Ar gases.

Gamma molybdenum nitride was confirmed by PND as crystallising in the cubic space group Fm-3m. In contrast to previous studies it was shown that there is an excess of nitrogen present in the sample which raised the apparent stoichiometry to $Mo_2N_{1.2}$.

Beta and gamma molybdenum nitrides were active for ammonia synthesis under 3:1 H_2/N_2 gas at 673 K. During the reaction the structure of the nitrides remained unchanged with the phases being active as ammonia synthesis catalyst throughout the course of the test procedure.

The work completed on the Co-Mo-N system thoroughly investigated the structure and activity of the phases. The initial Co_3Mo_3N (331) phase was confirmed by PXRD and PND diffraction. The reactivity testing of Co_3Mo_3N under 3:1 H_2/N_2 gas at 673 K showed no change to the structure of the nitride phase with the PXRD, PND and microanalysis results invariant from those seen prior to the reaction. This confirmed the

findings seen previously that the structure and nitrogen content are invariant when reacted under 3:1 H_2/N_2 gas.

Work previously completed by others on Co_3Mo_3N focussed on the structure of the nitride and a separate investigation focussed on the activity. The possible use of Co_3Mo_3N as a 'reservoir' of activated nitrogen had however not been considered. This was therefore studied through the use of diffraction and reactivity studies.

Using 3:1 H_2/Ar gas, the activity of the lattice nitrogen was probed; results shown from PXRD indicate a shift in the post reaction diffraction pattern and in combination with the reduction in nitrogen content confirmed the findings of Mckay. Experiments completed during this project confirmed the proposed structure for the new Co_6Mo_6N phase ('661'), which crystallises in the cubic space group *Fd-3m* isostrucutral with Co_6Mo_6C. Analysis of the crystallographic information has shown that ~50 % of the nitrogen in Co_3Mo_3N can be released in the presence of hydrogen and the remaining nitrogen migrates within the Mo-N sub-lattice.

The release of nitrogen was shown by the production of ammonia and nitrogen under 3:1 H_2/Ar gas. In order to be a viable store of activated nitrogen the nitrogenated phase needed to be restorable. The Co-Mo-N system has been shown to be fully reversible by reaction with 3:1 H_2/N_2 gas and under harsher conditions, with pure N_2. These results allow for possibilities as to the use of Co_3Mo_3N as a store of activated nitrogen. The ability to regenerate the system with nitrogen in the absence of hydrogen is economically and environmentally preferred.

It was observed that the surface of the nitride was loaded with NH_x species, which were able to be removed through treatment with Ar gas at elevated temperatures. Even with no surface NH_x species Co_3Mo_3N is a viable store of nitrogen. Evidence shows that the nitride retains an ability to produce ammonia once surface NH_x species are removed, although the amount of ammonia produced is only 30% of that obtainable otherwise.

Experiments showed that in order for the 331 phase to be reduced to the 661 phase the gas needs to contain hydrogen, which creates vacant sites on the surface. Once created the vacant site can be repopulated by nitrogen in the feed gas perpetuating the reaction cycle and reversibly producing ammonia.

Other ternary systems (iron molybdenum and nickel molybdenum nitride) were investigated in order to compare their structure and properties to the Co-Mo-N system. The analogously structured iron molybdenum nitride was formed via nitridation of

ferrous molybdate obtained from the iron (II) chloride and sodium molybdate. This method of synthesis gave a pure phase of Fe_3Mo_3N which allowed for a full characterisation by PXRD and PND. The comparison with Co-Mo-N showed that the iron system had a lower activity than Co_3Mo_3N for ammonia synthesis under both 3:1 H_2/N_2 gas and 3:1 H_2/Ar gas. Unlike the cobalt system under 3:1 H_2/Ar gas there was no change in the structure of the nitride. The system remains in the η-6 carbide structure throughout the reaction, with the nitrogen occupying the 16c site.

The nickel molybdenum nitride, Ni_2Mo_3N, crystallises with the β-Mn structure with cubic space group, $P4_132$. The diffraction data also show that a Ni metal impurity was present in all samples prepared. This impurity accounts for the total ratio of Ni:Mo in the system given the stoichiometry of the ternary phase. The data from the reactivity study shows that Ni_2Mo_3N is the least active of the three ternary systems studied. As with the iron molybdenum nitride, the structure of the nitride is unchanged after reaction with 3:1 H_2/Ar gas and also the nitrogen content is not changed. This could be explained through the nitrogen occupying a site which gives a very distorted octahedral arrangement within the lattice of the β-Mn structure.

Given the differences between the isostructural Fe_3Mo_3N and Co_3Mo_3N systems when reacted under 3:1 H_2/Ar gas (i.e. that a 661 phase is only observed in the cobalt system) a study of the quaternary Fe-Co-Mo-N phase system was undertaken. The quaternary phases formed were η-6 carbide structures material with both iron and cobalt occupying the 32e and 16d sites. Diffraction studies showed that there was a mixture of two quaternary phases present in each sample as prepared. Under 3:1 H_2/Ar gas the more cobalt-rich samples exhibited a possible reduction to the 661 phase compared with the more iron-rich samples show no such reduction. The systems were also shown to regenerate back to a single 331 phase under 3:1 H_2/N_2 gas at 973 K. The cyclability of the system implies its use as a store of activated nitrogen which can be exhausted and replenished under 3:1 H_2/N_2 gas and 3:1 H_2/Ar gases respectively.

7.2 *Future Work*

7.2.1 Ternary systems:

The Ni_3Mo_3N phase (known to be formed for the carbide Ni_3Mo_3C) remains a target material, which analogously to Fe_3Mo_3N and Co_3Mo_3N, would allow for comparison of activity vs structure vs valence electron count (electronic structure). This would allow for a complete comparison of the η-carbide structures in terms of the lattice nitrogen mobility.

Additionally a series of Co_xMo_yN systems (analogous to the Co_2Mo_4C, which crystallises into the η-6 carbide structure also) could also be investigated to see if the mobility of nitrogen is restricted to the Co_3Mo_3N stoichiometry alone or if the nitrogen is still mobile with a reduced Co content sample.

7.2.2 Quaternary systems:

The ability to form single phases of the nitride as shown by the reduction and regeneration of the quaternary systems in Section 6.3 present an opportunity for full characterisation of the systems. The ability to complete a full set of reactivity experiments on single phase samples accompanied by complimentary diffraction experiments would allow for a measure of the mobility of nitrogen within the lattice as a function of structure and stoichiometry.

The possibility that the quaternary systems behave similarly to the ternary systems, dependent on the content of the cobalt and iron, has not been fully investigated and would require the use of PND to confirm the structural changes in the system. Ideally a complementary parallel computational study might provide a route to understand the complex relationship between structure – composition – activity and physical properties Further work on other quaternary systems containing Co, Ni and Fe could be undertaken to expand the range of interstitial nitrides investigated. Work conducted previously has shown trying to add Ni into the cobalt system to produce a quaternary nitride changes the structure from an η-carbide to a β-Mn structure. These quaternary phases have not been studied for activated nitrogen storage. By studying more systems, it may become possible to predict the phases and target syntheses towards them accordingly.

8   Appendices

8.1   *Appendix 1 – Conductivity Measurements*

The mean conductivity of six different 0.0018 mol L^{-1} solutions of H_2SO_4 and $(NH_4)_2SO_4$ was determined. The Table below shows the conductivities observed:

Conductivity H_2SO_4 / μScm^{-1}	Conductivity $(NH_4)_2SO_4$ / μScm^{-1}
959	313
953	301
943	302
949	307
934	308
951	304
Mean ~ 948	Mean ~ 305

The calculations illustrate how the ammonia production rates were calculated with respect to the conductivity versus time plot for every ammonia synthesis experiment.

Moles of H_2SO_4 =   Concentration (H_2SO_4) x Volume (H_2SO_4)

=   0.00108 mol L^{-1} × 0.2 L

= 2.16×10^{-4} moles

Due to stoichiometric considerations 4.32×10^{-4} moles of ammonia are required to completely react with H_2SO_4.

Change in conductivity for reaction:

$H_2SO_4 + 2NH_3$ → $(NH_4)_2SO_4$

= 948 μScm^{-1} – 305 μScm^{-1}

= 643 μScm^{-1}
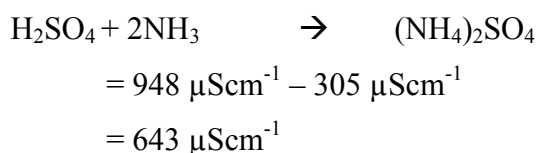
Number of moles of ammonia required / Total change in conductivity

= 4.32×10^{-4} moles / 643 μScm^{-1}

= 6.72×10^{-7} mol/μScm^{-1}

The gradient of the conductivity (μScm^{-1}) versus time plots are determined by multiplying the resultant value by the calibration value (6.72×10^{-7} mol/μScm^{-1}) and dividing by the mass of the material investigated (0.4g). As such the mass normalised ammonia production rate can be determined.

Under reaction conditions using a 3:1 H_2/N_2 gas mixture and operated at 673 K and 1 atm pressure, NH_3 has a limiting yield of 0.4 mol%.[1]

From the above information a theoretical equilibrium NH_3 synthesis rate can be calculated as shown below:

$$0.4 \text{ mol\% x } 60 \text{ mL.min}^{-1} = 0.24 \text{ mL.min}^{-1}$$

$$\frac{0.24 \text{ mL.min}^{-1}}{22400 \text{ mL(molar gas volume)}} = 1.07 \times 10^{-5} \text{moles.min}^{-1}$$

$$1.07 \times 10^{-5} \text{ moles.min}^{-1} \text{ x } 60 \text{ min} = 6.4285 \times 10^{-4} \text{ moles.hr}^{-1}$$

$$\frac{6.4285 \times 10^{-4} \text{ moles.hr}^{-1}}{0.4 \text{g (mass of material)}} = 1.607 \times 10^{-3} \text{ mol.g}^{-1}\text{hr}^{-1} = 1607 \ \mu\text{mol.hr}^{-1}\text{g}^{-1}$$

8.2   *References*

[1] M. Nagai; Appl. Catal. A: Gen.; 322 (2007) 178.